Radio Continuum Emission as a Star Formation Tracer: Bridging the Spatial Scales

Supervised by:
Prof. E. Brinks
Dr. R. Beswick
Dr. D.J.B. Smith

Author:
Jonathan Westcott

Centre for Astrophysics Research
School of Physics, Astronomy and Mathematics
University of Hertfordshire

Submitted to the University of Hertfordshire in partial fulfilment of the requirements of the degree of Doctor of Philosophy.

November 2018

Abstract

Radio continuum emission has been demonstrated to be an excellent tracer of recent star formation, yet current understanding remains empirical, and is primarily based upon integrated multi–frequency or resolved mono–chromatic radio continuum studies. In this thesis, we gain further insight into the relationship between the observed radio continuum emission and recent star formation through the use of spatially resolved, multi–frequency radio continuum observations, focusing our analysis on the relatively simple star–forming dwarf irregular galaxies, IC 10 and NGC 1569.

High—resolution ($\sim$1 pc) 1.5 GHz and 5.0 GHz e–MERLIN observations of IC 10, combined with a multi–wavelength classification scheme, reveal that the majority of the compact star–formation products found within low mass, star forming galaxies are HII regions, with radio supernova and supernova remnants being observed more rarely. By taking a census of these star–formation products, we derive useful lower limits on the instantaneous star–formation rate in this simple stellar system. We further demonstrate that high–resolution observations can be used to remove the contribution of contaminating background galaxies to integrated galaxy radio spectra, which can be a significant correction in very low mass systems.

On larger spatial scales ($\sim$100 pc), we developed a Bayesian Markov–Chain Monte–Carlo approach to separate the thermal and non–thermal radio continuum emission components on a resolved basis. We applied this procedure to VLA observations of NGC 1569 that span a wide frequency range (1–34 GHz). During our fitting procedure, we use Hα maps found in the literature to constrain the thermal radio continuum emission component. We find that NGC 1569 exhibits a high average thermal fraction at 1 GHz ($\sim$25%) which is in line with recent integrated studies, and that the average non—thermal spectral index for the main disk is $\alpha = -0.53$, which is consistent with the injection spectrum found in galactic supernova remnants. Taken together, these results indicate that NGC 1569 has recently finished a star formation burst, which is in close agreement with the literature where this galaxy is classified as being in a post–starburst phase, and that supernova remnants are the predominant source of cosmic ray electrons in this system. We further demonstrate that the resulting maps from our separation procedure can be used to further constrain additional quantities, such as the line of sight reddening at arcsecond resolution, providing for example a measure of internal extinction by dust in NGC 1569's HII regions as well as spatially resolved equipartition magnetic field strengths.

With our low–resolution VLA observations, we found that the supernova remnant, NGC1569–38, exhibits a break in its radio spectral energy distribution at ~ 7 GHz. We followed this observation up with e–MERLIN observations of NGC 1569 and found that the surrounding Interstellar Medium significantly contributes to the observed spectral energy distribution in the lower resolution maps. Based on NGC1569–38's observed surface brightness and minimum energy magnetic field strength compared to a sample of galactic and extra—galactic supernova remnants, we determine that NGC1569–38 is young and is just entering the Sedov–Taylor phase of expansion. We demonstrate that the observed break in a spatially resolved radio continuum spectral energy distribution of a young supernova Remnant, even at resolutions of about 100 pc, is due to contamination by emission from the surrounding Interstellar medium. To reveal effects such as cosmic ray electron ageing, higher resolution, matched to the size of the supernova remnant, multi–frequency radio spectra are required.

Declaration

I declare that no part of this work is being submitted concurrently for another award of the University or any other awarding body or institution. This thesis contains a substantial body of work that has not previously been submitted successfully for an award of the University or any other awarding body or institution.

The following parts of this submission have been published previously and/or undertaken as part of a previous degree or research programme:

1. Chapter 2 has been published as Westcott et al., 2017, *Monthly Notices of the Royal Astronomical Society*, **467**, 2113.
2. Chapter 3 has been published as Westcott et al., 2018, *Monthly Notices of the Royal Astronomical Society*, **475**, 5116.

Except where indicated otherwise in the submission, the submission is my own work and has not previously been submitted successfully for any award.

Acknowledgements

There are truly too many people to thank for their contributions to my thesis, but here I will have a go!

First and foremost, I would like to express my sincere gratitude to my supervisor Prof. Elias Brinks for his support over the duration of my PhD. His expertise and guidance has helped to shape my understanding of all aspects of radio astronomy and star formation over the last few years, for which I am eternally grateful.

Next, I would like to thank the other members of my supervisory team, Dr Rob Beswick and Dr Dan Smith, for their many useful comments and discussions over the course of this study. Without which, this thesis would not have been completed to the standard it is today.

I would also like to extend a special thanks to Volker Heesen and Luke Hindson for sharing their insight and time, both of which I am incredibly thankful for.

I cannot express my appreciation enough to all of the staff, students and friends I have made at the Centre for Astrophysics Research, in particular my office mates both past and present (as well as those next door!). Our conversations may not have been entirely physics related, but they were always incredibly entertaining!

Penultimately, I would like to thank Brian May for his incredibly generous financial contribution over the course of my Masters degree. If it wasn't for him, I would not be in this position today.

Finally, I would like to extend my appreciation to my friends and family for their incredible support over this journey. In particular, I would like to thank Ben, Rob, Rich, Tim, Matt, Adam, Will, Tom, Josh, Jim, Jack, Jono and Pat for being the best distractions I could hope for over the duration of my PhD. I would also like to specially thank my Grandfather, Herrick, for always taking a keen interest in my work, and finally, my parents for their generous support in all aspects of my life. Words cannot express how truly thankful I am.

Contents

List of Figures

List of Tables

List of Abbreviations

Acronym	**W**hat (it) **S**tands **F**or
AGN	Active Galactic Nuclei
AIPS	Astronomical Image Processing Software
CASA	Common Astronomy Software Applications
CRe	Cosmic Ray Electron
DSA	Diffusive Shock Acceleration
dIrr	Dwarf Irregular
e–MERLIN	The Expanded Multi Element Radio Linked Interferometer Network
FIR	Far–Infrared
FUV	Far–Ultraviolet
IF	Intermediate Frequency
IMF	Initial Mass Function
IRAS	The Infrared Astronomical Satellite
ISM	Interstellar Medium
LMC	Large Magellanic Cloud
LeMMINGs	Legacy e–MERLIN Multi–Band Imaging of Nearby Galaxies Survey
LITTLE THINGS	Local Irregulars That Trace Luminosity Extremes, The HI Nearby Galaxy Survey
LOFAR	The Low Frequency Array
MCMC	Markov–Chain Monte–Carlo
MERLIN	The Multi Element Radio Linked Interferometer Network
MWA	The Murchison Widefield Array
ngVLA	Next Generation Very Large Array
RFI	Radio Frequency Interference

SMC	Small Magellanic Cloud
SED	Spectral Energy Distribution
SFR	Star Formation Rate
SKA	The Square Kilometer Array
SN	Supernova
SNe	Supernovae
SNR	Supernova Remnant
SNRs	Supernova Remnants
UV	Ultraviolet
VLA	The Very Large Array
WR	Wolf–Rayet
WSRT	The Westerbork Synthesis Radio Telescope

Chapter 1

Introduction

1.1 The Link Between Radio–Continuum Emission And Star Formation

The link between radio continuum emission and massive stars ($\geq 8\,\mathrm{M}_{\odot}$) has been established since Bolton and Stanley (1949) first identified the Crab Nebula supernova remnant (SNR) as a bright, compact radio continuum source. Soon after this initial discovery, numerous other compact radio sources observed within the Milky Way were associated with known SNR (Hanbury Brown and Hazard, 1952; Baade and Minkowski, 1954) with Shklovskii (1953) identifying the synchrotron emission mechanism as the process producing the observed radio continuum emission (see the left panel of Figure 1.1). Synchrotron emission is emitted by cosmic ray electrons (CRe) that are interacting with magnetic fields, in this case magnetic fields found within the SNR themselves, and is characterised by a steep power–law spectrum at radio frequencies. Subsequently, the Rosette Nebula HII region was also observed to be a compact radio source by Ko and Kraus (1955), with the observed emission being attributed to the bremsstrahlung emission mechanism. Bremsstrahlung emission originates from the free–free interactions between charged particles in an ionised plasma (typically in a HII region; see the right panel of Figure 1.1), and is characterised by a flat power–law flux density spectrum at radio frequencies. Even from these early observations, it was clear that the products of massive star formation and evolution could explain many of the compact radio sources that are observed in the star–forming disk of the Milky Way. However, the origin of a

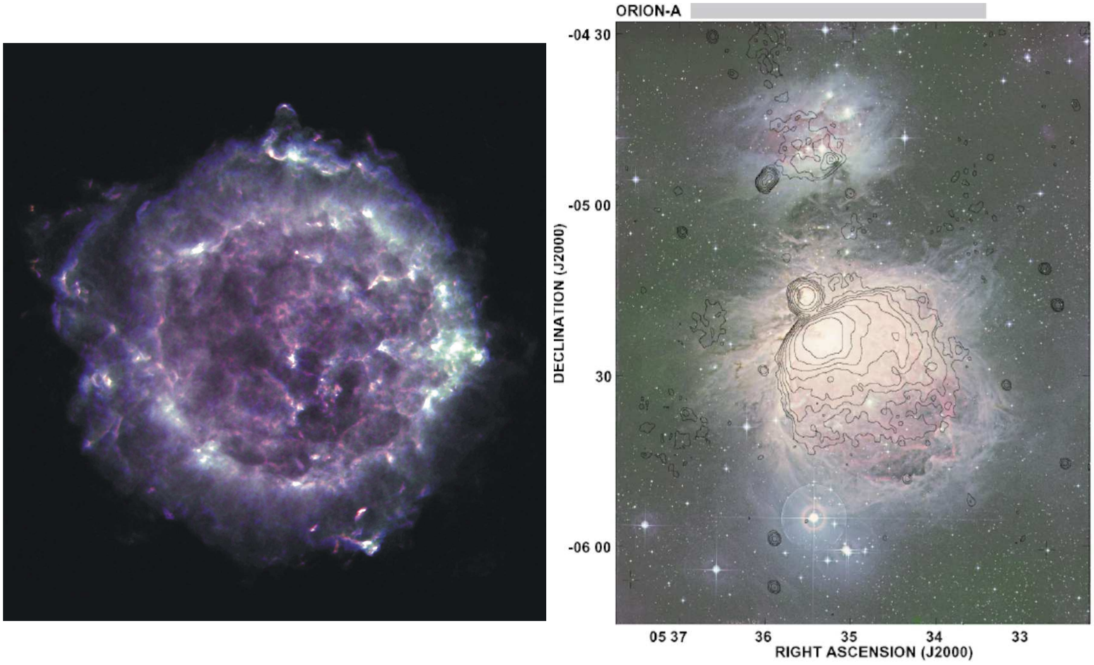

FIGURE 1.1: **Left Panel:** $6' \times 6'$ VLA colour radio map of the SNR Cassiopeia A, constructed from maps at 1.5 (red), 5.0 (green) and 10.0 GHz (blue). The colourscheme has been manipulated such that white regions correspond to regions of ongoing particle acceleration. Credit for the image goes to L. Rudnick, T. Delaney, J. Keohane, B. Koralesky and T. Rector from the NRAO (National Radio Astronomy Observatory). The white regions show where . **Right Panel:** 330 MHz VLA contours of the Orion Nebula, superimposed on a UK Schmidt photograph, taken from Subrahmanyan et al. (2001). The colours on the UK Schmidt photograph were constructed from plates taken in B, V and R Johnson–Cousins filters.

fainter, diffuse non–thermal disk and halo component that was also seen in these early observations remained a mystery (Large et al., 1959; Mills, 1959; Hanbury Brown and Hazard, 1959, 1960).

Shortly after these early observations were made, Ginzburg and Syrovatskii (1964) proposed that the diffuse non–thermal disk and halo components could be attributed to CRe, which were initially accelerated in supernova (SN) explosions, diffusing away from their sites of acceleration whilst interacting with magnetic fields found in the interstellar medium (ISM). Whilst these CRe diffuse throughout the ISM, they undergo numerous energy loss processes (including escape from the galaxy) which modify the radio spectrum they produce from the simple power–law they exhibit at injection. This interpretation gained traction with the development of Aperture Synthesis Interferometry (Ryle and Hewish, 1960), as nearby galaxies were now available to be studied at ~ arcmin resolutions. These higher resolution studies found that the distribution of young stars is correlated with the observed radio continuum emission (Pooley, 1969a,b;

Lequeux, 1971), yet the 'smeared out' nature of the non–thermal emission due to CRe transport continued to complicate the conclusive identification of SN explosions as the source of CRe (van der Kruit et al., 1977). The discovery of the diffusive shock acceleration mechanism (DSA; Krymskii, 1977; Axford et al., 1977; Bell, 1978a,b; Blandford and Ostriker, 1978) provided a convenient process to accelerate the charged particles in SNR shock fronts, and successfully explained both the radio properties of Galactic SNR (Harris, 1962; Lerche, 1980) and the cosmic ray energy spectra seen in particle detection experiments (e.g., Zavrtanik, 2000). These findings provided significant evidence that SN explosions are the principal accelerators of CRe, a view that is still currently being tested with gamma ray observations of SNR shock fronts interacting with molecular clouds (e.g., Tang, 2018).

From these $\sim 50\,\mathrm{yr}$ of observations, a simple paradigm emerges where the radio continuum emission from a normal star–forming galaxy[1] encompasses two main components; a thermal component originating from the ionised gas surrounding massive stars and a non–thermal component originating from cosmic ray electrons, which have been accelerated when these massive stars end their lives in supernova explosions, interacting with magnetic fields in the ISM (Condon, 1992). As both of these components are closely related to massive star evolution, and the typical lifetimes of massive stars are (in astronomical terms) very short (a few million years; e.g., Kennicutt and Evans 2012), radio continuum emission in principle offers a unique tracer of recent star–formation that is insensitive to the effects of extinction that plague other well studied star–formation indicators (such as optical spectral line emission or UV continuum emission; Calzetti 1997).

This link however was not truly recognised until the discovery of the Radio–FIR correlation by Helou et al. (1985). Using the IRAS telescope (Neugebauer et al., 1984, The Infrared Astronomical Satellite;), Helou et al. (1985) found that the observed far–infrared (FIR) emission is tightly correlated with $1.4\,\mathrm{GHz}$ radio continuum emission for star–forming galaxies, a relationship which was demonstrated to hold over at least 4 orders of magnitude in radio luminosity by Yun et al. (2001) (see Figure 1.2). As the FIR emission originates from dust that is heated by embedded massive stars and is frequently

---

[1] A normal star–forming galaxy is defined by Condon (1992) as a galaxy where the observed radio continuum emission does not originate from an Active Galactic Nuclei (AGN).

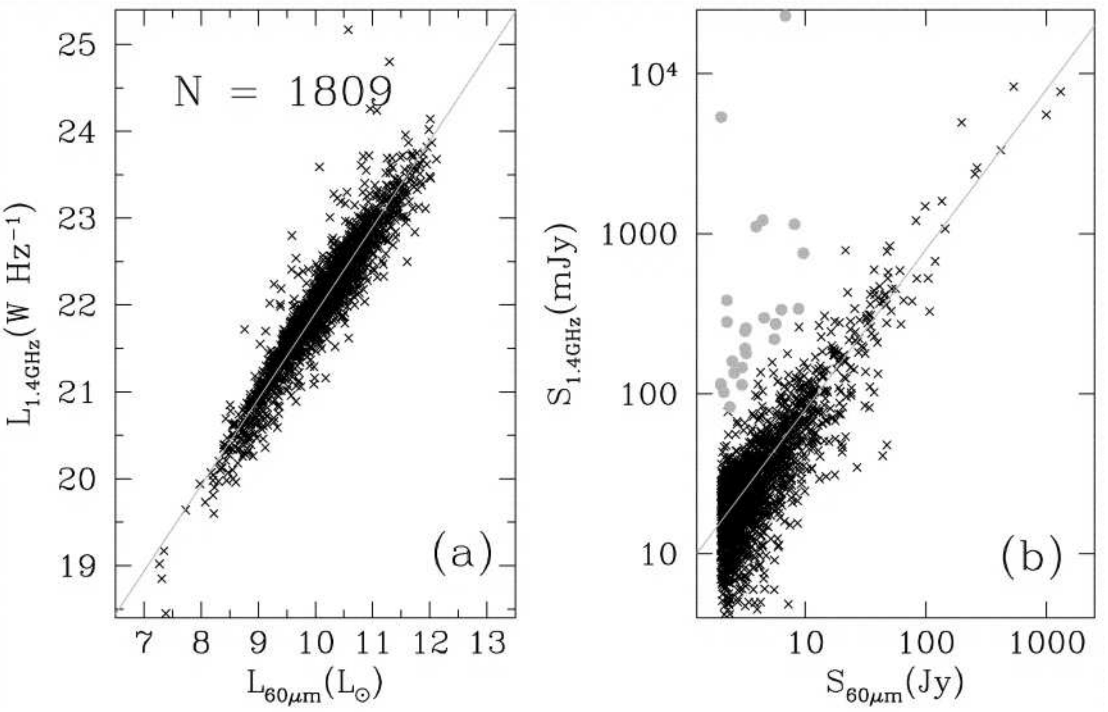

FIGURE 1.2: The Radio–FIR correlation taken from Yun et al. (2001). The left plot shows the 60 μm FIR luminosity from the IRAS 2 Jy survey (Strauss et al., 1990), plotted against the corresponding 1.4 GHz radio continuum luminosity from the NVSS survey (Condon et al., 1998). The right plot shows the observed flux densities the luminosity relationship is based on. The diagonal line corresponds to a one–to–one relationship between the radio and FIR luminosities (flux densities).

used as a robust star–formation rate tracer (Kennicutt, 1998; Calzetti et al., 2010; Kennicutt and Evans, 2012), the near linearity of this relationship shows that radio continuum emission can also be used as a robust tracer of recent star–formation (Condon, 1992; Kennicutt and Evans, 2012). As the observed radio continuum–FIR correlation is tight, and the physics driving the observed radio continuum emission is complex, radio continuum–star formation relationships are frequently bootstrapped from FIR–star formation rate relations (e.g., Bell, 2003). However this methodology is only motivated by the breadth and tightness of the correlation, as neither the FIR nor synchrotron radio continuum emission directly trace star–formation. Neither is there a simple physical mechanism that directly relates the two emission processes. Numerous authors in the literature have attempted to explain the origin of the observed correlation. Völk (1989) argues that the correlation follows if galaxies act as a calorimeters, where nearly all of the UV emission from the massive stars is absorbed and re–emitted in the FIR by dust, and the CRe responsible for the synchrotron emission radiate all of their energy whilst trapped within the galaxy. However, these conditions are only met in larger

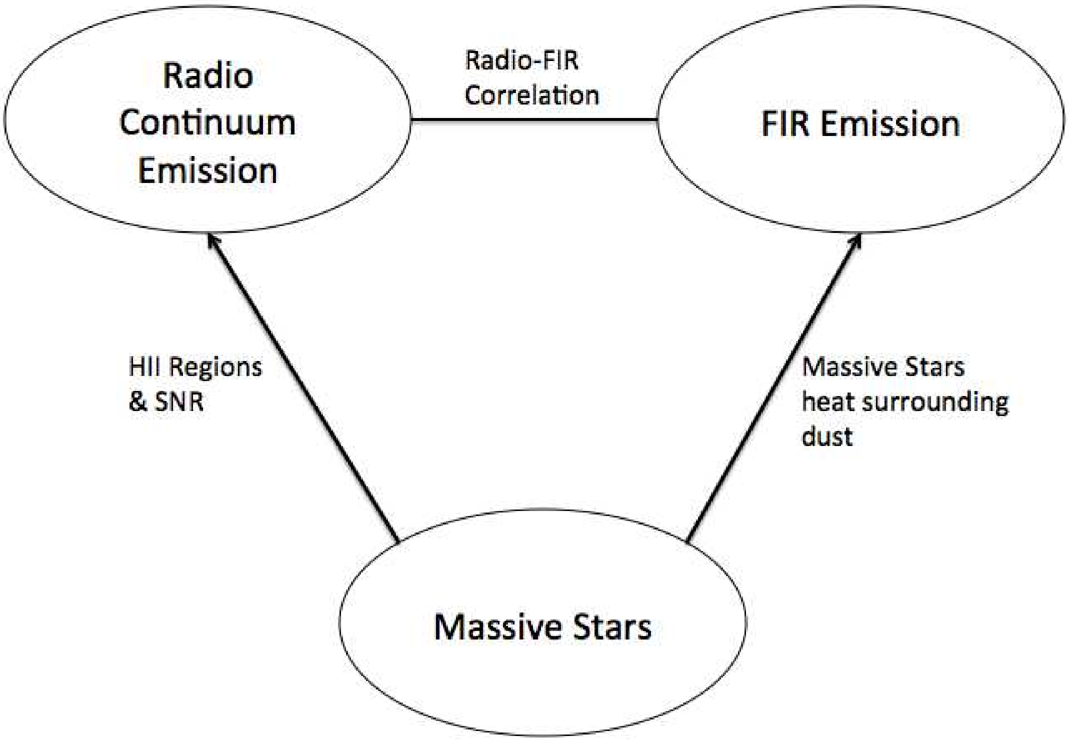

FIGURE 1.3: Schematic showing the relationship between massive stars and radio–continuum and FIR emission. Note that the radio–continuum emission and the FIR emission are not directly linked to one another.

star–forming galaxies, whereas, in smaller galaxies observations show that the dust does not fully absorb the UV photons from the massive stars (e.g., Wang and Heckman, 1996). Yet the Radio–FIR correlation is confusingly still observed to hold for these smaller systems (Bell, 2003; Roychowdhury and Chengalur, 2012; Hindson et al., 2018).

To explain why the correlation persists in smaller galaxies, many independent conditions need to be met which gives rise to what is known as the Radio–FIR 'conspiracy' (Bell, 2003; Lacki et al., 2010), and greatly reduces the confidence in the star formation rates derived through the Radio–FIR correlation (at least for smaller systems). Rather than study how the observed radio continuum emission relates to star–formation through the radio continuum–FIR correlation, it is more direct to instead understand the physics governing the radio continuum properties of a galaxy, and formulate a radio continuum–star formation relationship, based upon radio continuum emission alone (see Figure 1.3).

The aim of this thesis is to gain further insight into the relationship between the observed radio–continuum emission and recent star–formation by studying the relatively simple stellar systems, IC 10 and NGC 1569, at a multitude of spatial scales and spectral frequencies.

1.2 The Radio Continuum Emission Mechanisms

To be able to interpret the observed radio–continuum emission from a normal star–forming galaxy, we first need to understand the emission mechanisms responsible for the radio emission. Here we discuss the two relevant emission mechanisms (bremsstrahlung and synchrotron) in more detail.

1.2.1 Bremsstrahlung (Thermal) Radio Continuum Emission

Plasma is a state of matter that occurs when a gas is supplied with enough energy to dissociate electrons from their atomic nuclei, and is frequently observed in astronomical sources. In a plasma, charged particles undergo free–free Coulomb interactions (i.e., interactions where the charged particles remain unbound both before and after the interaction) and experience acceleration. The radiation produced by these accelerating charges is known as bremsstrahlung (or free–free) emission. The following largely follows the treatment presented in Longair (2011).

To derive the bremsstrahlung emission characteristics, we first consider the emission properties from a single free–free interaction. In this scenario, we assume an electron travelling at velocity, v, passes by an ion with charge Ze. We also assume that at time, t, the electron is at its closest approach to the ion with impact parameter b. As the electron has a much lower mass than the charged ion, we can assume that the ion is stationary for the interaction and it is the electron that undergoes acceleration and produces the observed radiation. Also, we assume that the electron is moving fast enough, so that its path is not significantly modified by the interaction, but not so fast that relativistic effects need to be taken into account (see Rybicki and Lightman 1979, or Longair 2011, for more detailed discussions). We present a schematic for this scenario in Figure 1.4.

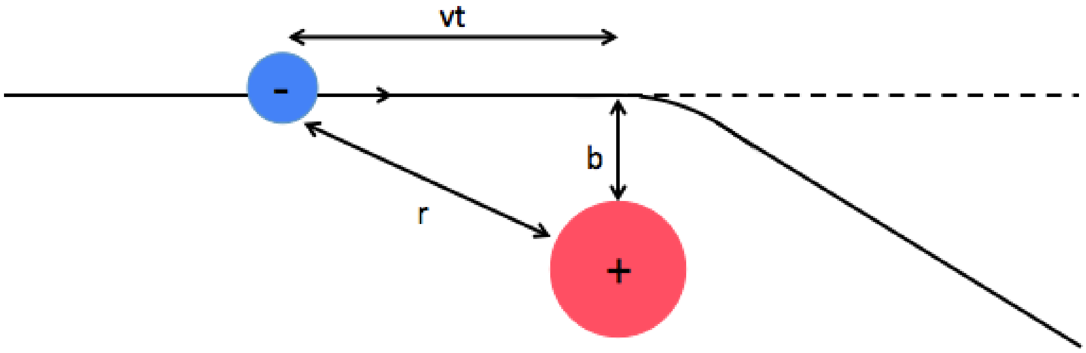

FIGURE 1.4: Schematic showing the bremsstrahlung (free–free) emission process. The schematic shows an electron (blue circle) travelling at velocity, v, interacting with a positively charged ion (red circle), with impact parameter b. The electron's path is modified by the Coulomb interaction with the ion, resulting in an acceleration (that produces the bremsstrahlung radiation).

At any time during the interaction, the force the electron will experience due to the Coulomb interaction with the ion is:

$$\mathbf{F}_C = \frac{Ze^2}{4\pi\varepsilon_0 \mathbf{r}(t)^2} = \frac{Ze^2}{4\pi\varepsilon_0(\mathbf{v}^2 t^2 + \mathbf{b}^2)}, \tag{1.1}$$

where Z is the charge number of the ion, e is the elementary charge and ε_0 is the permittivity of free space. The bold terms represent vector quantities. Next we decompose the force experienced by the electron into a direction parallel to its motion and a direction perpendicular to its motion, and divide by the electron mass to obtain the electron's parallel and perpendicular accelerations:

$$a_{\parallel}(t) = \frac{Ze^2 vt}{4\pi\varepsilon_0 m_e(v^2t^2 + b^2)^{\frac{3}{2}}}, \tag{1.2}$$

and

$$a_{\perp}(t) = \frac{Ze^2 b}{4\pi\varepsilon_0 m_e(v^2t^2 + b^2)^{\frac{3}{2}}}. \tag{1.3}$$

We plot Equations 1.2 and 1.3 in Figure 1.5.

The instantaneous total power emitted in all directions by an accelerating charge is given by Larmor's formula:

$$\frac{dE}{dt} = P(t) = \frac{e^2}{6\pi\varepsilon_0 c^3}|a(t)|^2, \tag{1.4}$$

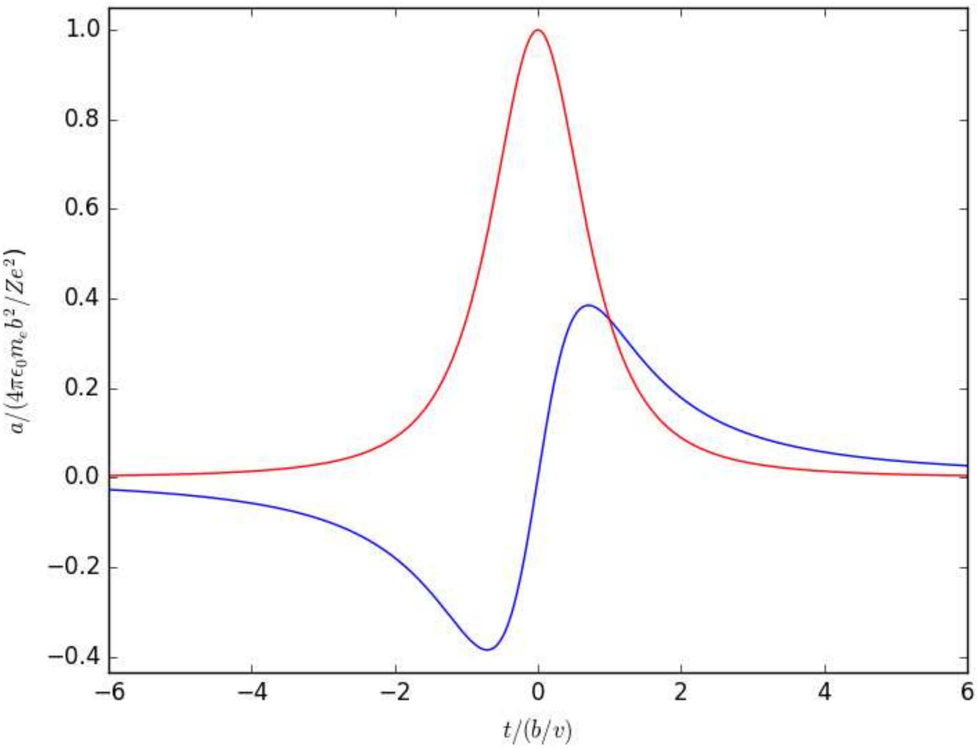

FIGURE 1.5: Plot showing the normalised acceleration the electron experiences during a (non–relativistic) free–free encounter, expressed in terms of the characteristic time, $\frac{v}{b}$. The blue line corresponds to the parallel acceleration (Equation 1.2) and the red line corresponds to the perpendicular acceleration (Equation 1.3).

i.e., the radiation emitted from the free–free interaction will occur in a pulse with a characteristic timescale, $\tau \sim \frac{b}{v}$ (see Figure 1.5). The frequencies required to produce the pulse can be obtained through Fourier analysis of the acceleration time dependence.

The (symmetrical) Fourier transform between time, t, space and angular frequency, ω, space is given by:

$$f(\omega) = \frac{1}{\sqrt{2\pi}} \int_{-\infty}^{\infty} f(t) e^{-i\omega t} dt, \tag{1.5}$$

and its inverse is given by:

$$f(t) = \frac{1}{\sqrt{2\pi}} \int_{-\infty}^{\infty} f(\omega) e^{i\omega t} d\omega, \tag{1.6}$$

where ω is related to frequency, ν through $\omega = 2\pi\nu$. Another useful result from the analysis of this Fourier transform pair is Parseval's (or Rayleigh's) Theorem:

$$\int_{-\infty}^{\infty} |f(t)|^2 dt = \int_{-\infty}^{\infty} |f(\omega)|^2 d\omega. \tag{1.7}$$

If we let $|f(t)|^2 = P(t)$ (Equation 1.4) then the integration on the left side of Equation 1.7 yields the total energy radiated during the pulse, E. Therefore $|f(\omega)|^2 = P(\omega)$ i.e. the energy radiated per angular frequency interval. Noting that the acceleration is real, we find:

$$E = \int_{-\infty}^{\infty} \frac{dE}{dt} dt = \int_{-\infty}^{\infty} \frac{e^2}{6\pi\varepsilon_0 c^3} |a(t)|^2 dt = \int_{0}^{\infty} \frac{e^2}{3\pi\varepsilon_0 c^3} |a(\omega)|^2 d\omega = \int_{0}^{\infty} \frac{dE}{d\omega} d\omega. \tag{1.8}$$

Following Longair (2011), letting $x = \frac{v}{b}t$, the Fourier transforms for the two orthogonal accelerations becomes:

$$\begin{aligned} a_{\parallel}(\omega) &= \frac{1}{\sqrt{2\pi}} \left(\frac{Ze^2}{4\pi\varepsilon_0 m_e bv} \right) \int_{-\infty}^{\infty} \frac{x}{(x^2+1)^{\frac{3}{2}}} e^{-i\omega\left(\frac{b}{v}\right)x} dx \\ &= \frac{1}{\sqrt{2\pi}} \left(\frac{Ze^2}{4\pi\varepsilon_0 m_e bv} \right) \left[2i \frac{\omega b}{v} K_0\left(\frac{\omega b}{v} \right) \right], \end{aligned} \tag{1.9}$$

and

$$\begin{aligned} a_{\perp}(\omega) &= \frac{1}{\sqrt{2\pi}} \left(\frac{Ze^2}{4\pi\varepsilon_0 m_e bv} \right) \int_{-\infty}^{\infty} \frac{1}{(x^2+1)^{\frac{3}{2}}} e^{-i\omega\left(\frac{b}{v}\right)x} dx \\ &= \frac{1}{\sqrt{2\pi}} \left(\frac{Ze^2}{4\pi\varepsilon_0 m_e bv} \right) \left[2 \frac{\omega b}{v} K_1\left(\frac{\omega b}{v} \right) \right]. \end{aligned} \tag{1.10}$$

In Equations 1.9 and 1.10, $K_0(y)$ and $K_1(y)$ are modified Bessel functions of the second kind, and have the form:

$$K_n(y) = \frac{\Gamma(n+\frac{1}{2})(2y)^n}{\sqrt{\pi}} \int_{0}^{\infty} \frac{\cos(\phi)}{(\phi^2+y^2)^{n+1/2}} d\phi. \tag{1.11}$$

It then follows that the total energy radiated in all directions in a single free–free interaction is distributed across frequency as:

$$\frac{dE}{d\nu} = \frac{Z^2 e^6}{6\pi^2 \varepsilon_0^3 m_e^2 c^3} \frac{\nu^2}{v^4} \left[K_0^2\left(\frac{2\pi b}{v}\nu \right) + K_1^2\left(\frac{2\pi b}{v}\nu \right) \right]. \tag{1.12}$$

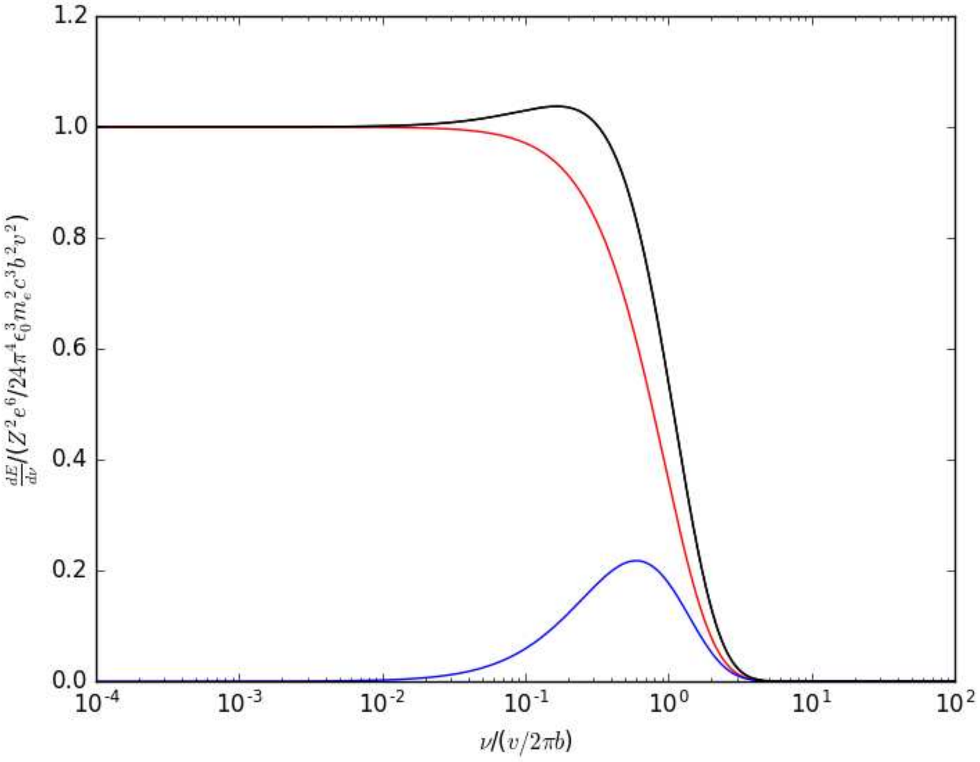

FIGURE 1.6: The total emission spectrum from a single bremsstrahlung interaction between two charged particles. The blue line corresponds to the emission from the parallel acceleration and the red line corresponds to the emission from the perpendicular acceleration. The black line shows the addition of the two components.

We present a plot of the bremsstrahlung emission spectrum for a single interaction in Figure 1.6. From this diagram we see that the perpendicular component has a very broad spectrum, which exponentially declines at frequencies larger than $\nu \sim \frac{v}{2\pi b}$, and the parallel component produces a comparatively narrow bump at roughly the same frequency. This behaviour is expected based upon the time dependence of the electron acceleration in the two component directions. In the parallel direction, the pulse is much longer compared to the perpendicular direction (see Figure 1.5).

To obtain the bremsstrahlung emission emissivity, we need to calculate the rate at which free–free interactions occur in an ionised plasma, and account for all possible free–free interactions (i.e., integrate over all possible impact parameters, b, and particle velocities, v).

The rate of free–free interactions per unit volume can easily be found by considering the number of electrons that we would expect to find passing an ion per unit time per unit volume with an impact parameter between b and $b+db$ and a speed between v and $v+dv$, and multiplying the result by the number of ions in the considered volume[2]:

$$\frac{dN}{dt dV} = n_e n_{ion} \left(2\pi b \, db\right) \left(v f(v) \, dv\right). \tag{1.13}$$

$f(v)$ is the normalised velocity distribution for the electrons that are producing the bremsstrahlung emission. For a plasma that is in thermodynamic equilibrium with its surroundings, $f(v)$ is the Maxwell–Boltzmann velocity distribution and only depends on the temperature of the plasma, T:

$$f(v,T) = \left(\frac{2}{\pi}\right)^{\frac{1}{2}} \left(\frac{m_e}{kT}\right)^{\frac{3}{2}} v^2 \exp\left(-\frac{mv^2}{2kT}\right), \tag{1.14}$$

where k is the Boltzmann constant. In this particular case, the bremsstrahlung emission is known as 'Thermal' emission. In general however, $f(v)$ could be any other non–thermal distribution (resulting in non–thermal bremsstrahlung).

Assuming the emission is isotropically emitted (i.e. dividing by an additional factor of 4π), the emission coefficient for bremsstrahlung is simply the rate of interactions per unit volume (Equation 1.13) multiplied by the energy spectrum for a single interaction (Equation 1.12), integrated over all possible free–free interactions:

$$\frac{dE}{dt dV d\nu d\Omega} = j_\nu = \frac{1}{2} n_e n_{ion} \int_0^\infty \left[\int_{b_{min}}^{b_{max}} \left(\frac{dE}{d\nu}\right) b \, db\right] v f(v,T) \, dv. \tag{1.15}$$

The final step to obtain the bremsstrahlung emission coefficient is to define the integration limits on the impact parameter, b_{min} and b_{max}. Classically, b_{min} can be be approximated by considering the maximum energy transferred to the electron during the free–free interaction (Longair, 2011):

$$b_{min} \approx \frac{Ze^2}{8\pi\varepsilon_0 m_e v^2}. \tag{1.16}$$

We can estimate b_{max} by inspecting Figure 1.6 and noting that the observed spectrum drops significantly for values where $\frac{2\pi\nu b}{v} > 1$ (Longair, 2011). Therefore:

$$b_{max} \approx \frac{v}{2\pi\nu}. \tag{1.17}$$

---

[2] See J.J. Condon's Essential Radio Astronomy Course for a detailed explanation of this result, available at https://www.cv.nrao.edu/ sransom/web/Ch4.html

Although the minimum and maximum impact parameters need to be assumed, in the lower energy limit (where radio emission is produced), the result of the impact parameter integral involves the natural logarithm of the ratio of $b_{\max}$ to $b_{\min}$ (Rybicki and Lightman, 1979; Longair, 2011). Therefore as long as the assumed limits are reasonably close to the true limits that should be used, the resulting uncertainties should be small.

For the assumed limits, Longair (2011) finds that the solution to the double integration in Equation 1.15 is:

$$j_\nu = \frac{1}{12\pi^3}\left(\frac{\pi}{6}\right)^{\frac{1}{2}}\frac{Z^2e^6}{\varepsilon_0^3c^3m_e^2}\left(\frac{m_e}{kT}\right)^{\frac{1}{2}}n_e\,n_{ion}\exp\left(-\frac{h\nu}{kT}\right)g_{ff}(\nu,T)\left[\mathrm{W\,m^{-3}\,Hz^{-1}\,Sterad^{-1}}\right]. \tag{1.18}$$

$g_{ff}(\nu,T)$ is known as the Gaunt free–free factor, and is determined by the assumed limits of integration. For the assumed b_{min} and b_{max}:

$$g_{ff}(\nu,T) = \frac{\sqrt{3}}{2\pi}\left[\ln\left(\frac{128\varepsilon_0^2k^3T^3}{m_e e^4Z^2\nu^2}\right) - 0.577^{\frac{1}{2}}\right]. \tag{1.19}$$

As the plasma is in thermodynamic equilibrium with its surroundings, we can easily obtain the bremsstrahlung absorption co–efficient, κ_ν, by applying Kirchoff's law:

$$\frac{j_\nu}{\kappa_\nu} = B(\nu,T), \tag{1.20}$$

where $B(\nu,T)$ is the Planck function:

$$B(\nu,T) = \frac{2h\nu^3}{c^2}\frac{1}{\exp\left(\frac{h\nu}{kT}\right)-1}. \tag{1.21}$$

We plot example thermal spectra in Figure 1.7. At low frequencies, the plasma is optically thick, and the observed spectrum approaches that of a Blackbody in the Rayleigh–Jeans limit ($I_\nu \propto \nu^2$). As we transition into the optically thin regime, the spectrum becomes effectively flat ($I_\nu \propto \nu^{-0.1}$) and remains this way until an exponential cutoff at frequency $\nu \sim \frac{kT}{h}$.

The Thermal Radio Contribution From Normal Star–Forming Galaxies

We expect to observe thermal radio continuum emission from any ionised plasma that is in thermodynamic equilibrium with its surroundings. In practice however, only the ionised gas in the HII regions surrounding massive stars is dense enough to produce

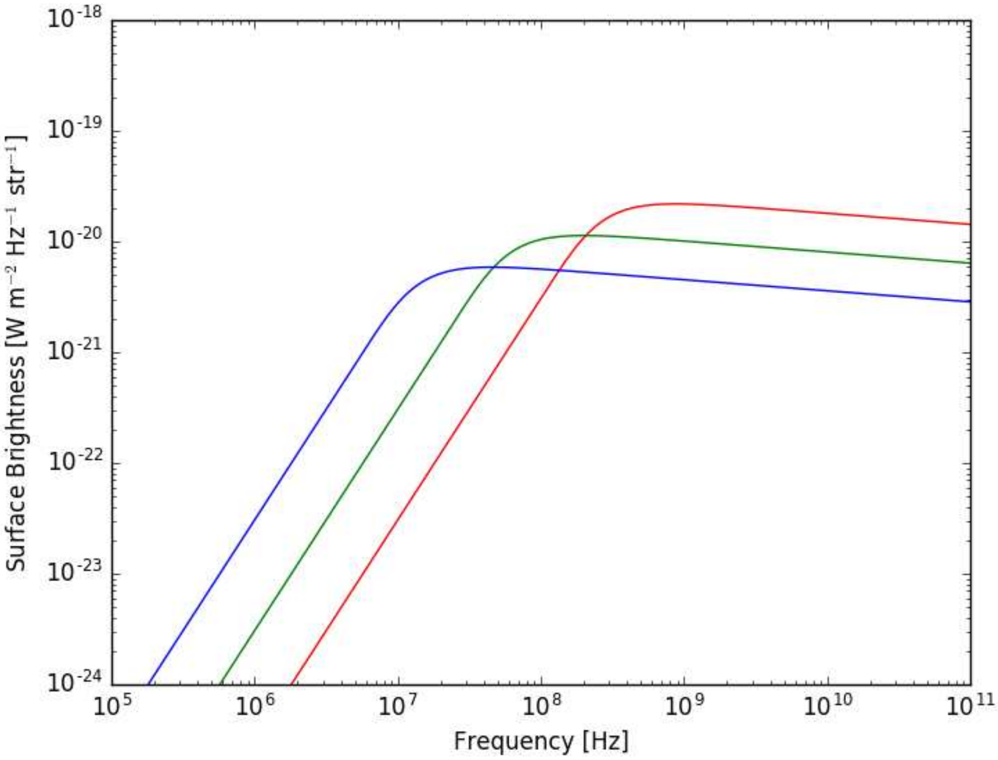

FIGURE 1.7: Example thermal radio spectra at various temperatures. The red line corresponds to $T = 10^3$ K, the green line corresponds to $T = 10^4$ K and the blue line corresponds to $T = 10^5$ K.

significant thermal radio continuum emission (Draine, 2011). Thus we can assume that almost all of the thermal radio continuum emission detected from normal star–forming galaxies originates from HII regions surrounding massive stars that are currently on the main sequence.

The quantity that we observe with radio telescopes is the source flux density, F_ν, which is defined as:

$$F_\nu = \int_{\Omega_{\mathrm{source}}} I_\nu(\phi, \theta) \cos(\theta)\, d\Omega \left[\mathrm{W\,m^{-2}\,Hz^{-1}}\right], \tag{1.22}$$

where I_ν is the specific intensity, ϕ is the azimuthal spherical polar co–ordinate, θ is the polar spherical polar co–ordinate and Ω_{source} is the source solid angle. I_ν is calculated from the basic equation of radiative transfer:

$$\frac{dI_\nu}{dl} = j_\nu - \kappa_\nu I_\nu, \tag{1.23}$$

where l is the path length through the emitting material. Assuming that the HII region is optically thin (which is observed to be the case for galactic HII regions at frequencies larger than 1 GHz; Hindson et al. 2016), that the emissivity everywhere within the HII region is constant and that the HII region has a cylindrical geometry, the solution to Equation 1.23 is:

$$I_\nu \approx j_\nu \, l. \tag{1.24}$$

As most observed astronomical sources are small (i.e., $\cos(\theta) \approx 1$), the observed flux density from the HII region is given by:

$$F_\nu \approx j_\nu \, l \, \Omega_{\text{source}} \approx \frac{j_\nu \, l A}{4\pi D^2} \approx \frac{j_\nu V}{4\pi D^2}, \tag{1.25}$$

where A is the apparent HII region surface area, D is the distance to the HII region and V is the HII region volume. Equation 1.25 importantly shows that the observed flux density is proportional to the thermal radio continuum emitting volume under optically thin conditions.

To calculate the observed thermal radio continuum emission originating from an HII region produced by a massive star, we need to estimate the volume of the HII region. The volume can be estimated by noting that an HII region is produced and maintained as long as the rate at which ionising photons are emitted from a given massive star exceeds the rate at which the ionised atoms recombine. Assuming that the massive star's spectrum is represented by a blackbody function at temperature T (Equation 1.21) and that the gas surrounding the massive star consists of Hydrogen only, the rate at which the ionising photons are produced is given through:

$$Q(R_*, T) = \int_{\nu_i}^{\infty} \frac{L_\nu}{h\nu} d\nu = 8\pi^2 R_*^2 \int_{\nu_i}^{\infty} \frac{B(\nu, T)}{h\nu} d\nu \, \left[\mathrm{s}^{-1}\right], \tag{1.26}$$

where L_ν is the luminosity of the star at frequency ν, R_* is the radius of the star and ν_i is the ionisation frequency for Hydrogen ($\nu_i = 3.3 \times 10^{15}$ Hz). We present a visualisation of the integration in Figure 1.8. As the radius, R_*, and temperature, T, of a star are both closely linked to its mass (e.g., Prialnik, 2009), the ionising photon production rate can be expressed in terms of stellar mass, $Q(R_*, T) = Q(M)$. Typically for O type stars ($M_* \sim 50\,\mathrm{M}_\odot$), $Q \sim 10^{49}\,\mathrm{s}^{-1}$.

Assuming that the massive star radiates isotropically, we expect the star to produce a spherically symmetric HII region, also known as a Strömgren sphere (Strömgren, 1939).

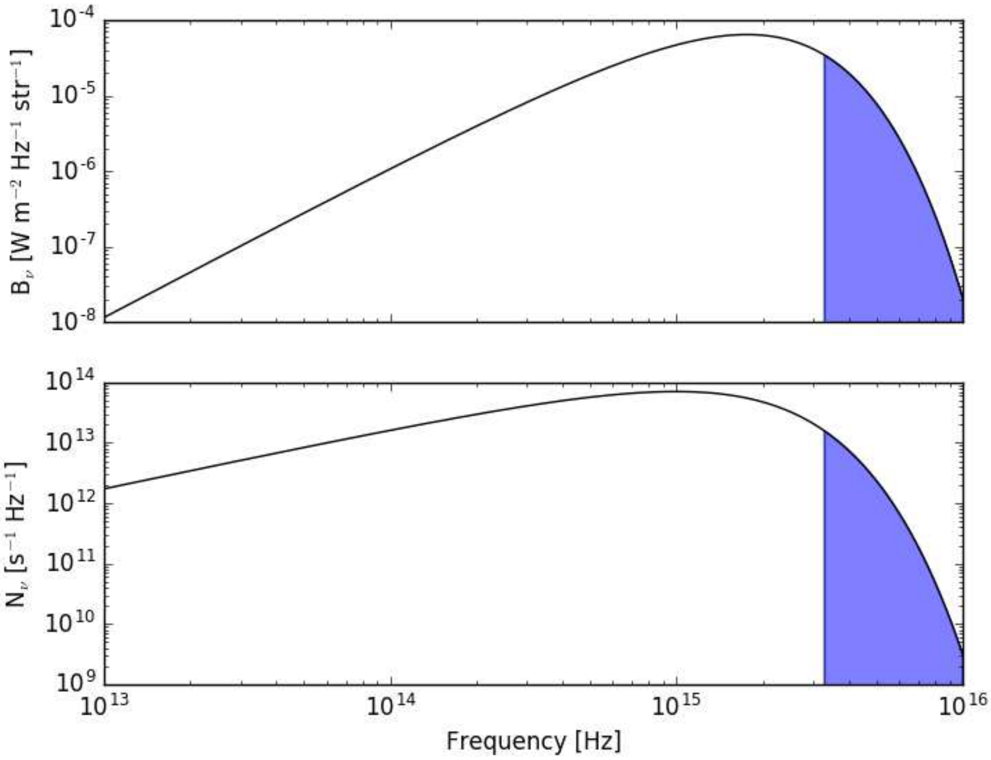

FIGURE 1.8: Visualisation of the integration in Equation 1.26. The top panel shows the Blackbody spectrum as a function of frequency (Equation 1.21) and the bottom panel shows the photon emission rate as a function of frequency. The vertical blue line shows the Hydrogen ionisation frequency and the shaded region shows the area considered in the integration.

The volume of the HII region can be estimated by balancing the total ionisation rate with the total recombination rate. Assuming for simplicity that the gas surrounding the massive star is uniformly distributed and that the gas is optically thick to ionising photons (i.e., Case B recombination), we estimate the total recombination rate through:

$$\frac{dN}{dt} = \int_0^R 4\pi r^2 n_e n_p \alpha_B(T) dr = \frac{4}{3}\pi R^3 n_e n_p \alpha_B(T), \tag{1.27}$$

where R is the radius of the volume in which the recombination is occurring and $\alpha_B(T)$ is the Case B recombination coefficient, which is given for Hydrogen in Draine (2011) as:

$$\alpha_B(T) = 2.54 \times 10^{-7} T_4^{-0.8163-0.0208\ln(T_4)} \left[\mathrm{m}^{-3}\,\mathrm{s}^{-1}\right]. \tag{1.28}$$

T_4 is the temperature of the gas surrounding the massive star in units of 10^4 K. The temperature of the gas depends on the thermodynamic balance between heating (from the photons emitted from the massive star) and cooling (through escaping line and continuum emission) processes, and is typically observed in HII regions to be $\approx 10^4$ K.

Finally, we obtain the volume of the HII region in terms of the ionisation and recombination rates, Q and $\alpha_B(T)$, by balancing the total number of ionising photons against the total number of recombinations and identifying R as the radius at which these rates are balanced (i.e., the HII region radius, R_{HII}):

$$V_{HII} = \frac{4}{3}\pi R_{HII}^3 \approx \frac{Q(M)}{n_e n_p \alpha_B(T)}. \tag{1.29}$$

Thus we find that the thermal radio continuum flux density observed for a HII region is:

$$F_\nu \approx \frac{j_\nu \, Q(M)}{4\,\pi D^2 n_p \, n_e \, \alpha_B(T)}. \tag{1.30}$$

The observed flux density from an HII region surrounding a massive star is directly proportional to the emission rate of ionising photons from the massive star. The total thermal radio continuum emission originating from a star–forming region (or the entire galaxy) at distance D is then:

$$F_{\nu,\mathrm{tot}} \approx \frac{1}{4\pi D^2} \sum_{i=1}^{N} \frac{j_{\nu,i} \, Q(M_i)}{n_{e,i} \, n_{p,i} \, \alpha_B(T_i)}, \tag{1.31}$$

where the subscript i represents the i'th star and N is the total number of stars that are being considered. As the ionising photon production rate is dominated by massive stars, the observed thermal radio continuum emission is effectively proportional to the total number of massive stars. As these stars have short main sequence lifetimes ($\sim$ 10 Myr, e.g., Kennicutt and Evans, 2012), the thermal radio continuum emission should be proportional to the instantaneous star formation rate. This has been demonstrated in both resolved studies of individual star–forming regions (Murphy et al., 2011) and in studies of the global properties of normal galaxies (Tabatabaei et al., 2017).

The thermal radio continuum emission originating from a galaxy offers a valuable tracer of recent star formation that is insensitive to the effects of attenuation and extinction due to dust along the line of sight to the source. However, there are still some complications that may affect its interpretation. In deriving the size of the HII region surrounding a massive star, we have assumed that all ionising photons are absorbed by surrounding gas. This cannot be the case in most normal star–forming galaxies as these galaxies are observed to be Far–UV sources (Gil de Paz et al., 2007). Additionally, the volume and temperature of the HII region and the ionising photon rate from the massive star itself will depend on the metallicity of the gas in the system. Finally, any dust in the HII region can absorb ionising photons and re–emit in the infrared, reducing the observed thermal radio continuum emission relative to the massive star ionising photon production rate. Furthermore, the thermal radio continuum emission can only be directly measured with observationally expensive high frequency ($> 10\,$GHz) observations, or multiple observations at lower–frequencies with advanced modelling to separate out the thermal from non–thermal radio emission (Condon, 1992).

These difficulties however are not dissimilar from those that plague other star–formation rate tracers (Kennicutt and Evans, 2012), yet the thermal radio continuum has the huge advantage due to its insensitivity to extinction, and to the fact that radio telescopes do not need to be put in space. Thus, the thermal radio continuum emission shows promise for being a leading star–formation tracer; however, more studies with large sample sizes are required to fully test its applicability.

The Relationship Between Thermal Radio Continuum and Hα Emission

As the thermal radio continuum emission originates from the ionised plasma associated with HII regions, it comes as no surprise that it is closely related to other tracers of ionised gas, the most popular of which is the Hα emission line.

In an ionised plasma (such as that in an HII region), electrons recombine with protons to form atomic Hydrogen, with the electrons in general remaining in an excited state, n. The electron will then undergo transitions to the ground state, and will emit photons at each transition. When an electron undergoes the $n = 3$ to $n = 2$ transition, it produces Hα line emission at $\lambda = 656.5\,$nm.

Assuming that the ionised gas cloud consists entirely of Hydrogen, we can calculate the Hα emission coefficient through:

$$j_{H\alpha,\nu} = \frac{n_e n_p \, \alpha_{H\alpha,\mathrm{eff}}(T)}{4\pi} h \nu \, \phi(\nu), \tag{1.32}$$

where $\alpha_{H\alpha,\mathrm{eff}}(T)$ is the effective recombination coefficient for recombination paths that involve the Hα transition, and is given in Draine (2011) as:

$$\alpha_{H\alpha,\mathrm{eff}}(T) = 1.17 \times 10^{-7} T_4^{-0.942-0.031\ln(T_4)} \left[\mathrm{m}^{-3}\,\mathrm{s}^{-1}\right]. \tag{1.33}$$

In Equation 1.32, $\phi(\nu)$ is the (normalised) quantum mechanical line profile as the line could be broadened due to several line broadening processes, such as Doppler broadening (Rybicki and Lightman, 1979; Hubeny and Mihalas, 2014). As most Hα filters integrate the emission over the entire line, the total Hα emissivity is given by:

$$j_{H\alpha} = \frac{n_e\, n_p\, \alpha_{H\alpha,\mathrm{eff}}(T)}{4\pi} h \int_0^\infty \nu\, \phi(\nu)\, d\nu. \tag{1.34}$$

If we assume that the H II region is optically thin to Hα emission, we find that the observed Hα flux density follows the same form as that found for the thermal radio continuum emission (Equation 1.25) i.e., the flux density is proportional to the volume of the emitting material:

$$F_{H\alpha} \approx \frac{j_{H\alpha} V}{4\pi D^2}. \tag{1.35}$$

As the thermal radio continuum and Hα emission originate from the same volume, we find that:

$$F_\nu \approx \left(\frac{j_\nu}{j_{H\alpha}}\right) F_{H\alpha}, \tag{1.36}$$

i.e., the thermal radio continuum and Hα flux densities are related through a temperature and frequency dependent scaling factor (Lequeux, 1980). This scaling factor is presented in Deeg et al. (1997) as:

$$F_\nu = 1.14 \times 10^{-14} \left(\frac{\nu}{\mathrm{GHz}}\right)^{-0.1} \left(\frac{T}{10^4\,\mathrm{K}}\right)^{0.34} F_{H\alpha}. \tag{1.37}$$

In principle, if an Hα map of a nearby galaxy is available, the thermal radio continuum properties should be predictable at any frequency, ν (and the reverse holds as well, of course). However, in practice Hα emission is subject to extinction from surrounding dust and usually underpredicts the thermal radio continuum emission; existing methods to determine the amount of extinction have their own problems and carry a large uncertainty themselves! Regardless of these difficulties, maps of the Hα emission are frequently used in the literature to estimate the thermal radio continuum emission properties in low frequency radio continuum studies, where non–thermal radio continuum emission (see below) dominates the observed emission (e.g., Heesen et al., 2014).

1.2.2 Synchrotron (Non–Thermal) Radio Continuum Emission

Early particle detection experiments at the beginning of the 20th century demonstrated that the ISM within the Milky Way is pervaded by relativistic charged particles known as cosmic rays (Hess, 1912). These charged particles interact with magnetic fields embedded in the ISM (e.g., Beck, 2015) through the Lorentz electromagnetic force and undergo acceleration. The radiation produced by these accelerating charges is known as synchrotron (or Magnetobremsstrahlung) emission, and dominates the diffuse low–frequency ($\sim 1\,\mathrm{GHz}$) emission properties observed in both the Milky Way as well as in nearby galaxies.

Before we derive the characteristics of synchrotron emission, we first consider the dynamics of a cosmic ray interacting with a magnetic field. Consider a cosmic ray with charge, Ze, traveling at velocity, v, through the ISM where it encounters a magnetic field of strength, B. The angle between the direction of the charged particles motion and the magnetic field is known as the pitch angle, α (i.e., the angle between the velocity and magnetic field vectors; see Figure 1.9). For this situation, the Lorentz electromagnetic force in the absence of an electric field is given by:

$$\mathbf{F}_L = \frac{d\left(\gamma m_0 \mathbf{v}\right)}{dt} = Ze(\mathbf{v} \times \mathbf{B}), \tag{1.38}$$

where the bold quantities are vectors, m_0 is the particle's rest mass and γ is the Lorentz factor (see Appendix A). The vector cross product implies that the Lorentz force always acts in a direction perpendicular to both the particle's velocity and magnetic field (i.e., $\mathbf{v} \cdot \frac{d\mathbf{v}}{dt} = 0$). Thus the cosmic ray's instantaneous acceleration both parallel and perpendicular to the velocity vector are then given through:

$$\begin{aligned} a_{\parallel} &= 0, \\ a_{\perp} = \frac{v_{\perp}^2}{r_g} &= \frac{Ze|v||B|\sin(\alpha)}{\gamma m_0}, \end{aligned} \tag{1.39}$$

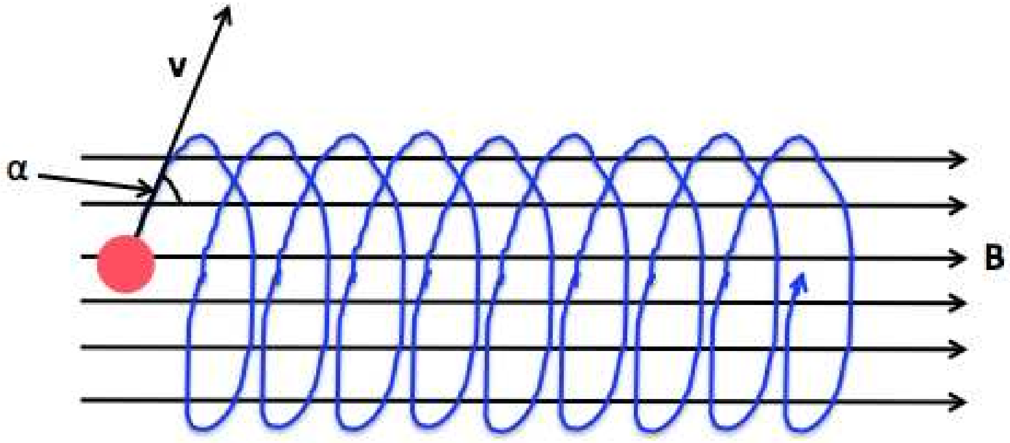

FIGURE 1.9: Schematic diagram showing the synchrotron emission process. In this schematic, a charged particle (represented by the red circle) is gyrating around a magnetic field, B, in the x–direction. The particle has a velocity, v, which is at an angle, α, to the direction of the magnetic field.

where $v_\perp$ is the velocity component of the cosmic ray that is perpendicular to the magnetic field vector and r_g is the particle's gyro–radius (radius of curvature). From Equation 1.39, the angular gyro–frequency is found through:

$$\omega_g = \frac{v_\perp}{r_g} = \frac{Ze|B|}{\gamma m_0}, \tag{1.40}$$

and the gyro–radius through:

$$r_g = \frac{v_\perp}{\omega_g} = \frac{\gamma m_0 |v| \sin(\alpha)}{Ze|B|}. \tag{1.41}$$

These properties imply that the cosmic ray will exhibit circular motion in the plane perpendicular to the magnetic field direction whilst the parallel velocity component remains unchanged. Thus the cosmic ray will follow a helical path in the direction of the magnetic field, as shown in Figure 1.9.

We now turn our attention to the observed emission properties from a single cosmic ray interacting with a magnetic field. The magnitude of the emitted power is proportional to the square of the charged particle's acceleration (see Equation 1.4) which itself is inversely proportional to the cosmic ray's rest mass (for the case of a charged particle interacting with a magnetic field). As the electron is the lightest charged particle that is ubiquitous in the ISM, we will assume that all of the observed emission from this process originates from cosmic ray electrons (CRe) and positrons (i.e., $Z = -(+)1$ and $m_0 = m_e$).

To understand the synchrotron emission process, it is useful to first study the non–relativistic case (gyro emission) and investigate how relativistic effects affect the received power. Consider the simple case of gyro emission originating from a electron orbiting a magnetic field with a pitch angle $\alpha = \frac{\pi}{2}$. In this case the gyro–frequency reduces to:

$$\omega_C = \frac{e|B|}{m_e}. \tag{1.42}$$

An observer in the plane of the particle's circular motion will observe the particle undergoing simple harmonic motion. The power emitted per solid angle for the accelerating charge is given in Longair (2011) as:

$$\frac{dE}{dtd\Omega} = \frac{e^2}{16\pi^2\varepsilon_0 c^3}\,|a|^2\,\sin^2(\psi), \tag{1.43}$$

where ψ is the angle between the direction of acceleration and the observer. As the charge rotates around the magnetic field, there are periods where the observer is parallel to the acceleration direction (in the middle of its simple harmonic oscillation) and periods where it is perpendicular to the observer (at the ends of the particles simple harmonic oscillation. Therefore, ψ is related to the gyro–frequency through $\psi = \omega_C t$, i.e., we expect to find a sinusoidal dependence of the observed power pattern as a function of time. Following the approach to obtain the frequency spectrum for bremsstrahlung emission (Equation 1.8), we find that the frequency spectrum will consist of a single delta function at $\nu_C = \frac{\omega_C}{2\pi}$ (assuming the particle is observed for an infinite period of time). We present the received power pattern from a gyro–emitting electron in the left panel of Figure 1.10.

Synchrotron emission differs from this result in two key ways: the radiation emission pattern is beamed along its direction of motion (see Appendix A) and the Doppler effect needs to be taken into account. Both of these effects are encapsulated when the dipole pattern is transformed from a moving frame of reference to a stationary observer frame. The dipole emission as observed by a stationary observer for the case that the direction of acceleration is perpendicular to the direction of motion is derived in Appendix A

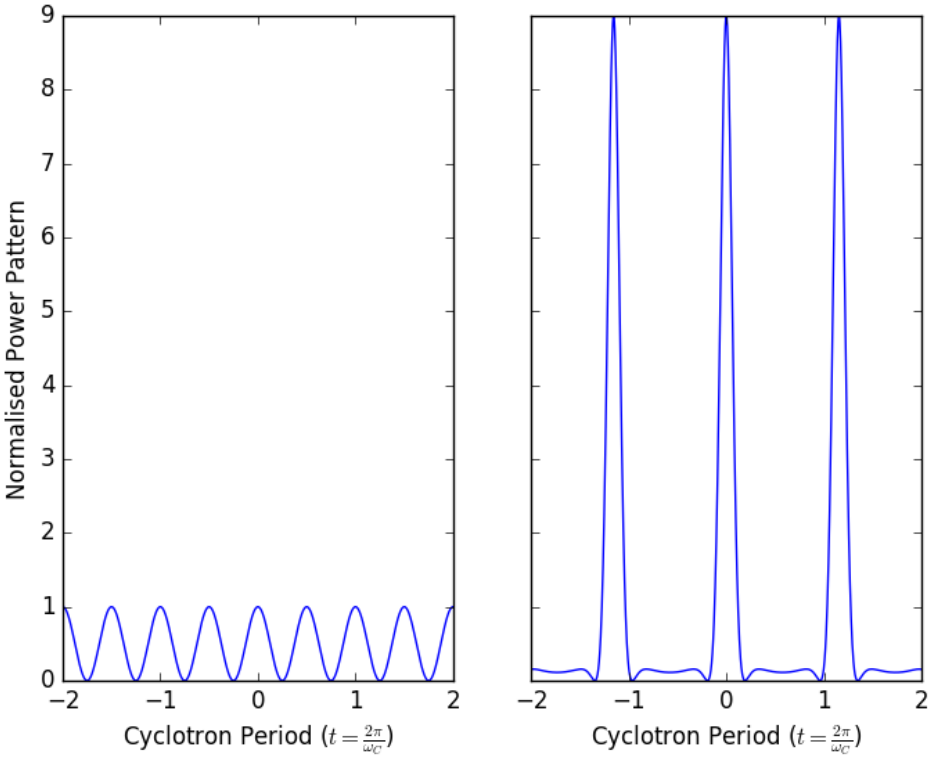

FIGURE 1.10: Diagrams comparing the observed pulse patterns for a gyro (left panel) and a synchrotron (right panel) emitting particle. Both axes are presented in terms of the non–relativistic gyro–frequency, ω_C. In the right panel (where the particle is travelling at $v = 0.5\,c$), the relativistic effects cause the emission to be beamed in the direction of travel (which is towards the observer at $t = 0$) and period of the total pulse pattern to be modified.

and has the form:

$$\frac{dE}{dt\,d\Omega} = \frac{e^2|a_\perp|^2}{16\pi^2\varepsilon_0 c^3}\,\frac{1}{(1-\beta\,\cos(\theta))^4}\left[1-\frac{\sin^2(\theta)\,\cos^2(\phi)}{\gamma^2(1-\beta\,\cos(\theta))^2}\right], \tag{1.44}$$

where θ is the angle between the direction of velocity of the CRe's motion and the observer and ϕ is the corresponding azimuthal angle which is defined to be $\phi = 0$ in the direction of acceleration. We can obtain the synchrotron pulse pattern for an observer in the plane of the circular motion (assuming $\alpha = \frac{\pi}{2}$) by letting $\theta = \omega_g t$. We present this result in the right panel of Figure 1.10. Instead of observing a sinusoidal time dependence of the observed power (like the gyro case), a synchrotron emitting particle exhibits more pulsed behaviour. The total time between pulses is longer than the gyro case by a factor of γ, yet the duration of the enhanced pulse is shorter due to a combination of relativistic beaming and the Doppler effect.

So far we have only considered the case where the CRe is confined to a circular orbit in the same plane as the observer. The Fourier analysis of the Synchroton pulse pattern at an arbitrary pitch angle is far more complicated, so we refer to the results found in Pacholczyk (1970), Rybicki and Lightman (1979) and Longair (2011). From Longair (2011), the total emissivity for a single electron radiating synchrotron emission is:

$$j_\nu = \frac{\sqrt{3}\, e^3 |B| \sin(\alpha)}{8\pi^2 \varepsilon_0 m_e} F\left(\frac{\nu}{\nu_{\rm crit}}\right) \left[{\rm W\,m^{-3}\,Hz^{-1}\,Sterad^{-1}}\right], \tag{1.45}$$

where $F(x)$ is given by:

$$F(x) = x \int_x^\infty K_{5/3}(z)\, dz, \tag{1.46}$$

and $\nu_{\rm crit}$ is the critical frequency, given by:

$$\nu_{\rm crit} = \frac{3}{2} \gamma^2 \nu_C \sin(\alpha), \tag{1.47}$$

where ν_C is the classical gyro–frequency, given by $\nu_C = \frac{\omega_C}{2\pi}$. We present the form of the frequency spectrum from a single electron in Figure 1.11. Due to the short timescale of the received pulse from a synchrotron emitting electron, the frequency spectrum is broad compared to the gyro emitting case, with a peak at $\nu \approx 0.29\, \nu_{\rm crit}$. At low frequencies compared to the critical frequency ($\frac{\nu}{\nu_{\rm crit}} \ll 1$), the frequency spectrum takes the form $F(\frac{\nu}{\nu_{\rm crit}}) \propto \nu^{\frac{1}{3}}$ and at high frequencies compared to the critical frequency ($\frac{\nu}{\nu_{\rm crit}} << 1$), the frequency spectrum drops off exponentially: $F(\frac{\nu}{\nu_{\rm crit}}) \propto \nu^{\frac{1}{2}} \exp(-\frac{\nu}{\nu_{\rm crit}})$.

As we have derived the emission properties from a single electron, j_ν, we now derive the emission properties from a population of CRe, J_ν. First, we need to know the distribution of charged particles as a function of energy $N(E)$, where E is related to γ through:

$$E = \gamma m_e c^2. \tag{1.48}$$

For a gas that is in thermodynamic equilibrium, $N(E)$ takes the form of the relativistic Maxwell–Boltzmann distribution (the Maxwell–Jüttner distribution), however in particle detection experiments, $N(E)$ is observed to take the form of a power–law, $N(E) = \kappa E^{-p}$ (Grenier et al., 2015). As this power–law distribution cannot be described by a state in thermal equilibrium, the observed synchrotron emission is known as non–thermal radio continuum emission. The total emissivity from a population of CRe can then be found by integrating over all possible interactions with the magnetic field (i.e.,

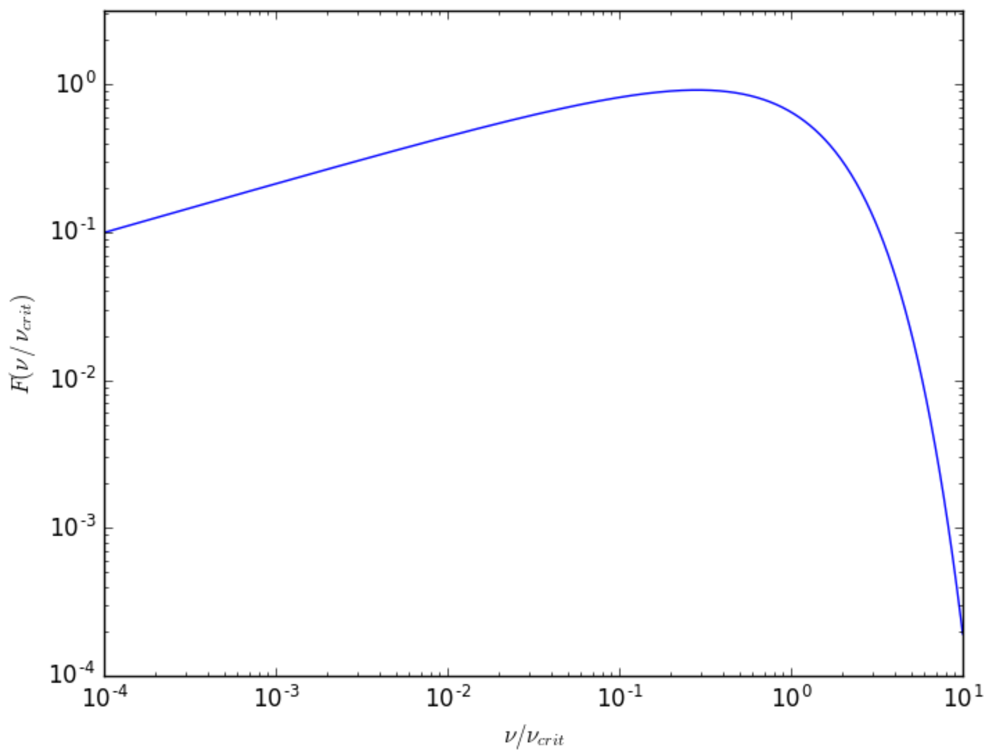

FIGURE 1.11: Plot of the dependence of $F(\nu/\nu_{\rm crit})$ on $\nu/\nu_{\rm crit}$. The x–axis is presented in terms of the critical frequency, $\nu_{\rm crit}$. To obtain the synchrotron emissivity for a single electron, $F(\nu/\nu_{\rm crit})$ needs to be multiplied by the constant displayed in Equation 1.45.

integrate the contributions of each charged particle at each energy over all pitch angles to the power emitted at frequency ν):

$$J_\nu = \int_0^\infty \int_0^\pi j_\nu(E,\alpha) N(E) f_\alpha(\alpha)\, d\alpha\, dE, \tag{1.49}$$

where $f_\alpha(\alpha)$ is the normalised pitch angle distribution. For a isotropically distributed pitch angles, $f_\alpha(\alpha) = \frac{1}{2}\sin(\alpha)$. Equation 1.49 assumes that the magnetic field is constant, which is not usually the case in astronomical sources. In general, the magnetic field may vary significantly within the source and should be described by a normalised distribution function, $f_B(B)$ (e.g., Eilek and Arendt, 1996). Thus, the emissivity from a population of charged particles is given by:

$$J_\nu = \int_0^\infty \int_0^\infty \int_0^\pi j_\nu(E,B,\alpha) N(E) f_\alpha(\alpha) f_B(B)\, d\alpha\, dE\, dB. \tag{1.50}$$

As the solution to Equation 1.50 must in general be evaluated numerically (Hardcastle,

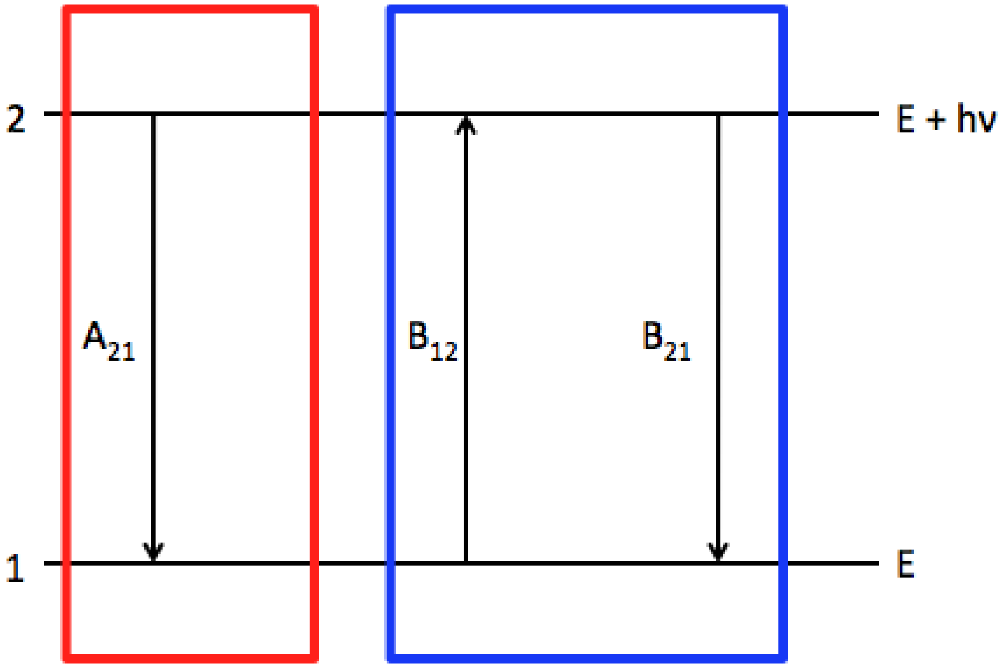

FIGURE 1.12: Schematic of the Einstein coefficents for a two state system. The two states (1 and 2) are separated by energy, $h\nu$. The red box highlights the processes that occur spontaneously and do not depend on the state of the radiation field the system is immersed in. The blue box highlights the processes that depend on the state of the radiation field the system is immersed in.

2013), we will assume for simplicity that B is constant to obtain analytical results. The solution to Equation 1.49 for a power–law particle energy distribution ($N(E) = \kappa E^{-p}$) that is isotropically distributed is given in Longair (2011) as:

$$J_\nu = \frac{\sqrt{3}e^3\kappa B}{16\pi^2\varepsilon_0 c m_e}\left(\frac{3eB}{2\pi\nu m_e^3 c^4}\right)^{\frac{(p-1)}{2}} a(p)\ \left[\mathrm{W\,m^{-3}\,Sterad^{-1}\,Hz^{-1}}\right], \tag{1.51}$$

where $a(p)$ is given by:

$$a(p) = \frac{\sqrt{\pi}}{2}\frac{\Gamma\left(\frac{p}{4}+\frac{19}{12}\right)\Gamma\left(\frac{p}{4}-\frac{1}{12}\right)\Gamma\left(\frac{p}{4}+\frac{5}{4}\right)}{(p+1)\Gamma\left(\frac{p}{4}+\frac{7}{4}\right)}. \tag{1.52}$$

As the synchrotron emission process cannot be described by a state that is in thermal equilibrium (the energies of the CRe are not represented by a Boltzmann distribution), we cannot use Kirchhoff's law to obtain the synchrotron absorption coefficient. Instead we calculate the absorption coefficient through the Einstein coefficients.

The Einstein coefficients describe the interactions between a photon and a two-state system (see Figure 1.12), and are defined as follows: A_{21} is the probability per time interval that a particle in state 2 spontaneously drops to state 1 and emits a photon; $B_{12}J$ is the transition probability per time interval that a particle in state 1 absorbs a photon and jumps to state 2; and $B_{21}J$ is the transition probability per time interval that a particle in state 2 drops to state 1 via stimulated emission. For both of the B coefficents, J is the mean intensity field (averaged over all solid angles) the two state system exists within. The Einstein coefficients are related to each other through:

$$A_{21} = \frac{2h\nu^3}{c^2} B_{21},$$

and

$$g_1 B_{12} = g_2 B_{21}, \tag{1.53}$$

where g_1 and g_2 are the statistical weights associated with states 1 and 2. The coefficients can also be related to the emission and absorption coefficients through:

$$j_\nu = \frac{h\nu}{4\pi} n_2 A_{21}$$

$$\kappa_\nu = \frac{h\nu}{4\pi} [n_1 B_{12} - n_2 B_{21}] \tag{1.54}$$

where n_1 and n_2 are the number densities of particles in states 1 and 2 respectively.

Longair (2011) notes that the coefficents shown in the above form are defined in terms of the number density per volume of phase space $d^3\mathbf{p}$, rather than per energy interval. Thus we must transform the emission and absorption coefficents from their phase space form to one in energy. For a pair of continuum states separated in momentum by $\frac{h\nu}{c}\mathbf{i}_k$, we can write the absorption coefficient as:

$$\kappa_{\nu,\mathrm{pair}} = \frac{h\nu}{4\pi}\left[N\left(\mathbf{p} - \frac{h\nu}{c}\mathbf{i}_k\right) B_{12}\, d^3\mathbf{p} - N(\mathbf{p}) B_{21}\, d^3\mathbf{p}\right], \tag{1.55}$$

where $N(\mathbf{p})$ is the 3-dimensional distribution of particle momenta. We can simplify Equation 1.55 by Taylor expanding $N(\mathbf{p} - \frac{h\nu}{c}\mathbf{i}_k)$, and noting that $g_1 = g_2 = 1$ for this

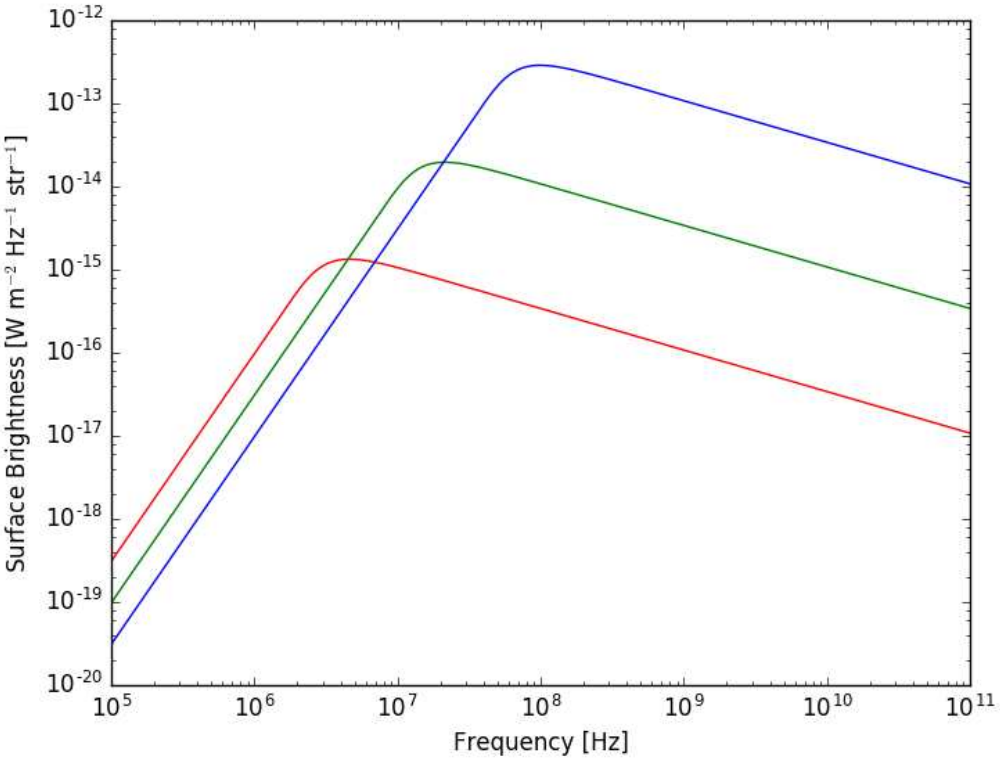

FIGURE 1.13: Example non–thermal radio spectra for populations of CRe interacting with various magnetic field strengths. The red line corresponds to a magnetic field strength, $B = 1\,\mu$G, the green line corresponds to $B = 10\,\mu$G and the blue line corresponds to $B = 100\,\mu$G.

continuum transition (Rybicki and Lightman, 1979):

$$\kappa_{\nu,\mathrm{pair}} = -\frac{h^2\nu^2}{4\pi c} B_{21} \left(\frac{dN(p)}{dp}\right) d^3\mathbf{p}. \tag{1.56}$$

To obtain the total absorption coefficient, we need to integrate this result over all possible momentum pairs:

$$K_\nu = -\frac{h^2\nu^2}{4\pi c} \int_0^\infty B_{21} \left(\frac{dN(p)}{dp}\right) 4\pi p^2\, dp = -\frac{c}{2\nu^2} \int_0^\infty j_\nu \left(\frac{dN(p)}{dp}\right) p^2\, dp. \tag{1.57}$$

Noting that $E = pc$, and that $4\pi p^2 N(p)\, dp = N(E)\, dE$, we transform Equation 1.57 into:

$$K_\nu = -\frac{c^2}{8\pi\nu^2} \int_0^\infty j_\nu(E) \frac{d}{dE} \left(\frac{N(E)}{E^2}\right) E^2\, dE. \tag{1.58}$$

This equation is general and can be used to obtain the absorption coefficent for any distribution of CRe energies involved in the synchrotron emission process. It is also important to note that the absorption coefficent will change for different energy distributions. For the power–law parameterisation ($N(E) = \kappa E^{-p}$), Longair (2011) finds that the absorption coefficent averaged over all pitch angles is:

$$K_\nu = \frac{\sqrt{3} e^3 c \kappa}{8\pi^2 \varepsilon_0 m_e} B^{\frac{(p+2)}{2}} \left(\frac{3e}{2\pi m_e^3 c^4} \right)^{\frac{p}{2}} \nu^{-\frac{(p+4)}{2}} b(p) \ \left[\mathrm{m}^{-1}\right] \tag{1.59}$$

where $b(p)$ is given by:

$$b(p) = \frac{\sqrt{\pi}}{8} \frac{\Gamma\left(\frac{3p+22}{12}\right) \Gamma\left(\frac{3p+2}{12}\right) \Gamma\left(\frac{p+6}{4}\right)}{\Gamma\left(\frac{p+8}{4}\right)}. \tag{1.60}$$

We plot example non–thermal spectra in Figure 1.13. Towards low frequencies, the emitting region is optically thick, and the observed spectra approaches $I_\nu \propto \nu^{\frac{5}{2}}$. This differs from the Rayleigh–Jeans behaviour found for thermal emission as the charged particles producing the non–thermal emission are not in thermal equilibrium. As we transition into the optically thin regime, we find that the non–thermal spectrum will take the form of a power–law, with a spectral index, α, that is related to the underlying particle distribution index, $I_\nu \propto \nu^\alpha$ where $\alpha = -\frac{(p-1)}{2}$. Power–law non–thermal spectra are typically found in astronomical sources at $\approx$GHz frequencies, with SNR typically exhibiting a power–law particle energy distribution with power law index $p \approx 2$ ($\alpha \approx -0.5$; Green, 2014) and star–forming galaxies typically exhibiting $p \approx 2.4$ ($\alpha \approx -0.8$; e.g., Condon, 1983).

The Origin of Cosmic Ray Electrons

In a gas in thermal equilibrium, the individual particles have velocities that are distributed according to the Maxwell–Boltzmann velocity distribution due to collisions between the individual particles in the gas. This process, however, does not describe the power–law energy distributions that are required to produce the observed non–thermal radio spectra seen in astronomical sources. Fermi (1949) presented a mechanism that could accelerate charged particles to the observed power–law distribution through collisions with randomly moving magnetic fields (mirrors) in the ISM. This mechanism became known as second order Fermi acceleration, as the energy gain per collision with a magnetic mirror is proportional to $\left(\frac{v_m}{c}\right)^2$ where v_m is the velocity of the mirror. However, this explanation for the observed power–law energy distribution is unsatisfactory for two main reasons:

1. As the velocities of the moving mirrors, v_m are small compared to the speed of light, the energy gain in each collision is very small. Also, as the mean free path for a Cosmic ray in the ISM is of order 0.1 pc (Longair, 2011), the timescale for acceleration is very long.
2. There is no physical reason for the injection index p to take the values of $p = 2$ to 2.4 that are typically observed in SNR and nearby galaxies. If the second order Fermi mechanism was the dominant acceleration process, then it would be surprising that such similar properties are observed over a wide range of environments.

In the late 1970's, a mechanism for particle acceleration was discovered where the energy gain per collision with magnetic mirrors either side of a shock front is proportional to $\frac{v_s}{c}$, where v_s is the shock velocity. This process is known in the literature as first order Fermi acceleration or Diffusive Shock Acceleration (DSA; Krymskii, 1977; Axford et al., 1977; Bell, 1978a,b; Blandford and Ostriker, 1978). This process is effectively the same as second order Fermi acceleration, except the accelerated particles only experience head on collisions.

We obtain the basic properties of DSA following the test particle approach of Bell (1978a). The next section largely follows the derivation of first order Fermi acceleration as presented in Longair (2011). Consider a shock wave propagating through the ISM with velocity v_s. We define the medium that has not yet been shocked as the upstream medium, and the medium that has already been shocked as the downstream medium. In a frame of reference where the shock is stationary, we find that the upstream medium appears to be travelling towards the shock at velocity $u_1 = v_s$ and that the downstream medium is traveling away from the shock at velocity u_2 (see Figure 1.14). From the Rankine–Hugoniot jump conditions (Longair, 2011), we can relate u_1 to u_2 through:

$$u_1 = \frac{\gamma + 1}{(\gamma - 1) + 2/M_1^2} u_2, \tag{1.61}$$

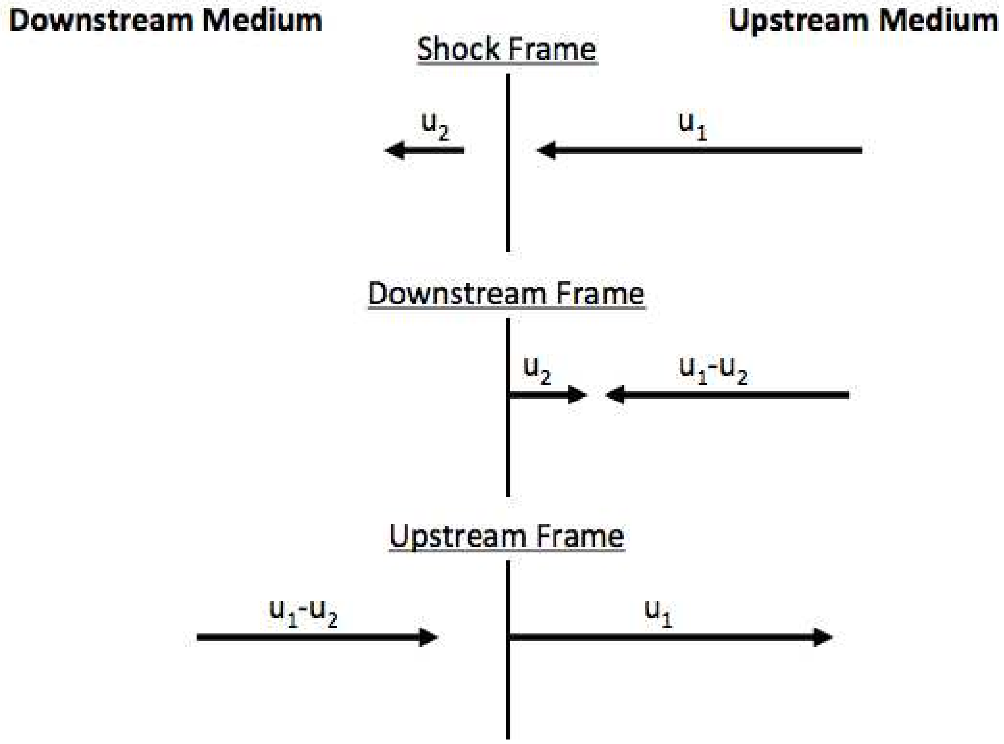

FIGURE 1.14: Schematic showing the relevant frames of reference for the DSA mechanism. The vertical line corresponds to the shock front, the area on the left corresponds to the downstream medium and the area on the right corresponds to the upstream medium. The top schematic corresponds to the frame where the shock is stationary, the middle where the downstream medium is stationary and the bottom where the upstream medium is stationary.

where γ is the adiabatic index of the upstream (un–shocked) medium and M_1 is the mach number of the shock in the upstream medium. In the limit of a strong shock ($M_1 \gg 1$), for a mono–atomic gas ($\gamma = \frac{5}{3}$) we find that $u_1 = 4u_2$.

There are two other relevant frames of reference involved in the acceleration process, one for the upstream medium and another for the downstream medium. In the case that the shock is non–relativistic ($v_s << c$), we find that a reference frame where the upstream medium is stationary would see the downstream medium travelling towards it at a velocity, $u_1 - u_2$. Likewise, in the reference frame where the downstream medium is stationary, it would see the upstream medium traveling towards it at the same velocity, $u_1 - u_2$. This symmetry between the upstream and downstream media gives rise to the always head on reflections that characterises the DSA mechanism. We illustrate these additional reference frames in Figure 1.14 (also see Figure 17.3 in Longair 2011).

We now introduce a relativistic cosmic ray (either a proton or electron) into the shock region. Assuming that the cosmic ray is isotropised in the upstream medium (i.e., on average it is 'at rest' with respect to the upstream medium) through interactions with magnetic inhomogeneities, it has a chance to diffuse across the shock into the downstream medium which is moving towards it at velocity, $u_1 - u_2$. When the cosmic ray interacts with magnetic fields in the downstream medium, it is quickly isotropised again through interactions with magnetic inhomogeneities and gains energy. As we have shifted between two different reference frames with relative velocity $u_1 - u_2$, we calculate the energy gain between the two media through the inverse Lorentz transformation (Equation A.5):

$$E = \gamma(E' + \beta p'_x c), \tag{1.62}$$

where γ is the Lorentz factor, $\beta = \frac{u_1 - u_2}{c}$ and p_x is the cosmic ray momentum in the x–direction. The primed quantities represent the Cosmic ray energy and momentum in the upstream (original) frame. Under the assumption that the shock is non–relativistic and that the cosmic ray is ultra–relativistic, we find:

$$E = \left(1 + \frac{u_1 - u_2}{c}\cos(\theta)\right)E',$$

or

$$\frac{\Delta E}{E'} = \frac{E - E'}{E'} = \frac{u_1 - u_2}{c}\cos(\theta), \tag{1.63}$$

where θ is the angle between the cosmic ray's direction of motion and the direction normal to the shock front. Equation 1.63 shows that each time the cosmic ray crosses the shock and is isotropised, it gains energy proportionally to the energy that it had on the other side of the shock. If we assume that the shock is planar and infinite in extent, all cosmic rays upstream will eventually return to the shock front and re–enter the downstream region. However, there is a chance that the particles in the downstream medium are advected away from the shock and never re–cross it. From these simple observations, we can ask two questions: what is the energy of a cosmic ray after k cycles (where a cycle is defined as diffusing to and from the upstream region from the downstream region) and how many particles will remain in the shock after these k cycles.

The cosmic ray energy after k cycles is given by:

$$E_k = \xi^k E_0, \tag{1.64}$$

where E_0 is the injection energy and ξ is the fractional energy gain per cycle. The number of cosmic rays remaining in the shock region after k cycles is easily found through:

$$N_k = P_{rem}^k N_0, \tag{1.65}$$

where N_0 is the total number of injected cosmic rays and P_{rem} is the probability that the cosmic ray remains in the shock region after one cycle. Combining Equations 1.64 and 1.65, we find the total number of cosmic rays with energy greater than E is:

$$N(>E) = N_0 \left(\frac{E}{E_0}\right)^{\ln(P_{rem})/\ln(\xi)}. \tag{1.66}$$

To obtain the number of cosmic rays per energy interval (the differential energy spectrum), we first multiply Equation 1.66 by a factor of -1 (as the equation is the integrated energy spectrum that starts integrating at higher energies first) and then differentiate the result with respect to energy. If P_{rem} and ξ are independent of energy, E, we find:

$$N(E) = -\frac{\ln(P_{rem})}{\ln(\xi)} \frac{N_0}{E_0} \left(\frac{E}{E_0}\right)^{\ln(P_{rem})/\ln(\xi)-1}, \tag{1.67}$$

i.e., we find a power–law energy distribution for the accelerated cosmic rays.

We now turn our attention to the determination of P_{rem} and ξ in terms of the shock velocity, v_s. Instead of directly calculating the probability that the cosmic ray remains in the shock after each cycle, P_{rem}, it is easier to first calculate the probability that the cosmic ray escapes the shock, P_{esc}, and note that $P_{rem} = 1 - P_{esc}$. As the cosmic ray cannot escape the shock in the upstream region, we only need to consider the escape probability in the downstream region. The probability of escape can then be easily determined by taking the ratio of the rate at which cosmic rays escape through advection in the downstream medium to the rate at which particles cross the shock from the upstream medium. Assuming that the number density of cosmic rays that are being accelerated is the same either side of the shock, n, the rate at which cosmic rays are advected downstream away from the shock front is:

$$R_{\text{out}} = n u_2. \tag{1.68}$$

As the cosmic rays are relativistic and isotropically distributed, the rate at which cosmic rays diffuse from the upstream region to the downstream region can be found through:

$$R_{\text{in}} = \int_0^{2\pi} \int_0^{\frac{\pi}{2}} \left(\frac{n}{4\pi}\right) c \cos(\theta) \sin(\theta) \, d\theta \, d\phi = \frac{1}{4} n c. \tag{1.69}$$

Therefore, the probability that a cosmic ray remains in the shock region after a single cycle is given through:

$$P_{rem} = 1 - \frac{R_{\text{out}}}{R_{\text{in}}} = 1 - \frac{4 u_2}{c}. \tag{1.70}$$

Finally, in the limit of a strong non–relativistic shock we find:

$$P_{rem} = 1 - \frac{u_1}{c} = 1 - \frac{v_s}{c}. \tag{1.71}$$

Next we calculate the fractional energy gain per cycle, ξ. The energy gain for each half cycle where the cosmic ray is traveling at angle θ to the shock front normal is given in Equation 1.63. To obtain the average energy gain per crossing, we integrate Equation 1.63 over the normalised probability of crossing the shock at angle θ: $p_\theta = 2 \sin(\theta) \cos(\theta) \, d\theta$ (Bell, 1978a; Longair, 2011). The average energy gain per crossing is then:

$$\left\langle \frac{\Delta E}{E'} \right\rangle = 2 \int_0^{\frac{\pi}{2}} \frac{\Delta E}{E'} \sin(\theta) \cos(\theta) \, d\theta = \frac{2}{3} \frac{u_1 - u_2}{c}. \tag{1.72}$$

As the energy gained by crossing from downstream to upstream, is the same as that gained from upstream to downstream, the total energy gain per cycle is:

$$\xi = 1 + \frac{4}{3} \frac{u_1 - u_2}{c} = 1 + \frac{u_1}{c} = 1 + \frac{v_s}{c}. \tag{1.73}$$

Noting that the Taylor expansion for $\ln(1+x) \approx x$, we combine Equations 1.71 and 1.73 to find:

$$\frac{\ln(P_{rem})}{\ln(\xi)} \approx -1. \tag{1.74}$$

Thus, the number of cosmic rays per energy interval is:

$$N(E) = \frac{N_0}{E_0}\left(\frac{E}{E_0}\right)^{-2}. \tag{1.75}$$

Remarkably, Equation 1.75 predicts that the cosmic ray energy spectrum should take the form of a power–law with an index $p \approx 2$ ($\alpha \approx -0.5$), which is identical to that found in galactic SNR (Green, 2014). As the only assumption required to produce the observed particle injection index is that the shock is strong, DSA provides a mechanism that is preferred over second order Fermi acceleration for accelerating CRe to the observed power–law distributions, especially as the acceleration timescale for DSA is short (e.g., Drury, 1983).

Cosmic Ray Electron Transport

Although DSA predicts the CRe power–law indices observed in SNR, it does not explain the $p \approx 2.4$ ($\alpha \approx -0.8$) power–law indices observed at $\sim$GHz frequencies in normal star–forming galaxies. As CRe (especially at low energies) typically have synchrotron emitting lifetimes that far exceed the lifetime of the SNR itself (Condon, 1992), the observed (integrated) radio properties from normal star–forming galaxies must result from the superposition of many CRe populations, each of which were accelerated in SNR shock fronts, interacting with magnetic fields in the ISM. As these CRe interact with ISM magnetic fields, they diffuse away from their sites of acceleration (producing the diffuse non–thermal emission component that is observed in both the Milky Way and other nearby star–forming galaxies) and experience energy losses that modify the CRe population energy spectra away from the simple power–law with index $p \approx 2$ found at the sites of acceleration.

The behaviour of the CRe after they have been injected into the ISM can be modeled through the diffusion-loss equation (Schlickeiser, 2002; Longair, 2011):

$$\frac{\partial N}{\partial t} = \nabla \cdot (D\nabla N) - \nabla \cdot (vN) + \frac{\partial}{\partial E}[bN] + Q, \tag{1.76}$$

where N is the CRe density as a function of position, time and energy, D is the (in general energy dependent) diffusion coefficent for the plasma the CRe are diffusing through (i.e., the diffusion term), v is the velocity field for the plasma the CRe are diffusing through (i.e., the advection term), b describes the energy loss rate from the processes the CRe experiences whilst diffusing through the ISM and Q encapsulates the CRe injection (i.e., the SNR). In Equation 1.76, ∇ is the gradient and is defined through:

$$\nabla = \frac{\partial}{\partial x}\mathbf{i} + \frac{\partial}{\partial y}\mathbf{j} + \frac{\partial}{\partial z}\mathbf{k}. \tag{1.77}$$

In the case that the diffusion and advection properties are independent of the CRe energy and that all CRe remain accounted for, we find that these processes do not modify the energy properties of the diffusing CRe (only their position). Thus we can investigate how the energy spectrum for a CRe population will change due to the loss processes by simplifying Equation 1.76 to:

$$\frac{\partial N}{\partial t} = \frac{\partial}{\partial E}\left[b N\right] + Q. \tag{1.78}$$

There are many energy loss processes (i.e., contributions to the b term) that modify the CRe energy distribution away from a simple power–law energy distribution they posses at injection, such as ionisation, bremsstrahlung and adiabatic losses. However in a normal star–forming galaxy, these loss processes are relatively unimportant compared to synchrotron and Inverse Compton losses at ∼GHz frequencies, so we focus on these here. Adiabatic losses in combination with synchrotron and Inverse Compton losses are considered in the context of an expanding SNR in Chapter 4.

We obtain the Synchrotron energy loss rate for a CRe by integrating the dipole emission pattern in Equation 1.43 over all solid angles and noting that the power radiated is invariant between reference frames:

$$b_S = \left(\frac{dE}{dt}\right)_S = \frac{e^4\,\gamma^2\,B^2\,v^2\,\sin^2(\alpha)}{6\,\pi\,\varepsilon_0\,c^3\,m_e^2}. \tag{1.79}$$

As $c^2 = (\mu_0\,\varepsilon_0)^{-1}$, we can rewrite Equation 1.79 as:

$$b_S = 2\left(\frac{e^4}{6\,\pi\,\varepsilon_0^2\,c^4\,m_e^2}\right)\left(\frac{v}{c}\right)^2 c\,\frac{B^2}{2\mu_0}\,\gamma^2\,\sin^2(\alpha) = 2\,\sigma_T\,c\left(\frac{v}{c}\right)^2\gamma^2\,U_{\mathrm{mag}}\,\sin^2(\alpha), \tag{1.80}$$

where σ_T is the Thomson cross–section and U_{mag} is the magnetic field energy density. To obtain the average Synchrotron energy loss rate over all pitch angles, we multiply by $f_\alpha = \frac{1}{2}\sin(\alpha)$ and integrate over all pitch angles to find:

$$b_S = \frac{4}{3}\sigma_T\, c \left(\frac{v}{c}\right)^2 \gamma^2 U_{\rm mag} = \frac{4}{3}\sigma_T\, c \left(\frac{v}{c}\right)^2 \left(\frac{E}{m_e\, c^2}\right)^2 U_{\rm mag}. \tag{1.81}$$

Equation 1.81 shows that the energy loss rate for Synchrotron emission is proportional to the square of the CRe energy. This result shows that CRe with higher energies will quickly radiate away their energy, whereas lower energy CRe will radiate their energy away more slowly. The combination of these two effects will manifest as a break in the CRe energy spectrum towards higher energies (see Figure 1.15), which results in a break in the observed frequency spectrum towards higher frequencies. This phenomenon is known in the literature as spectral ageing, and is frequently observed in the lobes of radio galaxies (e.g., Harwood et al., 2013) and in the halos of nearby star–forming galaxies (e.g. Heesen et al., 2016).

Inverse Compton losses occur when a relativistic CRe gives up some of its energy to a photon in the ambient radiation field. The details behind this interaction are complicated so we quote only the results from this analysis (see Rybicki and Lightman 1979; or Longair 2011; for detailed calculations). The average energy loss through Inverse Compton interactions is given by:

$$b_{IC} = \left(\frac{dE}{dt}\right)_{IC} = \frac{4}{3}\sigma_T\, c \left(\frac{v}{c}\right)^2 \left(\frac{E}{m_e\, c^2}\right)^2 U_{\rm rad}, \tag{1.82}$$

where U_{rad} is the radiation field energy density. The energy loss rate through Inverse Compton interactions is effectively identical to that of synchrotron energy loss rate with the exception that the Inverse Compton energy loss rate depends on the radiation field energy density instead of the magnetic field energy density. Due to these similarities, both the synchrotron and Inverse Compton energy loss rates are usually combined as follows:

$$b_{Tot} = b_S + b_{IC} = \frac{4}{3}\sigma_T\, c \left(\frac{v}{c}\right)^2 \left(\frac{E}{m_e\, c^2}\right)^2 (U_{\rm mag} + U_{\rm rad}). \tag{1.83}$$

Parameterising the energy loss rate as $b = aE^2$, we can find solutions to Equation 1.78 for arbitrary injection histories Q. For example, for a single injection event at $t = 0$ (i.e.,

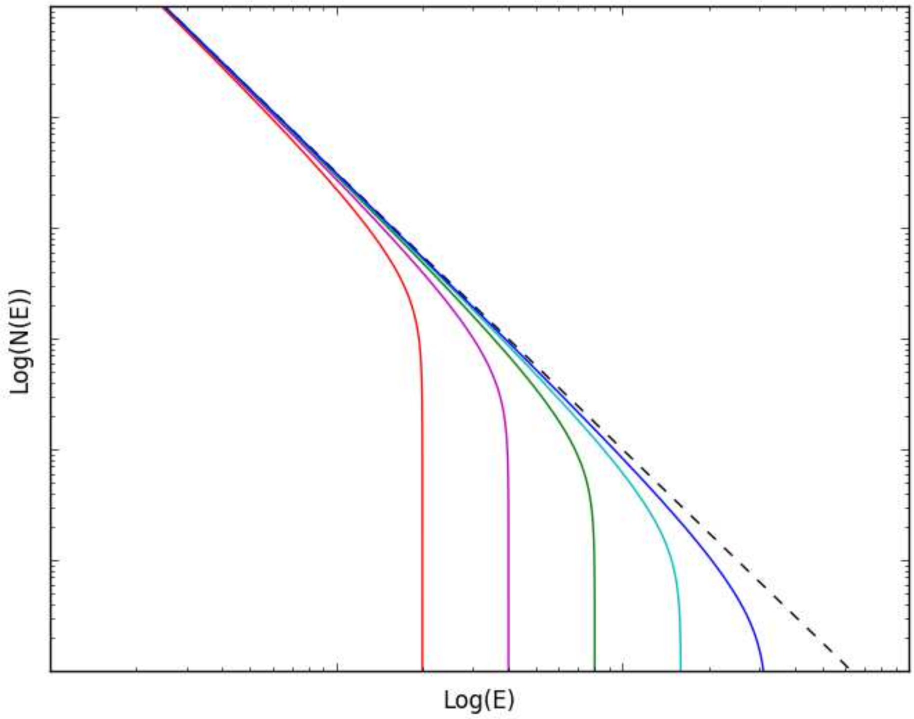

FIGURE 1.15: Plot of Equation 1.84 at various times. The black dashed line corresponds to the injection energy spectrum, and the coloured lines represent the energy spectrum at various times, the blue line being the youngest and the red the oldest. Here we show the case for $p = 2.5$ to emphasise the turn–off from the injection spectrum.

$Q(E,t) = \kappa E^{-p}\,\delta(t))$, the solution to Equation 1.78 is:

$$N(E,t) = \begin{cases} \kappa E^{-p}\,(1 - aEt)^{p-2} & \text{If } a\,E\,t_0 \leq 1, \\ 0 & \text{Elsewhere.} \end{cases} \tag{1.84}$$

Equation 1.84 is also known as the JP model (Jaffe and Perola, 1973), and we plot it for various times in Figure 1.15. Subject to synchrotron and Inverse Compton losses, the CRe energy spectrum retains its injection spectrum at low energies, but shows a turn off at higher energies which moves progressively towards lower energies as time goes on. To obtain the observed synchrotron spectrum, we would need to integrate over Equation 1.84 in Equations 1.49 and 1.58.

The energy losses that the accelerated CRe experience as they travel away from their sites of acceleration provide a mechanism to steepen the observed radio continuum spectrum to the power–law index $p \approx 2.4$ that is typically seen in normal star–forming galaxies. However, as the integrated spectrum is a superposition of many CRe populations (each in varying stages of loss), interpretation of the integrated radio continuum spectrum can become challenging. This motivates the requirement for high–resolution radio–continuum studies of nearby normal star–forming galaxies to understand how the integrated properties emerge from the combination of individual star–formation products.

Non–Thermal Radio Continuum Emission as a Star–Formation Rate Tracer

If SNRs are the dominant accelerators of CRe in normal star–forming galaxies, then the observed non–thermal radio continuum emission should directly trace the recent SN rate. As core–collapse Type II SNe occur far more frequently than Type Ia SNe in star–forming galaxies (e.g., Tsujimoto et al., 1995), we can assume that most of the synchrotron emitting CRe must have originated from the deaths of massive stars ($\geq 8\,\mathrm{M}_{\odot}$). As these massive stars typically have short lifetimes ($\sim$ 10 Myr), the non–thermal radio continuum emission should therefore provide a robust tracer of recent star formation.

The non–thermal radio continuum emission differs from other more direct star–formation rate tracers in a few aspects. Usually, star–formation rate tracers measure the properties of massive stars that are currently on the main sequence (Kennicutt, 1998), however the non–thermal radio continuum emission is produced when these stars end their lifetimes in SN explosions. Therefore, the non–thermal radio continuum emission traces star formation that occured roughly an average massive star main sequence lifetime ago, rather than the instantaneous star formation rate. In larger spiral galaxies, this is not usually a problem as the total star–formation rate remains roughly constant for long periods of time; however, in a galaxy with a bursty star–formation history, there may be a time lag between the emergence of non–thermal radio continuum emission as compared to other, more instantaneous star formation tracers. Additionally, the frequency at which the radio continuum observation is made influences the time period over which past star formation is traced. For example, a CRe emitting most of its energy at 1 GHz in a $10\,\mu$G magnetic field will exist for $\approx$ 30 Myr whereas a lower energy CRe emitting its energy at 100 MHz will exist for $\approx$ 100 Myr. Thus monochromatic star–formation rate calibrations will need to take into account the average magnetic field strength in the star–forming galaxy to correctly capture the star–formation rate averaged over a particular time frame. Finally, the non–thermal emitting CRe do not remain confined to their sites of acceleration and diffuse into the surrounding ISM. This smears out the resolved properties of normal star–forming galaxies, especially at low–frequencies where the non–thermal radio continuum emission dominates (see Section 1.2.3). Whilst the CRe diffuse away from their sites of acceleration they can escape the galaxy altogether, which can lead to the non–thermal radio continuum emission underestimating the star–formation rate as compared to other star formation tracers.

There is strong evidence in the literature for the observed non–thermal emission originating from SN explosions. For example, there are strong correlations between numerous star–formation rate tracers and the observed non–thermal radio continuum emission in both integrated (e.g., Murphy et al., 2011; Tabatabaei et al., 2017) and resolved (Heesen et al., 2014) studies. In dwarf galaxies however, the non–thermal radio continuum emission is found to significantly underestimate the star–formation rate if calibrations that are found for larger spiral galaxies are used, indicating that CRe escape may play a significant role in these systems (Hindson et al., 2018). We find further evidence for this picture in the flattening of the integrated radio continuum spectrum towards the injection spectrum at low–frequencies in non–starburst galaxies (Gürkan et al., 2018; Read et al., 2018; Klein et al., 2018). In the literature, this flattening has been usually interpreted as free–free absorption (e.g., Schober et al., 2017), however Chyży et al. (2018) have demonstrated that this process does not play a huge role in the integrated properties of nearby galaxies. The interpretation of this result is that the free–free absorbing medium (i.e., the individual HII regions) takes up a small fraction of the non–thermal emitting volume, and thus does not contribute significantly to the integrated non–thermal radio spectrum. This view is reinforced as individual HII regions have been shown to exhibit the effects of free–free absorption in both galactic and extra–galactic studies (Hindson et al., 2016; Kapińska et al., 2017; Basu et al., 2017).

In general, it is very challenging to predict the observed non–thermal radio continuum properties a priori, as we would need to know the galaxy wide magnetic field configuration, all of the relevant loss processes and diffusion mechanisms as well as the spatially and temporally resolved star–formation history of the galaxy to be modelled. If these quantities are known (or assumed), then the observed non–thermal radio continuum emission can be modeled through the diffusion loss equation with an injection parameter:

$$Q(\mathbf{r},E,t) = \sum_{i=1}^{N_{SN}} \kappa E^{-p} \, \delta(\mathbf{r}-\mathbf{r}_i) \, \delta(t-t_i), \tag{1.85}$$

where N_{SN} is the total number of SN explosions, $\mathbf{r}_i$ is the position of the i^{th} SN and t_i is the time at which the i^{th} SN occurs.

The shape of the integrated non–thermal spectrum can then take on a multitude of shapes depending upon the distribution of the SN explosions both in position and in time. For example, if all SN are uniformly distributed in the galaxy disk and all injected at the same time (such as in a global star–formation burst), then the integrated non–thermal properties will evolve according to Equation 1.84 and produce a significant break in the observed radio spectrum. Alternatively, if all of the SN are equally spread out in time as well (akin to a more constant star–formation rate), then the break will be smeared out due to the constant injection of newer CRe populations. These properties can make the interpretation of integrated non–thermal spectra difficult, and motivates the use of multi–frequency, spatially resolved studies to disentangle the various CRe populations responsible for the observed integrated properties.

1.2.3 The Integrated Radio Continuum Properties of Normal Galaxies

The integrated radio continuum properties of normal star-forming galaxies are the observables that are sampled with monochromatic radio–continuum observations, and generally comprise of the two discussed components; a thermal component from the HII regions surrounding massive stars that are currently on the main sequence, and a non–thermal component, originating from SN explosions that initially accelerated the synchrotron emitting CRe. We present example integrated radio continuum spectra in Figure 1.16.

Generally, the radio continuum spectral energy distributions (SED) of normal star–forming galaxies follow the same approximate shape. Starting at low–frequencies ($<$ 1 GHz), we find that the observed radio SED is dominated by the non–thermal component with a spectral index that closely resembles the injection index ($\alpha \approx -0.5$). As we transition to $\sim$ GHz frequencies, we find the non–thermal component tends to steepen due to CRe energy loss processes, and the thermal component starts to play a larger role in the observed radio SED. At mid radio continuum frequencies (1–10 GHz; Tabatabaei et al., 2017), we find the radio SED curves upwards as the non–thermal component drops off until we reach high frequencies ($> 10\,\mathrm{GHz}$) where the observed SED tends to be dominated by the thermal component. At higher frequencies ($\sim 30\,\mathrm{GHz}$), there may be a requirement for a component describing Anomalous Microwave Emission (AME; however the total contribution of AME to an integrated galaxy SED is not yet known due to generally poor frequency coverage at radio continuum frequencies $> 10\,\mathrm{GHz}$; Dickinson et al., 2018), and at $\approx 100\,\mathrm{GHz}$, we encounter the Rayleigh–Jeans tail of the thermal emission from cold dust in the ISM.

It is generally challenging to separate the radio continuum emission components from an integrated galaxy SED, as usually there are only a handful of data points that are available at radio frequencies. Furthermore, the non–thermal component is generally curved which is difficult to fit without prior knowledge of the nature of the star–formation (i.e., whether it is constant or bursty). High-resolution, multi–frequency observations of the individual star–formation products within nearby galaxies (such as HII regions and SNR) can help to reduce the degeneracy (Condon, 1992). We discuss the separation of radio emission components in more detail in Chapter 3.

A final quantity of interest is the thermal fraction at a particular frequency, which is defined through:

$$f_{th,\nu} = \frac{S_{th,\nu}}{S_{th,\nu} + S_{nt,\nu}}, \tag{1.86}$$

where $S_{th,\nu}$ is the thermal flux density at frequency ν and $S_{nt,\nu}$ is the non–thermal flux density at the same frequency. For normal star–forming galaxies, f_{th} is typically 10 % at 1.4 GHz (Condon, 1992). Although this fraction is generally observed to be a constant in larger galaxies, it may be significantly higher in smaller dwarf galaxies due to a combination of CRe escape and their generally bursty star formation histories.

Although the non–thermal radio continuum emission is much more complex than the thermal radio continuum emission, it is generally much brighter and more easily accessible by low frequency observations. Thus there is significant motivation for understanding and interpreting the non–thermal radio continuum emission in the era of the SKA and ngVLA.

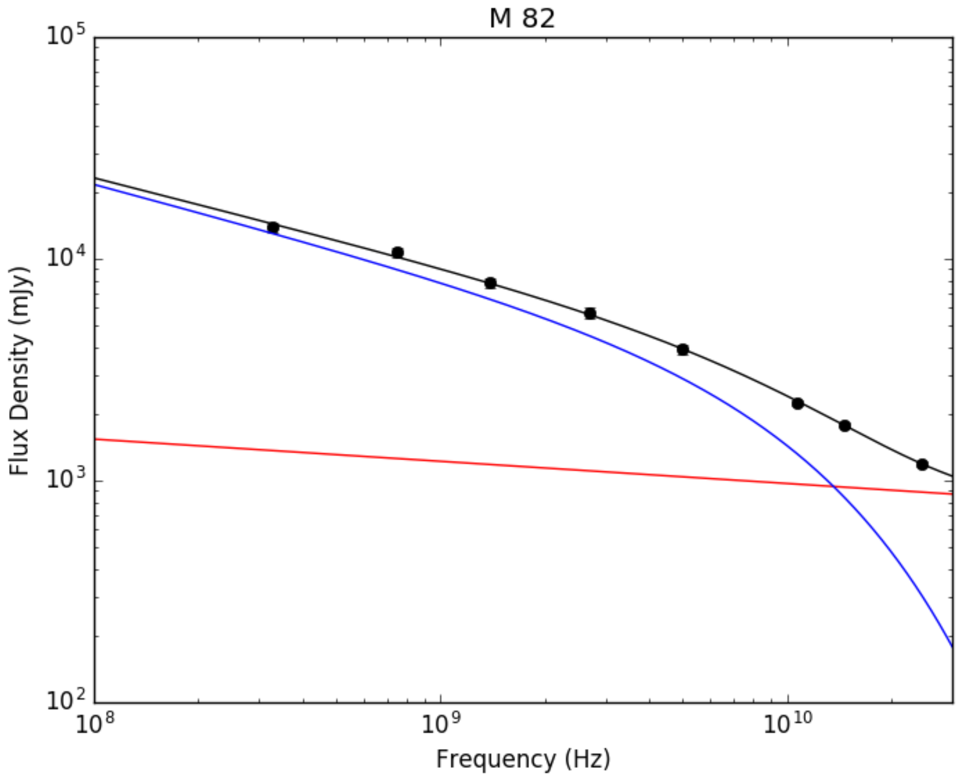

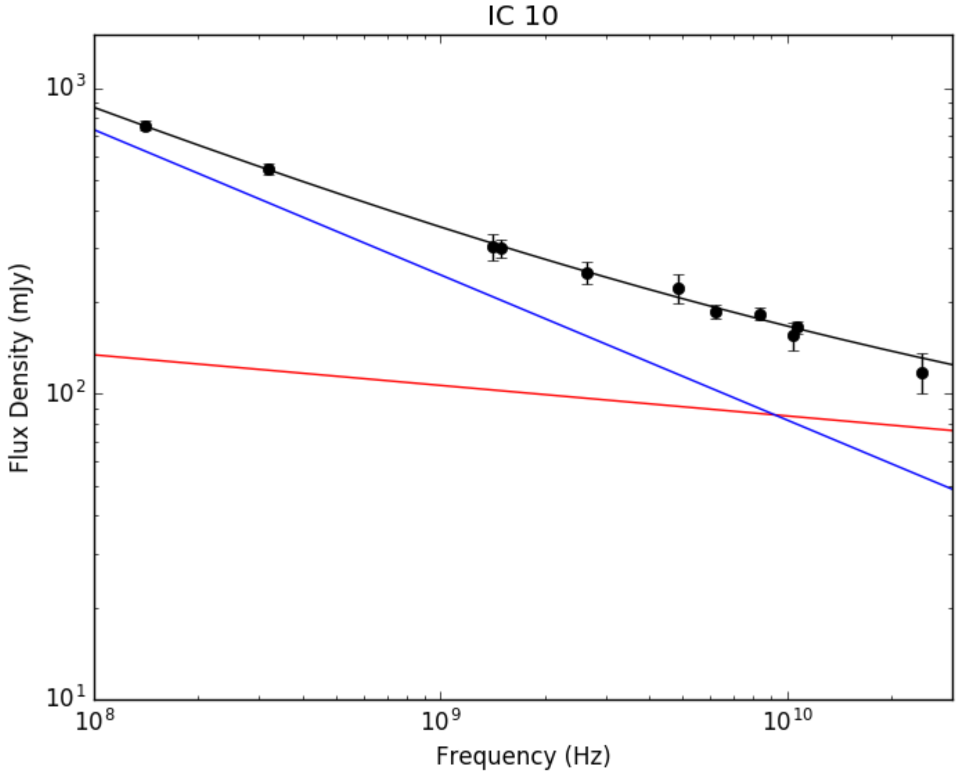

FIGURE 1.16: Example radio spectral energy distributions for M 82 and IC 10. The data compilations and corresponding model fits are taken from Klein et al. (2018) and Basu et al. (2017). The black datapoints (with corresponding errors) represent the individual monochromatic radio continuum observations, the red line corresponds to the separated thermal radio continuum component, the blue line corresponds to the separated non–thermal radio continuum component and the black line is the combination of the two. Note that the non–thermal component for M 82 is significantly curved compared to the non–thermal component recovered for IC 10.

1.3 A Brief Summary of Current Radio Continuum–Star Formation Calibrations

In normal star–forming galaxies, the observed radio continuum emission is strongly related to recent star–formation. This has motivated many authors to derive calibrations to link the observed mono–chromatic radio continuum emission to star–formation. Here we review some of these calibrations that are popularly used in the literature.

Early Efforts

One of the earliest attempts to utilize both the thermal and non–thermal radio emission components as a tracer of recent star formation is the study by Biermann (1976). In this pioneering work, Biermann adapted the galaxy evolution code from Tinsley (1972) to predict the thermal and non–thermal contributions for a model galaxy at 5 GHz. He made two simplifying assumptions about the radio continuum emission originating from normal star–forming galaxies in his model:

1. All thermal radio emission originates from HII regions, which surround massive stars that are currently on the main sequence.
2. All non–thermal radio continuum emission originates from SNR. Each SNR is assumed to be identical and independent from both its progenitor mass and surrounding gas density.

Both of these assumptions are reasonable across most normal galaxy environments. The first assumption is valid in nearly all cases as, in the absence of an accreting AGN, massive stars are the main source of ionizing UV photons that lead to the production of thermal radio emission (see Section 1.2.1). The second assumption also appears to be reasonable, due to the existence of a relationship between the observed SNR radio continuum surface brightness and SNR diameter (also known as the $\Sigma - D$ relationship; Clark and Caswell, 1976; Case and Bhattacharya, 1998; Urošević et al., 2005). In fact, theoretical interpretations of the $\Sigma - D$ relationship require that the blast energy and surrounding gas density for all SNR are similar (Duric and Seaquist, 1986). This is replicated in observations of SNR in the SMC, LMC and other nearby galaxies which have been shown to also follow this relationship, despite seemingly very different ISM conditions (Case and Bhattacharya 1998; Urošević et al. 2005; see Figure 1.17).

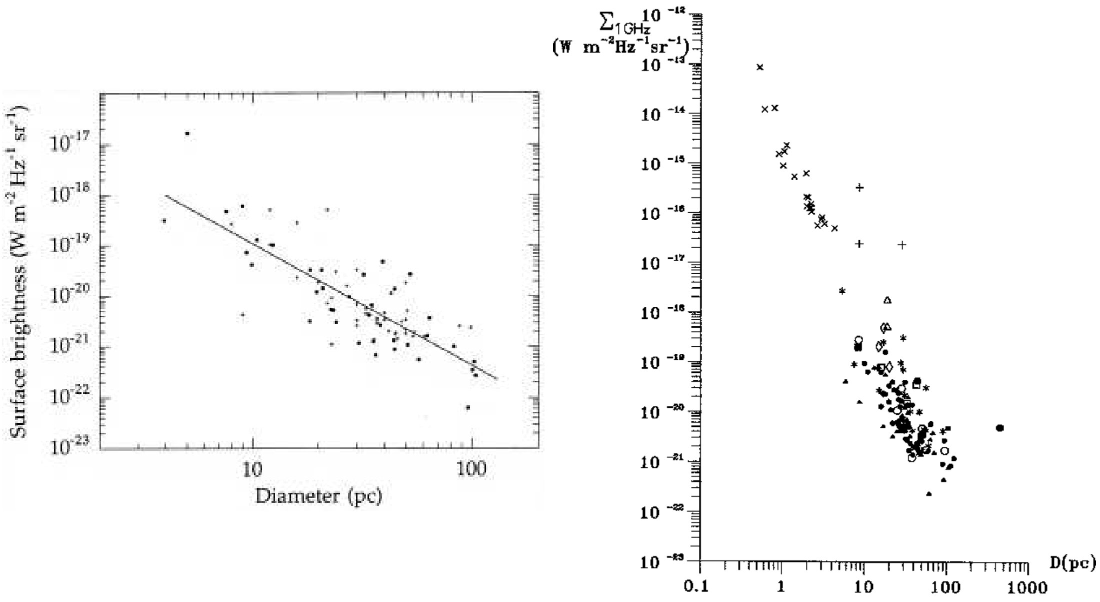

FIGURE 1.17: The diagram on the left shows the $\Sigma - D$ relationship for SNR taken from Case and Bhattacharya (1998). The diagram on the right shows the $\Sigma - D$ relationship for extra–galactic SNR, taken from Urošević et al. (2005).

Biermann used the $\Sigma - D$ relationship from Clark and Caswell (1976) to determine the total radio emission originating from an average SNR, and assumed a Salpeter IMF (Salpeter, 1955) in combination with an observed SFR to calculate the number of core–collapse SNe and thus, estimate the total non–thermal radio continuum emission originating from recent star formation. He found that this simple model substantially underpredicts the total radio emission when compared to observations and found that increasing the predicted non–thermal flux by a factor of $\sim$10 brings the model in line with observations. He also importantly noted that this model relies heavily on the assumed IMF, which may vary with metallicity (e.g., Geha et al., 2013).

Other authors also encountered similar difficulties whilst trying to reconcile the radio emission predicted by the $\Sigma - D$ relation with other observed galaxy properties. For example, Condon et al. (1982a) noted that the SN rate predicted by the $\Sigma - D$ relation may be an overestimate of the actual SN rate based on the morphology of the radio emission. They found that the observed radio emission is not entirely confined to discrete sources within the disks of normal galaxies as a significant diffuse component is also observed. Furthermore, by comparing the radio emission predicted by scaling the models from Rieke et al. (1980) to the SN rates predicted by the $\Sigma - D$ relation, they also found that the predicted radio luminosity is a factor of 10 higher than that observed. Jenkins (1984) also could not find a satisfactory explanation for the high supernova rate required to explain the non–thermal emission for NGC 5953 when compared to Hα observations.

It is clear from these early studies that radio–SFR diagnostics derived from the $\Sigma - D$ relationship alone underpredict the actual SFR by approximately an order of magnitude. This is primarily due to the $\Sigma - D$ relationship effectively only probing the Sedov–Taylor phase of SNR evolution (Taylor, 1950; Sedov, 1959) with the assumption that all of the detected non–thermal radio emission originates from this phase (Woltjer, 1972). The CRe that are accelerated in SNR typically have synchrotron emitting lifetimes that far exceed the observable lifetime of the SNR. Therefore, the CRe must continue to radiate, long after the SNR has faded into the ISM (Pooley, 1969a; Ilovaisky and Lequeux, 1972; Völk et al., 1989; Condon, 1992). This new approach explains the diffuse non–thermal structures observed in star–forming galaxies but requires various loss mechanisms to be invoked to explain the steeper spectral indices observed in spiral galaxies ($\alpha \sim -0.8$; Condon 1983) compared to the spectral indices of galactic SNR ($\alpha \sim -0.5$; Green 2014). Hence, as the non–thermal emission component is generally much stronger than the thermal emission component, understanding how CRe diffuse throughout galaxy disks (CRe transport) becomes critical to understanding how radio continuum emission is linked to star formation and the form of the radio–SF relation, especially at low–frequencies.

The Condon Relation

Condon and Yin (1990) noted that the SN rate predicted by earlier models using the $\Sigma - D$ relationship are too high and proposed a new model to account for the total non–thermal radio luminosity originating from SNRs. To find the total radio luminosity per SN, they simply took the integrated non–thermal radio luminosity from the Milky Way at 408 MHz from Berkhuijsen (1984) and divided it by the SN rate from Tammann (1982) to find:

$$L_{NT} \approx 1.3 \times 10^{23} \left(\frac{\nu}{1\,GHz}\right)^{\alpha} \nu_{SN}\left(yr^{-1}\right)\ \left[\mathrm{W\,Hz^{-1}}\right] \tag{1.87}$$

where L_{NT} is the non–thermal radio luminosity, ν is the frequency of interest in GHz, α is the non–thermal spectral index of the Milky Way ($\alpha \simeq -0.8$) and ν_{SN} is the supernova rate in yr^{-1}. The basic assumption behind this relationship is very similar to the second assumption that Biermann (1976) made, except we now assume that all SNR produce roughly the same non–thermal radio luminosity over their entire lifetime, including emission from CRe diffusion long after the SNR has faded into the ISM. In other words, we are assuming that the ratio L_{NT}/ν_{SN} is the same for all normal star forming galaxies. This is validated by Völk et al. (1989) who found that the CRe production per SN is the similar in both the Milky Way and the starburst galaxy M 82, which have two dramatically different ISM environments. Furthermore, Condon (1992) argues that there cannot be any significant variation in this ratio as it would violate the observed tight radio–FIR correlation (e.g. Helou et al. 1985; Yun et al. 2001). The universality of this ratio can easily be explained if the galaxies behave as calorimeters (Völk, 1989), and is reflected in more complex models for dense starburst galaxies but struggles for lower mass galaxies (Lacki et al., 2010). It is important to also note that this relationship is empirical and does not depend on the assumed IMF.

Condon (1992) turned Equation 1.87 into a simple model to account for all radio emission from normal star–forming galaxies. Noting that the SN rate is proportional to the SFR, Condon (1992) assumed a Miller–Scalo IMF (Miller and Scalo, 1979) to calculate the SN rate assuming that all stars more massive than $8\,\mathrm{M}_{\odot}$ explode as SNe. He then used Equation 1.87 to calculate the total expected non–thermal radio luminosity as a function of SFR. For the thermal contribution, he combined equations relating thermal emission to Hβ measurements from Caplan and Deharveng (1986), the Hα/Hβ flux ratios from Hummer and Storey (1987) and the Hα calibrations from Kennicutt (1983) to predict the thermal luminosity as a function of SFR. The two resulting Condon relations for the thermal and non–thermal emission are written as follows:

$$\left(\frac{L_T}{\mathrm{W\,Hz^{-1}}}\right) \sim 5.5\times10^{20}\left(\frac{\nu}{1\,\mathrm{GHz}}\right)^{-0.1}\left[\frac{\mathrm{SFR}(\mathrm{M}\geq 5\,\mathrm{M}_{\odot})}{\mathrm{M}_{\odot}\mathrm{yr}^{-1}}\right] \tag{1.88}$$

$$\left(\frac{L_{NT}}{\mathrm{W\,Hz^{-1}}}\right) \sim 5.3\times10^{21}\left(\frac{\nu}{1\,\mathrm{GHz}}\right)^{\alpha}\left[\frac{\mathrm{SFR}(\mathrm{M}\geq 5\,\mathrm{M}_{\odot})}{\mathrm{M}_{\odot}\mathrm{yr}^{-1}}\right] \tag{1.89}$$

where α is the observed non–thermal spectral index of the Milky Way. These equations currently predict the radio continuum emission resulting from star–formation considering only the stars that are more massive than $5\,\mathrm{M}_{\odot}$. To correct the SFR to include all stars, the SFR found by inverting these equations must be multiplied by a factor of 5.5 (Condon et al., 2002).

It is important to note that both these relationships are directly proportional to the SFR, and hence, the sum of these components should also be directly proportional to the SFR. This indicates that the total radio continuum emission should be an excellent, extinction free, tracer of recent star formation that holds as long as L_{NT}/ν_{SN} is the same for all normal star forming galaxies (and also assuming no variations in the IMF). As mentioned earlier, the existence of the radio continuum–FIR relation provides strong validation of the Condon relation, and its simplicity means that it is easily applicable to many cases where L_{NT}/ν_{SN} can be assumed to be constant.

The Bell Calibration

Although the Condon relationship is simple and depends only upon the observed radio continuum emission, the breadth and tightness of the radio continuum–FIR correlation proved to be an attractive basis for a radio continuum–star formation relationship. At a first glance, this procedure is reasonable as both the radio–continuum emission and FIR emission are known to closely trace recent star–formation (Kennicutt, 1998).

However, Bell (2003) found on closer inspection that the physics behind the observed correlation is complex. At low galaxy luminosities (masses), it was already known that the FUV emission originating from massive stars could more easily escape the galaxy. This indicates that the star–formation rates inferred from the FIR in these systems will underpredict the true star–formation rate. If the radio continuum emission is a perfect tracer of star–formation, we would expect to find a change in the radio continuum–FIR correlation towards these low luminosity systems. However, no such deviation is observed, which led Bell (2003) to conclude that the radio continuum emission must also understimate the true star–formation rate for these low–mass systems. In terms of the Condon relation, this result indicates:

1. The thermal radio continuum emission should be suppressed somewhat due to the ionizing UV photons escaping the HII regions surrounding massive stars.
2. The fraction L_{NT}/ν_{SN} is not constant in these low luminosity systems, indicating that CRe must be escaping the galaxy and are no longer contributing to the observed non–thermal radio continuum emission.

Assuming that the radio–continuum emission at 1.4 GHz deviates in the same way as the FIR emission in the low–luminosity systems, Bell (2003) constructed a radio continuum–star formation relationship from the FIR–star formation relation at 1.4 GHz:

$$SFR_{1.4\,\mathrm{GHz}} = \begin{cases} 5.52 \times 10^{-22}\, L_{1.4\,\mathrm{GHz}} & L_{1.4\,\mathrm{GHz}} > L_c, \\ \frac{5.52\times10^{-22}}{0.1+0.9(L_{1.4\,\mathrm{GHz}}/L_c)^{0.3}}\, L_{1.4\,\mathrm{GHz}} & L_{1.4\,\mathrm{GHz}} \leq L_c, \end{cases} \tag{1.90}$$

where $L_c = 6.4 \times 10^{21}\,\mathrm{W\,Hz^{-1}}$. This relationship agrees with the Condon relation to within a factor of 2, which is remarkable given that this relationship is empirically calibrated from the FIR emission. Further studies into the radio continuum–FIR correlation revealed that there are many factors that are balanced to maintain the correlation over the large range of galaxy luminosity it is observed to hold over, which became known as the ‘radio continuum–FIR conspiracy’ (Lacki et al., 2010). Despite the existence of this ‘conspiracy’, the Bell (2003) calibration remains one of the most popular radio continuum–star formation relationships used in current literature.

More Recent Calibrations

Since these earlier calibrations, more effort has been made to compare the radio–continuum emission properties to other star–formation indicators (not just the FIR). Murphy et al. (2011) demonstrated that, for individual star–forming regions, the thermal radio–continuum emission traced at 33 GHz is directly proportional to the observed 24 μm emission as well as the star–formation rate measured through hybrid tracers, such as Hα + 24 μm (Calzetti et al., 2007). These results demonstrated that the thermal radio continuum emission can be used as a direct tracer of the current number of massive stars, in line with theoretical expectations (see Section 1.2.1). Thus the thermal radio continuum emission empirically traces recent star–formation, with the advantage that the radio continuum emission is largely free of extinction effects. However, large area maps of nearby galaxies at 33 GHz remain unavailable, due to the small fields of view and poor sensitivities of instruments operating at 33 GHz.

This motivated Heesen et al. (2014) to assess the feasibility of using the brighter and more easily accessible non–thermal emission to trace star–formation on a resolved and integrated basis. On a resolved basis, Heesen et al. (2014) found that the non–thermal emission is related to the recent star–formation determined by other tracers, but not

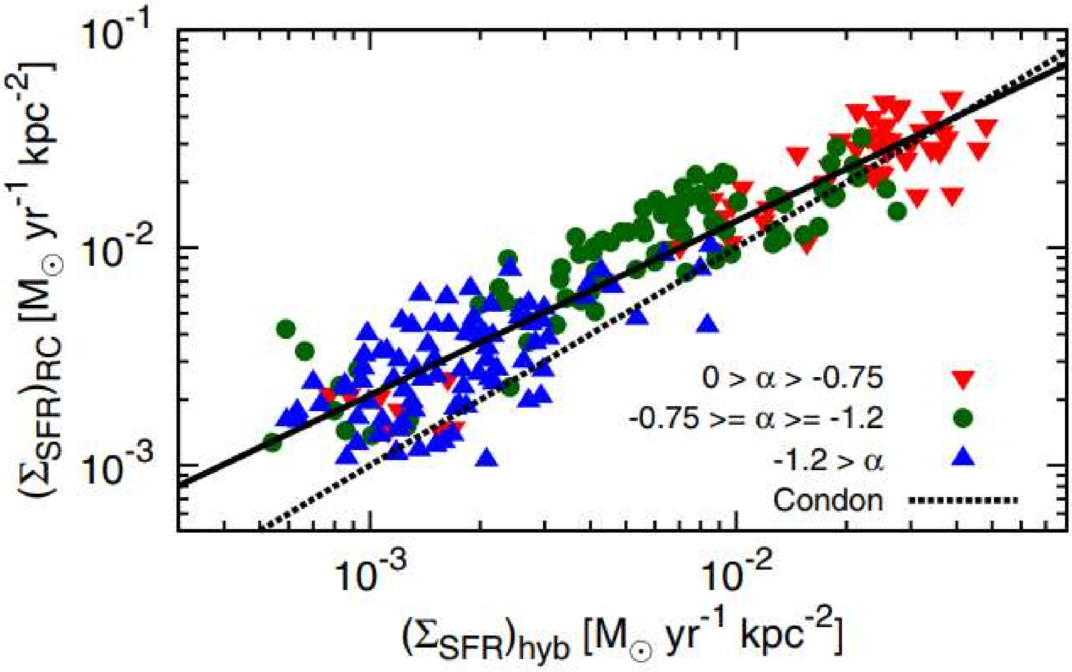

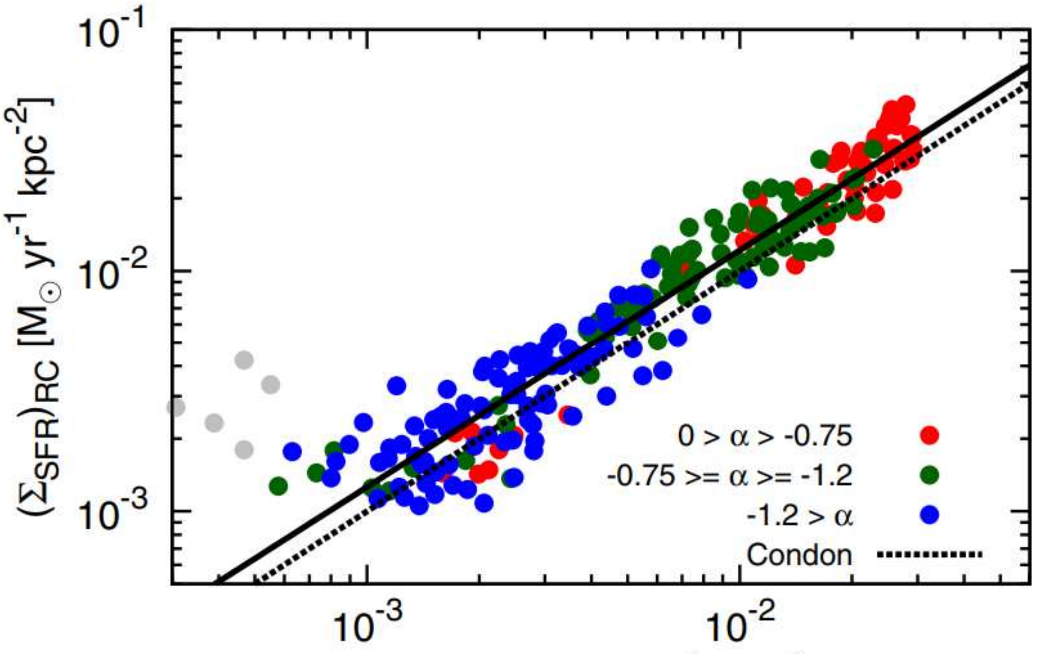

FIGURE 1.18: Plots showing the star–formation surface density obtained from the combination of FUV + 24 μm emission plotted against the star–formation surface density obtained through the Condon relation (effectively the surface brightness at 1.4 GHz) for both before (top) and after (bottom) convolution with a Gaussian kernel to simulate the effects of CRe transport.

linearly like the thermal radio continuum emission. They demonstrated that this non–linearity results from CRe transport by 'linearising' the resolved non–thermal radio continuum star–formation relation by convolving the star–formation maps with a Gaussian kernel to simulate CRe diffusion (see Figure 1.18). Interestingly, this interpretation agrees with an observation by Murphy et al. (2011), that the 1.4 GHz star–formation rate predicted through the radio continuum–FIR correlation (which predominantly traces the non–thermal emission) measured for their individual star–forming regions underestimates the star–formation rate inferred from the thermal radio continuum emission. Heesen et al. (2014) also examined the integrated non–thermal radio continuum star–formation relation for a small sample of 14 nearby galaxies. They found that the integrated non–thermal radio continuum emission is not linearly related to the star–formation rates found from hybrid star–formation rate tracers, but is instead sublinear, indicating a more complex origin.

The linearity of the thermal radio continuum emission and the sub–linearity of the non–thermal radio continuum emission has more recently been confirmed by Tabatabaei et al. (2017), who separated the thermal and non–thermal radio continuum emission components between 1 and 10 GHz on an integrated basis for a much larger sample of 51 KINGFISH (Kennicutt et al., 2011) galaxies. Tabatabaei et al. (2017) also find from their separation procedure that the average non–thermal spectral index for their sample is $\alpha_{NT} \approx -1.0$ which is consistent with the steady state behaviour of constant CRe acceleration subject to synchrotron and Inverse Compton losses, and an average thermal fraction $\approx 10\%$ at 1.5 GHz. These results are consistent with earlier observations (e.g., Condon, 1992), indicating that their separation procedure was successful. Tabatabaei et al. (2017) also define a mid–radio continuum bolometric luminosity that can be determined from 1.5 and 5.0 GHz measurements, and demonstrated that this hybrid luminosity is linearly related to star–formation.

We finish our discussion of the current radio continuum–star formation calibrations with a mention of the recent results from the Hindson et al. (2018) study of a large sample of nearby dwarf galaxies at 5 GHz. The thermal radio continuum emission from these small systems on an integrated basis is consistent with that found for the individual star forming regions in the Murphy et al. (2011) study, whereas the non–thermal radio continuum component is found to be significantly suppressed compared to the hybrid star–formation tracers. This result indicates that CRe are escaping these smaller systems without radiating away a significant portion of their energy. As these small systems are still observed to follow the radio continuum–FIR relation, this result provides direct evidence for the radio–FIR 'conspiracy' described in Bell (2003).

1.4 Thesis Structure

So far in this thesis, we have demonstrated the close relationship between the observed radio continuum emission and recent star–formation, and the factors that drive the observed emission. We now concentrate our discussion on dwarf irregular (dIrr) galaxies. These systems typically undergo short bursts of star formation that are isolated in space and time, giving us a snapshot of the contributions of various emission and loss mechanisms for a single star formation event. The interpretation of the radio continuum emission from these systems is far simpler than that for larger spirals, where many CRe from different star–formation events are superposed. The rest of the thesis is structured as follows:

In Chapter 2, we use e–MERLIN to study the compact star–formation products that are found within the dIrr galaxy, IC 10. Our primary goal is to obtain a census of the star–formation products (compact HII regions and SNR) within this galaxy, which can be used to constrain the star–formation rate, independently of other star–formation tracers. For this purpose, we developed a multi–wavelength scheme to classify the observed sources, which we use to identify star–forming products that belong to IC 10, as well as contaminating background sources that require subtraction from the integrated galaxy spectrum.

This is followed by Chapter 3, where we use VLA observations spanning a wide frequency range to separate the radio continuum emission components found within the dIrr galaxy, NGC 1569, on a resolved basis. In completing this goal, we developed a Bayesian separation procedure, where we use Hα maps to constrain the thermal radio continuum emission component. After we have separated the radio emission components, we use the resulting maps to constrain the line of sight extinction towards NGC 1569 at arcsecond resolution, and obtain estimates of its resolved equipartition magnetic field strengths.

The next chapter, Chapter 4, concentrates on one specific region in NGC 1569 which is dominated by a recent SN explosion, NGC1569–38. Our goal here is to ascertain to what extent synchrotron losses can explain its observed curved non–thermal radio spectrum, as derived in Chapter 3. To this purpose, we compare high resolution e–MERLIN maps at 1.5 GHz with VLA spectra, extracted following the method in Chapter 3. Using these observations, we derive estimates for the age and expansion velocity of NGC1569–38, and compare its minimum energy magnetic field strength with a sample of galactic and extra–galactic SNR.

Chapter 5 provides a summary of the results from the work presented in this thesis, and Chapter 6 provides a brief look into the near future plans.

Chapter 2

The Compact Star Formation Products In IC 10

2.1 Introduction & Motivation

All integrated and $\sim$kpc scale resolved studies of galaxies at radio frequencies effectively measure the surface averaged properties of many individual star–formation products and ISM surrounding them. To understand the origin of these averaged properties, it is necessary to start by understanding the emission on the smallest available spatial scales, i.e. understanding the radio emission originating from the individual star–formation products themselves. There are two key compact star–formation products that are observed with current high–resolution radio–continuum observations, individual HII regions and supernova remnants (SNRs).

To recap what was discussed in Chapter 1, HII regions are clouds of ionised hydrogen, that have been excited by embedded or nearby massive O and B type stars. This ionised hydrogen produces thermal radio–continuum emission, with a characteristic spectral index $\alpha = -0.1$ at $\sim$GHz frequencies. The extent of an HII region depends upon the rate at which Lyman continuum photons are emitted from these massive stars. Hence, under optically thin conditions, the observed thermal radio–continuum emission can be used to infer the total number of massive stars and, with an assumed IMF, be used to calculate an extinction–free star–formation rate (SFR) that is averaged over a similar timescale to that inferred from Hα observations (Kennicutt and Evans, 2012). HII regions exist until the massive stars that are powering them end their lives in supernova (SN) explosions (after 3–10 Myr).

SNR are characterised by shock waves that travel through the interstellar medium, following a SN explosion. In the shock fronts, DSA (Drury, 1983), a subset of Fermi acceleration, accelerates cosmic ray electrons (CRe) to relativistic velocities, where they then go on to interact with magnetic fields (which are enhanced by the shock; Guo et al. 2012) to produce non–thermal (synchrotron) radio continuum emission. From linear test particle DSA theory with strong shocks, we expect to observe a spectral index $\alpha = -0.5$, which is typically found in galactic SNR (Green, 2014). SNR are expected to occur 3–40 Myr after massive stars formed (assuming stars larger than 8 $M_\odot$ explode as SNe) and remain observable for $\sim 10^4$ yr. Although the SNR are themselves observable for a short time period, the large scale non–thermal emission observed in nearby galaxies (originating from CRe that have escaped from SNR and have diffused into the nearby ISM; Condon and Yin 1990) lasts for much longer timescales ($\sim$ 30 Myr).

There are other sources of radio emission that result from the evolution of stars, such as planetary nebulae (Terzian, 1968) and pulsars (Hewish et al., 1968). However these sources are too faint to be observable in nearby galaxies with current instruments (Bagchi, 2013; Leverenz et al., 2016). Radio SNe are bright enough to be detectable in high–resolution radio continuum observations; however, the chance of observing one are minimal due to their extremely short observable lifetimes (typically a couple of years; Weiler et al., 2002). We will therefore focus our study on only the brighter and longer lived HII regions and SNR.

Obtaining a census of the star–forming products that are found within a star–forming galaxy could in principle be used to place useful constraints on said galaxy's current star–formation rate. High–resolution interferometric radio–continuum studies are ideal for this purpose as the spatial scales that are observed by the interferometer can be tuned to focus on the spatial scales that individual star–formation products exist on, and radio emission is insensitive to extinction along the line of sight, providing a direct view of star–formation processes even in dusty environments (such as nuclear starbursts). The **L**egacy **e**–**M**ERLIN **M**ulti–band **I**maging of **N**earby **G**alaxie**s** (LeMMINGs; Baldi et al. 2018) survey aims, in part, to study the compact star–formation products and their relation to large scale radio emission across a wide range of galaxy types. The project is made up of two complementary surveys of nearby galaxies; a statistical survey of 280 galaxies taken in snapshot mode, comprising the entire Palomar spectroscopic bright galaxy sample north of declination +20 degrees, and a deep survey of 6 galaxies, the latter reaching an rms sensitivity of 8 and 3 μJy beam^{-1} at 1.5 GHz and 5 GHz respectively. The statistical survey will detect and resolve radio emission from bright SNe and SNRs to provide a complete census of energetic SF products in the local Universe. At higher sensitivities, the deep survey will also be able to detect the fainter emission from compact HII regions.

Rather than start with studying larger spiral galaxies, where the large scale radio emission characteristics may be complicated due to their potentially complex star–formation histories or AGN activity, we instead chose to start with nearby dwarf irregular (dIrr) galaxies. dIrr galaxies are small, simple stellar systems with typically bursty star–formation histories (McQuinn et al., 2010). This is advantageous for interpretation, as we would expect the large–scale radio emission characteristics to be dominated by the most recent burst of star–formation. Furthermore, entire dIrr galaxies are analogous to single $\sim$kpc^2 chunks of the outskirts of larger spiral galaxies (Bigiel et al., 2010; Elmegreen and Hunter, 2015), so by studying these simple systems, we can attempt to understand the processes that are occurring in the larger spirals.

In this chapter, we present high–resolution LeMMINGs observations of the dIrr galaxy, IC 10, and what we learn from its compact star–formation products.

2.2 IC 10

IC 10 (see Figure 2.1) is a nearby dIrr galaxy that is thought to be currently undergoing a starburst phase (Leroy et al., 2006). Optical studies reveal numerous HII regions (Hodge and Lee, 1990) and the highest density of WR–stars observed in the Local Group (Massey et al., 1992; Crowther et al., 2003). Moreover, stellar population analysis reveals a bursty SF history with the most recent burst finishing $\sim$10 Myr ago (Hunter, 2001; Vacca et al., 2007; Sanna et al., 2009). We present a brief summary of IC 10's properties in Table 2.1.

TABLE 2.1: Key IC 10 properties

Property	Value	Reference
α_{J2000} (hh mm ss)	00 20 17.34	–
δ_{J2000} ($^{\circ}\,'\,''$)	+59 18 13.6	–
Galaxy Type	IBm	1
Distance	0.7 Mpc	2
$\mathrm{SFR}_{\mathrm{H}\alpha-\mathrm{Sal}}$	$0.039 \pm 0.001\,\mathrm{M}_{\odot}\,\mathrm{yr}^{-1}$	3
$\mathrm{SFR}_{\mathrm{H}\alpha-\mathrm{MS}}$	$0.066 \pm 0.002\,\mathrm{M}_{\odot}\,\mathrm{yr}^{-1}$	3
Angular Size (Major Axis)	$11.'68$	4
Angular Size (Minor Axis)	$7.'12$	4
Position Angle	132°	4

Reference List: 1: Nilson (1973), 2: Sakai et al. (1999), 3: Hunter et al. (2012), 4: Jarrett et al. (2003). The IBm galaxy type corresponds to Irregular galaxies that are similar to the Magellanic clouds with a believed bar component. The subscripts on the SFRs indicate which IMF was used to calculate the SFR: Sal is assuming a Salpeter IMF (Salpeter, 1955) and MS is assuming a Miller–Scalo IMF (Miller and Scalo, 1979).

Recent HI investigations into the large–scale gas motions of IC 10 reveal a complex nature, consisting of a large HI envelope with an inner rotating disk and counter–rotating component (Shostak and Skillman, 1989; Wilcots and Miller, 1998; Ashley et al., 2014). The leading explanation for these different kinematical subsystems is that IC 10 is still accreting primordial gas (Wilcots and Miller, 1998), although new evidence hints towards a recent merger or interaction being responsible for the unusual gas kinematics and current starburst (Nidever et al., 2013; Ashley et al., 2014). Furthermore, numerous bubbles and shells are observed in the large scale HI distribution (Shostak and Skillman, 1989; Wilcots and Miller, 1998), hinting that IC 10 is coming towards the end of its current starburst phase (see the bottom–right panel in Figure 2.1). A number of radio continuum studies focused on the non–thermal superbubble towards the South–East of IC 10 (Yang and Skillman, 1993; Heesen et al., 2015), which is thought to be the result of either a collection of supernova remnants (Yang and Skillman, 1993) or a single hypernova event (Lozinskaya and Moiseev, 2007). At its centre resides the X–ray binary system, IC 10 X–1, which is likely related to the birth and evolution of the superbubble (Brandt et al., 1997; Bauer and Brandt, 2004).

IC 10 is located at a low galactic latitude (~-3°), making distance measurements challenging with estimates ranging from 0.5 Mpc to 3 Mpc (Demers et al., 2004; Kim et al., 2009). We will assume a distance to IC 10 of 0.7 Mpc (1 arcsec $\simeq$ 3.4 pc) as listed in Hunter et al. (2012). All distance dependent literature measurements used here have been scaled to this distance.

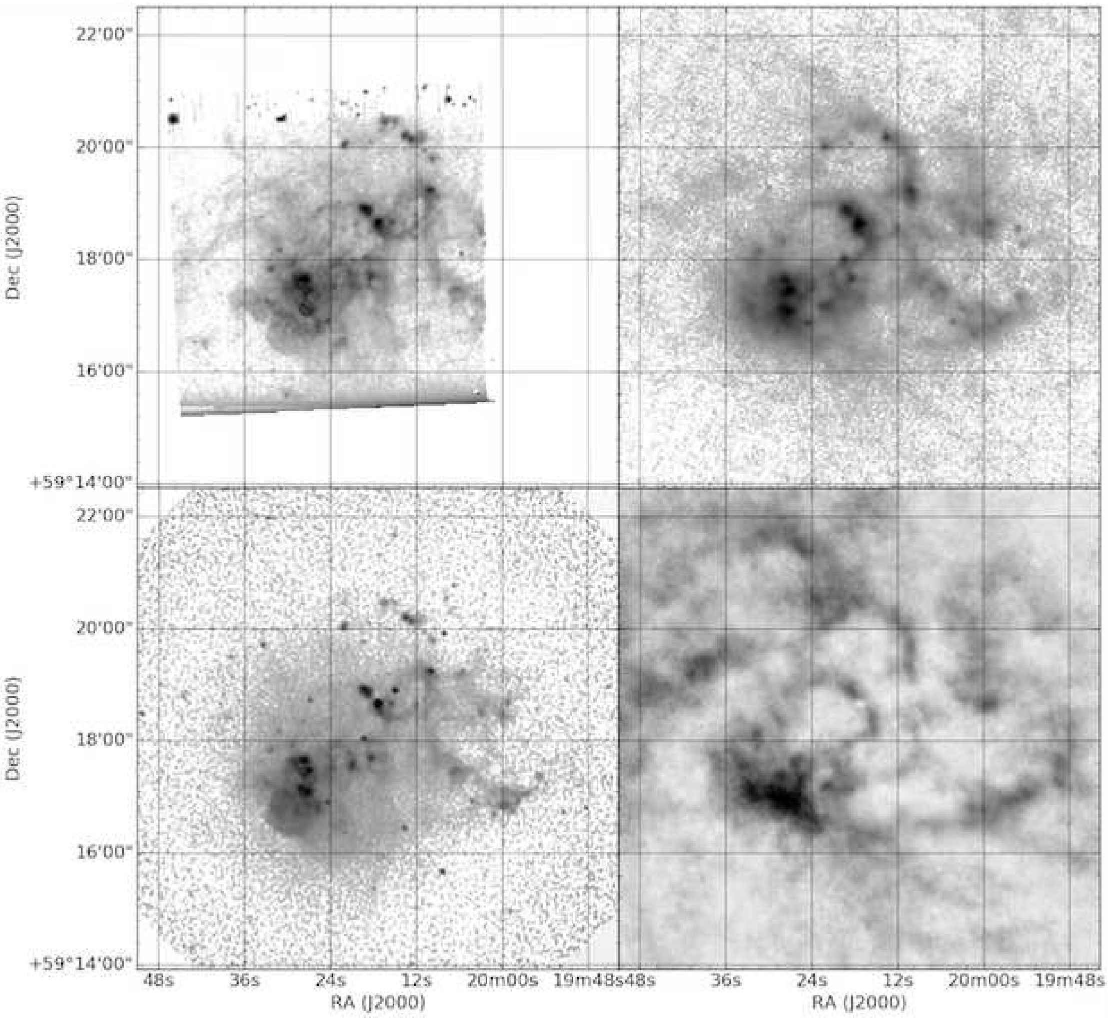

FIGURE 2.1: *Top Left:* Hα (continuum subtracted) map taken from Hunter and Elmegreen (2004). *Top Right:* Map of IC 10 at 70 μm taken with Herschel as part of the Dwarf Galaxy Survey (Madden et al., 2013). *Bottom Left:* 5 GHz VLA C & D array map of IC 10 taken from Heesen et al. (2015). *Bottom Right:* Naturally weighted HI map of IC 10 taken as part of LITTLE THINGS (Hunter et al., 2012). Note how the large-scale holes and shells in the HI distribution can be easily identified across multiple wavelengths.

This chapter is structured as follows; in Section 2.3 we describe our observations, data reduction and imaging method; in Section 2.4 we present our source detection method and the recovered source properties; in Section 2.5 we discuss our classification scheme and the interpretation of our results. Finally we present our conclusions in Section 2.6.

2.3 Observations and Data Reduction

Observations of IC 10 were made using e–MERLIN (the upgraded **M**ulti–**E**lement **R**adio **L**inked **I**nterferometer **N**etwork, an array consisting of 7 radio telescopes spread across the UK[1]) as part of LeMMINGs (Baldi et al., 2018), an e–MERLIN legacy project. The data were taken at 2 wavebands; 1.5 GHz (L–Band) and 5 GHz (C–Band) in 4 observing runs summarized in Table 2.2. The Lovell Telescope was only available for the February 2016 observation, resulting in a smaller field of view but higher sensitivity when compared to the other observing runs. The calibration and further data reduction was carried out using AIPS[2], following the calibration procedure detailed in the e–MERLIN cookbook[3].

2.3.1 Initial Flagging & Inspection

Before any calibration took place, each of the raw datasets were put through SERPent (Peck and Fenech, 2013) with default settings to remove any obvious radio frequency interference (RFI). SERPent is auto–flagging software, developed in ParselTongue (Kettenis et al., 2006), principally for use in the e–MERLIN pipeline (Argo, 2015). Additional manual flagging was carried out using the AIPS task IBLED, to remove any obvious RFI that SERPent had missed and to identify periods where the data were corrupted. This was justified as e–MERLIN sees a harsh and complicated RFI environment, especially at 1.5 GHz, and the telescope was in commissioning phase over the duration of the 2013 observations. Overall, $\sim 52\%$ of the data was flagged at 1.5 GHz and $\sim 10\%$ was flagged at 5 GHz.

2.3.2 1.5 GHz Data Reduction

Both 1.5 GHz observations followed the same observational set–up. The total bandwidth was split into 8 IFs (intermediate frequencies), each with 128 individual channels of bandwidth 0.5 MHz. The primary flux calibrator, 3C286, was used to set the flux scale, the point–like source, OQ208, was used to determine the passbands and

---

[1] A basic overview of the array can be found at `http://www.e-merlin.ac.uk/summary.html`

[2] AIPS, the Astronomical Image Processing Software, is free software available from the NRAO.

[3] Available at: `http://www.e-merlin.ac.uk/data_red/tools/e-merlin-cookbook_V3.0_Feb2015.pdf`

TABLE 2.2: Journal of IC 10 e–MERLIN observations

Obs Date (yyyy mmm dd)	Obs Frequency (MHz)	Total Bandwidth (MHz)	Time (h)	Lovell Inc? -
2013 Feb 09	1510.65	512	7.64	✗
2013 Nov 22	1526.65	512	16.24	✗
2015 Apr 18	5072.50	512	21.06	✗
2016 Feb 21	5072.50	512	9.24	✓

Notes: Obs Frequency is the central observed frequency and Time is the total time on source.

0027+5958 was used to determine the complex gain solutions to apply to IC 10. The observations both started with 30 min scans of both the primary flux calibrator and point source, and then went on to alternate between observations of IC 10 and the complex gain calibrator, spending 5 min on IC 10 and 1 min on the complex gain calibrator each iteration. After the initial flagging, each 1.5 GHz dataset was calibrated following standard e–MERLIN calibration procedures. Several rounds of phase only self–calibration were carried out on the complex gain calibrator and on IC 10 itself to further improve the quality of the final maps. Finally, the calibrated datasets were weighted using the AIPS task REWAY, so that telescopes with larger collecting area contribute more to the final maps, improving sensitivity. After the calibration, the first and last 15 channels in each IF were additionally flagged as they are in the least sensitive areas of the passband and were found to contribute mostly noise to the final maps.

The Cambridge antenna was not available for the November 2013 observation, resulting in a slightly larger synthesized beam as this antenna makes up the longest baselines in the e–MERLIN array. Additionally, IF 1 was entirely flagged in this observation as no reliable passbands could be obtained in this IF due to excessive RFI.

Both 1.5 GHz observations were calibrated independently and then combined. We verified that both datasets had the same flux scale by imaging 8 bright, unresolved sources within the primary beam but outside IC 10 (which were identified in preliminary imaging) and checking that the flux density measurements agreed to within 10 percent. The flux densities agreed for 7 sources, showing that our flux scale is satisfactorily consistent between the observations. We conclude that the outlier must be down to source variability between the observation dates. As the November dataset was taken at a slightly higher frequency than the February dataset, we used the AIPS task BLOAT to ensure that both observations covered the same frequency range before combining both

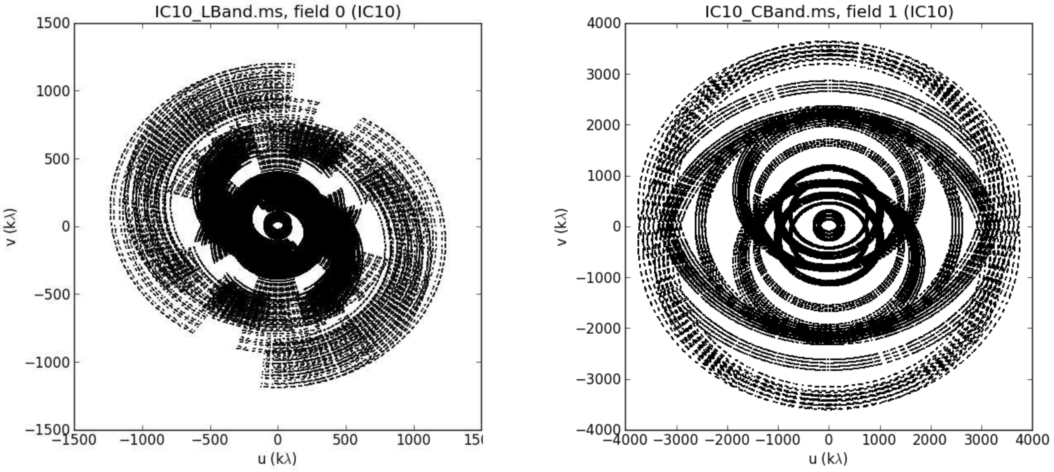

(a) **(b)**

FIGURE 2.2: Observed visibility distributions for the e–MERLIN observations of IC 10. **(a)** shows the combined 1.5 GHz *uv*–plane and **(b)** shows the combined 5 GHz *uv*–plane.

datasets using the task DBCON. The relative weights between the observations were determined by comparing the sum of weights returned by the AIPS task IMAGR during preliminary imaging. The combined *uv*–plane is displayed in Figure 2.2(a).

2.3.3 5 GHz Data Reduction

The 5 GHz observations followed a similar observing set up to the 1.5 GHz observations. The total bandwidth was split into 4 IFs, each with 128 individual channels 1 MHz wide. The primary flux calibrator, 3C286, was used to set the flux scale, the point source, OQ208, was used to determine the passbands and 0027+5958 was used to determine the complex gains to apply to IC 10. IC 10 and the complex gain calibrator were observed alternatingly, with 5 min on IC 10 to 3 min on the complex gain calibrator, finishing with 30 min scans of both the primary flux and point source calibrators. The first and last 5 channels were flagged because this is where the passband rapidly loses sensitivity. One round of phase only self–calibration on IC 10 was performed to further improve the quality of the final maps. Again, both calibrated datasets were weighted.

There were several issues with the February 2016 observation. The Mk2 antenna was not available for the duration of this observation and reliable gain solutions could not be found for the Darnhall antenna. The remaining data were combined with data taken in Apr 2015 to improve the noise level in the final maps. The combined 5 GHz uv-plane is displayed in Figure 2.2(b).

2.3.4 Imaging

IC 10's star forming disk was imaged at 1.5 GHz with a mosaic of 19 subfields, with each subfield covering $0'.3$ a side. The AIPS task SETFC was used to generate the list of fields to be imaged and a natural weighting scheme was used to maximise sensitivity. A small field centred on the bright source NVSS002108+591132 (which has a flux density equal to 13.5 mJy at 1.4 GHz and is located $9'.38$ from the observation pointing centre) was added to this list to remove its contaminating sidelobes. The individual subfields were cleaned down to 2.5 times the rms noise level of each map and were then mosaicked together using the AIPS task FLATN to produce a single widefield map of the entire disk. This widefield map was used to search for sources and blank subfields with no apparent sources were used to test the completeness of the chosen source extractor. The detected sources were directly imaged at 5 GHz to save time, also using a natural weighting scheme to maximise sensitivity. We corrected each detected source for the primary beam individually assuming that the e–MERLIN primary beam is accurately represented by a Gaussian function with FWHM 30′ at 1.5 GHz (excluding the Lovell telescope) and a FWHM of 5.6′ at 5.0 GHz (including the Lovell telescope). This was done to save time as each detected source was sufficiently small to be characterised by a single primary beam correction factor. We present the final maps of the bright detected sources associated with IC 10 at 1.5 GHz in Figure 2.3 and the associated 5 GHz detections in Figure 2.4.

Our final maps reach a noise level of $26\,\mu\text{Jy}\,\text{beam}^{-1}$ at 1.5 GHz and $12\,\mu\text{Jy}\,\text{beam}^{-1}$ at 5.0 GHz. These noise levels are significantly higher than the LeMMINGs target sensitivities of $8\,\mu\text{Jy}\,\text{beam}^{-1}$ and $3\,\mu\text{Jy}\,\text{beam}^{-1}$ at 1.5 GHz and 5 GHz respectively. This can mainly be attributed to the lack of the Lovell telescope in the majority of the presented observations as its inclusion results in a factor of 2 improvement in sensitivity (see e–MERLIN technical capabilities). Additionally, as the array was still in the commissioning phase for most of the observations, some antennas were not present for the entire duration of an observation. It is also likely that the increased noise level is due to the considerable flagging carried out and that low levels of unflagged RFI further

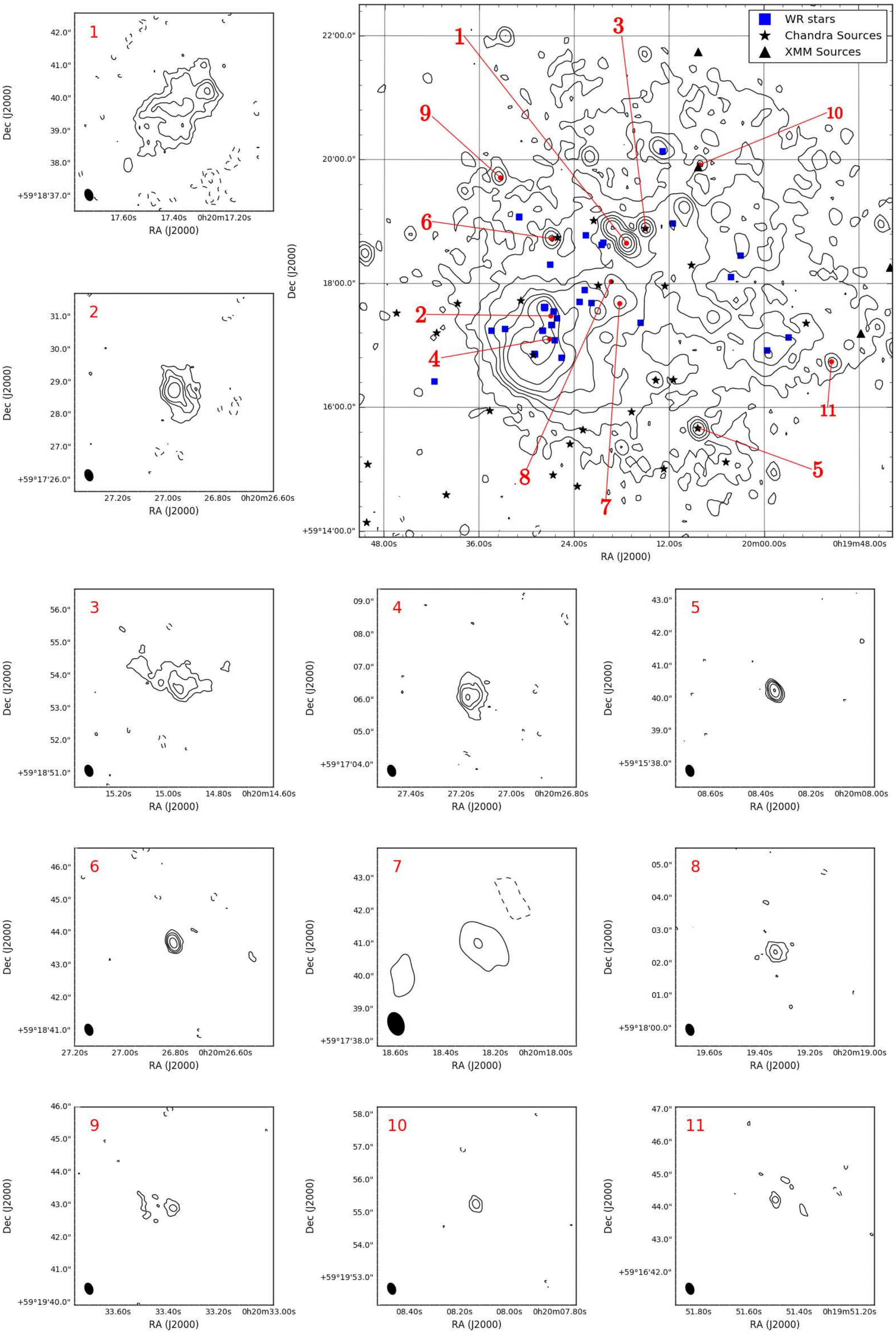

FIGURE 2.3: 1.5 GHz Radio contours of IC 10. **Top Right**: Combined VLA C+D array map of IC 10 at 1.5 GHz, taken from Heesen et al. (2015). The contours are set to -3, 5, 10, 20, 40, 80, 150, 300, 600 × the 13 μJy beam^{-1} noise level. The red numbers represent the locations of the detected e–MERLIN sources, the blue squares represent spectroscopically confirmed WR stars from Crowther et al. (2003), the black stars represent Chandra (resolution 3″) point source detections and the black upwards triangles represent XMM (resolution 13″) point source detections. All X–ray data are taken from Wang et al. (2005). The gridlines are the same as in Figure 2.1.

FIGURE 2.3: (Cont.) **Surrounding plots**: Naturally weighted 1.5 GHz e–MERLIN detections from this study. The beam size for each image is 0.″36 × 0.″24 and is displayed in the bottom-left of each map. The contours on each source are set to -3, 3, 6, 10, 20, 40 × the 26 μJy beam^{-1} noise level. The contours also correspond to brightness temperatures set at 690, 1400, 2300, 4600 and 9200 K. Each field measures 6″ a side. An identifying source number is located in the top–left corner of each contour map. **Additional Notes**: The map of Source 7 has been convolved to a resolution of twice the synthesized beam to show the low surface brightness emission. The contours on source 7 are set to the same levels as in the other contour maps, but the noise level in this case is 53 μJy beam^{-1}. The contours correspond to brightness temperatures set at 170 K and 340 K in this case only.

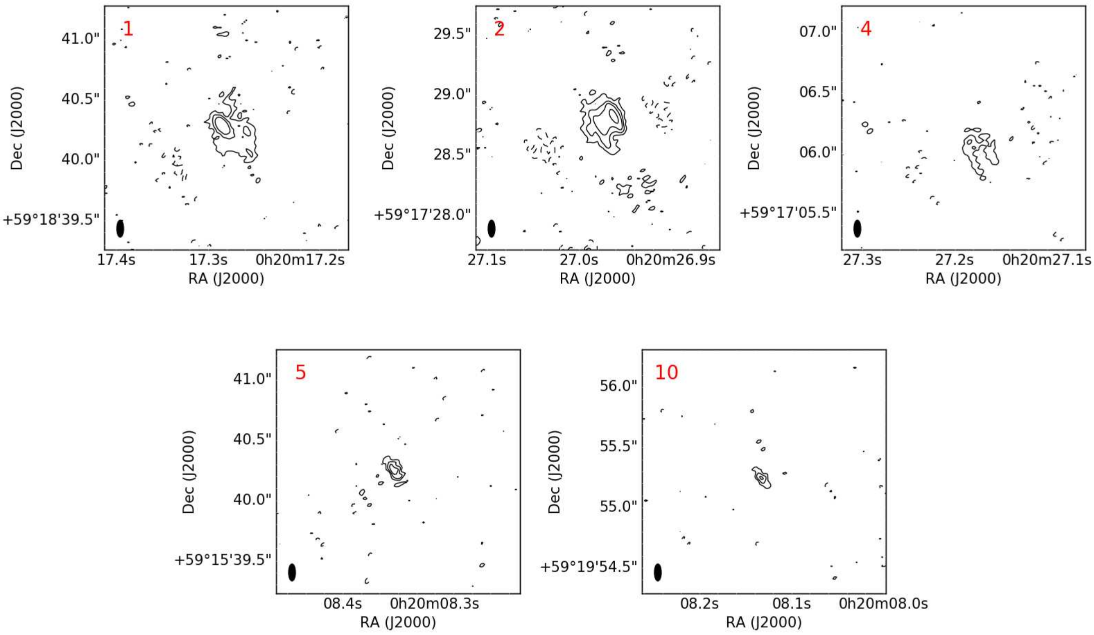

FIGURE 2.4: Naturally weighted 5 GHz e–MERLIN detections from this study. The beam size for this image is 0.″14 x 0.″06 and is displayed in the bottom–left of each contour plot. The contours on each source are set to -3, 3, 6, 10, 20, 40 × the 12 μJy beam^{-1} noise level. Each field measures 2″ on a side. An identifying source number is located in the top-left corner of each contour map.

contribute to the noise level in the final maps. Together, these factors largely explain the higher noise level.

2.4 Results

Radio continuum emission from normal star–forming galaxies originates from two main sources, thermal emission from ionized plasma found predominantly in HII regions, and non–thermal emission from cosmic ray electrons (CRe) that have been accelerated in SNR shock fronts. Due to the baseline distribution of e–MERLIN, effectively all extended emission on angular scales larger than $\sim 5''$ is not observed by the instrument. This effect makes e–MERLIN an ideal instrument to study compact structures in other galaxies, such as star–formation products like compact HII regions, Radio SNe and SNR, and unrelated background galaxies. It is unlikely that any of the sources we observe are X–ray binaries or Planetary Nebulae as these sources would have flux densities of order 1 μJy at the distance of IC 10 (Fender and Hendry, 2000; Leverenz et al., 2016). In this section we present our e–MERLIN detections within IC 10 and test the robustness of our detections.

2.4.1 Source Detection and Completeness

We used the widefield 1.5 GHz maps described in Section 2.3.4 to search for compact radio sources coincident with IC 10's star forming main disk. We carried out the search for sources using the widefield 1.5 GHz map for 3 main reasons:

1. As the primary beam for the 1.5 GHz observations is much larger than that for the 5 GHz observations, we can image larger portions of the sky whilst still maintaining Nyquist sampling of the synthesized beam. This is computationally quicker than imaging the whole sky at 5 GHz.
2. As the e–MERLIN array configuration does not change (unlike the VLA and WSRT), the 1.5 GHz observations sample larger spatial structures (or spatial frequencies) across the sky, compared to the 5 GHz observations. This means that the 1.5 GHz observations are more sensitive to extended emission that may not be observed at 5 GHz.
3. If the sources are dominated by non–thermal emission, they are likely to be much brighter at 1.5 GHz than 5 GHz due to the steep, negative power–law radio spectra that these sources typically exhibit.

In order to catalog detections from the widefield maps in a repeatable fashion, we used the source extraction software, AEGEAN (Hancock et al., 2012) to produce a list of candidate sources. AEGEAN is a threshold detection algorithim, which additionally uses the mean map curvature and a Floodfill algorithm to characterise more extended sources. The algorithm briefly works as follows:

1. Pixels that are brighter than a user defined detection threshold are used as starting points for the Floodfill algorithm. The Floodfill algorithm fills out to neighbouring pixels that are above the user defined floodfill threshold and produces a mask of the isolated emission.
2. A mean curvature map is produced by convolving the map with a 2–D Laplacian kernel. A curvature mask is produced for regions with negative curvature, as the negative curvature is considered to be due to the presence of a source.
3. The two masks are then combined to form a series of 'summits', which are used to determine the number of Gaussian components to be fit to the data, as well as to find some prior constraints for the shapes and positions of the fit Gaussians.
4. Each Gaussian component is simultaneously fitted and the fit parameters are returned in a table.

We set the detection threshold to 5 times the map rms noise level, the floodfill threshold to 4 times the map rms noise level and cross matched the resulting source list with the extended 1.5 GHz emission associated with IC 10's star forming disk, observed at a 5σ significance by Heesen et al. (2015). Through this procedure, we found 19 5σ detections that are coincident with IC 10's main star forming disk. 11 of these detections are coincident with unresolved features seen in the lower resolution VLA maps (see Figure 2.3), whereas the remaining 8 faint detections do not appear to be associated with any low resolution structure.

We test whether these 8 faint detections could be spurious by asking the question, how many spurious detections would we expect over the area IC 10's main disk takes up? If we assume that each beam is independent, the probability of n_{det} detections out of n total beams follows a binomial distribution:

$$P(n_{det} \text{ detections}) = \binom{n}{n_{det}} p^{n_{det}} (1-p)^{n-n_{det}}, \tag{2.1}$$

where p is the probability of a beam having a value larger than the detection threshold. If we assume that each beam value is drawn from a normal distribution with a standard deviation equal to the map noise, we determine:

$$p = \int_{5\sigma}^{\infty} \frac{1}{\sqrt{2\pi\sigma^2}} e^{-\frac{x^2}{2\sigma^2}} dx \approx 2.866515 \times 10^{-7}. \tag{2.2}$$

As there are 1.7×10^6 independent beams in the region of interest, the expected number of detected sources is:

$$np = 0.47, \tag{2.3}$$

with variance:

$$np(1-p) = 0.47. \tag{2.4}$$

From this simple calculation, we would expect 0.47 ± 0.47 spurious detections in the considered region, which shows it is plausible that one or two of the 8 we see could be spurious. The majority of these faint sources are therefore probably real and belong to features that are close to the detection limit. As these sources are not clearly associated with compact structure seen in lower resolution observations, we limit the rest of our analysis to the 11 sources that are coincident with unresolved features in the lower resolution maps.

Source Detection Completeness

After the source extraction procedure it was necessary to estimate how many true 5σ sources the source extractor may have failed to recover. Theoretically, we can calculate the fraction of sources that we are missing by assuming that the noise is constant across the widefield map and that each pixel value has been drawn from a normal distribution, with a standard deviation equal to the map rms noise level. In general, the probability that a $n\sigma$ source is detected above the 5σ detection threshold is given by:

$$P(n\sigma \text{ is detected}) = \int_{5\sigma-n\sigma}^{\infty} \frac{1}{\sqrt{2\pi\sigma^2}} e^{-\frac{x^2}{2\sigma^2}}\, dx = \frac{1}{2}\text{erfc}\left(\frac{5\sigma - n\sigma}{\sigma}\right), \tag{2.5}$$

where erfc is the complementary error function. This probability can be interpreted as the fraction of the sources that are recovered on average by the source extractor with a 5σ threshold, which we shall define as the Completeness fraction.

By setting the true source brightness ($n\sigma$) equal to the 5σ threshold, we find that we would expect to detect approximately half of the true 5σ sources in the image. This can be intuitively understood as at the threshold limit, the random noise is equally likely to add a small contribution to the source peak flux as it is to take away, preventing the source from being detected. The simple completeness model also predicts that we would expect a few sources with true flux densities below the noise level to be detected and a few sources with flux densities above the threshold to be missed.

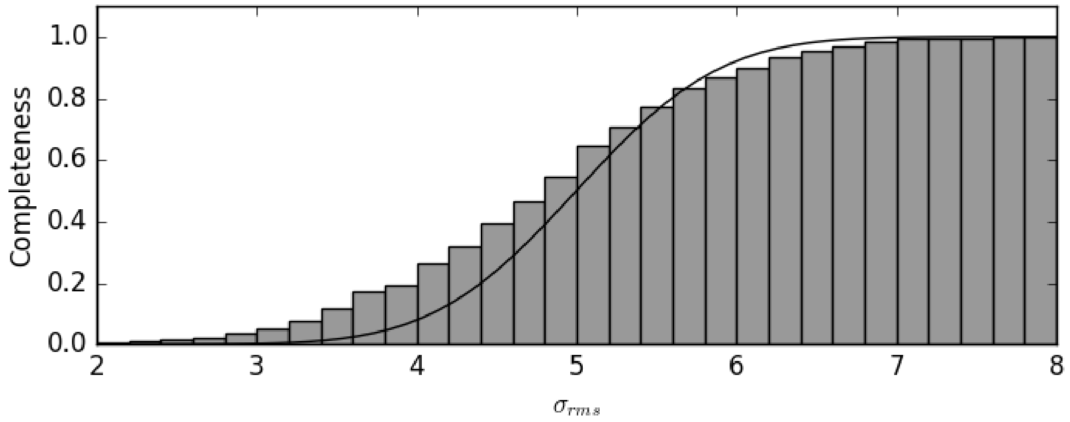

FIGURE 2.5: Completeness fraction from the source detection. The black line represents the theoretical expectation and the grey bars show the result from our Monte–Carlo simulation. The uncertainty in each bin is $\leq 5\%$ for all flux density bins greater than 4σ.

To validate our simple completeness model, we carried out a Monte–Carlo simulation to empirically assess the completeness of our source detection method. We took a blank field from the 1.5 GHz widefield imaging (i.e., a noise map) and randomly added 100 Gaussian sources, each the same size as the naturally weighted synthesized beam. We assigned each of the sources a peak flux density, drawn from a continuous, uniform probability distribution between 2 and 12 times the rms noise level of the maps. We then used Aegean to recover the placed sources, setting the detection threshold to 5 times the measured map rms noise level ($26\,\mu$Jy beam^{-1}). We then cross matched the recovered catalog with the placed catalog, in which we allowed a positional uncertainty equal to the diameter of the synthesized beam, to create a catalog of matched (recovered) sources. This process was repeated 1000 times to ensure a statistically robust answer.

We split the placed and recovered data into flux density bins, each with a width equal to 0.2 times the map rms noise level. We define the completeness fraction for each flux bin as:

$$C = \frac{N_{\rm M}}{N_{\rm P}}, \tag{2.6}$$

where $N_{\rm M}$ is the total number of matched sources with initial flux density inside the flux density bin and N_P is the total number of placed sources inside the same bin. We present the results of this exercise in Figure 2.5.

The Monte–Carlo simulation results follow a similar overall shape to the theoretical expectation; however, they differ in that the theoretical prediction overpredicts the number of recovered sources at $\sim 6\sigma$ and underpredicts the number of recovered sources at $\sim 4\sigma$. This shows that one of our starting assumptions used to derive the expected completeness may not be correct, either the pixel values are not drawn from a normal distribution, or the noise level is not constant across the map.

As the uncertainty for a single pixel depends upon the uncertainties of all individual observed visibillities, it is unlikely that the pixel values will not be drawn from a normal distribution due to the central limit theorem. Therefore the difference is likely to be due to the noise level varying across the map. This is illustrated if we use AEGEAN's sibling program BANE to estimate the map noise level. Briefly, BANE selects every Nth pixel to form a grid (typically the pixels are separated by 4 synthesized beams), and then calculates the standard deviation of the pixel values within a box of size M by M pixels (typically all of the pixels out to the next grid pixel). These standard deviations are then linearly interpolated to calculate an estimate for how the noise level varies across the image. From this analysis, we find that the noise level varies between 22 and 38 μJy beam^{-1}, with a median noise level at 26 μJy beam^{-1}. This explains the observed discrepancy, as sources are more easily detected or missed at the enforced threshold in regions where the noise level is enhanced. A non–uniform noise level can occur if there are residual calibration errors that have not been corrected for during the calibration procedure, or if there are bright sources that have not been properly treated during the imaging process.

2.4.2 Flux Density Measurement

We measure the integrated flux densities for the 11 sources using two different methods, depending upon whether the source is unresolved or resolved. For unresolved sources, we fit a single Gaussian component using the AIPS task JMFIT and estimate the integrated flux density by integrating over the fitted Gaussian. For resolved sources, we generate a mask by only considering emission associated with each source above a $3\,\sigma$ level, where σ is the map rms noise level (measured off source). We then integrate the masked emission to obtain the integrated flux density.

The uncertainties on the integrated flux density measurements are estimated through:

$$\sigma_{\mathrm{Total}} = \sqrt{\sigma_{\mathrm{Map}}^2 + \sigma_{\mathrm{Scale}}^2}, \tag{2.7}$$

where σ_{Map} is either equal to the fit uncertainties returned by JMFIT for unresolved sources, or it is equal to $\sqrt{N}\sigma$ for resolved sources where N is the number of independent beams that fit within the masked image. σ_{Scale} is the uncertainty in the flux scale which is conservatively taken to be at a 10 % level.

As we did not correct the widefield map for the effects of the primary beam, the measured flux densities will underestimate the true source flux density, the degree of which depends non–trivially upon the source's distance from the pointing centre of the observation. As e–MERLIN is a heterogeneous array, the exact primary beam shape is complicated and requires holographic measurements of each of the antennas to correctly determine. We therefore assume that the e–MERLIN primary beam can be parameterised as a 2–dimensional Gaussian, as specified in the e–MERLIN technical capabilities document[4]. For the 1.5 GHz observations (excluding the Lovell antenna), the Gaussian has a FWHM of 30′ and for the 5 GHz observations (including the Lovell telescope), the Gaussian has a FWHM of 5.6′. For each source, we calculate the source's distance from the pointing centre and use the primary beam model to correct the flux density attenuation. We present the measured flux densities in Table 2.3.

2.4.3 Angular Size Measurement

For the convenience of other authors who may need to plot the spatial extent of the observed sources without necessarily having access to the raw widefield map, we measure the angular sizes and position angles of each of the resolved sources at 1.5 GHz by fitting an ellipse to the source's 3σ isophote.

To fit the ellipse, we first generate a mask of the 3 σ emission originating from the source. We then would like to find the ellipse that best covers the masked area, which can be easily found through a least squares minimisation procedure. However, as the sources can have a complex morphology, we first need to estimate the ellipse parameters to form the starting point for the minimisation algorithm.

---

[4] Available at `http://www.e-merlin.ac.uk/tech/`

TABLE 2.3: Properties of Sources Detected in IC 10

Source No	IAU Designation	α_{J2000} (hh mm ss)	δ_{J2000} ($^{\circ}\,'\,''$)	$S_{1.5\,\mathrm{GHz}}$ (mJy)	$S_{5.0\,\mathrm{GHz}}$ (mJy)	Peak T_{B} (K)	Spectral Index
1*	WBBH J002017+591839.7	00 20 17.390	+59 18 39.68	8.06 ± 0.82	1.02 ± 0.11	≥ 5200	*−0.3 ± 0.2*
2*	WBBH J002027+591728.7	00 20 26.952	+59 17 28.66	3.39 ± 0.35	2.28 ± 0.24	≥ 7700	*−0.1 ± 0.2*
3*	WBBH J002015+591853.9	00 20 14.988	+59 18 53.88	2.23 ± 0.25	-	≥ 2600	*−1.0 ± 0.2*
4*	WBBH J002027+591706.1	00 20 27.160	+59 17 06.12	1.83 ± 0.20	0.36 ± 0.06	≥ 4900	*−0.4 ± 0.2*
5	WBBH J002008+591540.2	00 20 08.348	+59 15 40.21	1.29 ± 0.14	0.28 ± 0.04	≥ 11000	−1.3 ± 0.2
6	WBBH J002027+591843.7	00 20 26.807	+59 18 43.69	0.99 ± 0.11	-	≥ 8500	≤−2.3
7*	WBBH J002018+591740.9	00 20 18.249	+59 17 40.92	0.93 ± 0.14	-	≥ 700	*−0.4 ± 0.2*
8*	WBBH J002019+591802.3	00 20 19.334	+59 18 02.33	0.87 ± 0.16	-	≥ 7700	*−0.2 ± 0.2*
9	WBBH J002033+591942.9	00 20 33.390	+59 19 42.89	0.49 ± 0.11	-	≥ 4100	≤−1.7
10	WBBH J002008+591955.2	00 20 08.137	+59 19 55.23	0.37 ± 0.07	0.14 ± 0.03	≥ 3200	−0.8 ± 0.3
11	WBBH J001951+591644.2	00 19 51.498	+59 16 44.20	0.26 ± 0.06	-	≥ 2000	≤−1.2

Notes: Sources with a * are extended sources and their spectral indices (italicized) are derived from the low–resolution spectral index maps presented in Heesen et al. (2011). All other spectral indices are derived from the e–MERLIN observations. The peak brightness temperatures have been derived from the 1.5 GHz observations.

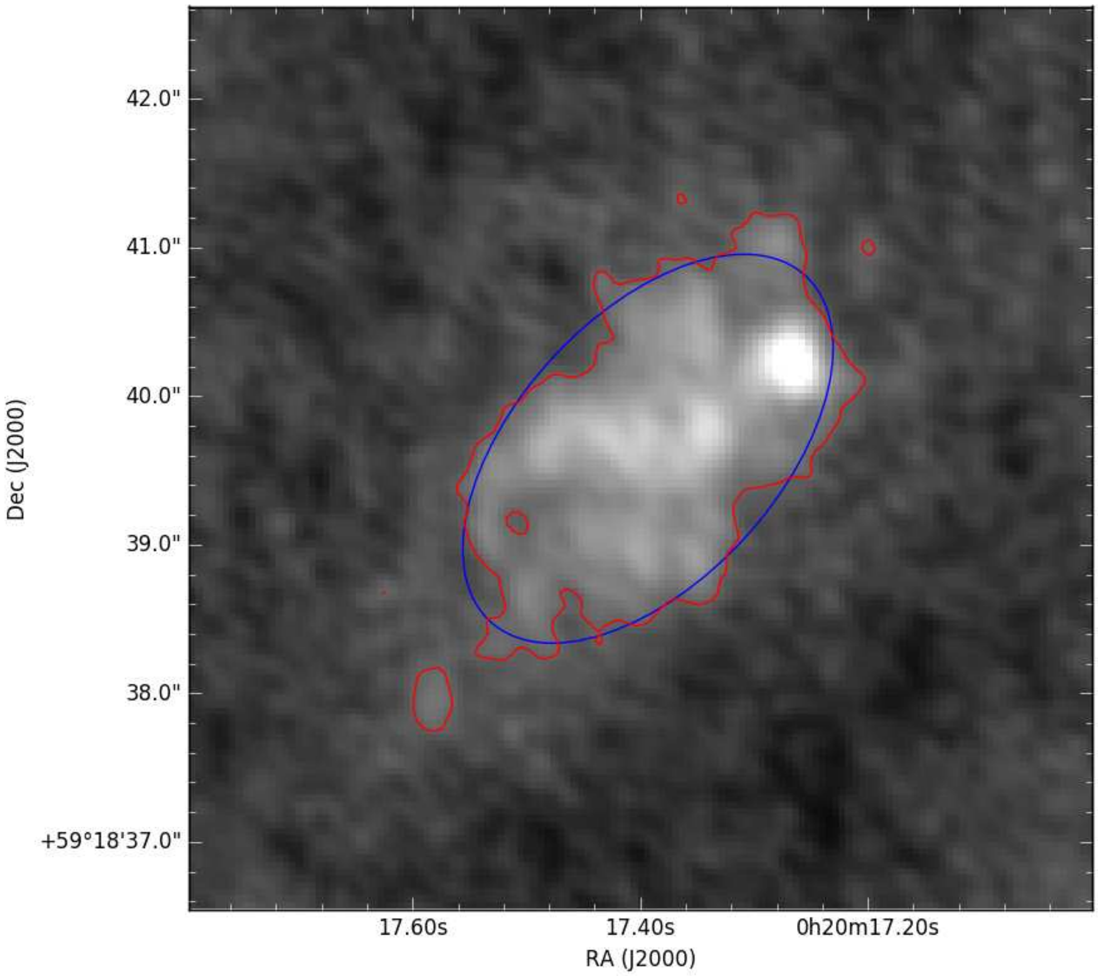

FIGURE 2.6: An example of our ellipse fitting procedure. The red line corresponds to the 3σ isophote and the blue line corresponds to the fitted ellipse.

We estimate the ellipse parameters by first treating each pixel in the mask as a 'datapoint' and use the list of points to calculate a covariance matrix for the mask. The covariance matrix in this case can (roughly) be interpreted as the linear transformation required to transform 2–dimensional, normally distributed data (with $\sigma_x = \sigma_y = 1$), to the observed mask data. The eigenvector of this matrix with the largest eigenvalue corresponds to the direction in which the observed mask data has the largest variance, i.e. the direction of the major axis, and the other eigenvector corresponds to the direction of the minor axis. From these eigenvectors, the position angle of the ellipse can be easily calculated; however, the lengths of the sought major and minor axes do not directly correspond to the derived eigenvalues. Instead they correspond to the variance in the major and minor axis directions, not to the entire range of the mask. We therefore take the square root of the eigenvalues and use them to calculate the area of the '1σ' ellipse. We scale this ellipse to the same area as the mask to estimate the major and minor axes

TABLE 2.4: Observed Angular Sizes of Extended and Resolved Sources at 1.5 GHz

Source No	Major Axis ($''$)	Minor Axis ($''$)	Position angle ($^\circ$)
1*	3.15	1.77	137.7
2*	1.73	1.12	16.9
3*	2.41	0.85	71.2
4*	1.37	0.82	7.6
7*	2.35	1.58	35.7
8	0.69	0.59	123.7

Notes: The superscript * in the Source No column indicates that the source is extended. The position angle of each source is measured anti-clockwise from the North.

lengths. Finally, the means of both the x and y co–ordinates for the datapoints in the mask correspond to the centre point of the ellipse.

We then take these estimates as the starting point of our least squares minimisation procedure, where we minimise the residuals between the mask and a filled model ellipse. In general, the parameters obtained from the minimisation procedure did not change much from those found through our initial parameter estimation. An example of an ellipse fitted by this procedure is presented in Figure 2.6. We do not quote any uncertainties on the fitted ellipses as they are used for visualization purposes only. We note however that uncertainties could be easily derived through a Markov–Chain Monte–Carlo sampler, such as the Metropolis–Hastings algorithm (see Chapter 3. For marginally resolved and unresolved sources, we fit 2–D Gaussian functions using the AIPS task JMFIT to determine the angular size, position angle and sky co-ordinates. The angular size properties for extended and resolved sources at 1.5 GHz are summarized in Table 2.4 and we present the sky co-ordinates in Table 2.3.

2.4.4 Spectral Index Measurement

The dependence of radio emission with frequency is often approximated as a power law. A radio source's spectral index, α, is then defined as:

$$S_\nu \propto \nu^\alpha, \tag{2.8}$$

where S_ν is the radio source's measured flux density at frequency ν. The spectral index is a powerful classification tool, as each radio continuum emission mechanism has a characteristic spectral index. For example, an optically thin HII region is dominated at radio frequencies by thermal (free–free) emission with $\alpha = -0.1$ whereas $\alpha \leq -0.5$ for non–thermal (synchrotron) dominated emission from SNRs.

Typically, the spectral index is found by comparing the measured flux density at two different frequencies through:

$$\alpha = \frac{\ln\left(\frac{S_1}{S_2}\right)}{\ln\left(\frac{\nu_1}{\nu_2}\right)}, \tag{2.9}$$

where S_1 is the flux density measured at frequency ν_1 and S_2 is the flux density measured at frequency ν_2. If we assume that the measurements S_1 and S_2 are independent with normally distributed uncertainties, and that the uncertainty on the observed frequency is negligible, the uncertainty on α is estimated through:

$$\delta_\alpha = \left| \frac{1}{\ln\left(\frac{\nu_1}{\nu_2}\right)} \sqrt{\left(\frac{\delta_{S_1}}{S_1}\right)^2 + \left(\frac{\delta_{S_2}}{S_2}\right)^2} \right|, \tag{2.10}$$

where δ_{S_1} and δ_{S_2} are the uncertainties on S_1 and S_2. It should be noted that this equation is formally correct only when the uncertaintes on the flux densities are small relative to the flux densities themselves.

There are two main caveats with using the observed spectral index to classify sources:

1. There are situations where spectral indices from different emission mechanisms can look the same. For example, non–thermal emission may appear flat, like thermal emission, if it is significantly attenuated by an absorption mechanism (such as free–free absorption or synchrotron self absorption). This problem can be circumvented by modelling the source's radio spectral energy distribution using observations sampling the 100 MHz to 100 GHz frequency range. Alternatively (and much more cheaply observationally) the sources can be matched spatially with emission in a different wavelength regime (such as the optical Hα emission line) to infer the emission mechanism.

2. If an interferometer is used to obtain the radio maps, the measured spectral index will strongly depend on the angular scales that are sampled at the observed frequency. If the source is extended, the measured spectral index will be biased if a map at one frequency is sensitive to large scale emission, whereas a map at

> another frequency is not. This problem can be mitigated by ensuring that the same region of the *uv*–plane is imaged in both maps. This procedure does not completly fix the problem, as radio emission at different frequencies may have differing spatial structure (such as large scale halos surrounding galaxies seen at low frequencies), and therefore produce different imaging artifacts which would bias any measured spectral indices. Reliable spectral indices can be derived from interferometers that sample the *uv*–plane differently, under the conditions that the observed source is unresolved at both frequencies and it is not embedded in any large scale extended emission.

As both the 1.5 GHz observations and 5 GHz observations were made with e–MERLIN (where the antenna positions cannot be changed) they do not sample the same spatial frequencies, which is illustrated in Figure 2.2. Therefore, we can only directly measure the spectral indices of unresolved sources with the presented observations. We note that these spectral index measurements may be biased towards steeper spectral indices as all of these sources were selected because they are coincident with extended emission (see Figure 2.3). For unresolved sources that are detected at one frequency only, we determine limits for the observed spectral index by calculating the spectral index assuming that the non–detection has been detected at a 5σ significance.

For the resolved sources, we estimate the spectral index by comparing the source position with the in band spectral index map presented in Heesen et al. (2011). This map is made at a much lower resolution than the presented e–MERLIN observations, and hence can only give us a general idea about the spectral index of the resolved sources combined with emission from their immediate surrounding environment. We present the observed spectral indices for each source in Table 2.3.

2.4.5 Brightness Temperature Measurement

A final classification diagnostic that can be derived from the radio data alone is the source's brightness temperature, T_b. The brightness temperature corresponds to the temperature of a blackbody at frequency, ν, that has the same brightness as the source.

In the Rayleigh–Jeans limit, it is defined through:

$$T_b = \frac{c^2 I_\nu}{2k\nu^2} \approx \frac{c^2 S_\nu}{2k\nu^2 \Omega}, \tag{2.11}$$

where c is the speed of light in a vacuum, k is the Boltzmann constant, I_ν is the specific intensity (or surface brightness at frequency ν), S_ν is the source flux density and Ω is the solid angle subtended by the source.

The observed brightness temperature is a useful diagnostic for differentiating between sources that are dominated by thermal or non–thermal emission mechanisms, such as HII regions and SNR, because of the fact that the brightness temperature cannot exceed the source temperature. To illustrate this, we start from the equation of radiative transfer:

$$\frac{dI_\nu}{ds} = -\kappa_\nu I_\nu + j_\nu, \tag{2.12}$$

where s is distance along the line of sight, κ_ν is the absorption coefficient and j_ν is the emission coefficient. If we divide through by κ_ν and define $d\tau_\nu = \kappa_\nu ds$ (τ_ν is the optical depth at frequency ν), the equation of radiative transfer changes to:

$$\frac{dI_\nu}{d\tau_\nu} = -I_\nu + \frac{j_\nu}{\kappa_\nu} = -I_\nu + \Phi_\nu, \tag{2.13}$$

where $\Phi_\nu = \frac{j_\nu}{\kappa_\nu}$ is known as the source function. If we assume that the source function is constant throughout the source, that the absorption and emission are taking place in the same volume and that there is no background emission, the solution to Equation 2.13 is:

$$I_\nu(\tau_\nu) = \Phi_\nu \left(1 - e^{-\tau_\nu}\right), \tag{2.14}$$

where:

$$\tau_\nu = \int_0^s \kappa_\nu ds \approx \kappa_\nu s. \tag{2.15}$$

From Equation 2.14, we see that in optically thick conditions ($\tau \to \infty$), the specific intensity will tend towards the source function.

If the source is thermal (i.e., it is in thermal equilibrium), the source function will be equal to that of a blackbody at the source temperature. In the Rayleigh–Jeans regime, it then follows that:

$$T_b \approx T \left(1 - e^{-\tau_\nu}\right), \tag{2.16}$$

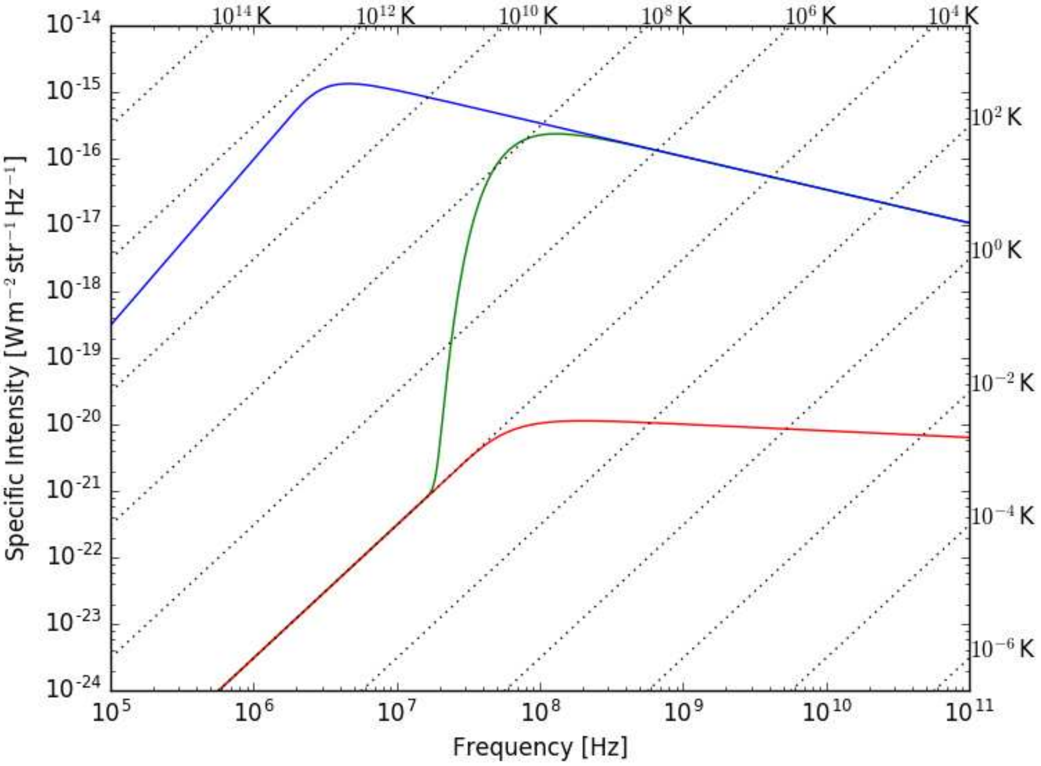

FIGURE 2.7: Example spectra for a non–thermal source (blue) and a thermal source (red). The black dotted lines correspond to lines of constant brightness temperature, and the green line corresponds to the non–thermal source being observed through the thermal source. The temeperatures of the lines of constant brightness temperature are labeled on the top and right axes.

where T is the source temperature. For thermal free–free emission, the source temperature is equal to the electron temperature and we see from Equation 2.16 that the brightness temperature cannot exceed the electron temperature. This is illustrated by the red line in Figure 2.7, which shows the spectra for a thermal radio continuum source with a temperature equal to 10^4 K. The source has a flat characteristic spectral index ($\alpha = -0.1$) until it becomes optically thick, where it then follows the line of constant brightness temperature that is equal to the source temperature.

Equation 2.16 also holds for non–thermal sources; however, the details are more complicated as the power–law electron energy distribution cannot be represented by a Boltzmann distribution at a single temperature. As a consequence, the source function does not become equal to a blackbody under optically thick conditions, hence the optically thick part of the non–thermal spectrum does not nessesarily follow a line of constant brightness temperature (i.e. $I_\nu \not\propto \nu^2$). More importantly for us, the brightness temperature of the non–thermal emission can be many orders of magnitude higher than that of a thermally emitting source.

To show this, we first need to obtain the source function, Φ_ν, for the non–thermal source. From Longair (2011), the emission and absorption coefficents for a power–law electron energy distribution ($N(E) = AE^{-p}$) are given by:

$$j_\nu = \frac{\sqrt{3}e^3 BA}{16\pi^2 \varepsilon_0 c m_e}\left(\frac{3eB}{2\pi\nu m_e^3 c^4}\right)^{\frac{(p-1)}{2}} a(p)\ \left[\mathrm{W\,m^{-3}\,Sterad^{-1}\,Hz^{-1}}\right] \tag{2.17}$$

where

$$a(p) = \frac{\sqrt{\pi}}{2}\frac{\Gamma\left(\frac{p}{4}+\frac{19}{12}\right)\Gamma\left(\frac{p}{4}-\frac{1}{12}\right)\Gamma\left(\frac{p}{4}+\frac{5}{4}\right)}{(p+1)\Gamma\left(\frac{p}{4}+\frac{7}{4}\right)} \tag{2.18}$$

and

$$\kappa_\nu = \frac{\sqrt{3}e^3 cA}{8\pi^2 \varepsilon_0 m_e} B^{\frac{(p+2)}{2}}\left(\frac{3e}{2\pi m_e^3 c^4}\right)^{\frac{p}{2}} \nu^{-\frac{(p+4)}{2}} b(p)\ \left[\mathrm{m^{-1}}\right] \tag{2.19}$$

where

$$b(p) = \frac{\sqrt{\pi}}{8}\frac{\Gamma\left(\frac{3p+22}{12}\right)\Gamma\left(\frac{3p+2}{12}\right)\Gamma\left(\frac{p+6}{4}\right)}{\Gamma\left(\frac{p+8}{4}\right)}. \tag{2.20}$$

It then follows that the source function is given by:

$$\Phi_\nu = \frac{j_\nu}{\kappa_\nu} = \frac{1}{2c^2}\left(\frac{3e}{2\pi m_e^3 c^4}\right)^{-\frac{1}{2}} \frac{a(p)}{b(p)} B^{-\frac{1}{2}} \nu^{\frac{5}{2}}\ \left[\mathrm{W\,m^{-2}\,Sterad^{-1}\,Hz^{-1}}\right]. \tag{2.21}$$

Here we see that the source function is in fact proportional to $\nu^{\frac{5}{2}}$ rather than the ν^2 expected for a thermal source. To be able to use Equation 2.16 for non–thermal emission, we need to define an effective temperature for the synchrotron radiating CRe. This can be achieved by finding the effective temperature that a blackbody must posses to produce the observed specific intensity (i.e. Equation 2.11):

$$T_{\mathrm{eff}} = \frac{1}{4k}\left(\frac{3e}{2\pi m_e^3 c^4}\right)^{-\frac{1}{2}} \frac{a(p)}{b(p)} B^{-\frac{1}{2}} \nu^{\frac{1}{2}}\ [\mathrm{K}]. \tag{2.22}$$

Finally, we make the approximation that a CRe with energy E radiates all of its energy at frequency $0.29\nu_c$, where ν_c is the critical frequency defined through:

$$\nu_c = \frac{3}{2}\left(\frac{E}{m_e c^2}\right)^2 \frac{eB}{2\pi m_e}. \tag{2.23}$$

The effective temperature then changes to:

$$T_{\mathrm{eff}} \approx \left(\frac{0.29}{32}\right)^{\frac{1}{2}} \frac{a(p)}{b(p)} \frac{E}{k} \; [\mathrm{K}] \,, \tag{2.24}$$

and for the case that $p = 2$:

$$T_{\mathrm{eff}} \sim 0.19 \frac{E}{k} \; [\mathrm{K}] \,. \tag{2.25}$$

As shown in Equation 2.16, the brightness temperature will tend towards the source temperature under optically thick conditions. For synchrotron emitting CRe, the effective temperature and the frequency of the emitted radiation change with CRe energy (assuming a constant magnetic field), hence the deviation from the ν^2 dependence for a constant temperature source under optically thick conditions. Furthermore, as the CRe energy is ultra–relativistic, the effective temperature can be incredibly large. For example, from Equation 2.25 the effective temperature for a 1 GeV electron is $\sim 10^{12}$ K.

We plot an example non–thermal spectrum in Figure 2.7. When the source is optically thin, it exhibits a spectral index $\alpha = -0.5$, but when it becomes optically thick, this dependence changes to $\alpha = \frac{5}{2}$. The peak brightness temperature in this example is $\sim 10^{11}$ K, which is not too disimilar from those observed in AGN cores with VLBI observations (e.g. Kovalev et al., 2005).

Now we have a method for differentiating between emission mechanisms based upon brightness temperatures. Since the brightness temperature for a thermal source is limited to the source temperature under optically thick conditions, which is typically $\sim 10^4$ K, if we observe a source brightness temperature that is significantly larger than 10^4 K, it must be a non–thermal source.

The observed brightness temperature is however subject to several caveats:

1. Due to the finite size of the instrument used for the observation, the true source flux density will be spread out over the instrument's point spread function. If the source is unresolved by the observing instrument, the brightness temperature will be underestimated. This can be seen in Equation 2.11, if Ω gets larger but S_ν remains constant, the observed brightness temperature decreases.

2. If an interferometer is used for the observation, then emission on large angular scales may be missed, leading to an underestimate of the source brightness temperature. This issue particularly affects sources that are resolved by the interferometer, and can be seen in Equation 2.11 as the missing flux will effectively make S_ν smaller.

3. The brightness temperature only corresponds to the source temperature under optically thick conditions. If the source is optically thin, then the brightness temperature will underestimate the source thermodynamic temperature. This is shown in Figure 2.7 as the observed brightness temperature decreases towards the bottom–right of the plot, where the sources are optically thin.

4. If a background source is observed through an optically thick source, the observed brightness temperature will tend towards that of the foreground source. This is shown by the green curve in Figure 2.7 where we show a non–thermal source (blue) being observed through an optically thick thermal source (red). At the frequency where the foreground (thermal) source becomes optically thick, the observed emission is exponentially attenuated until it reaches the source function for the foreground source, which it then follows. The background (non–thermal) source's brightness temperature observed in the optically thick regime would again underestimate the source's true brightness temperature.

From these caveats, we see that any observed brightness temperature should be interpreted as a lower–limit to the true brightness temperature. For each of the observed sources, we present brightness temperature contours in Figure 2.3 and quote the observed peak brightness temperature for each source in Table 2.3.

2.5 Discussion

2.5.1 Source Classification Criteria

It is very difficult to classify sources found in radio continuum maps at a single frequency based upon their morphology and brightness temperature alone. Instead a multi–wavelength approach should be adopted to obtain reliable source classifications. Here we list the criteria we use to classify the observed sources:

1. **Brightness Temperature:** As discussed earlier, the source brightness temperature can be used to immediately differentiate between thermal and non–thermal sources, assuming that the source is optically thick. For this reason, it is the first criterion that we consider to isolate sources that are dominated by non–thermal emission processes. As HII regions are typically observed to have temperatures $\sim 10^4$ K (Hindson et al., 2016), if any source is observed to have a brightness temperature larger than 10^5 K, we will assume that it is a non–thermal source (i.e. either a SNR or an unrelated background source, such as an AGN).

2. **Spectral Index:** As discussed earlier, each radiation mechanism produces a spectral slope that is characterised by the spectral index, α. For sources that are dominated by thermal emission, the spectral index can take values between $-0.1 \leq \alpha \leq 2$. For sources dominated by non–thermal emission, the spectral index can in general take the values $\alpha \leq \frac{5}{2}$, however this range can be narrowed down. Galactic SNR typically have spectral indices in the GHz frequency regime that are in the range $-0.4 \leq \alpha \leq -0.6$ (Green, 2014), whilst compact AGN have been observed to have steeper spectral indices ($\alpha \leq -1.0$; e.g. Randall et al., 2011). From these constraints, if a source is measured to have a spectral index $\alpha \leq -0.6$, it is likely to be a background AGN, if a source has a spectral index between $-0.4 \leq \alpha \leq -0.6$ it could plausibly be a SNR and if the source has a spectral index $\alpha \geq -0.1$, it could plausibly be an HII region. It should be noted however that if the source is resolved and its spectral index is measured from the lower resolution maps presented in Heesen et al. (2015), the spectral index may be contaminated by emission mechanisms from other sources (such as diffuse non–thermal emission).

3. **Coincident X–Ray Emission:** X–ray continuum emission is normally observed to originate from gas that has been shock heated to temperatures $\geq 10^6$ K (Vink, 2012), from accretion disks surrounding massive objects (Fabbiano, 2006; Padovani et al., 2017), from photons that have been boosted up to X–rays through Inverse Compton scattering, or through the synchrotron emission process (Rybicki and Lightman, 1979; Longair, 2011). Although HII regions have been shown to radiate X–rays (e.g. Tsujimoto et al., 2006), they are very faint compared to those from SNR (e.g. Vink, 2012) or AGN (e.g. Georgakakis et al., 2015). Therefore, if we see X–ray emission spatially coincident with a detected source, it is likely that the source is either a young SNR or a background AGN. We use the XMM–Newton

and Chandra data presented in Wang et al. (2005) to search for X–ray sources that are coincident with our detected sources, and we plot the results in Figure 2.3.

4. **Coincident Hα Emission:** Hα spectral line emission principally originates from the recombination of free electrons with protons in an ionized medium to form neutral hydrogen. Immediately after the electron has combined it is likely to be in an excited state, and it will cascade down through various energy states before it reaches the ground state. When the electron passes through the $n = 3 \rightarrow 2$ transition it leads to Hα emission at wavelength ≈ 656 nm. Therefore we expect to detect Hα emission in the presence of ionized hydrogen. HII regions by definition are regions of ionized hydrogen, so we would expect to find bright, co–spatial Hα emission. For SNR, the gas within the SNR interior (that has been shocked both by the outer and the reverse shock) is too hot for recombination to occur, hence there is little observed Hα emission originating there. Instead, Hα emission is typically observed in the expanding shock front, where interstellar hydrogen that has been shock–ionized by the outer shock recombines (e.g. Gerardy and Fesen, 2007). This emission is faint however and depends upon the environment the SNR is expanding into. As core collapse SN are associated with massive stars ($\geq 8\,M_\odot$) which have short lifetimes, we would expect to find them within regions of star–formation (i.e. spatially close to HII regions). Therefore, if we see a compact radio source co–located with Hα emission, the source is likely either an HII region or a SNR. AGN also produce significant Hα emission, however as the filters used to observe Hα have a narrow bandwidth ($\sim 30\AA$), the Hα emission will be redshifted out of the observable wavelength range, even at low redshifts ($z \geq 0.02$). We use the Hα map presented in Hunter and Elmegreen (2004) to search for co–spatial Hα emission with our detected sources, and plot their Hα map in the top left of Figure 2.1.

5. **Coincident 70 μm Emission:** 70 μm continuum emission primarily originates from dust that has been heated to temperatures of ~ 50K. There are two main processes that heat the dust to these temperatures, the first is related to star formation and the second is related to AGN activity. In the case of star formation, massive stars produce copious UV emission which is absorbed and re–emitted as infrared by surrounding dust (Draine, 2011). As these massive stars produce the

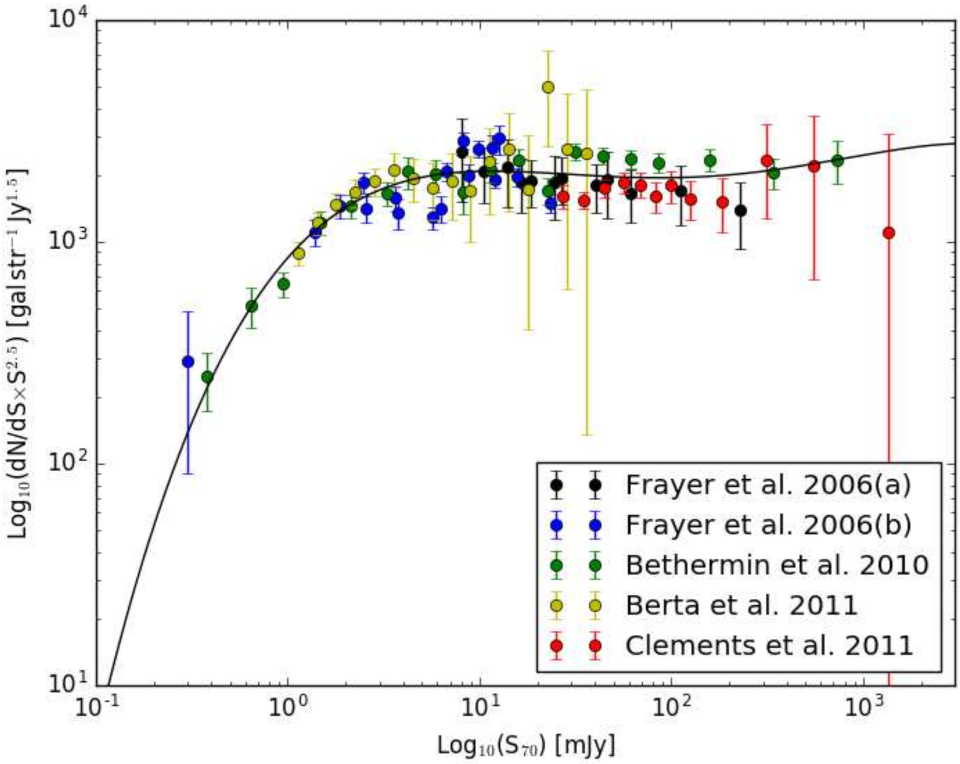

FIGURE 2.8: Compilation of normalised 70 μm differential source count measurements, taken from Frayer et al. (2006a,b); Béthermin et al. (2010); Berta et al. (2011) and Clements et al. (2011). The black line represents the best fitting 3rd order polynomial function to the observed data.

observed HII regions and SNR that we see with radio observations, we would expect to see 70 μm emission associated with regions of recent star formation. Dust is also heated in the accretion disks surrounding AGN (e.g., Jaffe et al., 2004), so we would also expect them to produce significant 70 μm emission. Although IC 10, background star–forming galaxies and background AGN all produce 70 μm emission, we do not expect to see any emission from background sources. This is illustrated if we consider the normalised source counts at 70 μm measured by Frayer et al. (2006a,b); Béthermin et al. (2010); Berta et al. (2011) and Clements et al. (2011), which we present in Figure 2.8. We adopt a model for the data by fitting polynomial functions until we find the best fit through comparing the reduced χ^2 statistic between fits. The best fit was found to be a 3rd order polynomial, which we plot over the data in Figure 2.8. After dividing by $S^{2.5}$ to obtain the differential source counts, we integrate the differential source counts between 3 times the rms noise level (0.3 mJy) for the 70 μm used for this analysis (Madden et al., 2013, which is presented in the top right of Figure 2.1) and 1000 mJy. We find that we would expect ~ 0.005 sources that are coincident with IC 10's main disk, i.e. it is very unlikely that any of the emission that is seen in the map at 70 μm originates from background sources. Therefore if we see co–spatial 70 μm emission with a radio source, it is likely to be a star–formation product belonging to IC 10 (i.e. an HII region or SNR).

6. **Coincident HI Emission:** Finally we consider HI emission that originates from neutral atomic hydrogen found within the ISM. HI emission arises due to a hyperfine ground state transition, where an electron's spin state decays from parallel with respect to that of the proton spin to anti–parallel, producing emission at 1420.4051 MHz. Stars typically form in molecular clouds (Larson, 1981), which themselves appear to form when neutral atomic hydrogen approaches a saturation density (Bigiel et al., 2008). Therefore we would expect to see HI emission near regions where star formation has recently started. After stars have formed, the combined effect of stellar winds and SNe drive the gas away from the star formation site, generating bubbles in the ISM. This is seen in the HI map of IC 10 from Hunter et al. (2012), which we present in the bottom–right of Figure 2.1. Therefore, we would expect to find young HII regions associated with HI emission and older HII regions and SNR towards the centres of the observed bubbles.

So far we have only considered a classification scheme that is largely time independent (i.e., we have assumed that IC 10 has not changed between each of the presented observations). Currently, we only have access to e–MERLIN maps at one epoch, however it has been shown that with a long enough time baseline ($\sim$ 10 yrs), it is possible to measure SNR expansion rates to further constrain observed source properties (Beswick et al., 2006; Fenech et al., 2008).

2.5.2 Expected Number Of Background Sources

Before we classify each of the detected sources on an individual basis using the scheme discussed above, it is useful to first estimate the number of background sources that we would expect to fall within IC 10's main star–forming disk. We can estimate the total number of background sources by analysing differential source counts at 1.4 GHz

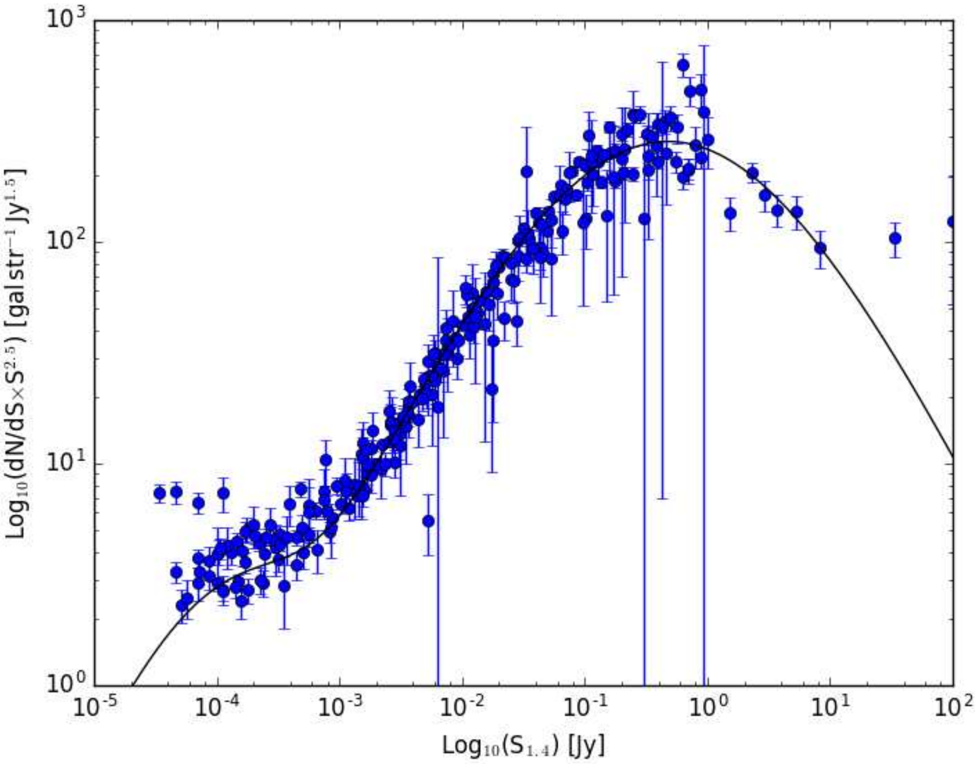

FIGURE 2.9: Compilation of 1.4 GHz differential source count measurements taken from Fomalont et al. (1974); Machalski (1978); Condon et al. (1982b); Condon and Mitchell (1982); Windhorst et al. (1984, 1985); White et al. (1997); Gruppioni et al. (1997, 1999); Ciliegi et al. (1999); Richards (2000); Prandoni et al. (2001); Hopkins et al. (2003); Seymour et al. (2004); Simpson et al. (2006) and Morrison et al. (2010). The black line represents the best fitting analytic shell model from Kellermann and Verschuur (1988).

from the literature, and assuming that the Universe is isotropic and homogeneous (i.e., it looks roughly the same in all directions). A differential source count is defined as the number of sources at a particular flux density ($S_{1.4\mathrm{GHz}}$) that is typically found in 1 steradian of sky area and is usually presented in such a way as to emphasize deviations from a non–expanding Universe governed by Euclidean geometry, where the differential source counts would be proportional to $S^{-\frac{5}{2}}$. The source counts for sources with flux densities ≥ 1 Jy are usually measured using shallow, wide area surveys as sources of this brightness tend to be rare, whereas the fainter populations ≤ 1 mJy can only be measured with deep, pencil–beam surveys. We present a compilation of differential source count measurements from both survey types in Figure 2.9.

It is apparent from Figure 2.9 that the source counts follow an approximately inverted parabolic shape at flux densities between 1 mJy $\leq S_{1.4\mathrm{GHz}} \leq 10$ Jy, which appears to flatten out at both higher and lower flux densities. To correctly model the observed source counts, detailed knowledge about the geometry of the Universe and how the 1.4 GHz galaxy luminosity function evolves with redshift is required, which is an area of active research (and beyond the scope of this thesis; Massardi et al., 2010; Bonato et al., 2017). Instead, we adopt the simplified shell model presented by J.J. Condon in Kellermann and Verschuur (1988) as our source counts model. The shell model assumes that most observed radio sources are confined to a thin shell at redshift $z \approx 0.8$ with an average spectral index $\alpha \approx -0.7$, and that the 1.4 GHz galaxy luminosity function at a given redshift can be found by scaling the local 1.4 GHz luminosity function. We assume that the local luminosity function can be represented by two parabolic approximations as presented in Condon et al. (2002), one for the population of AGN and another for the normal star–forming galaxies. We then use a least squares fitting procedure to fit the model to the assembled source count complation. We present the best fitting shell model as the black line in Figure 2.9. The inverted parabolic shape is then interpreted as the contribution from AGN at the shell redshift, the flattening at high flux densities can be interpreted as the contribution from galaxies that are closer than the shell redshift and the flattening at low flux densities is due to the contribution of fainter star–forming galaxies. The shell model provides a good fit to the observed source counts except at high flux densities, however as there are relatively few bright sources, it will not significantly affect our estimate for the total number of background galaxies.

We estimate the total number of background galaxies by first dividing the normalised differential source count model by $S^{\frac{5}{2}}$ and then multiplying the model by the completeness estimates given in Section 2.4.1. We then integrate the resulting function between 1 μJy and 10 Jy to obtain the expected number of background sources. From this analysis we expect 5 ± 2 sources that we detect to be background sources that are not related to IC 10.

2.5.3 Individual Source Notes

In this section we briefly discuss each source in turn with reference to the classification criteria discussed in Section 2.5.1.

Source 1 (WBBH J002017+591839.7)

This is the brightest source that we detect in our e–MERLIN observations and it also has the largest angular size. There is evidence in the presented contour maps for a 'clean bowl', hinting that we are missing flux from this source due to the lack of short spacings in the e–MERLIN array. This source has a peak brightness temperature $\geq 5000\,\mathrm{K}$ at 1.5 GHz and has a relatively flat low–resolution spectral index, $\alpha \sim -0.3$. There is no observed X–ray emission associated with this source, but there is emission observed in both the Hα and 70 μm maps. The source is coincident with a depression between two 'holes' in the large scale HI emission, as shown in the bottom–right of Figure 2.1. In view of this evidence, we classify this source as a compact HII region within IC 10.

Source 2 (WBBH J002027+591728.7)

This source is resolved with a peak brightness temperature $\geq 8000\,\mathrm{K}$ at 1.5 GHz and is observed to have a flat low–resolution spectral index equal to $\alpha \approx -0.1$. There is no observed X–ray emisison associated with this source, but this source is spatially coincident with significant Hα and 70 μm emission. The source is coincident with a peak in the large scale HI emission, indicating that star–formation is possibly being fuelled at this location. Furthermore, there are several Wolf–Rayet stars that are located nearby (Massey et al., 1992; Crowther et al., 2003). It is therefore likely that this source is a compact HII region within IC 10.

Source 3 (WBBH J002015+591853.9)

This source has an unusual extended morphology, and is located spatially close to Source 1. This source has a comparatively low brightness temperature $\geq 3000\,\mathrm{K}$ and has a steep low–resolution spectral index $\alpha \approx -1.0$. This source is associated with X–ray emission, but not with compact sources in either the Hα or 70 μm maps. There is no apparent coincident HI emission with this source. Source 3 is separated by ~ 23" from Source 1, which corresponds to a distance of 78 pc at IC 10's assumed distance. Following Hindson et al. (2018), assuming the stars have a stellar velocity dispersion equal to $5\,\mathrm{kms}^{-1}$, and that a SN progenitor lives for $\sim 55\,\mathrm{Myr}$, the furthest distance we would expect a massive star to travel from its birthplace is $\sim 250\,\mathrm{pc}$. Therefore, we cannot rule out that Source 3 is not a SNR whose progenitor originated from the star–formation episode that created Source 1. That being said, based upon the steep low–resolution spectral index observed for this source, we prefer to classify it as a contaminating background galaxy.

Source 4 (WBBH J002027+591706.1)

Source 4 is spatially located close to Source 2 and shares similar properties. It is resolved, with a peak brightness temperature ≥ 5000 K and a relatively flat low–resolution spectral index $\alpha \approx -0.4$. There is no X–ray emission associated with this source, but there is significant associated Hα and 70 μm emission. This source is coincident with a peak in the observed large scale HI distribution, which indicates that star–formation may be ongoing at this location. Source 4 is located in the outskirts of the non–thermal superbubble (Yang and Skillman, 1993; Heesen et al., 2015), and there are several Wolf–Rayet stars nearby. From this evidence, we classify Source 4 as a compact HII region within IC 10.

Source 5 (WBBH J002008+591540.2)

This source is unresolved in both the 1.5 and 5 GHz e–MERLIN observations and located towards the southern outskirt of IC 10's main disk. The source has a brightness temperature ≥ 11000 K and has a steep observed spectral index $\alpha = -1.3$. There is coincident X–ray emission but no associated emission in the Hα or 70 μm maps. From these observations, it is likely that this source is a contaminating background galaxy.

Source 6 (WBBH J002027+591843.7)

This source is unresolved and located towards the North-East of IC 10's main disk. The source has a brightness temperature equal to ≥ 9000 K at 1.5 GHz, but it is not detected in our 5 GHz e–MERLIN observations. We therefore measure an upper–limit for the spectral index $\alpha \leq -2.3$. The source is spatially close to but separate from a Chandra X–ray source, and is not associated with Hα or 70 μm emission. The source appears co–spatial with one of the shells apparent in the HI distribution, however based on the other evidence, it is likely to be a contaminating background galaxy.

Source 7 (WBBH J002018+591740.9)

This source has a resolved, diffuse structure with a sharp peak above the 5 σ_{rms} detection threshold, and is located roughly in the centre of IC 10's main disk. In Figure 2.3 we display a contour map that we convolved to a resolution of twice the naturally weighted synthesised beam to highlight this diffuse emission. We carried out the same analysis as for the other sources but with a beam that was twice the size. The peak brightness temperature for this source was found to be just 700 K, with a low–resolution spectral index equal to $\alpha \approx -0.4$. The source is not associated with X–ray emission, but is with emission in both the Hα and 70 μm maps. There is additional emission at a 3 σ significance level located $\sim 2''.5$ (8 pc) towards the south–east, which may be related to the source. Source 7 is likely a star–formation product within IC 10, however with the current e–MERLIN observations it is difficult to ascertain whether it is a peak in a diffuse HII region or part of an evolved SNR shell. Future VLA 1.5 GHz A–array observations would be required to determine the full extent of the source and VLA 10 GHz A–array observations would be required to obtain a high–resolution spectral index for this source to aid in source classification.

Source 8 (WBBH J002019+591802.3)

This source is partially resolved and located towards the centre of IC 10. Source 8 has a high brightness temperature equal $\geq$ 8000 K and a relatively flat low–resolution spectral index $\alpha \approx -0.2$. There is no observed X–ray emission associated with this source, but there is significant associated emission in both the Hα and 70 μm maps. Although the source is quite compact in the 1.5 GHz e–MERLIN map, it is apparently resolved out in the 5 GHz e–MERLIN map. It is therefore likely that Source 8 is a peak in a more extended HII region located within IC 10.

Source 9 (WBBH J002033+591942.9):

This source is unresolved and located towards the North–East of IC 10's main star forming disk. The source appears to have an extension to the East in the 1.5 GHz e–MERLIN map but is not detected in the 5 GHz e–MERLIN map. We obtain a peak brightness temperature $\geq$ 4000 K for this source, and a upper limit to the spectral index $\alpha \leq -1.7$. The source is not associated with X–ray, Hα of 70 μm emission, and appears spatially isolated from IC 10's main disk. Due to this evidence, we classify Source 9 as a contaminating background galaxy.

Source 10 (WBBH J002008+591955.2)

Source 10 is unresolved and located towards the North–West of IC 10's main star–forming disk. The source has an observed peak brightness temperature $\geq$ 3200 K and a relatively steep spectral index $\alpha \approx -0.8$. The source is coincident with an XMM X–ray source; there is no corresponding emission in either the Hα or 70 μm maps. This source appears offset from a shell in the observed HI distribution. This evidence suggests that Source 10 is a contaminating background source.

Source 11 (WBBH J001951+591644.2)

Source 11 is a faint, unresolved source that is located towards the West of IC 10's main disk. It is seen in the 1.5 GHz e–MERLIN map, but not the 5 GHz e–MERLIN map. We observe a peak brightness temperature ≥ 2000 K and derive an upper limit for the spectral index $\alpha \leq -1.2$. This source is not associated with an X–ray source or 70 μm emission. We cannot check whether there is any associated Hα emission as the Hunter and Elmegreen (2004) map does not extend to this part of the galaxy. Due to its isolation from the rest of the galaxy, we classify Source 11 as a contaminating background galaxy.

To summarize, we determine that 4 sources are HII regions within IC 10, 6 sources are contaminating background galaxies and 1 source is likely a star–formation product within IC 10, but it is currently unclear whether it is part of an HII region or part of a SNR shell.

2.5.4 Compact HII Regions Within IC 10

As discussed above, we determined that sources 1,2,4 and 8 are likely to be (or at least part of) HII regions located within IC 10. The source of ionising Lyman continuum photons that produce these HII regions are the young massive O and B type stars (Strömgren, 1939). If we assume that all detected radio emission from these sources at 1.5 GHz is thermal in origin, we can calculate the production rate of Lyman continuum photons required to produce the observed radio emission. By comparing these results with the outputs from stellar population synthesis models, we can determine an estimate for the total stellar mass contained within the star clusters responsible for the observed HII regions.

To estimate the total production rate of Lyman continuum photons for each detected compact HII region, we apply Equation 2 from Condon (1992):

$$\left(\frac{N_{UV}}{\mathrm{s}^{-1}}\right) \gtrsim 6.3 \times 10^{52} \left(\frac{T_e}{10^4\,\mathrm{K}}\right)^{-0.45} \left(\frac{\nu}{\mathrm{GHz}}\right)^{0.1} \left(\frac{L_T}{10^{20}\,\mathrm{WHz}^{-1}}\right) \tag{2.26}$$

TABLE 2.5: Determined HII Region properties

Source	N_{UV}	Stellar Cluster Mass	# SNe
1	$\geq 3.1 \times 10^{50}\,s^{-1}$	$\geq 22000\,M_{\odot}$	$\gtrsim 266$
2	$\geq 1.3 \times 10^{50}\,s^{-1}$	$\geq 9500\,M_{\odot}$	$\gtrsim 115$
4	$\geq 7.0 \times 10^{49}\,s^{-1}$	$\geq 5200\,M_{\odot}$	$\gtrsim 63$
8	$\geq 3.3 \times 10^{49}\,s^{-1}$	$\geq 2400\,M_{\odot}$	$\gtrsim 29$

Notes: # SNe is the total number of expected SNe over the entire lifetime of the HII region assuming a Miller–Scalo IMF with all stars greater than $8\,M_{\odot}$ exploding as SNe.

where T_e is the electron temperature, ν is the observed frequency and L_T is the HII region luminosity. We note that estimates of the Lyman continuum photon production rate using this formula will be a lower limit, as not only are we resolving out some of the extended emission associated with these soures, some Lyman continuum photons may also be absorbed by dust within the HII regions themselves. Assuming an electron temperature $T_e = 10^4\,K$ and an observing frequency $\nu = 1.5\,GHz$, we calculate and present the Lyman continuum photon production rate required to produce the observed HII regions in Table 2.5.

We then used Starburst99 (Leitherer et al., 1999) to produce models for the Lymann continuum production rate as a function of time for various stellar cluster masses. We assume a Miller–Scalo IMF (Miller and Scalo, 1979), that all star formation takes places in a single instantaneous burst at t=0 and that all stars larger than $8\,M_{\odot}$ explode as SNe. We also assume Geneva evolutionary tracks with standard mass loss at a metallicity of Z=0.004 (Charbonnel et al., 1993) as this metallicity closely reflects that observed for IC 10 (Garnett, 1990; Leroy et al., 2006). We plot the derived models, along with the measured Lyman Continuum production rate in Figure 2.10.

Each of the models for the Lyman continuum production rate have the same shape, the production rate is constant for the first $\sim 10^{6.5}$ yr before sharply declining due to the massive stars that produce the Lyman continuum emission exploding as SNe. As we do not know the age of the observed HII regions, we do not know if any of the massive OB stars have already exploded as SNe. However, as these sources are also observable in the Hα map (see Figure 2.1), it is likely that no SNe have yet disrupted the Lyman continuum production rate and that we are observing these HII regions in the early constant production phase. Comparing our observed Lyman continuum production rate with the constant phase predicted from Starburst99 will therefore give a reasonable estimate of the lower limit for the stellar cluster mass.

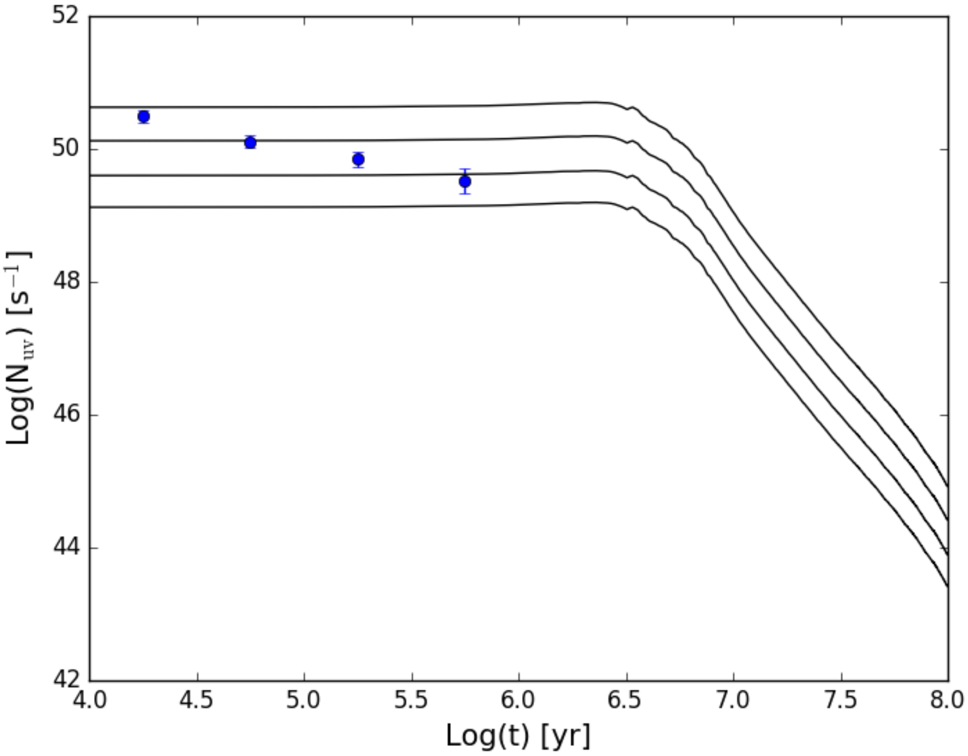

FIGURE 2.10: Starburst99 models of the Lyman continuum production rate as a function of time for 4 cluster masses. The solid lines represent the Lyman continuum production rate for clusters of mass (from top to bottom) $10^{4.5}$, 10^{4}, $10^{3.5}$ and 10^{3} M$_{\odot}$. The blue points represent the Lyman Continuum production rates derived (from left to right) for sources 1,2,4 and 8. Note that we do not know the age of the observed HII regions and so the position on the time axis was arbritraily chosen to clearly identify where each source lies with respect to the constant Lyman continuum production phase.

We determine the stellar masses for each detected HII region by interpolating between the constant production phase for each Starburst99 model. The derived lower limits for the cluster masses along with the total number of expected SNe originating from these clusters are presented in Table 2.5. These estimates do not vary hugely with assumed metallicity, but do with assumed IMF. Re-running the simulations again assuming solar metallicity results in a 5 percent increase in the cluster mass, however, re-running the simulations assuming a Salpeter IMF (Salpeter, 1955) results in a 50 percent decrease in the cluster mass. The derived cluster masses for sources 1 and 2 are larger than the average stellar cluster found within the LMC whereas sources 4 and 8 reflect a more typical cluster mass (Hunter et al., 2003). For reference, the derived cluster mass for source 1 is approximately half that of 30 Doradus in the LMC (Hunter et al., 1995; Andersen et al., 2009).

Using the derived cluster masses required to produce the observed radio–continuum emission, we can obtain a rough estimate for the star–formation rate contained within the observed compact HII regions in IC 10. As we cannot tell the age of the HII region, the star formation rate we derive should be interpreted as the star–formation rate averaged over the time the HII region has existed for. We will therefore assume that the HII regions we are observing in IC 10 are all at the point where the first massive stars will explode as SNe, which is around $10^{6.5}$ yr (~ 3 Myr). By adding up the cluster masses in Table 2.5 and dividing by $10^{6.5}$yr, we obtain a star–formation rate equal to $\mathrm{SFR}_{TH} \approx 0.01\,\mathrm{M}_{\odot}\mathrm{yr}^{-1}$. This number should be interpreted as a lower limit for the star–formation rate within IC 10 based upon the fact that radio–continuum emission is likely to be resolved out in the presented high–resolution observations, some of the ionizing Lyman continuum photons may have been absorbed by dust within the HII regions themselves or escaped the HII regions, and that we do not know exactly when the stars formed leading to the HII regions (it should also be noted that we have assumed that all stars formed instantaneously in the Starburst99 simulations, which effectively makes the star–formation rate meaningless unless it is averaged over a characteristic timescale). As both thermal radio–continuum emission and Hα emission originate from hydrogen that has been ionized by nearby massive stars, they trace star formation over the same timescale (Kennicutt and Evans, 2012). Therefore we can directly compare the star–formation rate derived from Hα observations with the star–formation rate we determine from the thermal radio continuum. Hunter et al. (2012) derive $\mathrm{SFR}_{H\alpha} \approx 0.07\,\mathrm{M}_{\odot}\mathrm{yr}^{-1}$ (where we have scaled the originally presented SFR to be compatible with a Miller–Scalo IMF; Miller and Scalo 1979), which is almost an order of magnitude larger than our rough estimate from the compact HII regions. Although there are many observational effects that affect the interferometric radio observations (such as the missing flux issue), this result demonstates that high–resolution radio continuum studies of extra–galactic HII regions can be used to place useful limits on a galaxy's star–formation rate averaged over the last $10^{6.5}$ yr.

Finally, the 320 MHz GMRT observations by Basu et al. (2017) show that sources 1 and 2 exhibit the signature of free–free absorption, which has been further confirmed for source 1 with 140 MHz LOFAR observations presented by Heesen et al. (2018b). This is a useful confirmation that the presented classification is correctly identifying compact HII regions.

2.5.5 SNR Within IC 10

None of the observed e–MERLIN sources have yet been conclusively classified as SNR, with only one source possibly fitting into that category. As IC 10 is observed to have a high star–formation rate surface density ($\approx 0.08\,\mathrm{M}_{\odot}\mathrm{yr}^{-1}\mathrm{kpc}^{-2}$; Hunter et al. 2012), it is important to ask why we do not observe many SNR with the presented observations.

First we will consider the total number of SNR that we expect to observe within IC 10, based on its current observed star–formation rate. Assuming that the star–formation rate is constant, the supernova rate can be found through:

$$\nu_{\mathrm{SNe}} = \phi_{\mathrm{SFR}} \times \frac{\int_{\mathrm{M}_{SNe}}^{\mathrm{M}_{upper}} \xi(m)dm}{\int_{\mathrm{M}_{lower}}^{\mathrm{M}_{upper}} m\xi(m)dm} \left[\mathrm{yr}^{-1}\right], \tag{2.27}$$

where ϕ_{SFR} is the current measured star–formation rate in $\mathrm{M}_{\odot}\mathrm{yr}^{-1}$, M_{upper} and M_{lower} are the assumed upper and lower stellar mass limits, M_{SNe} is the SNe mass threshold above which stars that are more massive are assumed to explode as SNe, and $\xi(m)$ is the initial mass function normalised so that $\int_{\mathrm{M}_{lower}}^{\mathrm{M}_{upper}} \xi(m)dm = 1$. The numerator in the fraction is the relative fraction of stars that will explode as SNe and the denominator is the average stellar mass for the assumed IMF. For a Miller–Scalo IMF (Miller and Scalo, 1979) with $\mathrm{M}_{lower} = 0.1\,\mathrm{M}_{\odot}$, $\mathrm{M}_{upper} = 100\,\mathrm{M}_{\odot}$ and $\mathrm{M}_{SNe} = 8\,\mathrm{M}_{\odot}$, the supernova rate is related to the star–formation rate through:

$$\nu_{\mathrm{SNe}} = 0.012\phi_{\mathrm{SFR}}. \tag{2.28}$$

Given that the SFR in IC 10 is observed to be $\approx 0.07\,\mathrm{M}_{\odot}\mathrm{yr}^{-1}$ (Hunter et al., 2012), and that a SNR is typically observable for 10^4 yr (Strong et al., 2007), we would expect to observe $\approx 8 \pm 3$ SNR, where the uncertainties arise from the Poisson counting uncertainty. Under these assumptions, it is unlikely that it is entirely by chance that we are not observing any compact SNR. There are three possible reasons for this:

1. **We are resolving out emission from SNR**

   A potential way we may be missing SNR is by resolving them out. As e–MERLIN consists of predominantly long baselines (6–220 km), it is only sensitive to emission that occurs on small angular scales. e–MERLIN essentially begins to resolve out sources that have angular sizes larger than $2''$ at 1.5 GHz[5]. Studies of SNR in the Magellanic clouds (Filipovic and Bozzetto, 2017) reveal an average SNR diameter equal to ~ 40 pc, which is similar to the average sizes of SNR found in M 33 (Long et al., 2010) and M 31 (Lee and Lee, 2014). Scaling this to our assumed distance of 0.7 Mpc, we would expect an average SNR in IC 10 to have an angular size equal to $\sim 12''$. As the average SNR size is much larger than the scale at which e–MERLIN begins to resolve out emission, it is plausible that we are resolving out SNR candidates with the presented observations. This can already be seen in IC 10 if we focus on the non–thermal superbubble (Yang and Skillman, 1993; Heesen et al., 2015). The non–thermal superbubble is believed to be the result of either a hypernova (Lozinskaya and Moiseev, 2007) or a collection of smaller SNe (Yang and Skillman, 1993), however it is not observed in the presented e–MERLIN observations due to its large angular size ($\sim$ 50"). It should be noted that even though we are resolving out SNR, we should still be sensitive to bright compact structure associated with expanding SNR shells.

Most of the SNR that are ~ 40 pc in size are in the Sedov–Taylor phase of their evolution, where observable SNR will spend most of their time ($\sim 10^4$ yr; Strong et al. 2007). We can also ask the question of how many SNR we would expect to see that are smaller than 2". A rough calculation using equations detailed in Draine (2011) reveals that SNR appearing to be $2''$ in size would be $\sim$40 yr in age and still in the short–lived free expansion phase (Draine, 2011). Therefore we would expect a very small fraction of potentially observable SNR to not be resolved out in the presented e–MERLIN observations. It is therefore likely that we are resolving out most, if not all of the SNR within IC 10.

2. **There may be environmental factors that affect SNR detectabillity**

   There are other factors that may affect the detectability of SNR. For example the brightness of the non–thermal synchrotron emission depends upon the strength of magnetic fields the CRe are interacting with. Base magnetic fields are amplified in SNR shockfronts (Guo et al., 2012), although predicting the degree to which they are amplified is complicated (e.g. Matthews et al., 2017). From the Rankine–Hugoniot jump conditions, we would expect at least an enhancement in the magnetic field of a factor ~ 4 for strong shocks, based upon compression

---

[5] See e–MERLIN Cycle 4 capabillities available at `http://www.e-merlin.ac.uk/observe/cycle4.html`

alone (Draine, 2011). The base magnetic field strength is related to the density of the gas in the ISM (Vallée, 1995; Niklas and Beck, 1997), which is typically smaller in dwarf galaxies (Hunter et al., 2012). Therefore, if the base magnetic field is smaller, we would expect a SNR to be fainter. It is possible then that SNR within IC 10 are fainter than those taking place in denser environments (such as M 82 and Arp 220). Furthermore, SNR expanding into less dense environments will expand at a faster rate, meaning that they will be resolved out earlier in their evolution.

This situation may be occurring within the non–thermal superbubble, where we do not observe any compact radio sources. The initial growth of superbubbles in general is thought to originate from the winds of massive stars, which rarify their immediate environment (Krause et al., 2013). As these stars explode as SNe, their shockwaves will quickly propagate through the rarified ISM until they reach the outer, dense superbubble shell, where they can produce substantial radio emission. Although the magnetic field strength within the superbubble is high ($44 \pm 8\,\mu$G; Heesen et al. 2015), its low density would mean that shocks will quickly become resolved out by e–MERLIN.

3. **We may be observing IC 10 at a special time**

   Finally, it is also plauseable that we are simply observing IC 10 at a special time, where the observed massive stars have formed in the most recent star–formation burst but have not yet had time to explode as SNe. Evidence for this scenario includes the large numbers of short lived Wolf–Rayet stars (with lifetimes $\sim 10^5$ yr; Crowther 2007) observed within IC 10 (Crowther et al., 2003), and the high observed thermal fraction at 1 GHz ($\sim 30\,\%$) found in studies of its integrated radio continuum properties (Klein et al., 2018). Furthermore, the 'holey' appearance of the large scale H I distribution indicates that IC 10 has a bursty star formation history (Wilcots and Miller, 1998), which means that our assumption of constant star formation will break down. Therefore, our estimate of 8 ± 3 observable SNe may be an overestimate if the star–formation rate has increased significantly over the last 10 Myr. The non–thermal superbubble in this scenario would correspond to the massive stars that formed towards the beginning of the star–formation burst, that have recently exploded as SNe (within the last 4 Myr; Heesen et al. 2015).

As we expect to find so few SNR in general, it is unlikely that we are observing any young SNR with the presented e–MERLIN observations. Instead we are more likely to be observing compact HII regions and background sources. In general, e–MERLIN would be well suited to observe SNR at 1.5 GHz in galaxies that are at distances $>$ 4 Mpc. At this distance, the average SNR would appear $\sim 2''$ in size and the SNR would not be resolved out due to the lack of short baselines in the e–MERLIN array. For galaxies that are closer than 4 Mpc, e–MERLIN observations should be combined with VLA A–array observations which provide the required sensitivity to large scale emission in order to identify possible SNR candidates within these galaxies.

2.5.6 Updated Integrated Flux Density Measurment

Total flux density measurements of galaxies are typically determined through single dish observations, which are often contaminated by background sources. As dwarf irregular galaxies are intrinsically faint in radio continuum, the background sources could dominate the observed radio emission, resulting in an incorrect measurement of the total radio emission from the galaxy itself (Hindson et al., 2018). With this current study, we identify potential background sources and use our high–resolution maps to update literature integrated flux density measurements accordingly.

We use the measurements from Chyży et al. (2016), which are 377 ± 11 mJy at 1.43 GHz and 222 ± 9 mJy at 4.85 GHz, as the integrated flux measurements for IC 10. These measurements have already been corrected for the presence of 4 background sources that are observed in the halo of the galaxy, but not for the existence of background sources within the main star–forming disk. We use our high resolution e–MERLIN maps to identify background sources within IC 10's main disk, but measure the total flux density for these sources from lower resolution VLA maps presented in Heesen et al. (2015). The e–MERLIN sources can easily be identified in the lower resolution VLA maps and by using this method, we minimise the amount of flux that we miss due to missing short spacings.

As the VLA maps were taken at 1.5 GHz and 6 GHz, we use the spectral index between the Chyży et al. (2016) measurements ($\alpha = -0.43 \pm 0.09$) to find the expected integrated flux densities at these frequencies. We then measure the flux density of sources that are determined to be background sources from the VLA maps using the AIPS task JMFIT.

We subsequently subtract these sources (sources 3, 5, 6, 9, 10 and 11), along with 4 additional faint sources detected in IC 10's halo to obtain a corrected flux density of 352 ± 11 mJy at 1.5 GHz and 199 ± 9 mJy at 6 GHz.

Subtracting the contaminating background sources in IC 10's main disk results in only a 4 per cent decrease in the flux density at 1.5 GHz and a 2 per cent decrease at 6 GHz. Contaminating background sources therefore do not contribute significantly to the overall flux density measured from IC 10 at radio wavelengths, and previous analysis concerning its integrated properties remains valid.

2.6 Conclusions

We present high-resolution e–MERLIN observations of the compact radio sources coincident with the main star–forming disk of the nearby dwarf Irregular galaxy IC 10 at both 1.5 GHz and 5 GHz. Our main conclusions are as follows:

1. Our e–MERLIN observations reveal 11 compact radio sources at 1.5 GHz coincident with IC 10's star–forming main disk, 5 of which also have detections at 5 GHz. We classify our sources based on their brightness temperature, measured spectral index (if the source is unresolved at both 1.5 GHz and 5 GHz) or low–resolution literature spectral index (if the source is extended) and whether the source is coincident with emission at X–ray, Hα, 70 μm and HI emission.
2. From this multi–wavelength classification procedure, we classify 4 sources (1,2,4 and 8) as compact HII regions within IC 10, 6 sources (3,5,6,9,10 and 11) as contaminating background galaxies and one source (7) that is yet to be firmly classified, although it is likely a star–formation product within IC 10. The number of observed background sources is in good agreement with that expected from analysing literature source counts (5 ± 2 coincident background sources).
3. Most of the observed sources that are associated with IC 10 are compact HII regions. Based on Starburst99 models, we determine lower limits for the stellar cluster masses required to produce the observed compact HII regions; the largest of which is about half the size of 30 Doradus in the LMC. We estimate a lower limit for the star–formation rate within the detected compact HII regions,

$\mathrm{SFR}_{\mathrm{H\,II}} \geq 0.01\,\mathrm{M}_{\odot}\mathrm{yr}^{-1}$, which is roughly an order of magnitude smaller than the total star–formation rate found from Hα studies ($\mathrm{SFR}_{\mathrm{H}_{\alpha}} \approx 0.08\,\mathrm{M}_{\odot}\mathrm{yr}^{-1}$). This demonstrates that extinction–free radio–continuum studies of compact H II regions in other galaxies can be used to place valuable constraints on the current star–formation rate.

4. Based on the timescale over which SNR are typically observable and the limited sensitivity to structures more extended than $2''$, we expect that we will not be able to detect any SNR with the current e–MERLIN observations. The only SNe we would expect to be able to detect are very young SNR, but it is unlikely that we would observe any due to a combination their short observable timescales and the low total SFR observed in IC 10. We explore other possible factors that could affect SNR detectability in dwarf Irregular galaxies and conclude that e–MERLIN alone is well suited to study SNR in galaxies located at distances greater than 4 Mpc due to the spatial frequencies covered by the array. For galaxies closer than 4 Mpc, additional VLA observations are required to fully cover the spatial scales that SNR candidates occupy.

5. We present updated integrated flux densities for IC 10, where we subtract the contribution from background sources from literature and our own data. We find a 4 per cent reduction in the measured flux at 1.5 GHz and a 2 per cent reduction at 4.85 GHz. These adjustments are minimal, hence previous literature analysis concerning its integrated radio properties remains valid.

Further observations are required to fully classify the observed resolved sources. Ideally, VLA A–array observations taken at 10 GHz will match the *uv*–coverage of the current 1.5 GHz observations and allow for reliable spectral indices for all detected sources to be determined. Further A–Array observations at 1.5 GHz would provide sensitivity to larger spatial scales to aid in the detection and characterisation of SNR.

Because of the low integrated SFR of individual dIrr galaxies, the small numbers of detected sources are subject to low-number statistics. In order to make progress, rather than targeting individual dIrr systems, an ensemble would need to be observed and statements made on a statistical basis. In contrast, larger star–forming spiral and starburst galaxies will contain many more compact sources and could be analysed on a galaxy by galaxy basis.

Chapter 3

The Radio Continuum Properties of the dIrr Galaxy NGC 1569

3.1 Introduction and Motivation

As we have already discussed in Chapter 1, the observed radio continuum emission from normal star–forming galaxies are made up of two key emission processes that are both closely related to recent star–formation (Condon, 1992). The thermal radio continuum emission has been shown to be a direct tracer of instantaneous star–formation that holds across many different galaxy types (Murphy et al., 2012; Tabatabaei et al., 2017). Although thermal radio emission is an ideal, extinction–free tracer of star–formation (Murphy et al., 2011), it is intrinsically faint due to its low brightness temperature of typically 10^4 K, and is typically overwhelmed at frequencies < 30 GHz by non–thermal radio continuum emission, and at frequencies > 200 GHz by the thermal re–radiation of stellar light by dust. The non–thermal emission originates from CRe that have been accelerated in supernova shock–fronts (Krymskii, 1977; Axford et al., 1977; Bell, 1978a,b; Blandford and Ostriker, 1978; Drury, 1983; Reynolds, 2008) and is much brighter and more accessible at $\sim$ GHz frequencies. Yet its relationship to star–formation is far more complicated than thermal radio emission, as CRe acceleration, diffusion (where the CRe experience losses, mainly due to interactions with magnetic fields in the ISM or Inverse Compton scattering) and escape determine the observed non–thermal radio emission characteristics.

Regardless of which emission mechanism is studied, both emission components need to be reliably separated, and their associated uncertainties characterised, before any analysis can take place. The ideal separation procedure involves taking radio observations that fully sample radio frequency space, and fitting the thermal and non–thermal components simultaneously. In practice however, only a few (2–3) radio frequencies are available, which results in large degeneracies between the fitted thermal and non–thermal components (Niklas and Beck, 1997). Furthermore, standard χ^2 fitting procedures may underestimate the true uncertainties associated with the separation (Condon, 1992). To counter this problem, authors tend to use extinction–corrected Hα emission maps as a proxy for the thermal radio emission (e.g. Heesen et al. 2014), and subtract this contribution to isolate the non–thermal emission. Although this method significantly reduces the degeneracy between the two components, the corrections for galactic foreground and internal absorption can be highly uncertain (Basu et al., 2017), and are not normally properly accounted for in the rest of the analysis. As demonstrated by Tabatabaei et al. (2017), a Bayesian methodology can be used to reliably estimate the uncertainties associated with the separation, and this type of analysis allows prior information to easily be incorporated to reduce the fit degeneracies (Sharma, 2017). This motivated us to develop a Bayesian methodology that uses the Hα emission as a prior, to separate the thermal and non–thermal radio emission components in a given galaxy on a beam by beam basis.

In this chapter, we present our Bayesian separation procedure and the results obtained by applying it to VLA observations of the dIrr galaxy, NGC 1569.

3.2 NGC 1569

NGC 1569 (Figure 3.1) is a nearby (located at a distance of 3.2 Mpc; Lelli et al., 2014) dIrr galaxy that, similarly to IC 10, has recently undergone a recent starburst phase. Analysis of NGC 1569's super star clusters (Hunter et al., 2000) and colour magnitude diagram (Angeretti et al., 2005; McQuinn et al., 2010) indicates that the starburst phase started ~ 100 Myr ago and finished ~ 10 Myr ago. Additional observations of the turbulent gas kinematics found in HI observations (Johnson et al., 2012) and evidence for galactic outflows found in Hα (Waller, 1991), HI (Johnson et al., 2012), radio–continuum (Lisenfeld et al., 2004), and X–ray (Martin et al., 2002) observations provide

FIGURE 3.1: $2' \times 2.'7$ field of view composite Hubble Space telescope map of NGC 1569 from the observations presented in Grocholski et al. (2008). The map was constructed from the F606W (V), F814W (I) and F658N (Hα) filters.

further evidence for this recent starburst phase picture. Large-scale HI observations of the sky surrounding NGC 1569 indicate that an interaction with the dwarf irregular galaxy UGCA 92 is a possible cause of the recent starburst (Johnson, 2013). Although the starburst phase has finished, the current star–formation rate within NGC 1569 is observed to be high compared to its lifetime average (see Figure 8 in McQuinn et al. 2012), and is considerably higher than that normally found for dwarf galaxies ($\sim 0.01\,\mathrm{M_{\odot}yr^{-1}}$; Hunter and Elmegreen 2004; Hunter et al. 2012). We present a summary of NGC 1569's key properties in Table 3.1.

These observed properties make NGC 1569 an ideal candidate to test separation methods for 3 main reasons:

1. It is nearby, bright and well studied in many wavelength regimes. There is a great deal of ancillary data, which the recovered results can be compared against.
2. As most of the recent star–formation occurred in a single burst, the non–thermal radio emission properties can be characterised by a single CRe population. Furthermore, as NGC 1569 is small, few CRe will experience spectral aging before escaping the main disk into the halo (Israel and de Bruyn, 1988; Kepley et al.,

TABLE 3.1: Key NGC 1569 properties

Property	Value	Reference
α_{J2000} (hh mm ss)	04 30 49.0	–
δ_{J2000} ($^{\circ}\,'\,''$)	+64 50 53	–
Galaxy Type	IBm	1
Distance	3.4 Mpc	2
$\mathrm{SFR}_{\mathrm{H}\alpha}$ (Distance scaled)	$0.59\,\mathrm{M}_{\odot}\,\mathrm{yr}^{-1}$	3
Angular Size (Major Axis)	$4.'68$	4
Angular Size (Minor Axis)	$2.'15$	4
Position Angle	118°	4
Inclination	63°	4

Reference List: 1: de Vaucouleurs et al. (1991), 2: Lelli et al. (2014), 3: Hunter and Elmegreen (2004), 4: Jarrett et al. (2003).

2010). This is a far simpler modelling problem compared to a larger spiral galaxy, where CRe population mixing and losses make separating the non–thermal component more challenging.

3. The current star–formation rate is high, the thermal radio emission is also bright and much easier to detect and isolate.

This chapter is structured as follows; in Section 3.3 we describe our observations, data reduction, imaging method and discuss the impact that missing flux from short spacings may have on our results; in Section 3.4 we describe our fitting procedure; in Section 3.5 we describe the results retrieved from applying our fitting procedure to VLA observations of NGC 1569; in Section 3.6 we estimate the reddening along the line of sight to NGC 1569 and estimate resolved equipartition magnetic field strengths. Finally, we present our conclusions in Section 3.7.

3.3 Observations and Data Reduction

We observed NGC 1569 with the NRAO[1] VLA at L (1.5 GHz), S (3.0 GHz), C (5.0 GHz) and X (9.0 GHz) band over a 3 yr period as a part of the LITTLE THINGS project (Hunter et al., 2012; Hindson et al., 2018). In addition to these observations, we retrieved a Ka band (33.8 GHz) observation of NGC1569 from the VLA archive (project

---

[1] The National Radio Astronomy Observatory is a facility of the National Science Foundation operated under cooperative agreement by Associated Universities, Inc.

code 11B-078) and reduced it using the same methodology as the other datasets (see below). We present a summary of all observations in Table 3.2.

Each VLA observation follows the same observing strategy. All start with a scan of the primary flux calibrator followed by alternating scans of NGC 1569 and the complex gain calibrator, J0449+6332. The observing runs then finished with an additional scan of the primary flux calibrator. For the majority of observations, 3C138 was used as primary flux calibrator, but for the 5 GHz and 33.8 GHz observations, 3C147 was used instead. In all presented observations, the primary flux calibrator was also used to calibrate the bandpass for each observed spectral window.

Before carrying out any calibration, several flagging procedures were employed to remove as much contaminating radio frequency interference (RFI) as possible. For each dataset, we started with a run of the Common Astronomy Software Applications (CASA, McMullin et al., 2007) flagger in TFCROP mode to initially remove any obvious RFI in the uncalibrated data. We then carried out an initial phase calibration, selecting channels which were determined to be free of RFI to obtain preliminary complex gain solutions. We used these solutions to derive a preliminary bandpass solution, which we then applied to the data. We then employed the CASA flagger in RFLAG mode on this bandpass–corrected data to remove any additional RFI that the earlier flagging procedure may have missed. Finally, we flagged the first and last 5 channels at the beginning and end of each spectral window to reduce the noise contribution from the edges of the bandpasses. We then took the flag tables from this procedure and applied them to the original dataset as a starting point for calibration. This flagging method proved effective at removing the majority of RFI in lower frequency observations (< 5 GHz), where RFI becomes a more prominent issue.

We then calibrated each dataset independently following standard calibration procedures in CASA. After finding and applying initial antenna gain solutions, we visually inspected the data to manually remove any RFI that had not been flagged in our initial flagging attempts. Each dataset was then phase only self–calibrated to convergence using a model consisting of the clean components obtained by incrementally imaging the data. We then finished with a final round of amplitude and phase self–calibration. In all self–calibration iterations, we placed additional outlier fields on any bright sources that were present within the VLA primary beam to take into account their contribution.

TABLE 3.2: Summary of VLA observations of NGC 1569.

Frequency (GHz)	Project Code	Band	Array Configuration	Bandwidth (MHz)	Observation Date (dd/mm/yyyy)	Time on Source (min)
1.5	14B-259	L	B	1024	10/02/2015	27
3.0	14B-259	S	B	2024	10/02/2015	24
5.0	12A-234	C	C	2048	16/03/2012	35
9.0	14B-259	X	C	2024	16/10/2014	15
33.8	11B-078	Ka	D	2048	18/12/2011	81

TABLE 3.3: Noise Measurements for the maps used in our analysis. All maps have been convolved to a common resolution of 6.3″.

Band	Central Frequency (GHz)	RMS Noise (μ Jy beam^{-1})	Taper Radius (kλ)
L	1.26	56	32
L	1.78	65	20.5
S	2.50	71	21.5
S	3.50	77	29
C	5.00	40	19
C	7.40	45	21
X	8.50	45	31
X	9.50	43	33
Ka	33.80	55	22

Once the datasets were calibrated, we checked our flux scale by comparing preliminary maps from our VLA observations with other maps available in the literature. We checked our 1.5, 3.0 and 5.0 GHz calibrations by comparing the integrated flux densities of several unresolved sources that are not related to NGC 1569 with those found in lower resolution maps from the Westerbork Synthesis Radio Telescope (WSRT; published in Kepley et al. 2010). We find that our flux scale is consistent with the literature at these frequencies to within 10%. At higher frequencies, however, the smaller primary beam greatly limits the number of sources we can compare. To check the flux scale for these observations, we compare the spectral index (α; $S_\nu \propto \nu^\alpha$) derived using all of our available observations to those in the literature for some bright, well studied compact sources within NGC 1569. For example, for frequencies in the 1.5 GHz to 10 GHz range, we derive a spectral index of $\alpha = -0.54 \pm 0.06$ for an unresolved supernova remnant (SNR) located towards the south–east of NGC 1569 (designated NGC1569-38; Chomiuk and Wilcots 2009). This is in excellent agreement with spectral indices derived by Greve et al. (2002) and Chomiuk and Wilcots (2009) who find $\alpha = -0.56 \pm 0.03$ and $\alpha = -0.58 \pm 0.15$ respectively. We do not have any additional checks for the 33.8 GHz fluxscale, however the derived spectral indices for various HII regions found in the Hα map presented in Hunter and Elmegreen 2004 have a characteristic flat spectrum ($\alpha \simeq -0.1$), lending confidence that our flux calibration at 33.8 GHz is also correct.

3.3.1 Imaging

All of the presented observations are affected by missing flux effects due to the lack of short baselines in the VLA, which is to be expected from the combination of frequencies observed and array configurations used and NGC 1569's angular size (see Table 3.1). We discuss how this may affect the observed spectral indices in Section 3.3.3.

To make sure that our derived spectral indices are as accurate as possible, it is critical that each map used in our analysis is sensitive to the same spatial scales. As interferometers sample the Fourier transform of the sky intensity distribution (the uv–plane), we can ensure we are sensitive to similar spatial scales by only using samples within a particular region of the uv–plane to obtain an image. The uv–range is defined as the inner and outer edges (usually measured in wavelengths) of an annulus, centred on the origin of the uv–plane, where samples inside the annulus are used for imaging. In this paper, we limit our analysis to the uv–range $3.4 - 30\,\mathrm{k}\lambda$ as this range is well sampled by all our observations. The drawback to limiting the uv–range is that we resolve out a large fraction of the extended emission associated with NGC 1569, greatly limiting our analysis of diffuse emission on scales greater than $\sim 30''$.

As NGC 1569 is bright, we are able to split the observed bandwidth into two halves for the 1.5, 3.0, 5.0 and 9.0 GHz observations. By doing this, we almost double our available data points, allowing for a more robust analysis of NGC 1569's resolved spectral properties. We do not split the 33.8 GHz observations as the thermal emission that this waveband is primarily tracing is faint and the receivers are inherently more noisy than those at lower frequencies. By averaging over the entire 33.8 GHz bandwidth, we maximise our sensitivity in this waveband.

We used multi–scale multi–frequency cleaning (Rau and Cornwell, 2011) to produce our final maps for analysis, 'cleaning' to convergence at scales equal to the synthesized beam, twice the synthesized beam and 5 times the synthesized beam with a Briggs robust parameter of 0.5. Multi–scale multi–frequency clean differs from more traditional cleaning algorithms as it models the cleaned source as a collection of truncated paraboloids rather than a collection of point sources, and additionally takes into account source flux density variation across the observed bandwidth. These properties are ideal for imaging NGC 1569 as the source is extended, and each map spans

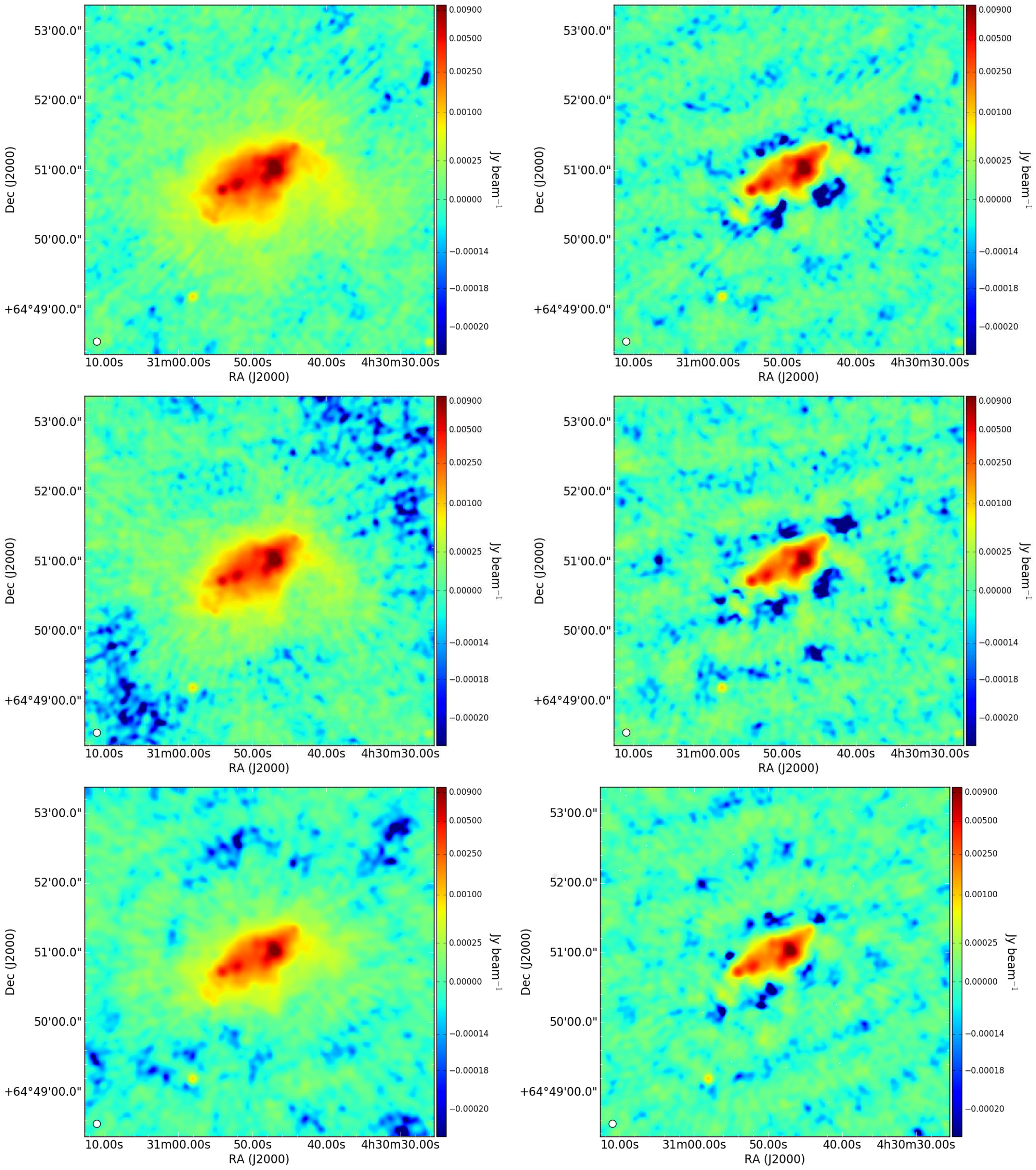

FIGURE 3.2: Radio maps of NGC 1569 at the frequencies specified in Table 3.3. The top maps show NGC 1569 at 1.26 GHz, the middle maps at 1.78 GHz and the bottom maps at 2.5 GHz. The maps on the left were imaged using the entire *uv*–range available from the observations in Table 3.2, and the maps on the right were imaged using the limited *uv*–coverage (3.4–30 kλ). All maps have been corrected for primary beam attenuation and the units for all maps are in Jy beam^{-1}. All maps have been stretched to the same log scale to emphasise low surface brightness emission, and all have been convolved to a Gaussian PSF with FWHM 6.3″ (an outline of the beam is shown in the bottom–left of each image).

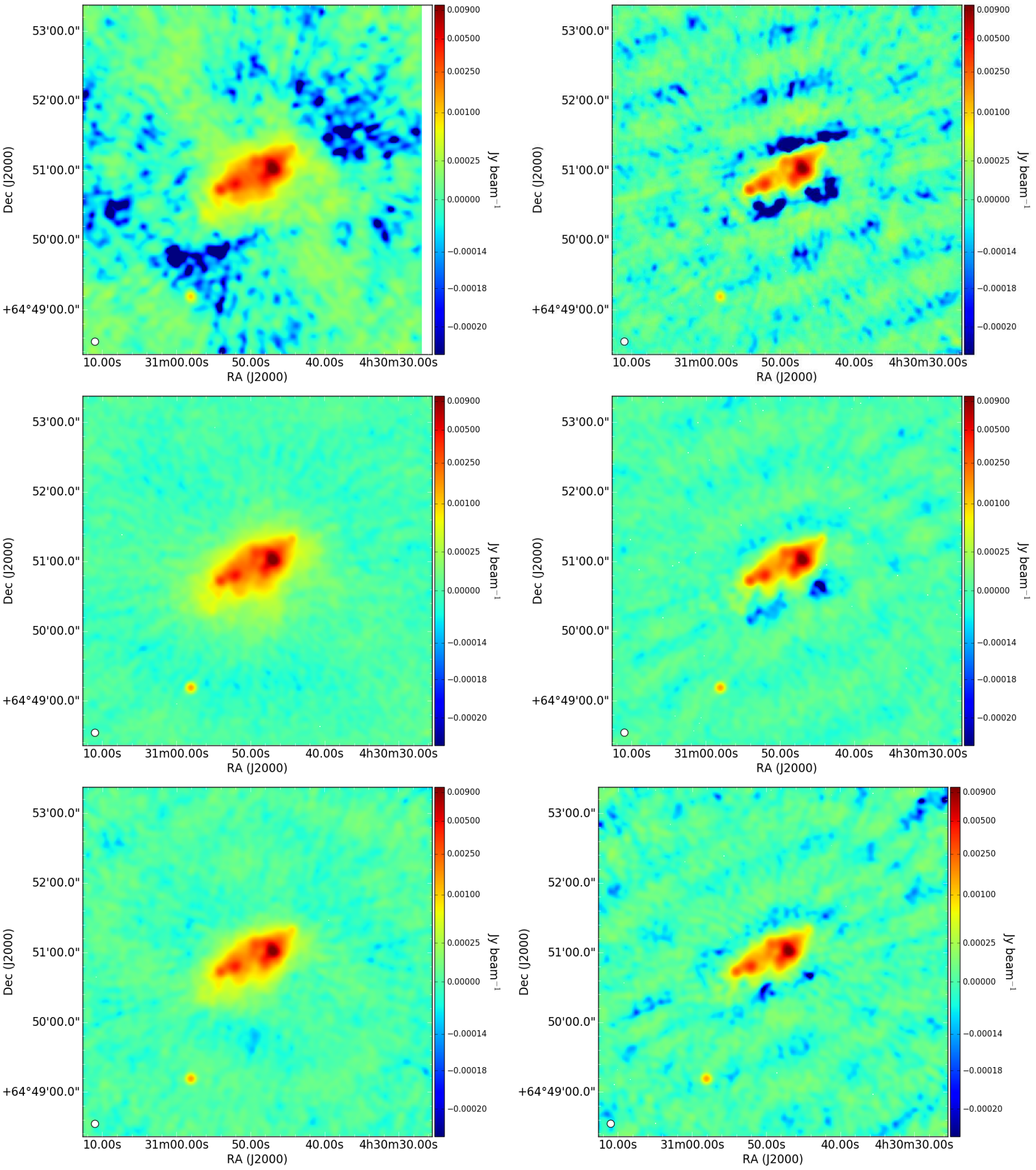

FIGURE 3.2 (cont.): The top maps show NGC 1569 at 3.5 GHz, the middle maps at 5.0 GHz and the bottom maps at 7.4 GHz.

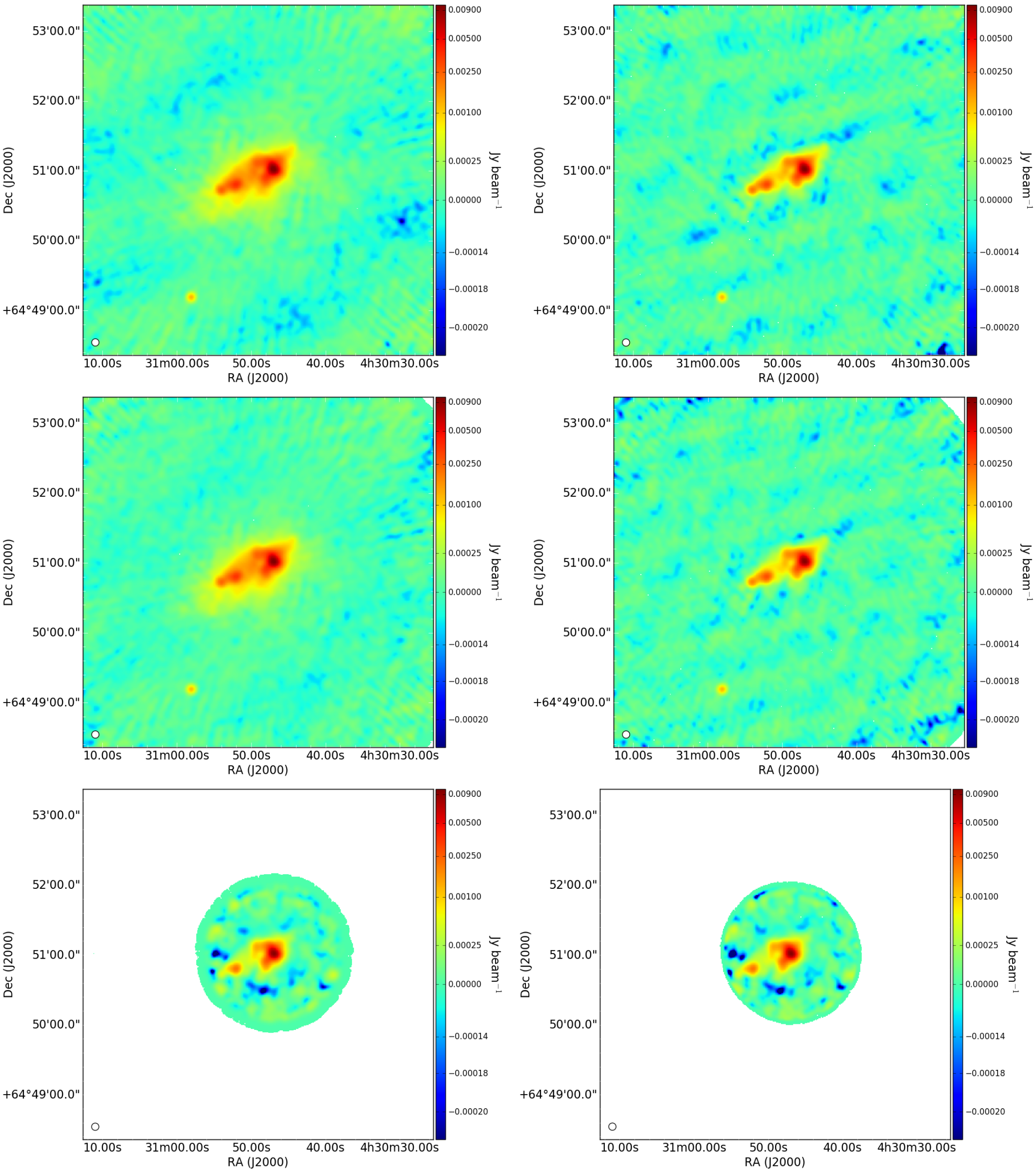

FIGURE 3.2 (cont.): The top maps show NGC 1569 at 8.5 GHz, the middle maps at 9.5 GHz and the bottom maps at 33.8 GHz. We have blanked emission where the primary beam falls to 20% of its peak value. This mainly affects the 33.8 GHz map, where the emission is confined to a circle.

a large fractional bandwidth (especially at lower frequencies where it reaches $\sim 40\%$ at 1.26 GHz). Furthermore, multi–scale multi–frequency clean reaches convergence quicker than more traditional cleaning algorthms, whilst robustly retaining the total flux. Comparison with other cleaning algorithms (e.g., Cornwell, 2008) reveals that residuals from multi–scale multi–frequency clean are less pronounced than other cleaning algorithms and that the deconvolution errors are small, which motivated its use in this work. Whilst imaging, we additionally apply a circular Gaussian taper whilst imaging to ensure that the final synthesized beams for all maps are as similar as possible. We present the taper parameters in Table 3.3. Whilst cleaning the 1.5 and 3.0 GHz data, we placed an outlier field on the bright background source, NVSS J042932+645627, to account for its contaminating sidelobes. There was no need to do this for any other background sources as they were sufficiently faint. This was only an issue in these wavebands as this source fell outside the primary beam in all higher frequency observations. Once we imaged all our data, we corrected the maps for primary beam attenuation using the CASA task PBCORR and then convolved all maps to a common resolution. The convolution was carried out using the CASA task IMSMOOTH with the TARGETRES parameter set to True. This uses the clean beam parameters from a given map to determine a convolving kernel that will result in a desired Gaussian point spread function (PSF). We convolved all maps to a circular Gaussian PSF with FWHM 6.3″ (corresponding to a linear resolution of 98 pc at 3.4 Mpc; Grocholski et al. 2008). Finally, we regridded all maps to the lowest resolution map. We present the final maps at each frequency in Figure 3.2 and the off source noise levels for each of the final maps is presented in Table 3.3.

3.3.2 Thermal Model Construction

In addition to the presented radio continuum maps, we use the Hα emission map from Hunter and Elmegreen (2004); Hunter et al. (2012) to obtain prior information for the thermal emission component. We apply the equations from Deeg et al. (1997) to convert from Hα flux to thermal radio continuum flux at 1 GHz. In the conversion, we assume an electron temperature of 10^4 K (Deeg et al., 1997). It should be noted that this value can vary significantly, as shown in studies of a large sample of galactic HII regions (Hindson et al., 2016). Furthermore, Nicholls et al. (2014) find that an electron temperature of 1.4×10^4 K is more appropriate in metal poor dwarf galaxies. As the derived thermal emission weakly depends upon electron temperature ($F_{TH} \propto T_e^{0.34}$), we do not expect that the assumed electron temperature will significantly affect our results. We also implicitly assume that the radio continuum emitting plasma is co–spatial with the Hα emitting medium, that the conditions for Case B recombination hold (i.e., all ionising photons are absorbed) and that the thermal radio continuum emitting plasma is in thermal equilibrium. Following Hunter and Elmegreen (2004), we assume a 20 % systematic uncertainty in the Hα flux scale, which we combine in quadrature with the uncertainty associated with the Hα isolation method (20 %, Vilella-Rojo et al., 2015), the uncertainty on the NII contribution (1 %) and the photometric uncertainty from the map itself. We do not apply any corrections for galactic foreground or internal extinction at this stage.

As the Hα emission originates from the recombination of electrons with protons that have been ionized by Lyman continuum emission originating from massive stars, it is effectively cospatial with the thermal radio continuum emission, which originates from the ionized plasma surrounding said massive stars. In other words, the Hα emission effectively has the same spatial distribution as the thermal radio continuum emission. We can therefore create a thermal model that is compatible with the interferometric observations by simulating the corrected Hα map as a radio image with the CASA task SIMOBSERVE. We 'clean' the simulated dataset with an identical method to that discussed in Section 3.3.1 and present the developed thermal model in Figure 3.3. This resulting model is sensitive to the same spatial scales as the interferometric observations; however, it still suffers greatly from the effects of extinction. We therefore use the measurements of the thermal emission from these maps as a lower limit in our fitting routine, which we describe in Section 3.4.

3.3.3 The Effects of Missing Flux

Care must be taken when analysing any data from interferometric observations as the resulting maps may suffer from problems due to the lack of short baselines in the interferometer array. These problems arise when there is considerable large scale emission that is resolved out by the interferometer, and manifests itself as a negative artefact centred on the source (commonly known as a 'clean bowl'). As radio sources typically have different structures in different frequency regimes (e.g., a halo surrounding

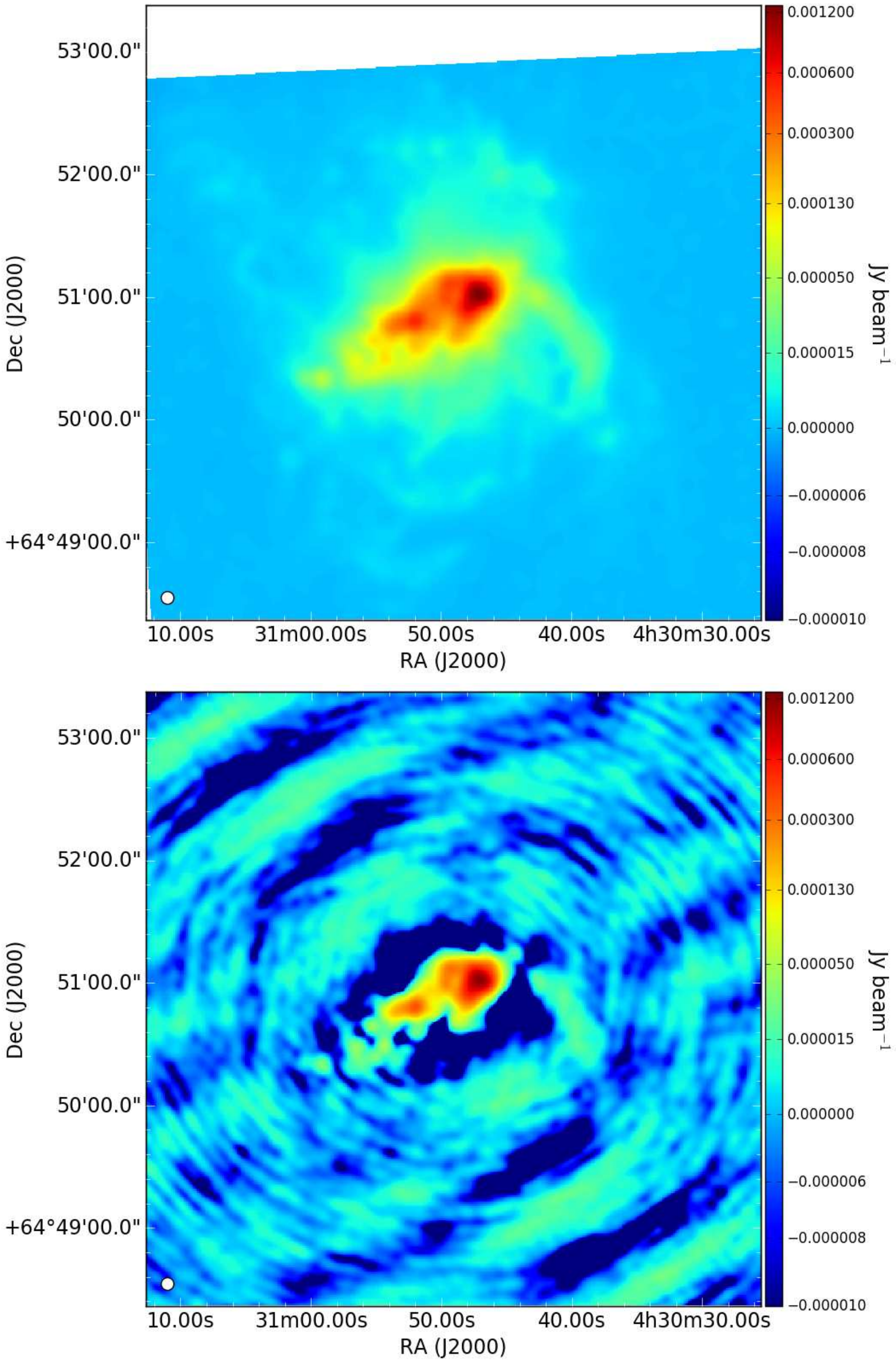

FIGURE 3.3: Models of NGC 1569's thermal emission. The top panel presents the thermal emission model derived by directly applying the equations in Deeg et al. (1997) to the Hα map from Hunter and Elmegreen (2004). The bottom panel presents our developed model for the thermal emission, as discussed in Section 3.3.2. Both maps have been convolved to a Gaussian PSF with FWHM 6.3″. Some key differences between these maps include that a large portion of the extended emission from the top panel is resolved out in the bottom panel and also the emergence of low–level artefacts from the interferometric imaging procedure.

a galaxy will appear much brighter and more extended in lower frequency observations than in higher frequency ones), it is unlikely that the magnitude and shape of the negative artefacts will be the same at all observed frequencies. Additionally, the interferometer has different responses at different frequencies (e.g., the sampling of the *uv*–plane will never be identical in any two radio observations at different frequencies), which could further influence measured spectral indices. The combination of these two effects could jeopardize any efforts to measure spectral indices on a resolved basis. As the presented observations of NGC 1569 suffer significantly from these effects (see Figure 3.2), it is necessary to explore how our measured spectral indices may be affected by the interferometric nature of the observations and our chosen imaging procedure.

To test how our measured spectral indices may be affected, we first constructed models of NGC 1569 at the frequencies presented in Table 3.3. The models consist of 3 distinct components, a large scale halo with a steep spectral index ($\alpha = -0.7$), a more compact main disk component with a flatter spectral index ($\alpha = -0.3$) and a set of high resolution emission components consisting of a collection of unresolved SNRs ($\alpha = -0.5$; Green 2014) and HII regions ($\alpha = -0.1$; Condon 1992). We model NGC 1569's large scale halo by deconvolving the 1.5 GHz WSRT map from Kepley et al. (2010) and isolating the large scale emission components using the CASA task DECONVOLVE. To model the main disk component, we image our 1.5 GHz observations with the entire available *u*v–range (1-50 kλ) and use the clean components that do not correspond to unresolved sources as our disk model. Finally, we take the unresolved sources removed whilst creating the model of the main disk and assign them as either SNR or HII regions as identified in the literature (Chomiuk and Wilcots, 2009; Waller, 1991). The final maps are constructed by scaling and summing these model components at the frequencies in Table 3.3. We show the 1.25 GHz model in Figure 3.4. Although these single component spectral index models are a simplification of reality, analysing them should identify regions where our spectral index analysis may break down.

We then simulate observations of our model galaxy with the CASA task SIMOBSERVE, using the observing parameters presented in Table 3.2. We imaged the simulated datasets with the same imaging parameters as detailed in Section 3.3.1 to produce maps that are comparable to those observed. To measure the resolved spectral indices, we assemble the imaged maps into a datacube. For each pixel in the datacube, we fit a power law via a least–squares method to measure the resolved spectral index. For comparison purposes, we carry out the same fitting routine for the un–simulated models, which we convolve and regrid to the same resolution.

Figure 3.4 shows how the recovered spectral indices differ from the input model on a pixel–by–pixel basis. We can see that the spectral index for the bright unresolved sources within NGC 1569 are unchanged and that the spectral index for resolved sections tends to be slightly flatter than the model. The flattening is most pronounced towards the edges of the mask, as this is where the fainter emission begins to compete with the surrounding negative 'clean bowl'. On the other hand, the North–West corner of NGC 1569 appears to be slightly steepened, which is likely an artefact from the 'spur' towards the west of the galaxy. The largest deviation is a flattening of $\Delta\alpha \approx 0.1$, however this only is the case for a couple of pixels. In general it is much smaller with the average deviation being a flattening of order $\Delta\alpha \approx 0.03$. As we carry our fitting procedure on a beam–by–beam basis (see Section 3.4), we are averaging over the few 'extreme' pixels towards the edge of the mask, which will mitigate their effect on the recovered spectral index.

The flattening tendency can be understood as follows: Although we are resolving out the significant large scale emission from NGC 1569, it is distributed over a large area. On a beam–by–beam basis, this large–scale component contributes little to the detected bright emission from the main disk. As the large–scale halo emission has a steep spectral index, the contribution from the halo would be larger in lower frequency observations than in higher frequencies. When the large–scale emission is resolved out, it corresponds to a larger subtraction of emission in the maps at lower frequencies, resulting in flattening. As the flattening is small across NGC 1569's main disk, it is bright enough such that the missing flux from short spacings does not affect our recovered main disk spectral indices significantly.

Although in general the difference in spectral index is small, it should be noted that there is considerably more scatter around the assumed model power–law in the data–points sampling the 1-10 GHz range. This scatter is due to the interferometer having different responses at different frequencies, primarily due to the different ways the *uv*–plane is sampled at each observed frequency.

This exercise indicates that the systematic errors introduced by missing flux from short baselines and our chosen imaging scheme are small ($\sigma_\alpha \sim 0.03$) when compared with

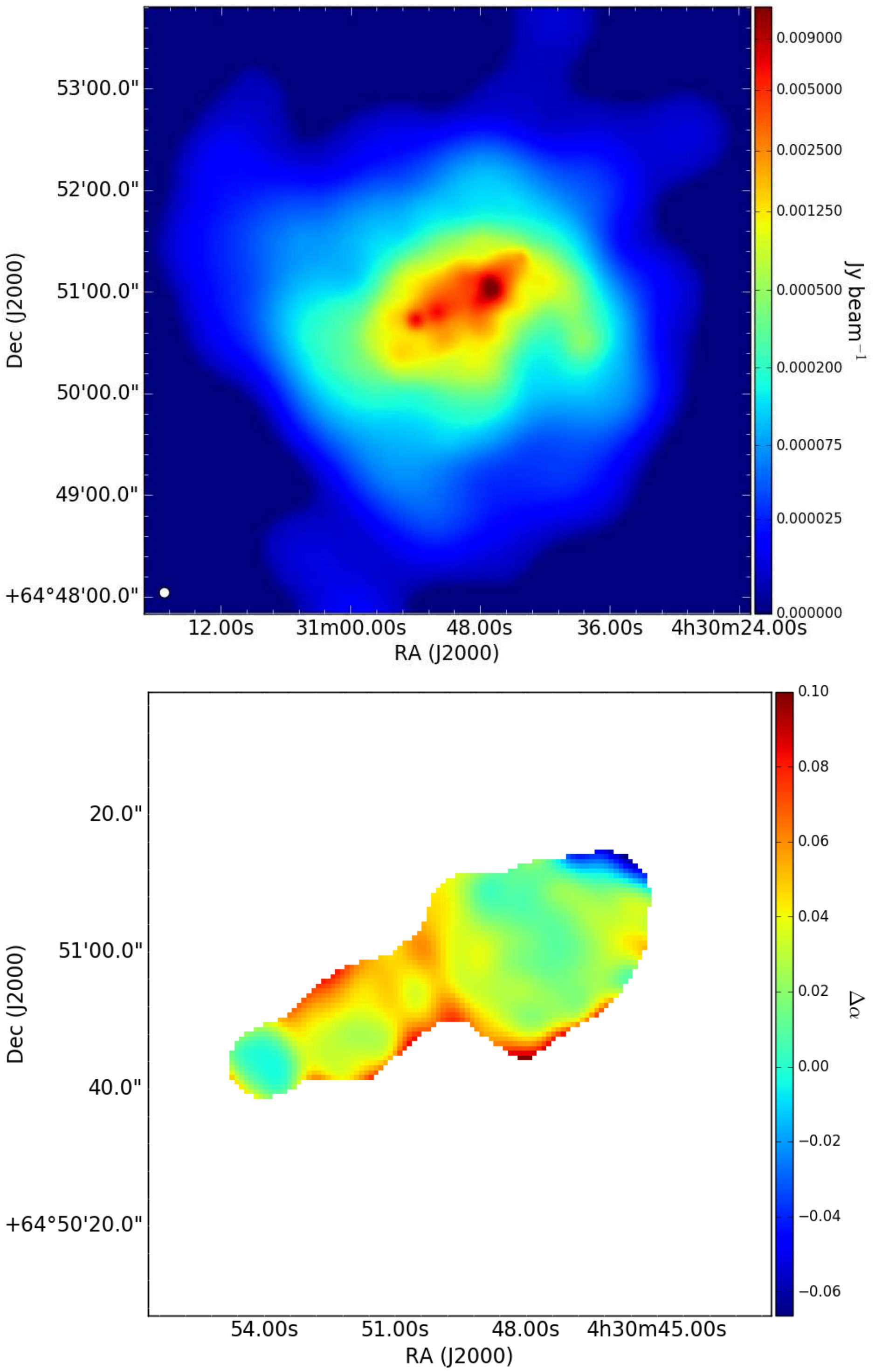

FIGURE 3.4: The top panel shows the 1.25 GHz model of the radio emission, convolved to a Gaussian with 6.3″ FWHM. This model consists of a large scale halo component, a more compact main disk component and some unresolved components within the main disk. The bottom panel shows the residuals after subtracting the total spectral indices recovered from our simulated images from the assumed model. Positive deviations indicate that the total spectral index is flattened whereas negative deviations indicate that the total spectral index is steepening.

the uncertainties from our fitting procedure (see Figure 3.6). As we have a broad enough frequency coverage and the parts of NGC 1569 we are spatially sensitive to are bright enough, we can reliably carry out a resolved spectral index analysis on our presented high–resolution VLA observations.

3.4 Bayesian Model Fitting Methodology

In this section, we discuss the rationale for adopting a Bayesian methodology to separate the various radio emission components from the observed SED, the model that we have chosen to fit, and our general fitting procedure.

3.4.1 What Is Bayes' Theorem?

Bayes' theorem is a simple statement about conditional probability that has a staggeringly broad set of applications, from analysing the results of clinical trials to email spam filters. Recently, Bayesian methods have become more widely used in the astronomy and physics fields (Loredo, 2013), primarily due to advances in computing resources and improved sampling algorithms.

Bayes' theorem can be easily derived from basic set theory as follows: Consider a plane with area Ω where each point on the plane corresponds to each possible outcome of an event. Now consider two overlapping regions of this plane, which correspond to desired outcomes A and B (see Figure 3.5). In this formulation, the probability that a desired outcome occurs is simply the area of outcome space taken up by the desired outcome divided by the total area of all outcomes (i.e. $P(A) = \frac{A}{\Omega}$). The conditional probability that outcome A occurs given that outcome B has occurred is:

$$P(A|B) = \frac{A \cap B}{B} = \frac{P(A,B)}{P(B)}, \tag{3.1}$$

where $A \cap B$ is the intersection of sets A and B (i.e. the set that is contained in both sets A and B) and $P(A,B)$ is the joint probability that events A and B occur. Similarly, the probability that outcome B occurs given that event A has occurred is:

$$P(B|A) = \frac{B \cap A}{A} = \frac{P(B,A)}{P(A)}. \tag{3.2}$$

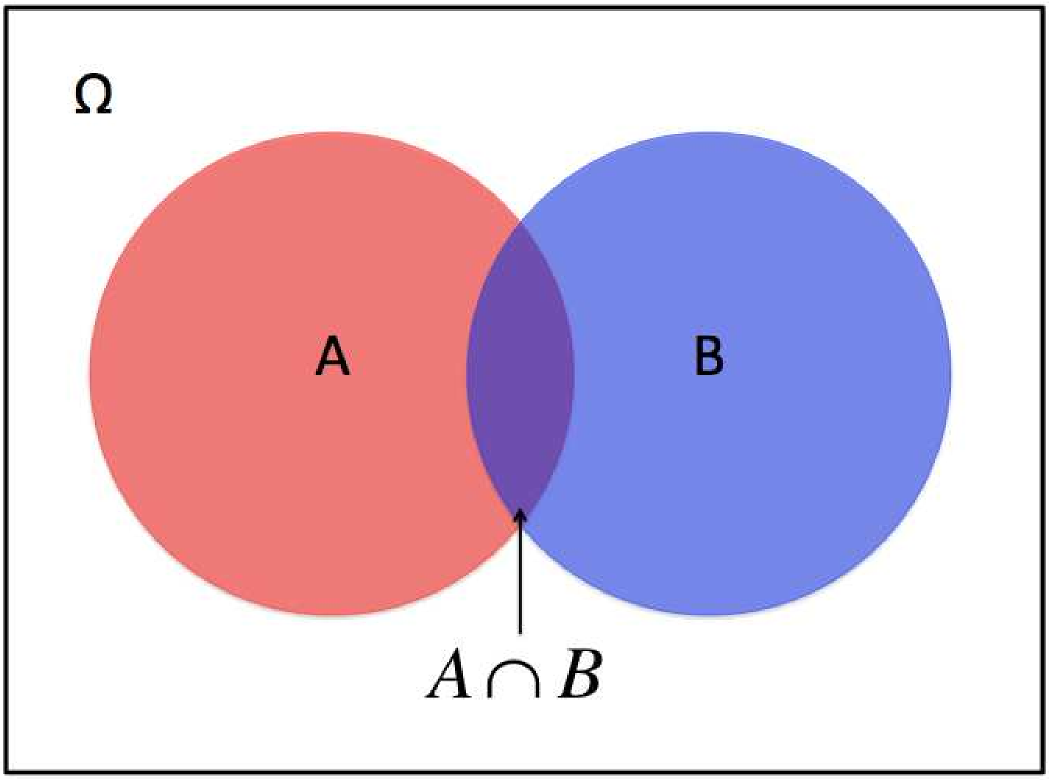

FIGURE 3.5: Schematic diagram for aiding in the derivation of Bayes' theorem.

Noting that $P(A,B) = P(B,A)$, we combine Equations 3.1 and 3.2 to arrive at Bayes' theorem:

$$P(A|B) = \frac{P(B|A)P(A)}{P(B)}. \tag{3.3}$$

3.4.2 Model Fitting With Bayes' Theorem

We apply Bayes' theorem to the problem of fitting a model, M, with tuneable model parameters, θ, to a set of observed datapoints, D. In this case, the probability that a particular set of model parameters are true, given the observed data and assumed model is:

$$P(\theta|D,M) = \frac{P(D|\theta,M)P(\theta|M)}{P(D|M)}. \tag{3.4}$$

In Equation 3.4 each of the terms have particular names and interpretations. $P(D|\theta,M)$ is known as the likelihood and is interpreted as the probability of observing D, assuming that the model M with parameters θ are correct. $P(\theta|M)$ is known as the prior and represents everything that we know a priori about the model parameters, θ, within the confines of the assumed model. $P(D|M)$ is known as the evidence and corresponds to the probability of observing the data, D, given the assumed model is true. Finally $P(\theta|D,M)$ is called the posterior and represents the new knowledge about the fitted parameters after taking into account the observed data.

There are several methods that can be employed to compute the posterior distribution. The simplest and most computationally expensive method is to solve Equation 3.4 for each possible combination of fitted parameters over the entirety of parameter space. This approach can only be applied in simple cases, where parameter space is finite and discretised with only a few dimensions. For the case where parameter space is continuous, it is computationally impossible to fully compute the posterior via the brute force method. Instead it must be approximated through the use of a sampling algorithm.

A popular choice of sampling algorithm is the Metropolis–Hastings algorithm (Hastings, W.K., 1970), which is one of a family of Markov–Chain Monte–Carlo (MCMC) sampling methods. In this algorithm, a series of 'walkers' are initially distributed throughout parameter space and allowed to take a step in a random direction. The size and direction of the step are determined by drawing a sample from a proposal function (of which there are many options in the literature, each with their own advantages and disadvantages). The posterior is then calculated at this new location and compared to the posterior at the walker's current location to compute an acceptance ratio, $a = \frac{P_{\rm new}}{P_{\rm old}}$. A random number is then drawn from a uniform distribution between 0 and 1 and compared to the acceptance ratio. If the drawn number is less than or equal to the acceptance ratio, the walker steps to the new postion, otherwise the walker will remain at its current location. If the walkers are left to walk around parameter space for a large number of steps, they will proportionally record steps in regions with high posterior probability compared to regions of low posterior probability. Hence the recorded samples can be used to approximate the sought posterior probability distribution.

Finally, once the posterior has been computed, it is useful to extract constraints for each of the individual parameters of interest. This can be accomplished by marginalising the posterior over all other fitted (so called nuisance) parameters. For example, if 3 parameters are fitted $(\theta_1, \theta_2, \theta_3)$, we can retrieve the marginalised posterior distribution for θ_1 through:

$$P(\theta_1|D,M) = \int_{\theta_2=-\infty}^{\infty} \int_{\theta_3=-\infty}^{\infty} P(\theta_1, \theta_2, \theta_3|D,M)\, d\theta_3\, d\theta_2. \tag{3.5}$$

This process of marginalisation is equivalent to projecting the full posterior distribution onto the dimensions corresponding to the parameters of interest (in the above case θ_1). This integration is carried out for free by the MCMC sampling algorithm, as parameter constraints can be easily recovered by simply analysing the samples recorded along the dimension corresponding to the parameter of interest.

3.4.3 A Method For Separating The Radio Emission Components From An Observed SED

Equation 3.4 illustrates two key advantages of using a Bayesian MCMC fitting procedure over more classical model fitting methods. By adopting an MCMC approach, a large range of parameter space can be efficiently probed, leading to a statistically robust approximation to the posterior probability distribution, from which, probability distributions for each of the parameters of interest can be easily retrieved, by marginalising over all other model parameters. Secondly, prior information, based upon other observations, can be easily included to further constrain fitted parameters.

Both of these benefits should be taken advantage of when attempting to decompose a given radio continuum SED into its various radio emission components. As this type of problem is typically degenerate (Niklas and Beck, 1997; Callingham et al., 2015; Tabatabaei et al., 2017), classical χ^2 fitting methods may underestimate the true uncertainties associated with the parameter constraints following the separation (Condon, 1992). The marginalised posteriors from the Bayesian approach in this case may better reflect the uncertainties associated with the separation process. Furthermore, the addition of prior knowledge from other data (e.g., optical spectral line observations) can also help to reduce the degeneracies between the fitted parameters, resulting in better constraints. The main disadvantage of using a MCMC approach is the required computational resources, but this no longer is a significant hurdle with current technological developments.

Model Definition

As discussed earlier, it is understood that a typical radio continuum spectrum from a purely star forming galaxy is made up of two main components: a thermal component, originating from ionized plasma surrounding massive stars (HII regions), and a non–thermal component, originating from CRe that have been accelerated in SNR shock fronts (see Condon 1992 for a review). As shown by Hindson et al. (2016), HII regions can be assumed to be optically thin at frequencies above 1 GHz. If we further assume that the non–thermal component can be parameterised by a simple power–law, an expression for the observed radio continuum spectrum can be written as:

$$S_\nu = S_T \nu^{-0.1} + S_{NT} \nu^{\alpha}, \tag{3.6}$$

where S_ν is the measured flux density at frequency ν, S_T is the thermal flux density normalisation, S_{NT} is the non–thermal flux density normalisation (both in Jy), ν is frequency and α is the non–thermal spectral index.

Although this model is simple, it effectively describes the observed radio continuum emission at mid–radio continuum frequencies for a large number of galaxies (1–10 GHz; Condon 1992; Tabatabaei et al. 2017); however, there are several additions that could be made to improve the model. For example, if additional lower frequency observations are made, we could include the effects of free–free or synchrotron self absorption (Tingay and de Kool, 2003; Callingham et al., 2015; Hindson et al., 2016; Kapińska et al., 2017), or if additional observations at higher frequencies are made, a break in the non–thermal spectrum due to spectral ageing and Inverse Compton scattering could also be included (Lisenfeld et al., 2004; Harwood et al., 2013; Heesen et al., 2015). Furthermore, a component due to Anomalous Microwave Emission (AME; Dickinson et al. 2018) could also be included if the observations densely sample the 10-60 GHz frequency range. AME has been shown to be a significant contributor to the observed Milky Way emission at ~ 30GHz ($> 50\%$ e.g., Alves et al., 2010), yet has not been conclusively detected in any extra–galactic sources other than a star–forming region in NGC 6946 (Scaife et al., 2010; Murphy et al., 2011) and a detection in the Magellanic clouds (Bot et al., 2010). Limits on the AME contibution for a small sample of larger dusty galaxies have been made by Peel et al. (2011), who find that the AME contribution in these systems is much smaller than that observed in the Milky Way ($< 25\%$ at

30 GHz). In this current study, we cannot model this contribution effectively as there is only one data point at 33.8 GHz, so we neglect its contribution. If there is significant AME contamination at 33.8 GHz, this will affect the fitted parameters by overestimating the recovered thermal component and underestimating the recovered non–thermal component. Furthermore, the recovered spectral indices will be steeper than their true (i.e., intrinsic) values. Further radio continuum observations between 10 and 50 GHz and complementary observations probing the thermal emission originating from dust could be used in the future to constrain the AME contribution to NGC 1569.

Following Tabatabaei et al. (2017), Equation 3.6 can be parameterised to avoid dependencies of the chosen units on frequency space as:

$$S_\nu = A\left(\frac{\nu}{\nu_o}\right)^{-0.1} + B\left(\frac{\nu}{\nu_o}\right)^{\alpha}, \tag{3.7}$$

where $A = S_T\,\nu_o^{-0.1}$, $B = S_{NT}\,\nu_o^{\alpha}$ and ν_o is a reference frequency (which is assumed to be 1 GHz). This is the model that we choose to fit to our observed data in our model fitting routine.

Model Fitting Routine

Before we carry out our model fitting routine, we first mask the maps so that we only consider emission that has a significance greater than 5 σ in all observed maps. We then regrid these masked maps onto hexagonal pixels, where each hexagonal pixel has an area that is the same as the synthesised beam. We carry out this procedure because it reduces computational time and also ensures that each hexagonal pixel is more or less independent from each other hexagonal pixel. We determine the uncertainty on the recovered flux density for each hexagon by adding in quadrature a contribution from the off source noise (presented in Table 3.3) with an assumed 5% fluxscale uncertainty (Perley and Butler, 2017). It should be noted that the on–source noise will be larger than the off–source noise due to uncertainties introduced whilst modelling the source during imaging. Harwood et al. (2013) estimate that the off source noise should be multiplied by a factor of ~ 3 to account for this effect. For the presented observations of NGC 1569, this effect should be negligible for hexagons that are significantly above the 5 σ threshold as the 5 % fluxscale uncertainty will dominate the uncertainty, but for hexagons closer to the edges of the mask, this effect may be more significant. Ultimately these larger uncertainties will result in poorer constraints for the fainter hexagons, which are likely also susceptible to missing flux effects (see Section 3.3.3.) Caution should be taken when interpreting the results from these hexagons. We finally construct a data–cube out of the hexagonalised maps with Right ascension on one axis, Declination on the second, and frequency on the third axis.

For each hexagonal pixel in the RA–Dec plane, we slice through the datacube to get a series of flux densities as a function of frequency, to which we fit the model detailed in Section 3.7. Assuming that each map is independent, that the flux density uncertainties for each data point are normally distributed and that the uncertainty in the frequency that each map is taken at is negligible, we use a standard χ^2 objective function to determine the likelihood for a set of measured flux densities given a set of model parameters (Hogg et al., 2010). This probability can be written as follows:

$$P(D|\theta, M) = \prod_i \frac{1}{\sqrt{2\pi\sigma_i^2}} \exp\left[\frac{-(D_i - S_i(\theta))^2}{2\sigma_i^2}\right], \tag{3.8}$$

where D_i is the observed flux density for the i'th data point for a given pixel, σ_i is the measured uncertainty for that data point and $S_i(\theta)$ is the model flux density at the frequency of the i'th datapoint. θ corresponds to our given parameters, which are A, B and α from Equation 3.6. Equation 3.8 makes up the first half of the right hand numerator in Equation 3.4.

Next we turn our attention to the assumed priors, $P(\theta|M)$. As with any Bayesian analysis, one needs to be very careful about how priors are defined for the parameters that are to be fitted (Gelman, 2008). As this step is somewhat subjective, we will describe the functional form for each of the assumed prior probability distributions for each parameter, and the motivation for these choices in turn.

For the thermal normalisation constant, A, we define an informative prior that depends upon the thermal emission measured from the Hα thermal model (see Section 3.3.2; Figure 3.3). As the Hα emission is vulnerable to extinction effects, we assume that the thermal emission measured from these maps is a lower limit for the true thermal emission. We translate this to a uniform prior with a Gaussian taper towards the lower limit:

$$G(A,\mu,\sigma_{H\alpha},A_{\max}) = \left(\sqrt{\frac{\pi}{2}}\sigma_{H\alpha} + [A_{\max}-\mu]\right)^{-1} \begin{cases} \exp\left(\frac{-(A-\mu)^2}{2\sigma_{H\alpha}^2}\right), & \text{if } A \leq \mu \\ 1, & \text{if } \mu < A \leq A_{\max} \\ 0, & \text{otherwise} \end{cases}, \tag{3.9}$$

where μ is the thermal emission measured from the thermal model, $\sigma_{H\alpha}$ is the uncertainty on this measurement and $A_{\max}$ is the upper–limit to the probability density function, which is primarily included for normalisation purposes (and is assumed to be an order of magnitude larger than the largest flux density data–point used while fitting). This prior is different to a uniform prior that is usually assumed in the literature (e.g. Tabatabaei et al. 2017) as it not only restricts values of A to positive values, which is physically motivated, but also reduces tails in the posterior probability distribution that stretch to very small A. This improves the constraints on the thermal normalisation constant (see Figure 3.6).

For the non–thermal normalization constant, B, we adopt a uniform prior that is constrained to be always larger than 0:

$$H(B,B_{\max}) = \frac{1}{B_{\max}} \begin{cases} 1, & \text{if } 0 \leq B < B_{\max} \\ 0, & \text{otherwise} \end{cases}, \tag{3.10}$$

where $B_{\max}$ is the upper–limit to the probability density function which is primarily assumed for normalisation purposes (which again we assume to the an order of magnitude larger than the largest flux density data–point used while fitting.) This prior is physically motivated as there is no process that can produce a completely absorbed non–thermal spectrum in a dwarf galaxy in the frequency range we are studying. This prior also removes degeneracies where a large thermal normalisation can be coupled with a negative non–thermal normalisation to reproduce the observed spectral energy distribution.

For the non–thermal spectral index α, we note that the non–thermal spectral index for the main disks of star–forming galaxies is typically found to be $\alpha \sim -0.8$ (Condon and Yin, 1990) and that the non–thermal spectral index usually varies between ~ -0.5 to ~ -1.2 due to the injection and transport of CRe within the galaxy disks (Berkhuijsen, 1986; Longair, 2011; Tabatabaei et al., 2017). We define a prior on the non–thermal spectral index that consists of a broad normal distribution, centred on $\mu_\alpha = -0.8$ with a standard deviation $\sigma_\alpha = 0.4$:

$$I(\alpha, \mu_\alpha, \sigma_\alpha) = \frac{1}{\sqrt{2\pi\sigma_\alpha^2}} \exp\left[\frac{-(\alpha - \mu_\alpha)^2}{2\sigma_\alpha^2}\right]. \tag{3.11}$$

For a given set of model parameters, the prior probability is the multiplication of each prior distribution:

$$P(\theta|M) = G(A, \mu, \sigma_{H\alpha}, A_{\max})\, H(B, B_{\max})\, I(\alpha, \mu_\alpha, \sigma_\alpha). \tag{3.12}$$

This equation makes up the second half of the right hand numerator in Equation 3.4. Although both the likelihood and the prior are themselves normalised, the posterior is not normalised as we have not taken into account the Bayesian evidence $P(D|M)$ (which can be extremely difficult to compute). However, as we only really care about the relative probabilities whilst computing the posterior for model fitting (and parameter estimation) purposes, we can neglect it for the rest of this study (as we are only considering a single model).

We use the Python package, EMCEE (Foreman-Mackey et al., 2013), to sample the posterior probability distribution. EMCEE makes use of the affine-invariant ensemble sampler for MCMC presented in Goodman and Weare (2010). This sampler follows the standard Metropolis–Hastings algorithm, but with a proposal function that scales itself at each step depending upon the locations of a sub–sample of the placed walkers. For each hexagonal aperture, we set up 100 walkers and allowed them each to take 1000 steps in parameter space. The initial walker positions were randomly selected from uniform probability distributions. These distributions covered the range between 0 and 10 times the flux of the lowest frequency data point that is being fit for both A and B, and between 0 and -2.2 in α. We find this was warranted as the lowest frequency data point is normally the brightest and it is very unlikely that the recovered normalizations will be significantly larger than its value. We find that the walkers tended to converge after ~ 100 steps so we conservatively 'burn in' after 200 steps, yielding 80,000 samples of the sought posterior probability distributions. In the presented results, we quote the 50th percentile of the samples as the best fit, and the 16th and 84th percentiles as the

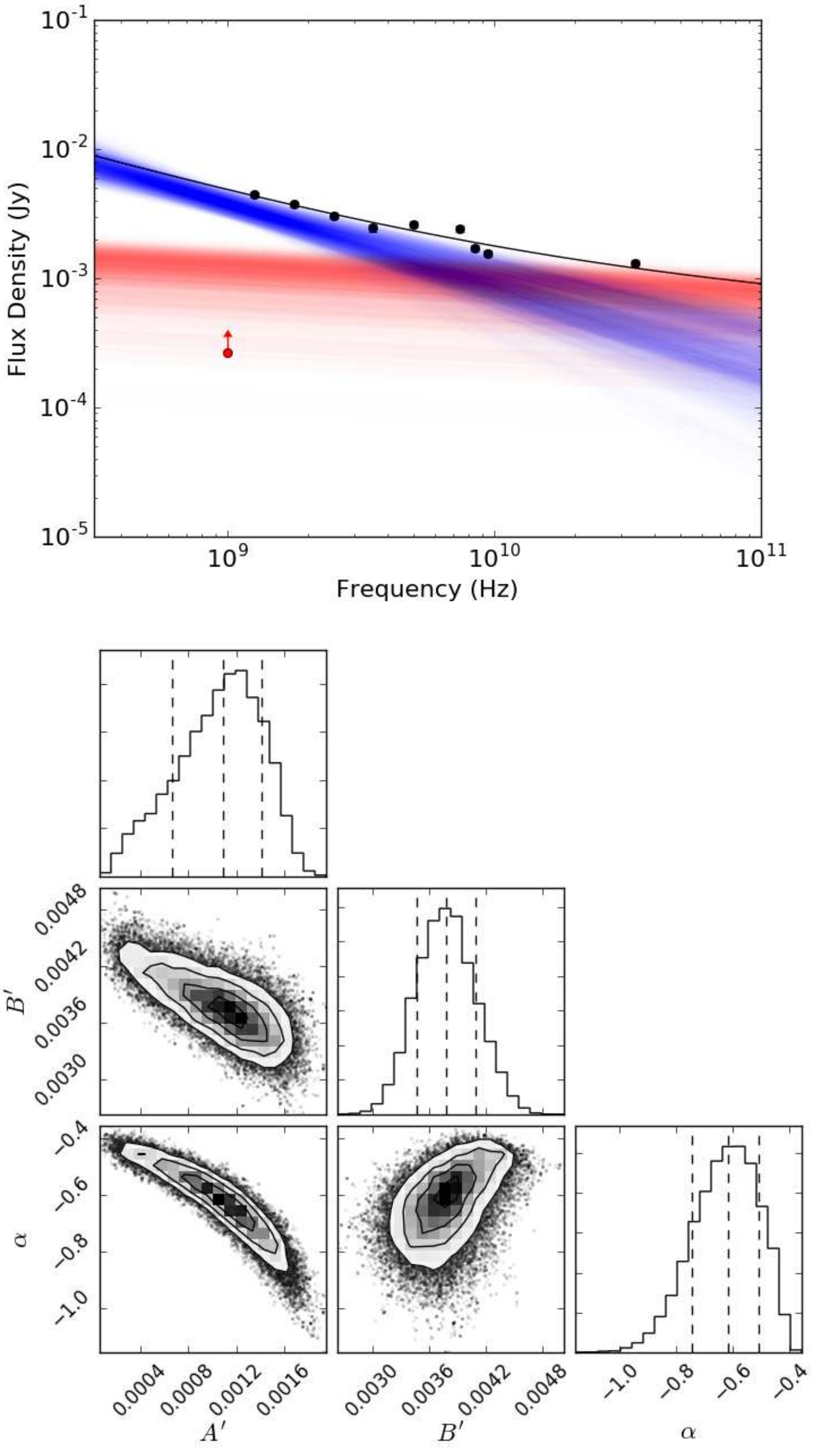

FIGURE 3.6: An example fit from the discussed fitting procedure. The top figure presents an example SED for a hexagonal pixel. The black data points show the measurements from the data–cube; the red point is the lower limit as measured from the thermal model, and the black line represents the best fit to the data. The uncertainties on the flux density measurements are comparable to the size to the black datapoints. We additionally plot 250 models, drawn randomly from the posterior probability distributions, where the red lines represent the thermal component and the blue lines represent the non–thermal component. The bottom figure shows the corner plot associated with this fit, where the dotted lines correspond to the 16th, 50th and 84th quartiles. For reference, in this fit $A = 1.09^{+0.32}_{-0.42}$mJy, $B = 3.78^{+0.32}_{-0.31}$mJy and $\alpha = -0.62^{+0.11}_{-0.13}$.

$1\,\sigma$ deviations. An example fit and corresponding corner plot are presented in Figure 3.6.

The assumed priors on the non–thermal normalisation and the non–thermal spectral index are generally much broader than the recovered constraints, showing that the recovered constraints are primarily being driven by the observed data. In general, the prior on the thermal normalisation does however have a small impact on the thermal constraint by suppressing the tail in the distribution towards low thermal normalisations. From the bottom panel of Figure 3.6, it is clear that the constraints on the recovered parameters are generally correlated, which indicates that the thermal prior may have a small knock–on impact on the recovered non–thermal constraints. This manifests by constraining the upper tail of the non–thermal normalisation posterior and an upper tail on the non–thermal spectral index posterior. In all cases however, the constraints from the thermal prior only affect the tails of the posterior distributions, and do not affect the recovered parameter constraints significantly. We test how our assumed priors influence our fits by re–running our fitting procedure, but not including any datapoints. The thermal and non–thermal normalisations are unconstrained over the region of parameter space we are limiting our analysis too and the spectral index is only constrained to the broad normal distribution we assumed as our prior. This confirms that the observed data–points are driving the observed fits, and that the assumed priors are only aiding in constraining the parameters of interest.

3.5 Results

In this section we present the results of the fitting procedure discussed in Section 3.4. In Figure 3.7, we present maps of how the recovered thermal normalisation A, non–thermal normalisation B and the spectral index α vary across NGC 1569's main disk.

3.5.1 Integrated Properties

We obtain NGC 1569's integrated properties by summing the flux density over each of the hexagonal pixels presented in Figure 3.7. It should be noted that these integrated flux measurements should strictly be treated as lower limits. Due to the interferometric

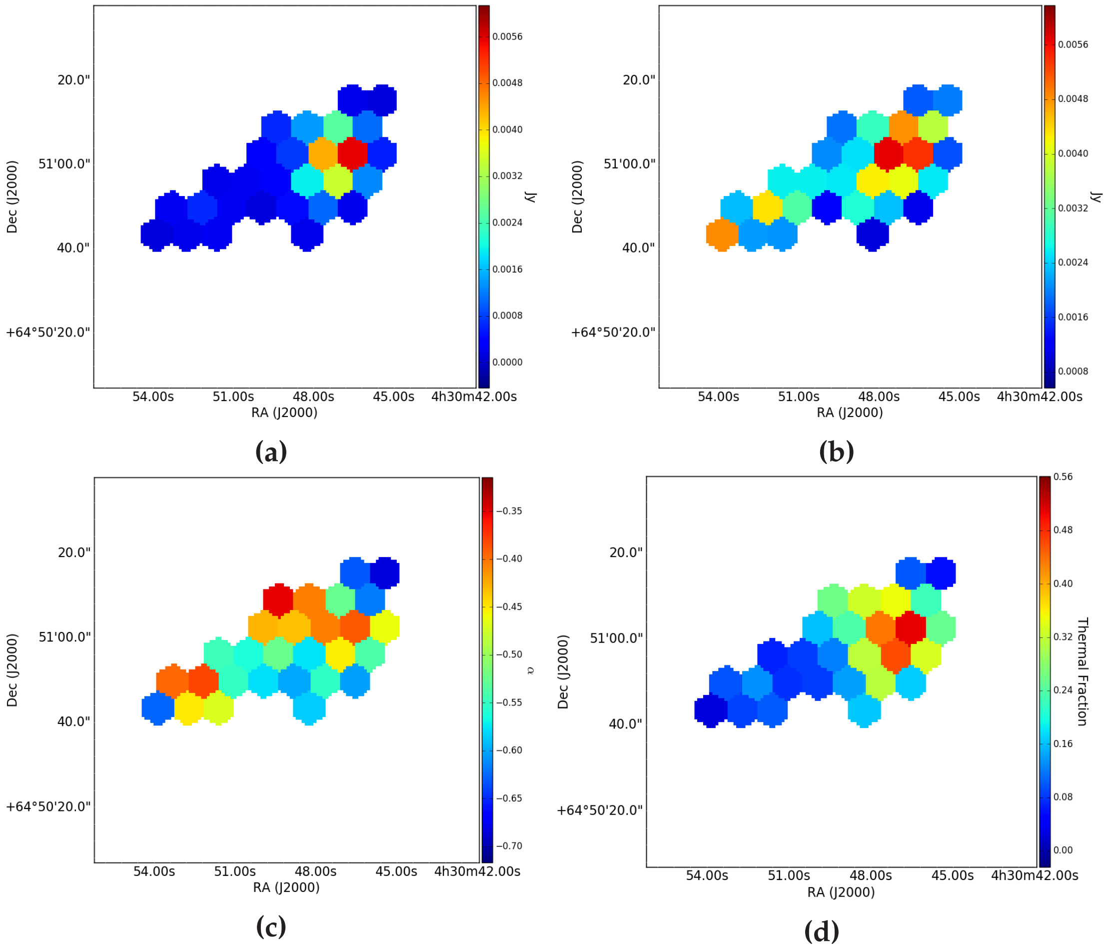

(a) **(b)**

(c) **(d)**

FIGURE 3.7: Maps of the best fitting model parameters from the fitting procedure discussed in Section 3.4. Each hexagonal pixel has an area that is the same as the synthesized beam. Figure 3.7**a** presents the recovered thermal contribution in units of Jy, Figure 3.7**b** presents the recovered non–thermal contribution in units of Jy, Figure 3.7**c** presents the recovered non–thermal spectral indices and Figure 3.7**d** presents a map of how the thermal fraction varies across the disk.

nature of the observations, we are resolving out a large proportion of the emission associated with NGC 1569 on scales larger than $\approx 30''$ (see Section 3.3.3). However, we do recover the majority of the flux from the bright regions within NGC 1569's main disk. This is illustrated if we compare our maps of the main disk (see Figure 3.2) with Westerbork observations from Kepley et al. (2010), which are sensitive to emission on larger scales. Integrating over the bright regions that we are sensitive to, we recover $\approx$ 75 % of the emission at 1.5 GHz, $\approx$ 70 % of the emission at 3 GHz, $\approx$ 75 % of the emission at 5 GHz and $\approx$ 70 % of the emission at 8.5 GHz (see Table 3.4 for a summary).

Integrated Thermal Emission

As we are typically resolving out 25–30 % of the radio emission from NGC 1569's main

Frequency (GHz)	VLA Main disk (mJy)	WSRT Main disk (mJy)	WSRT Total (mJy)
1.26	122 ± 6	159 ± 8	385 ± 20
2.50	91 ± 5	124 ± 6	269 ± 14
5.00	80 ± 4	104 ± 5	187 ± 9
8.50	50 ± 3	70 ± 4	130 ± 7

TABLE 3.4: Comparison of integrated flux density measurements from this study (VLA) and the maps from Kepley et al. (2010) (WSRT). Main disk indicates the integrated flux density over a mask which considers emission brighter than $5\,\sigma$ in the VLA maps (see Figure 3.2), and Total indicates the flux density measured over the entire galaxy (including the halo). All WSRT measurements were scaled to our observed frequencies assuming a total spectral index $\alpha = -0.4$, and uncertainties were calculated assuming a 5% uncertainty in the flux scale.

disk, it is useful to compare the integrated results from our Bayesian fitting procedure with the literature, after attempting to correct for the missing flux component. If we consider the thermal emission at 1 GHz (see Figure 3.7**a**), our Bayesian fitting procedure recovers an integrated flux density of $28.1^{+2.8}_{-3.1}$ mJy. This is significantly larger than the 8.98 ± 2.7 mJy we find by integrating the thermal model based on Hα emission over the same area (see Figure 3.3). This difference indicates that there is significant extinction along the line of sight to NGC 1569, and is discussed further in Section 3.6.1.

It is difficult to correct the observed total thermal flux density for missing flux, as we do not know the relative contributions of the thermal and non–thermal emission for the missing component. If we assume that the overall thermal fraction within NGC 1569's main disk does not change significantly (see below), this measured value is corrected up to ~ 40 mJy, which we shall use for comparison with the literature. To first order, we use the Hα map from Hunter and Elmegreen (2004), combined with the Spitzer 24μm from Bendo et al. (2012) (applying the corrections from Kennicutt et al. 2009) to obtain an independent estimate of the total thermal emission over NGC 1569's main disk. Assuming a galactic foreground reddening, $E(B-V) = 0.56$ mag (Israel, 1988), and applying the equations from Deeg et al. (1997), we determine that there is ≈ 56 mJy thermal radio emission originating from the bright main disk, although this number is sensitive to the assumed reddening from the galactic foreground. Not only is this reasonably close to our corrected thermal emission, it is also in good agreement with the ~ 55 mJy that is found by extrapolating the 8 GHz observations of compact HII regions by Israel (1980), but it is significantly smaller than the ≈ 80 mJy at 1 GHz found from resolved fits to the radio SED by Lisenfeld et al. (2004). This discrepancy could be due to the form of the non–thermal emission model they fit, which includes a break towards higher frequencies, and could recover more thermal emission than the simple power–law model we consider in this study. This exercise shows that our fitting procedure is returning plausible values for the thermal component, indicating that our separation procedure was successful.

We obtain an estimate for the upper limit on the total thermal emission from the main disk by assuming that all of the resolved out emission is of thermal origin. This results in a total main disk thermal emission of ~ 90 mJy at 1 GHz. Although this value does not rule out the value found by Lisenfeld et al. (2004), it is unlikely that all of the missing flux is of thermal origin as the non–thermal component is typically more diffuse and therefore more likely to be resolved out.

Integrated non–Thermal Emission

Similarly, if we consider the non–thermal emission at 1 GHz, we recover an integrated flux density of $81.0^{+2.9}_{-2.6}$ mJy. Again, it is difficult to compare this measurement to other literature values, due to the different spatial scales that the literature radio observations are sensitive to. Lisenfeld et al. (2004) obtain ≈ 80 mJy for the non–thermal emission integrated across the main disk at 1 GHz, which similar to what we find applying no corrections for missing flux. This is surprising as we would expect the Lisenfeld et al. (2004) value to recover more extended emission than ours, as they have better sensitivity to large scale emission. This again suggests that they may be over predicting the recovered thermal emission within the main disk.

If we again assume that the thermal fraction remains the same for the missing flux, we obtain a corrected non–thermal flux density of ~ 130 mJy, which we shall use for comparison with the literature. To obtain an independent, first order estimate for the non–thermal radio emission, we scale the disk integrated emission at 1.38 GHz from Kepley et al. (2010) to 1 GHz (see Table 3.4, assuming an integrated spectral index, $\alpha = -0.4$ (Lisenfeld et al., 2004), to find ≈ 170 mJy total radio emission. We then subtract the thermal emission from the main disk found from the combined Hα and 24 μm measurement to isolate the non–thermal emission, resulting in a main disk non–thermal flux density of ~ 120 mJy. This is again reasonably close to what our Bayesian fitting procedure returns, indicating that our separation procedure is correctly separating the thermal and non–thermal components. Again, for further reference, if we assume that all of the missing flux is of non–thermal origin, we obtain an upper limit for the non–thermal emission of $\sim 140\,\mathrm{mJy}$.

Thermal Fraction

A useful quantity for comparison purposes is the thermal fraction, which is defined as:

$$f_T(\nu_o) = \frac{S_T(\nu_o)}{S_\nu(\nu_o)} = \frac{A}{A+B}. \tag{3.13}$$

Using Equation 3.13, we combine the integrated thermal and non–thermal normalisations to obtain a thermal fraction of $0.26^{+0.02}_{-0.03}$ at 1 GHz. This is much larger than is typically found for normal spiral galaxies (≈ 0.1; Condon 1992; Tabatabaei et al. 2017), and more closely reflects the higher thermal fractions found from the analysis of other dwarf galaxies (Israel, 1980; Klein et al., 1989; Heesen et al., 2011). This conclusion does not change if we calculate the thermal fraction instead using the estimated upper and lower limits for the thermal and non–thermal components. The lower limit for the thermal fraction is $\sim 20\,\%$ and the upper limit is $\sim 50\,\%$, showing that the thermal fraction is certainly higher in NGC 1569's main disk than in normal spiral galaxies. This fraction is likely to decrease however if we include the large scale non–thermal halo surrounding NGC 1569 (Israel and de Bruyn, 1988; Kepley et al., 2010). This is because the thermal emission is concentrated in the main disk where the massive stars are located, whereas the non–thermal emission is partially spread over a large halo surrounding NGC 1569 (Kepley et al. 2010; see Figure 3.4**a**), it is therefore likely that we are preferentially resolving out non–thermal emission over thermal emission in the present observations.

Non–Thermal Spectral Index

Finally, we measure a disk averaged non–thermal spectral index of $\alpha = -0.53^{+0.02}_{-0.02}$. This is shallower than typically found in normal spiral galaxies ($\alpha \approx -0.8$; Condon and Yin 1990) and better reflects the spectral index of a galactic SNR ($\alpha \approx -0.5$; Green 2014). This suggests that a young CRe population is responsible for the non–thermal emission that we are observing within the main disk, and is justified as it is likely that these CRe were accelerated in the most recent starburst phase (that finished $\approx 10\,\mathrm{Myr}$ ago; Angeretti et al. 2005; McQuinn et al. 2010). It should be stressed that this measured non–thermal spectral index is strictly correct only on the spatial scales that the observations are sensitive to. If there is a large–scale component within the main disk that is primarily comprised of an older population of CRe, the measured non–thermal spectral index may be steeper. This is however unlikely to be the case as NGC 1569's main disk is much brighter than the surrounding halo (see Section 3.3.3).

3.5.2 Resolved Properties

NGC 1569's resolved properties are presented on a hexagon by hexagon basis, ensuring that each individual pixel is more or less independent from each of the others.

Thermal Emission

The recovered thermal emission (Figure 3.7**a**) closely reflects the spatial structure from the prior thermal model (see Figure 3.3), with a bright, compact source towards the North–West of the galaxy and a fainter source towards the South–East. Both of these sources are spatially coincident with known HII regions detailed in Waller (1991). The morphology of the recovered thermal emission closely reflects that recovered by Lisenfeld et al. (2004), who applied a similar separation procedure but with better sensitivity to larger scale emission. Within the uncertainty of our fits, we recover the same thermal emission in the North–West major HII region as Lisenfeld et al. (2004), as the bright North–West source is compact, compared to the more extended nature of the rest of the disk (see Section 3.3.3). However, we recover only roughly half of the emission across the rest of NGC 1569's main disk, which could be due to the aforementioned lack of short baselines or the Lisenfeld et al. (2004) fit potentially overestimating the thermal radio emission within the main disk.

Non–Thermal Emission

The recovered non–thermal emission (Figure 3.7**b**) takes on a more diffuse morphology than the recovered thermal emission. The emission is concentrated in three peaks; One near, yet offset from the major peak in the recovered thermal map, a second coincident with the minor peak in the recovered thermal map and a third towards the South–Eastern tip of the mask. It is not surprising that two of the peaks coincide in both the thermal and non–thermal maps, as this radio emission likely originates from current regions of star formation. It should be noted that the offset peak is coincident with the SNR candidate, N1569-17 (Chomiuk and Wilcots, 2009). However, as we are averaging over a relatively large area, it is difficult to separate the compact source properties from the surrounding ISM. The peak towards the South–East is spatially coincident with the well studied SNR, NGC1569-38 (Chomiuk and Wilcots, 2009), and has no corresponding peak in the recovered thermal maps. Here the fitting procedure has correctly identified that this source is dominated by non–thermal emission.

Thermal Fraction

Overall, the non–thermal emission is generally brighter than the thermal emission, which is highlighted in Figure 3.7**d**. This figure shows how the thermal fraction varies across NGC 1569's main disk. The thermal fraction is highest (≈50%) near the current region of major star formation, towards the West of the main disk. The thermal fraction then gradually decreases to ≈15% towards the East of the main disk. The peak in the thermal fraction lines up with the site of on–going major star formation (see the Hα map; Figure 3.3), which is expected as most compact sources identified within normal galaxies are HII regions, dominated by thermal emission (Condon, 1992).

Non–Thermal Spectral Index

The recovered non–thermal spectral indices are generally between -0.4 and -0.7 across NGC 1569's main disk. As shown in Figure 3.8, there appears to be a correlation between the recovered thermal fraction and the recovered spectral indices. This is expected as a higher thermal fraction indicates there is recent star formation occurring, and any CRe that are accelerated would be very young. However, as the uncertainties on both the recovered spectral index and thermal fraction are large, we do not detect any significant variation in the recovered spectral index across the main disk.

The variations in the spectral index as seen in 3.7**c** are possibly due to two different effects. One is the effect that the missing flux from short spacings has on the recovered spectral indices, which is discussed in more detail in Section 3.3.3. This likely explains the flattening towards the South–East of the main disk and the steepening towards the North–West. The second effect is that the uncertainties on the recovered spectral indices are much larger in regions with high thermal fractions. This is because it becomes more difficult to constrain the non–thermal properties as the thermal emission becomes more dominant. This likely explains the flattening towards the centre of NGC 1569, although the uncertainties on this measurement are large. These recovered non–thermal spectral

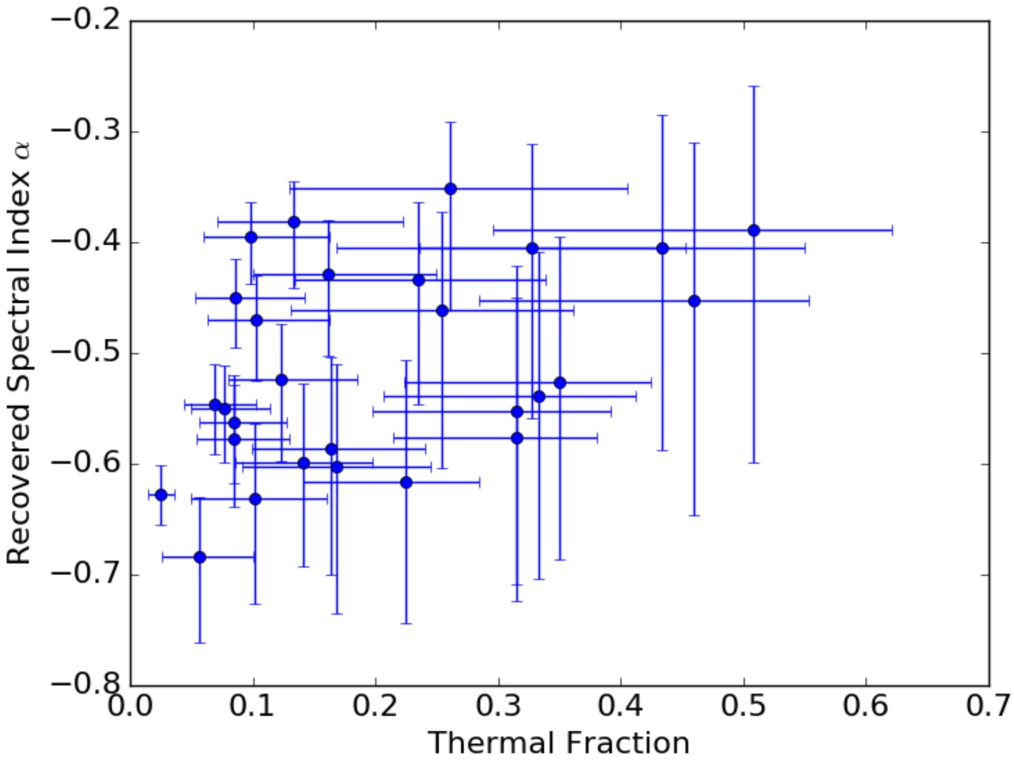

FIGURE 3.8: Plot of the recovered thermal fraction against the recovered spectral index. Each data point corresponds to a hexagon from Figure 3.7. The data points are the 50th percentile from the fit posterior probability distributions, and the uncertainties show the 16th and 84th percentiles of the same distribution.

indices are consistent with what is expected for a young CRe population (Longair, 2011; Green, 2014).

One additional interesting observation is that the recovered spectral index for the well studied SNR, NGC1569-38, is steeper when the 33.8 GHz observation is included, compared to when it is ignored in the fit. Closer inspection reveals that there is a potential break in its SED, which may be linked to spectral ageing effects. We discuss this source in more detail and the potential nature of the break in Chapter 4.

3.6 Discussion

3.6.1 Reddening Estimates

Traditionally, to isolate the non–thermal emission properties of a galaxy, authors generally use scaled Hα emission as a proxy for the thermal emission and, after correcting for extinction effects due to line of sight dust, subtract it from the total radio intensity maps (e.g. see Heesen et al. 2014). There are two main problems that could arise from this procedure: 1) the extinction estimate used to correct for the galactic foreground can be very uncertain, especially in regions at low galactic latitude (Schlegel et al., 1998; Schlafly and Finkbeiner, 2011) and 2) applying a single 'blanket' correction for the entire galaxy does not capture any differential extinction that may be occurring within the galaxy itself.

In our fitting procedure, we do not make any assumptions about extinction along the line of sight. Instead we use the thermal model derived from an Hα map that has not been corrected for extinction as a lower limit for the thermal emission component. As we expect our radio observations to be largely free from any extinction effects, by comparing our recovered thermal emission to the thermal model, we can estimate the reddening along various lines of sight to NGC 1569. From the Cardelli et al. (1989) extinction curves we assume $A_{H\alpha} = 2.54 \times E(B-V)$, which we combine with Pogsons relation to find:

$$E(B-V) = \left(\frac{-2.5}{2.54}\right)\log_{10}\left(\frac{S_{H\alpha}}{S_T}\right)[\mathrm{mag}]\,, \tag{3.14}$$

where $S_{H\alpha}$ is the flux density measured from the thermal model at 1 GHz (see Figure 3.3) and S_T is the thermal flux density recovered by our fitting procedure at 1 GHz (see Figure 3.7**a**).

We present the resolved reddening properties in Figure 3.9**a**. There appears to be significant variation across NGC 1569's main disk, with the recovered $E(B-V)$ ranging from as high as ≈ 0.8 mag in the main star forming regions to ≈ 0.1 mag in some of the more diffuse areas. It should be noted however that the uncertainties on the reddening can be quite large, as shown in Figure 3.9**b**. We also find that regions which are observed to be bright in Hα emission tend to also be more reddened, which makes sense as star–formation is observed to occur in dusty obscured environments (e.g. Kennicutt

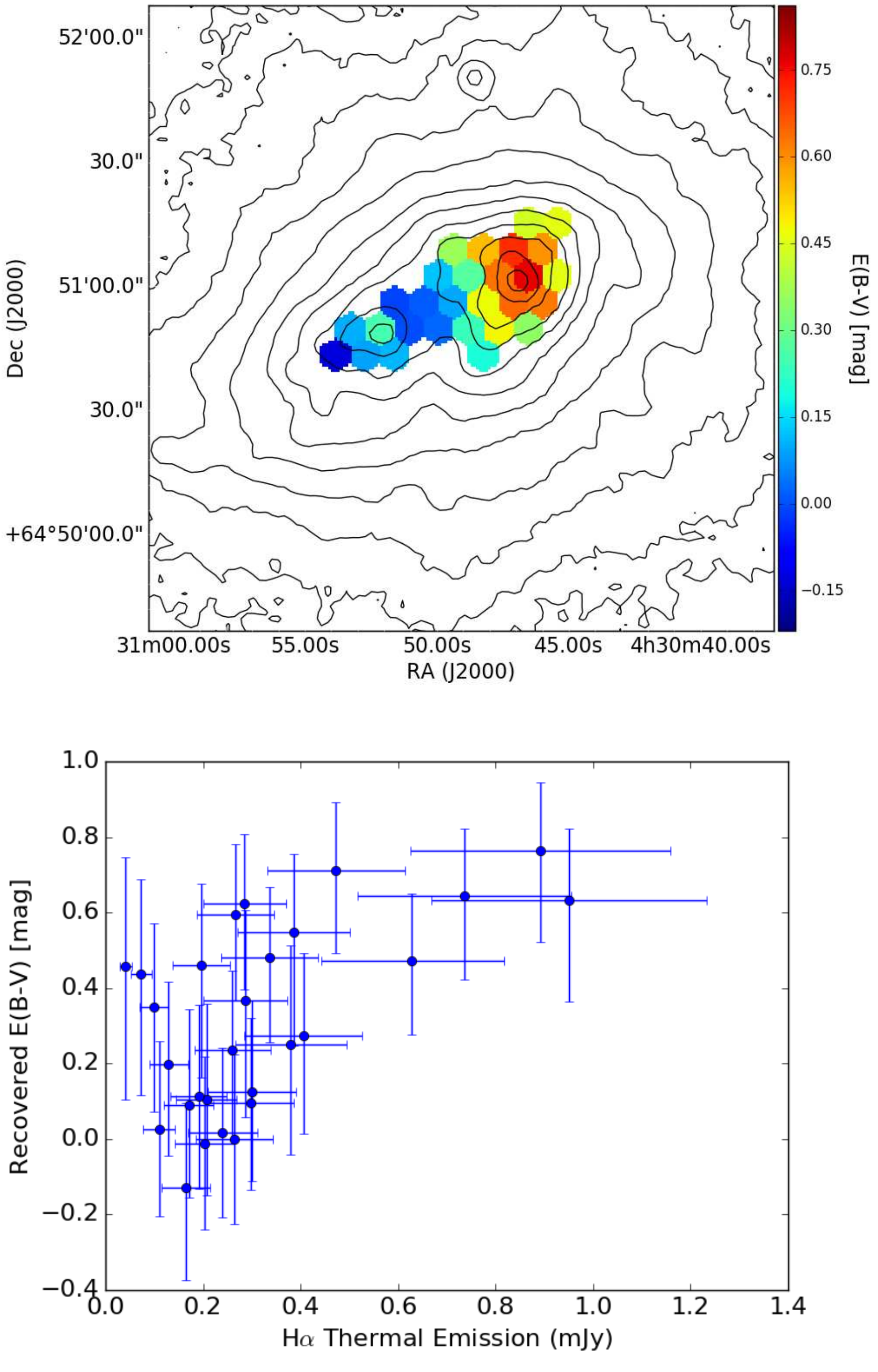

FIGURE 3.9: The top panel shows how the estimated reddening, $E(B-V)$, varies across NGC 1569's main disk with overlaid Spitzer 24μm contours from Bendo et al. (2012). The contours start at 0.36 MJy sr^{-1} and increase in factors of 2. The bottom panel shows the thermal emission inferred from the Hα map at 1 GHz (Figure 3.3) plotted against the recovered reddening.

and Evans, 2012) . In Figure 3.9**a** we have plotted Spitzer 24μm contours from Bendo et al. (2012). The reddening distribution we recover from the radio maps closely follows the warm dust traced by the 24μm emission, and indicates that the variation we are observing is due to internal extinction within NGC 1569 itself.

The reddening distribution matches up well with other literature extinction measurements. For the main star forming region (Waller–2; Waller 1991), we find that $E(B-V) = 0.76^{+0.18}_{-0.24}$ mag. This agrees well with literature measurements from the Balmer decrement method, which finds $E(B-V) \approx 0.75$ mag (Devost et al., 1997; Relaño et al., 2006). Towards the secondary peak in star formation (Waller–7; Waller 1991) we find $E(B-V) = 0.25^{+0.26}_{-0.25}$ mag. This is smaller than those found in the literature, as at a similar resolution to this study, Relaño et al. (2006) find $E(B-V) \approx 0.6$ mag and a higher resolution study by Devost et al. (1997) finds $E(B-V) \approx 1.0$ mag. Closer inspection of the posterior probability distributions for this tile reveals that the thermal emission is poorly constrained at this location, and that differences in the *uv*–plane sampling are primarily responsible for the significant difference (see Section 3.3.3). We also find that the most likely value for the reddening from the fitting procedure can be negative in tiles where the thermal fraction is low. This is primarily due to the poorer constraints on the thermal emission in these regions of the main disk and are accompanied with larger uncertainties. In order to obtain more precise reddening estimates, longer observations, that have been corrected for missing short spacings, are required to improve constraints on the thermal emission component.

We apply Equation 3.14 to the integrated thermal properties determined from our fitting procedure to find the average reddening across NGC 1569's main disk. We find an average reddening $E(B-V) = 0.49 \pm 0.05$ mag, which is in excellent agreement with both Burstein and Heiles (1982) and Israel (1988) who find $E(B-V) \approx 0.5$ mag. These studies assume that all of the observed reddening is due to the galactic foreground, however Figure 3.9**a** shows that there must be significant internal extinction contributing to the overall reddening. Therefore these authors may be over–estimating the galactic foreground extinction.

We attempt to separate the reddening due to galactic foreground extinction, $E_F(B-V)$, and the reddening due to internal extinction, $E_I(B-V)$, however we stress that the reddening uncertainties are quite large (see Figure 3.9**b**) and hence these results should be regarded as tentative. We estimate the reddening due to the galactic foreground by taking the median reddening across NGC 1569's main disk. This is motivated as we would expect a uniform reddening correction to exist across the entirety of the main disk for the foreground extinction, and an average over the main disk is biased upwards due to significant reddening in the bright, compact star–forming regions. The median recovered reddening is $E(B-V) = 0.33$ mag, which is less than $E(B-V) \approx 0.5$ mag found by Burstein and Heiles (1982) and Israel (1988) or the $E(B-V) \approx 0.6$ mag found by Schlafly and Finkbeiner (2011). This is possibly due to the Burstein and Heiles (1982) measurement being averaged over a large area of the sky (0.6 deg^2), where significant variations on scales of $\sim$100 pc could occur (e.g. see the dust maps from Schlegel et al. 1998), and the Israel (1988) measurement was made by analysing the integrated properties over the entire galaxy, not taking into account any small scale variations. If we assume the foreground reddening is $E_F(B-V) = 0.3$ mag, we see variations due to internal extinction which can be as large as $E_I(B-V) \approx 0.5$ mag. This reflects the internal extinction corrections that are measured for larger spiral galaxies (Kennicutt, 1998; James et al., 2005), suggesting that the star–formation processes may be similar in this region of NGC 1569.

3.6.2 Equipartition Magnetic Field Strengths

The distribution of non–thermal radio continuum emission from a typical galaxy is closely related to its underlying magnetic field strength, as CRe radiate non–thermal radio emission in the presence of magnetic fields (Rybicki and Lightman, 1979; Beck et al., 1996; Longair, 2011). In principle, magnetic field strengths can be determined from radio observations accompanied with γ–ray or X–ray observations to gain additional information on the number density of CRe that are responsible for the observed radio continuum emission. However, as these observations are not widely available, an assumption about the relation between CRe and magnetic field strength has to be made (Beck and Krause, 2005). The most commonly applied approach is to assume that the total energy densities of the cosmic rays and the magnetic fields are approximately equal. This is motivated as the cosmic rays in a galaxy are strongly coupled to the magnetic fields, and exchange energy until they reach equilibrium (Beck and Krause, 2005). Although equipartition assumptions do not strictly apply to starburst galaxies, Kepley et al. (2010) argue that the magnetic fields derived for NGC 1569 via equipartition assumptions reflect the true magnetic field strengths, based on work by Thompson et al. (2006).

We apply the revised equipartition magnetic field equations from Beck and Krause (2005) to obtain estimates of the resolved magnetic field strengths. This equation is derived by computing the energy density bound up within the magnetic fields and balancing it with the cosmic ray energy density. The energetics of the cosmic rays are usually dominated by the more massive cosmic ray protons inside a galactic disk. As we do not detect any emission from these charged particles, we estimate the cosmic ray proton energy density from the CRe energy density that is inferred from the radio observations. This is accomplished in practice by assuming a ratio of the number densities of cosmic ray protons to electrons, **K**, at a particular energy. Further details of the basis of the equation can be found in an analogous calculation of the minimum energy magnetic field strength, which we present in Chapter 4.

For NGC 1569, we assume that the ratio of the CR electron to proton number densities is $\mathbf{K} = 100$ (Beck and Krause, 2005), that NGC 1569 has a non–thermal emission scale height of 0.4 kpc (Banerjee et al., 2011; Elmegreen and Hunter, 2015) and that NGC 1569 is at an inclination of 60° (Jarrett et al., 2003). We assume the value of $K = 100$ as this roughly corresponds to that directly observed in particle detection experiments on Earth at $\sim$GeV energies (Beck and Krause, 2005; Hu, 2009). However, the cosmic ray transport in NGC 1569 is not necessarily the same as in the Milky Way, as indicated by the steeper spectral index observed for the Milky Way ($\alpha \approx -0.75$, Bennett et al., 2003) compared to that observed in NGC 1569 $\alpha \approx -0.5$. If we assume that the cosmic rays in NGC 1569 have not yet undergone significant losses at $\sim$GHz emitting frequencies (which may be more physically reasonable for this system), the ratio of number densities reduces to $K \approx 40$ (see Chapter 4) and the recovered equipartition magnetic field strengths reduce by $\sim 25\%$. We further assume that the magnetic fields are predominantly randomly orientated, as no ordered magnetic fields have been observed in deep polarization studies of the main disk (Kepley et al., 2010). Finally, as equipartition magnetic field strength from the revised equations in Beck and Krause (2005) cannot be determined when $\alpha \geq -0.5$ (due to a diverging integral), we fix NGC 1569's spectral index to the average over all of the fitted tiles ($\alpha = -0.53$). This is a reasonable assumption to make as NGC 1569's spectral index does not appear to vary much across

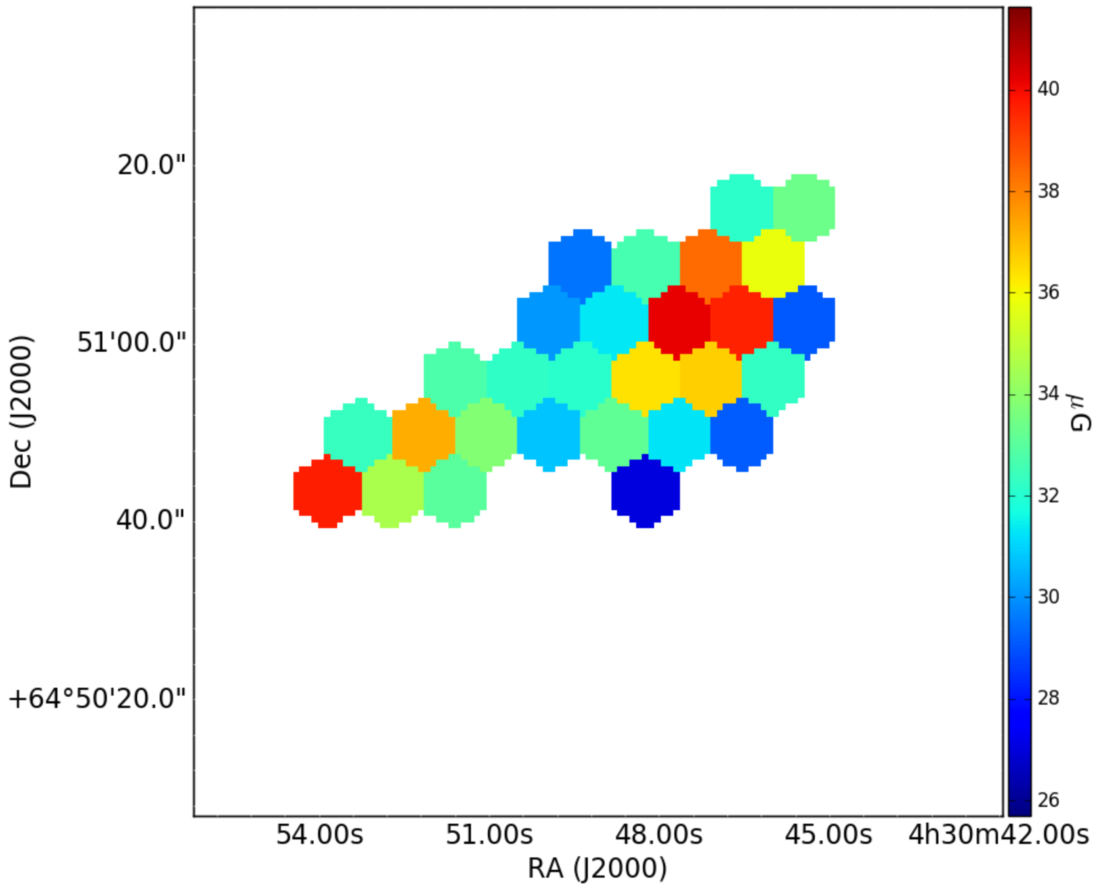

FIGURE 3.10: Recovered equipartition magnetic field strengths, in μG, assuming a non–thermal emission scale height of 0.4 kpc. The hexagonal pixels are the same as those in Figure 3.7.

the main disk. Furthermore, this assumption enables a straight–forward comparison of the recovered magnetic field strengths with the literature. We present a map of the recovered equipartition magnetic field strengths in Figure 3.10.

The spatial distribution of the recovered equipartition magnetic fields is effectively identical to the recovered non–thermal emission, with a peak towards the main star forming region and another cospatial with the SNR NGC1569-38 (Chomiuk and Wilcots, 2009). This is because, with a constant non–thermal spectral index, the derived equipartition magnetic field strength is effectively proportional to the recovered non–thermal flux density:

$$B_{eq} \propto \left(\frac{(K+1)F_{\nu}}{l} \right)^{\frac{1}{(3-\alpha)}}, \tag{3.15}$$

where B_{eq} is the equipartition magnetic field strength, K is the assumed ratio of number densities of cosmic ray protons to electrons, F_ν is the recovered non–thermal flux density at frequency ν, α is the non–thermal spectral index and l is the path length through the non–thermal emitting medium.

The recovered equipartition magnetic field strengths are largest in the region of major star formation and in the SNR NGC1569-38, where it reaches $37.9^{+2.8}_{-2.3}\mu$G and $37.4 \pm 0.4\,\mu$G respectively. The magnetic fields are weakest in more diffuse regions of the main disk, with the lowest magnetic field strength measured being $25.5^{+0.6}_{-0.7}\mu$G. Averaged over the entire main disk, we find an equipartition magnetic field strength of $32.1 \pm 0.3\,\mu$G. We emphasize that the quoted uncertainties are derived from the uncertainties on the non–thermal normalisation only, so the true uncertainties are likely to be much larger. Furthermore, as with most conclusions drawn from high–resolution interferometric observations, these magnetic field strengths should formally be regarded as lower limits due to missing flux. However, as the recovered magnetic field strength weakly depends upon the recovered flux (see Equation 3.15), we expect this to have a small effect on the recovered magnetic fields.

The recovered magnetic field strengths are in good agreement with those found by Kepley et al. (2010). In the peak associated with the main star forming region, Kepley et al. (2010) find a magnetic field strength of 38μG compared to the $37.9^{+2.8}_{-2.3}\mu$G found in this study. However, these measurements are much larger than those found in other post–starburst dwarf galaxies, although this is probably related to the assumed disk scale height. Assuming a disk scale height of 1 kpc for example will reduce the recovered magnetic field strengths by 33 % (see Equation 3.15). Chyży et al. (2016) assume a disk scale height of 1 kpc whilst studying the post starburst dwarf irregular IC 10. They find that the peak magnetic field strengths in regions of on–going star–formation are as high as 29 μG. We obtain a very similar magnetic field strength if we assume the same scale height ($29.2^{+2.2}_{-1.6}\mu$G), although it should be noted that Basu et al. (2017) find from their SED analysis that these regions in IC 10 can be modelled as being dominated by thermal emission, meaning the uncertainty in the Chyży et al. (2016) result could be large. Regardless, the recovered magnetic field strengths are much larger than that found in other dwarf galaxies (Chyży et al., 2011; Roychowdhury and Chengalur, 2012) and in larger Magellanic–type galaxies (Jurusik et al., 2014). This is possibly due to either the large number of SNR occurring after the starburst, generating and maintaining turbulence which amplifies the magnetic field strength via the small scale dynamo (Chyży et al., 2011, 2016), or because of the fact that this resolved study is focused on high surface brightness emission whereas the older literature studies are mainly based on emission integrated over the entire galaxy, or a combination of the two.

Although our recovered magnetic field strengths likely underestimate the true magnetic field strength due to missing flux, it is unlikely that it is significantly affecting our results as the equipartition magnetic field strengths vary weakly with recovered flux (see Equation 3.15). If we are missing 30 % of the flux due to missing short spacings, our recovered equipartition fields will only underestimate the true equipartition magnetic field strengths by $\sim 10\,\%$. We find that the magnetic field strengths are similar to those found in turbulence dominated spiral arms and central regions in normal galaxies, where the magnetic field strength is $\approx 20 - 30\,\mu$G (Basu and Roy, 2013; Beck, 2015). This suggests that the relativistic environment in NGC 1569's main disk could be similar to star–forming regions found in the spiral arms of normal star–forming galaxies. It is important to note that there are many assumptions that go into estimating equipartition magnetic field strengths, each of which have large associated uncertainties. Therefore, the estimates reported here should be interpreted at an order of magnitude level only.

3.7 Conclusions

We adopt a Bayesian methodology to separate the thermal and non–thermal radio continuum emission components from VLA maps spanning a broad frequency range on a resolved basis. In our fitting procedure, we include prior information about the thermal normalisation extracted from literature Hα maps. Our main conclusions are:

1. On an integrated basis, we recover $28.1^{+2.8}_{-3.1}$ mJy thermal radio continuum emission and $81.0^{+2.9}_{-2.6}$ mJy non–thermal radio continuum emission at 1 GHz, although these values should be treated as lower limits due to the interferometric nature of the observations. We estimate that we are resolving out $\approx 30\%$ of the main disk flux density at all observed frequencies, hence the relative spectral properties (thermal fraction and non–thermal spectral index) are preserved. These measurements correspond to a high thermal fraction of $0.26^{+0.02}_{-0.03}$ at 1 GHz, which reflects what is found in other studies of dwarf galaxies. However, if the entire

galaxy is considered, this fraction should be treated as an upper limit. It is likely to decrease slightly if the halo, which is dominated by non–thermal emission, is included.

2. On a resolved basis, we find that the recovered thermal emission closely follows the structure of the prior Hα map and is consistent with the separation carried out by Lisenfeld et al. (2004). There are two main peaks in the thermal distribution, which both match up with known HII regions. We recover less thermal emission in the Western peak than previous measurements, which is likely due to differences in the sampling of the *uv*–plane between observations. The recovered non–thermal emission is more diffuse than the recovered thermal emission and is also generally brighter. The non–thermal emission consists of three emission peaks, two of which line up with known regions of current star formation and one corresponding with the known SNR NGC1569-38. The resolved thermal fraction is $\approx 15\%$ across most of the main disk, and increases to $\approx 50\%$ in the region of major star formation.

3. The resolved spectral indices are generally between $\alpha = -0.4$ and -0.7 and tend to be flatter in regions of active star formation. Within uncertainties, the resolved non–thermal spectral index does not appear to vary significantly across NGC 1569's main disk. The average non–thermal spectral index across the main disk is $\alpha = -0.53 \pm 0.02$. This spectral index is shallower than that found for normal spiral galaxies, and closely reflects the injection index found in young SNR. This indicates that the CRe population producing the non–thermal emission is young and probably originates from the recent starburst phase the galaxy has undergone.

4. By comparing the prior Hα map that has not been corrected for extinction with our recovered thermal emission map, we estimate the reddening along the line of sight to NGC 1569. Integrated over the main disk we find that the overall reddening is $E(B-V) = 0.49 \pm 0.05$ mag. This is in excellent agreement with the galactic foreground estimates from the literature. However, variations in the reddening across NGC 1569's main disk indicate that internal extinction is significantly contributing to this estimate. By taking the median reddening across the main disk, we estimate that the reddening due to the galactic foreground is $E_F(B-V) \approx 0.3$,

with internal extinction contributing on average $E_I(B-V) \approx 0.2$. On a resolved basis however, the variations in internal reddening can be as large as $E_I(B-V) \approx 0.5$, which is similar to that found in larger spiral galaxies.

5. Using the recovered non–thermal emission characteristics, we derive estimates for the equipartition magnetic field strengths. Assuming a scale height of 0.4 kpc, we find that our recovered equipartition magnetic field strengths vary between 25μG to 38μG across the main disk. Our recovered magnetic field strengths are similar to those found in the post–starburst dwarf irregular galaxy, IC 10, but are in general larger than those found for dwarf galaxies. These magnetic field strengths are similar to those found in the spiral arms and central regions of normal spiral galaxies, indicating that the relativistic ISM may be similar in both.

Future studies applying the presented separation procedure should ideally use maps that have been corrected with single dish observations. Not only would this improve the constraints on the fitted parameters by reducing the scatter in the galaxy SED, it would also greatly simplify the interpretation of the recovered fit parameters.

Chapter 4

High–Resolution observations of the SNR NGC1569–38

4.1 Introduction and Motivation

As discussed in Chapter 1, SNR are currently thought to be the primary source of cosmic rays in normal star–forming galaxies (H.E.S.S. Collaboration et al., 2018). In SNR shock fronts, CRe are accelerated through the DSA mechanism (see Drury 1983 for a review) and released into the ISM, where they interact with interstellar magnetic fields to produce observed diffuse non–thermal radio continuum emission (Rybicki and Lightman, 1979). As the observed supernova explosion rate is closely related to a galaxy's recent star formation history, it comes as no surprise that the observed non–thermal radio continuum emission is closely correlated with other star–formation tracers (Heesen et al., 2014; Tabatabaei et al., 2017). However, the physics behind this relationship are complex (e.g. Lacki et al., 2010) and depend on the initial energy spectrum of the CRe that are injected into the ISM, subsequent transportation away from their sites of acceleration where the CRe experience various energy gains and losses, and their eventual escape from the galaxy. Galactic CRe transport has been analysed at great depth in the literature (e.g. Strong et al., 2007) and clues on how CRe escape galaxy disks have been found in radio observations of nearby galaxy haloes (Heesen et al., 2018a,b). However, how the CRe escape from their sites of acceleration remains a mystery, which can be rectified through detailed studies of galactic and extra–galactic SNR along with their surrounding environments.

Whilst studying the resolved radio–continuum properties of NGC 1569 (see Chapter 3), we noticed that the compact source located towards the south–east of NGC 1569's main disk possesses an unusual radio spectrum that warranted further study (see Figure 4.4). This source matched spatially to the well studied SNR NGC1569–38 (Chomiuk and Wilcots, 2009), and has been shown in the literature to be a compact non–thermal source (Greve et al., 2002) with associated X–ray emission (Martin et al., 2002) and infrared [FeII] line emission (Labrie and Pritchet, 2006). Furthermore, a shell–like morphology is visible in Hubble optical [OIII] and [SII] maps (Shopbell et al., 2000), cementing NGC1569–38's status as a *bona fide* SNR.

NGC 1569 was also observed as part of the LeMMINGs deep survey (Baldi et al., 2018), providing complementary high–resolution radio continuum observations to the already discussed VLA observations (see Chapter 3). In this chapter, we analyse the high–resolution radio continuum properties and provide a more in depth analysis of its radio spectrum as observed in the VLA observations.

This chapter is structured as follows; in Section 4.2 we describe our observations, data reduction and imaging method; in Section 4.3 we present the results from our high–resolution LeMMINGs observations and revisit the VLA observations of NGC1569–38; in Section 4.4 we estimate NGC1569–38's age and expansion velocity, present deeper analysis of its radio SED and analyse its minimum energy magnetic field strength. Finally we present our conclusions in Section 4.5.

4.2 Observations and Data Reduction

NGC 1569 was observed at 1.5 GHz (L–Band) with e–MERLIN as part of LeMMINGs (Westcott et al., 2017; Williams et al., 2017; Baldi et al., 2018), an e–MERLIN legacy project. All antennas, including the 76 m Lovell telescope, were available for the full duration of the 9–hr observation, taken on 2015 April 25. The total 512 MHz bandwidth was split into 8 IFs (intermediate frequencies), each with 128 individual channels of bandwidth 0.5 MHz. The primary flux calibrator, 3C286, was used to set the flux scale; the point–like source, OQ208, was used to determine the passbands and

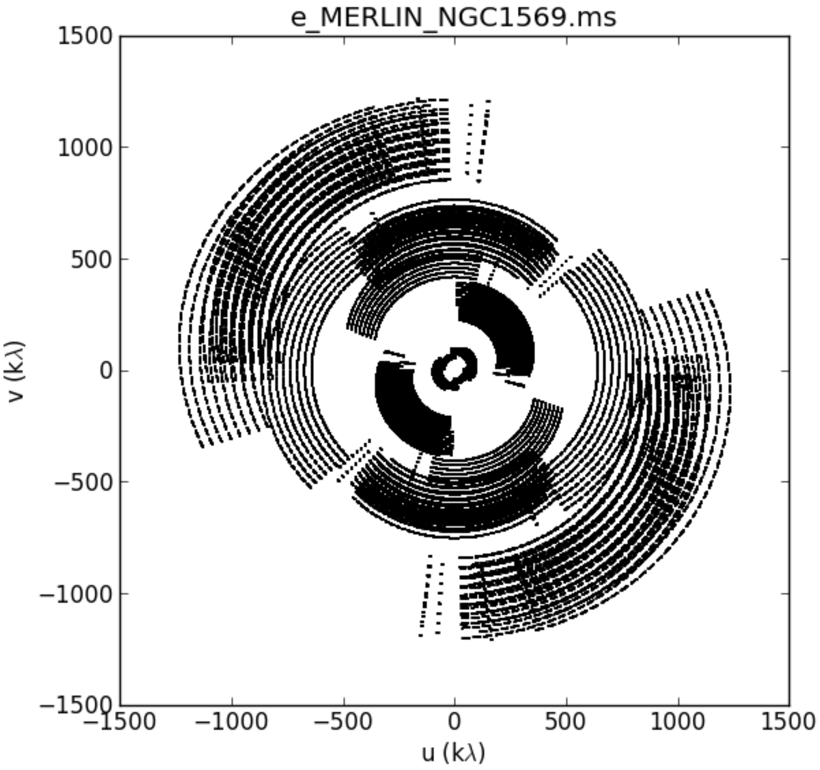

FIGURE 4.1: Observed *u–v* visibillity distribution for the e–MERLIN observation of NGC 1569.

relative antenna gains, and J0449+6332 was used to determine the complex gains to apply to NGC 1569. The observations started with alternating scans of NGC 1569 and 0449+6332, spending 7 min on NGC 1569 and 3 min on 0449+6332 for each iteration, resulting in 4.9 hr total time on source. We present the observed *uv*–plane for NGC 1569 in Figure 4.1. The observation finished with a 45–min scan of 3C286 and a 30–min scan of OQ208.

Before we carried out any calibration, we first used SERPent (Peck and Fenech, 2013; Argo, 2015) with default settings to remove any obvious radio frequency interference (RFI). We conducted further manual flagging to remove any other obvious RFI from the data that SERPent had missed using the AIPS task IBLED. In total, we estimate that we flagged $\sim 20\,\%$ of the data taken of NGC 1569.

The calibration and data reduction were carried out using AIPS[1], following the standard calibration procedure detailed in the e–MERLIN cookbook[2]. After the calibration, we

---

[1] AIPS, the Astronomical Image Processing Software, is free software available from the NRAO.
[2] Available at: `http://www.e-merlin.ac.uk/data_red/tools/e-merlin-cookbook_V3.0_Feb2015.pdf`

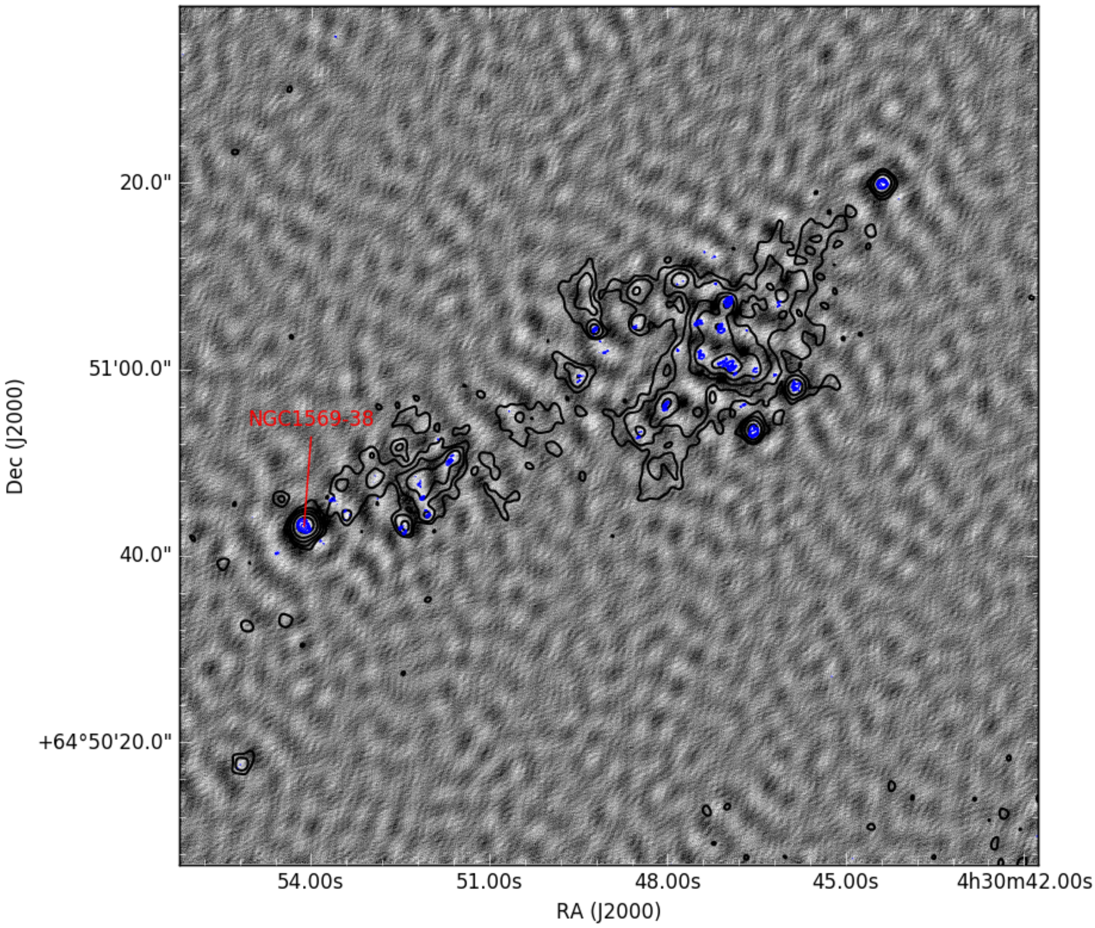

FIGURE 4.2: Naturally weighted e–MERLIN map of NGC 1569. The blue contours are set to 5, 7, 10 and 20 times the 18 μJy beam^{-1} noise level and highlight the observed compact sources within NGC 1569. The black contours correspond to the VLA A–array image presented in Chomiuk and Wilcots (2009) and are set at 3, 6, 12, 24 48, 96, 192 times their 26 μJy beam^{-1} noise level. We have labelled the position of NGC 1569–38 in red.

flagged the first and last 15 channels in each IF as they form the least sensitive areas of the passband and contribute mostly noise (these flagged channels are included in the $\sim 20\,\%$ data loss mentioned earlier). We then carried out several rounds of phase–only self–calibration on the NGC 1569 field to improve the quality of the final maps, using the bright background sources NVSS J042932+645627 and NVSS 042952+644251 to aid calibration. To further improve sensitivity, the calibrated *u*–*v* data were weighted to enhance the contribution from telescopes with a larger collecting area, using the scheme recommended in the e–MERLIN cookbook.

We imaged NGC 1569 with the AIPS task IMAGR using the Clark CLEAN deconvolution algorithm (Clark, 1980). During imaging, we used a natural weighting scheme to maximise sensitivity to any extended structure (the e–MERLIN array is sensitive to structures smaller than $\sim 2''$, as set by the shortest baseline measured) and we placed outlier fields on the bright background sources, NVSS J042932+645627 and NVSS 042952+644251 to account for their contaminating sidelobes. This weighting scheme resulted in a $0''.53 \times 0''.22$ synthesized beam. Following the Gaussian parameterisation of the e–MERLIN primary beam (including the Lovell telescope) presented in the e–MERLIN technical capabilities, we find a primary beam attenuation correction factor at the location of NGC1569–38 of 1.002 which we apply to all presented flux density measurements of the SNR. Our final maps of NGC1569 reach a noise level of 18 μJy beam^{-1}. We present the resulting final map in Figure 4.2.

4.3 Results

4.3.1 High–Resolution e–MERLIN Observations Of NGC1569–38

NGC1569–38 is resolved in our high–resolution e–MERLIN observation, and has an elongated near Gaussian shape (see Figure 4.3). We measure the apparent size and integrated flux density of the compact source by fitting a 2 dimensional Gaussian function using the AIPS task IMFIT and present the fitted parameters in Table 4.1. The presented uncertainties are those returned by IMFIT, apart from the integrated and peak flux densities, where we have combined the returned uncertainty in quadrature with a conservative 10% uncertainty in the absolute flux scale. As NGC1569–38 is smaller than the largest resolvable angular size of $\sim 2''$ for e–MERLIN at 1.5 GHz (see e–MERLIN technical capabilities), we are confident that we are recovering all of the emission from the SNR, and that the measured integrated flux density is an accurate representation of the true integrated flux density at 1.5 GHz.

We directly compare our observation of NGC1569–38 with earlier MERLIN observations presented in Greve et al. (2002). There is very good positional agreement between NGC1569–38 and the corresponding source M–6 (as the SNR is labelled in their paper), and the sources appear (by eye) to be of similar angular size. We observe however a slightly different morphology with our presented e–MERLIN observations. This is most likely due to differences in the sampling of the *uv*–plane. Our observation is

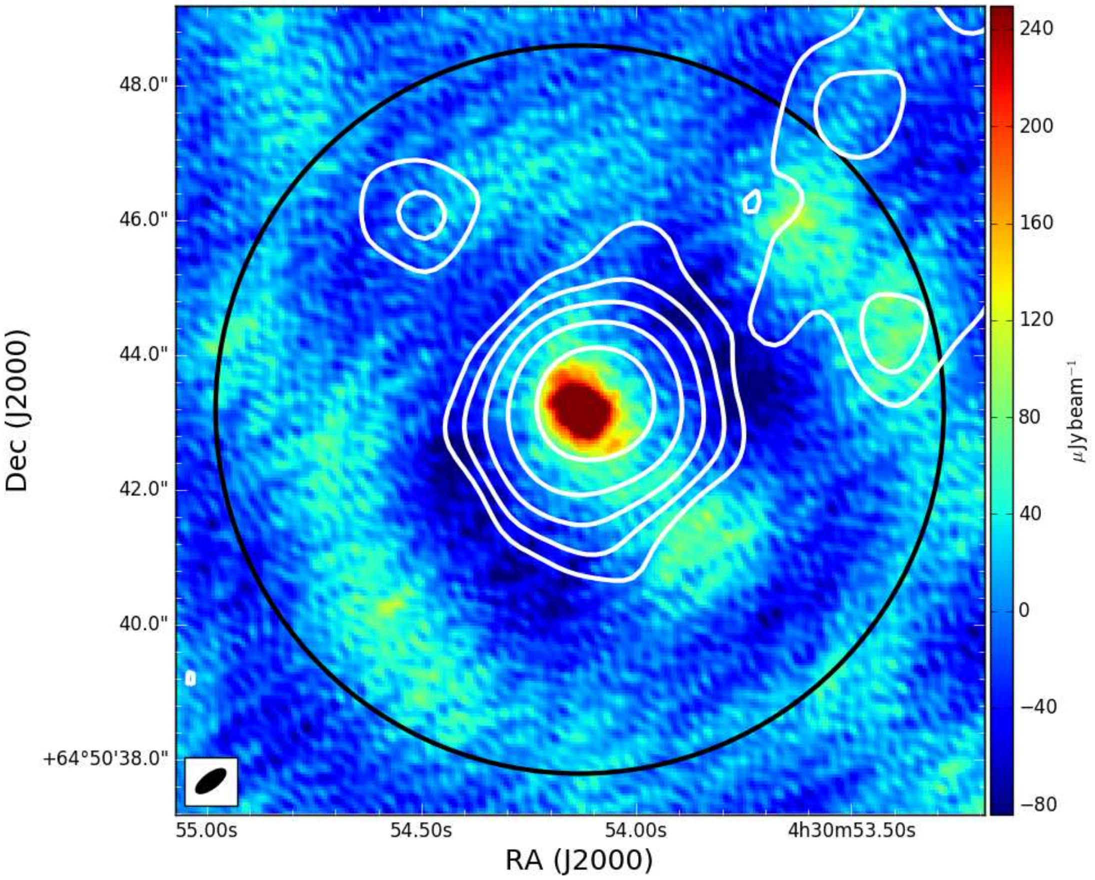

FIGURE 4.3: Zoom in of the 1.5 GHz e–MERLIN detection of NGC1569–38. The white contours correspond to the VLA A–array map presented in Chomiuk and Wilcots (2009). The black circle represents the aperture that we integrate over when studying the flux properties from lower resolution VLA maps in Section 4.3.2. We show the $0.''46 \times 0.''21$ e–MERLIN synthesized beam in the bottom left of the map.

short, resulting in an elliptical synthesized beam, whereas theirs was taken over a 36 hr time period, resulting in a circular beam. Furthermore, it is possible that Greve et al. (2002) used a different weighting scheme during imaging, which could further affect how NGC1569–38 appears.

Assuming that NGC1569 is located at a distance of 3.36 ± 0.2 Mpc (Grocholski et al., 2008), we find that NGC1569–38 has a diameter equal to 13 ± 1 pc. This is a factor of 2 smaller than the ~ 26 pc found by scaling the measurement by Greve et al. (2002) to our assumed distance. The source of this difference is unknown as it is not discussed how Greve et al. (2002) measure the diameter of M–6, but it is plausible that the difference may be due to mixing up radius and diameter. Similarly, it is unclear how Greve et al. (2002) measure NGC1569–38's integrated flux density. They obtain a total flux density equal to 1.54 ± 3 mJy which we are consistent with, within their large uncertainty range.

TABLE 4.1: Fitted parameters from IMFIT, based upon 1.5 GHz e–MERLIN observations of NGC1569–38.

Property	Recovered Value
α (hh mm ss)	04 30 54.238
δ ($^\circ\ '\ ''$)	+64 50 43.17
Major Axis (FWHM)	1.05 ± 0.06 arcsec
Minor Axis (FWHM)	0.60 ± 0.05 arcsec
Position Angle	38.2 ± 6.5 deg
Peak Flux Density	0.422 ± 0.047 mJy beam^{-1}
Integrated Flux Density	3.12 ± 0.36 mJy

Note: The right ascension and declination correspond to the centre of the SNR. The presented major and minor axis measurements have been deconvolved for the effect of the synthesized beam.

Our measured integrated flux density is however significantly smaller than the 4.67 ± 0.08 mJy found using the VLA in A–configuration by Chomiuk and Wilcots (2009). This is unlikely to be due to missing flux from NGC1569–38, as the SNR is much smaller than the largest angular scale measurable by e–MERLIN at 1.5 GHz. Instead it is more likely due to their lower resolution synthesized beam ($1''.4 \times 1''.4$) including additional emission from the diffuse ISM surrounding the SNR, which we resolve out with the presented e–MERLIN observation. The VLA observing at 1.5 GHz in A–configuration is sensitive to emission on angular scales smaller than $\sim 35''$, whereas e–MERLIN is only sensitive to emission on angular scales smaller than $\sim 2''$. This result reveals that 25 to 40 % of the emission attributed to NGC1569–38 by Chomiuk and Wilcots (2009) may be due to radio continuum emission originating from the diffuse ISM surrounding NGC1569–38. This result emphasizes the requirement for high spatial resolutions when studying extra–galactic SNR.

4.3.2 Low–Resolution VLA Observations of NGC1569–38 And The Surrounding ISM

To further analyse the combined radio properties of NGC1569–38 and the surrounding ISM, we use the VLA observations presented in Chapter 3 (Westcott et al., 2018) to obtain a radio SED for analysis. These observations are at a much lower resolution than the e–MERLIN observation (with a synthesized beam equal to 6.3″ x 6.3″) and are sensitive to emission on larger angular scales (as large as ∼1′). As demonstrated earlier, we expect that the surrounding ISM plays a more dominant role in the observed

TABLE 4.2: NGC1569–38 Flux Densities measured by the VLA

Frequency (GHz)	Flux Density (mJy)	Frequency (GHz)	Flux Density (mJy)
1.26	7.40 ± 0.34	7.40	3.49 ± 0.17
1.78	6.24 ± 0.20	8.50	2.63 ± 0.15
2.50	5.11 ± 0.15	9.50	2.28 ± 0.15
3.50	4.03 ± 0.14	33.80	0.59 ± 0.20
5.00	4.18 ± 0.16	1.0_T*	0.34 ± 0.11

Note:* corresponds to the predicted thermal emission estimated from the Hα map presented in Hunter and Elmegreen (2004).

radio properties at lower resolutions. Although we do not have high spatial resolution, the maps densely sample the 1–34 GHz range enabling detailed study of the region's combined (SNR + ISM) spectral properties.

We measure the flux density of NGC1569–38 and the surrounding ISM from the VLA maps by integrating the emission found within an aperture of diameter $10'.8$ centred on the co–ordinates of NGC1569–38 (which is represented by the black circle in Figure 4.3). We present the measured flux densities at each frequency from this analysis in Table 4.2, and plot them in Figure 4.4. We have corrected the presented measurements for the effects of primary beam attenuation at each observed frequency. We calculate the associated uncertainties by adding in quadrature the uncertainty in the flux scale, the variability of the primary flux calibrators (Perley and Butler, 2017), the uncertainty in the primary beam correction[3] and the uncertainty due to map noise. Normally the total uncertainty is $\sim 5\%$ apart from the 33.8 GHz observations where the uncertainty reaches $\sim 34\,\%$. This is primarily due to the fact that NGC1569–38 lies towards the edge of the primary beam at 33.8 GHz (at 30 % its maximum value) and the map noise is significantly enhanced at this distance from the pointing centre. We also note that the measurements at 5.0 and 7.4 GHz appear enhanced by $\sim 20\%$ compared to the observations at other frequencies. The source of this offset could not be identified, however it is likely to be due to a calibration issue as both of these maps were based on the same VLA observation and both have the same offset. As the source of the offset could not be identified, we include these datapoints in the rest of the analysis, but we also note that our results do not change significantly if we ignore them.

---

[3] See `https://library.nrao.edu/public/memos/evla/EVLAM_195.pdf`

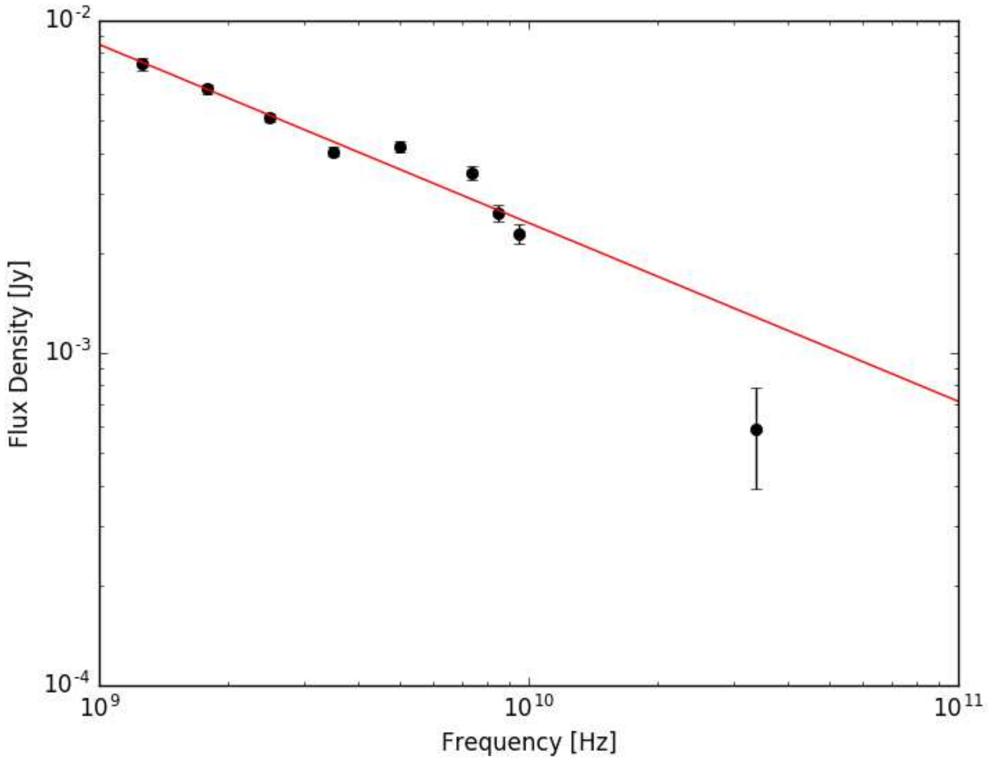

FIGURE 4.4: Observed radio SED of NGC1569–38 and its surrounding ISM. The black datapoints correspond to the observations presented in Table 4.2, and the red line corresponds to a power–law fit to the data.

The observed datapoints appear to be distributed according to a power–law, but deviate at frequencies $> 10\,\text{GHz}$. This is illustrated if we fit a power–law of the form:

$$S_{\nu} = K \left(\frac{\nu}{\nu_o} \right)^{\alpha}, \tag{4.1}$$

to the datapoints with frequencies lower than 10 GHz. In Equation 4.1, K is the normalisation at reference frequency ν_o (taken to be 1 GHz) and α is the observed spectral index. From a least squares fitting procedure, we determine $K = 8.48 \pm 0.64\,\text{mJy}$ and $\alpha = -0.54 \pm 0.06$. It is immediately obvious from the fit that NGC1569–38 only accounts for 38–55% of the observed emission at 1.5 GHz and shows that there is significant contamination from the surrounding ISM. The relatively shallow observed spectral index indicates that that the observed radio continuum emission is non–thermal in origin and reflects what is typically observed in galactic and extra–galactic SNR (Urošević et al., 2005; Green, 2014). The 33.8 GHz datapoint falls lower than expected for the simple power–law model, which is an indication that CRe loss processes are preferentially affecting the higher energy electrons. The uncertainties on this datapoint are however large, but the deviation is still significant at a $3.5\,\sigma$ level. It should be noted that the following analysis critically depends upon the validity of the 33.8 GHz datapoint, as it is the only datapoint that exhibits a significant deviation from the fitted powerlaw. The uncertainties associated with this datapoint are already large, but could be significantly larger if the difference between on–source and off–source uncertainty are taken into account (Harwood et al., 2013). It is therefore likely that we are underestimating the uncertainties associated with this point, which greatly reduces the significance of the deviation. Furthermore, we did not apply an opacity correction whilst calibrating the data, although inspecting the VLA weather summary for these observations indicates that the zenith opacity is small at the time the Ka observation was made ($\tau \approx 0.03$ Nepers). NGC 1569 was located a low elevation during the Ka observations, resulting in a larger opacity correction than that at the zenith angle. Taking this correction into account results in a $\sim 5\%$ increase to the flux scale, which also slightly reduces the deviation from the fitted powerlaw. To obtain better constraints on the existance of a possible break associated with NGC1569–38, further high frequency (> 10 GHz) radio observations that are centred on the SNR (to reduce the impact of the primary beam) are required. Although the observed deviation could simply be due to observational uncertainty, we will continue with our analysis as we can still learn about how a SNR could in theory possess a SED with a spectral break. We present further in depth modelling of the observed SED in Section 4.4.4.

4.4 Discussion

4.4.1 Estimating NGC1569–38's age and expansion velocity

As we have measured the diameter of NGC1569–38 with the presented e–MERLIN observations, we can derive tentative estimates of the SNR age and expansion velocity by using the analytic models presented in Truelove and McKee (1999). We conduct a Monte–Carlo simulation, where we generate models for how the SNR radius and expansion velocity evolve with time, assuming a variety of initial explosion conditions (the explosion kinetic energy, the ejected mass, the ambient particle density and the ejecta power–law index). We then compare these generated models to the observed diameter (13 ± 1 pc) to constrain how the SNR age and expansion velocity.

We generate 10,000 SNR expansion models by drawing 10,000 samples from distributions that encompass plausible explosion initial conditions and applying the analytic equations from Truelove and McKee (1999). We assume that the explosion initial conditions can be drawn from a uniform distribution in log space between 1–100 $M_\odot$ for the ejected mass and between 0.1–10 cm^{-3} for the ambient particle number density. For the initial kinetic energy, we draw the samples from a base–10 lognormal distribution, centred on 10^{51} erg (Janka, 2012) with $\sigma = 1.0$ (i.e. 1 dex). We further assume that the ejecta power–law index can be integer values between $n = 7 - 12$ (which is relevant for Type II SNe progenitors; Chevalier 1982) and that the SNR is expanding into a uniform medium. We present the distributions resulting from this Monte–Carlo analysis in Figure 4.5.

We find that the distribution summarising the constraint on the SNR age follows a base–10 log–normal distribution, with a median age equal to 4000 yr and with a standard deviation $\sigma_t = 0.5$ dex (the 1 σ_t range is 1200–13500 yr). The distribution summarising the constraint on the expansion velocity similarly follows a base–10 log–normal distribution with a median velocity equal to 960 kms^{-1} and a standard deviation $\sigma_v = 0.54$ dex (1 σ_v range is 275–3300 kms^{-1}). From the SNR's size, it is likely to be young and just entering the Sedov–Taylor phase of expansion and is still in the process of accelerating CRe.

The current constraints are weak and permit a large range of SNR ages and expansion velocities. The constraints can be improved with further observations of NGC1569–38's expansion velocity. Deep X–ray spectroscopy could shed light on the mechanisms producing the observed emission (Martin et al., 2002), and by observing the non–thermal properties, place further constraints on the expansion velocity (Allen et al., 2015). Additionally, the expansion velocity could be directly measured using multi–epoch VLBI observations with a long enough time baseline (Fenech et al., 2008).

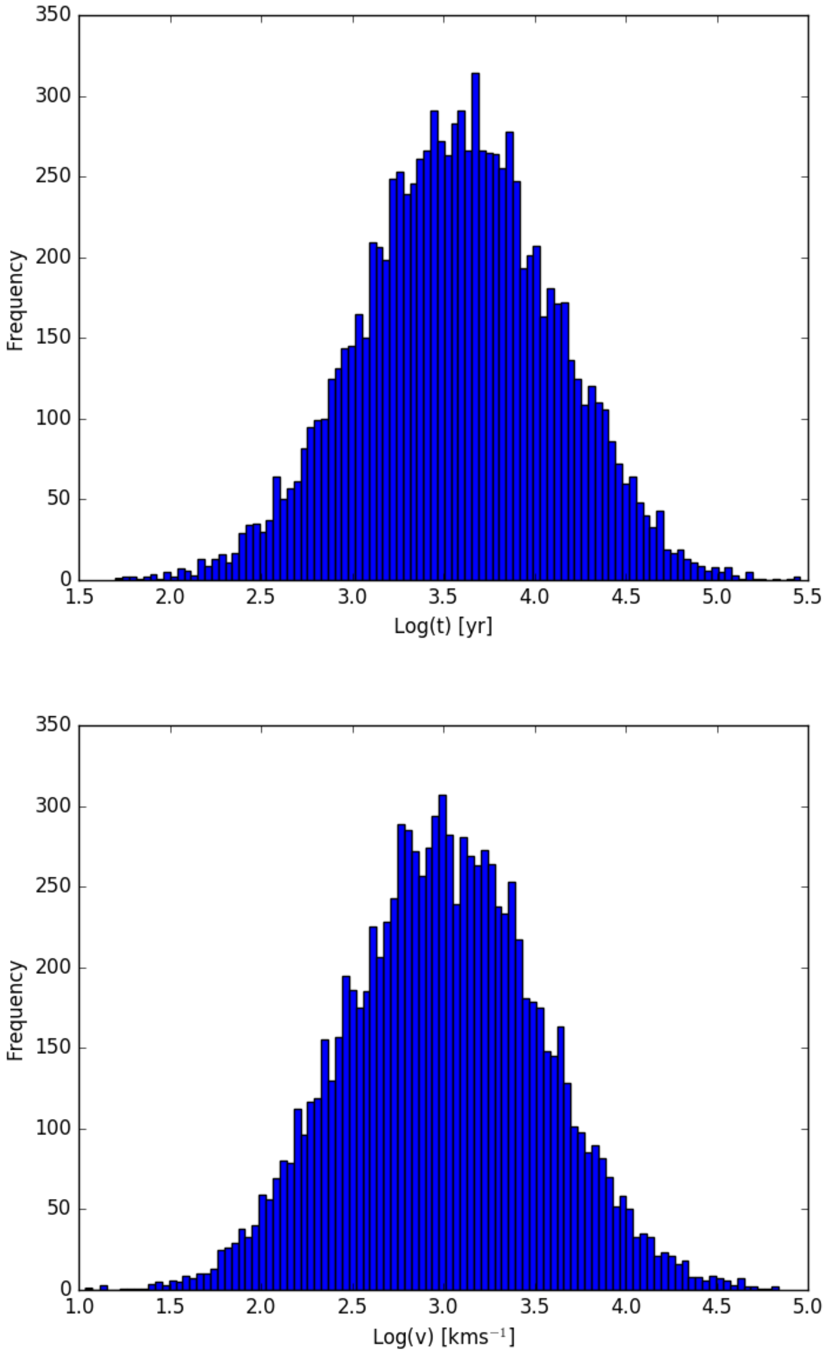

FIGURE 4.5: Distributions resulting from the Monte–Carlo simulations used to determine NGC1569–38's age and expansion velocity. The top plot shows age and the bottom plot shows expansion velocity.

4.4.2 Can The Observed Break Be Attributed To NGC1569–38?

Broken power–law radio spectra have recently been observed in integrated studies of both Galactic (Xiao et al., 2008; Pivato et al., 2013; Onić et al., 2017; Loru et al., 2018) and extra–galactic (Crawford et al., 2008; Bozzetto et al., 2010; de Horta et al., 2012) SNR, where the spectral breaks are found between 1.5 and 6 GHz (Xiao et al., 2008; Pivato et al., 2013). In previous studies, the break is typically attributed to CRe losses, primarily due to a combination of synchrotron emission and Inverse Compton scattering (Pivato et al., 2013); however some authors attribute the break to observational bias (Bozzetto et al., 2010; Urošević, 2014). Furthermore, breaks are only expected in very evolved SNR, where the accelerated CRe have had enough time to undergo radiative losses (Urošević, 2014). Other than radiative losses and Inverse Compton scattering, CRe escape with an energy dependent diffusion coefficient can also produce a break towards high frequencies. Here we analyse these two scenarios to see whether the observed break can be attributed to NGC1569–38 itself.

Is The Observed Break Due To A Combination Of Radiative Losses And Inverse Compton Scattering?

To visualize how radiative losses and Inverse Compton scattering can produce a break in the observed radio SED, we need to think about how cosmic rays can escape from the shock region in the DSA process. Cosmic rays gain energy whenever they are able to completely cross the contact discontinuity in a shockwave. On either side of the shock, the Cosmic rays undergo a random walk, where they scatter off magnetic field inhomogeneities. Upstream of the shock (outside the SNR), the accelerated Cosmic rays can only escape the shock front if they can diffuse away at a velocity larger than the shock velocity. At early times the shock velocity can be as high as $\sim 10,000\,\mathrm{km\,s^{-1}}$, so it is likely that all accelerated Cosmic rays will always be advected back across the shockfront. Downstream however (inside the SNR) it is possible for the accelerated Cosmic rays to be advected away from the shock front into the SNR interior, where they can no longer be accelerated. These Cosmic rays will remain trapped until the shockfront has slowed down enough to facilitate their diffusion into the surrounding interstellar medium. At early times we would therefore expect all of Cosmic rays that have been accelerated by the SNR shock front to be found within the SNR interior. Here they undergo adiabatic losses due to the SNR expansion and the CRe will also undergo radiative losses, due to interaction with magnetic fields found within the SNR, and potentially produce a break in the observed non–thermal radio SED.

If the cosmic ray acceleration is constant over the entire age of the SNR (which is a reasonable assumption if the density profile of the medium the SNR is expanding into is $\propto r^{-2}$; Vink 2008), then the observed non–thermal radio continuum emission will take the form of a broken power–law, analogous to that derived in Heavens and Meisenheimer (1987) and Urošević (2014). At low frequencies ($\sim$GHz), the observed spectral index α reflects the injection spectrum, but at higher frequencies it is steepened by $\alpha_{HE} = \alpha - 0.5$. The break can be interpreted as the superposition of many different CRe populations that are each in various stages of energy loss inside the strong magnetic fields. The observed break frequency then approximately corresponds to the oldest CRe population that has been advected into the SNR interior but has not yet lost all of its energy due to adiabatic losses.

To calculate whether a break can form at GHz frequencies due to radiative losses, we construct a simple model to predict where we would expect to observe a break as a function of SNR age. The location of the break frequency is dictated by the magnetic field strength the CRe population can interact with and the timescale over which they can interact:

$$\nu_{\rm break} = 1.12 \times 10^{6} \left(\frac{t}{\rm Myr}\right)^{-2} \left(\frac{B}{\mu{\rm G}}\right)^{-3} {\rm GHz}. \tag{4.2}$$

(Equation 4.2 has been adapted from Beck and Krause 2005). In our simple model, we assume that a CRe population can only undergo radiative losses over the adiabatic timescale at the time at which they were advected into the SNR interior. We choose the adiabatic timescale as our 'ageing' time, as after this timescale the CRe will have lost their energy to the expansion of the SNR and will no longer be dominating the observed radio continuum properties.

First, we need to generate a model for how the magnetic field strength the accelerated CRe 'see' varies as the SNR expands into the surrounding ISM. The magnetic field strength immediately behind a shock front is expected to be related to the shock speed through:

$$B_d \propto \sqrt{\rho_o V_s^3}, \tag{4.3}$$

where B_d is the downstream (SNR interior) magnetic field strength and ρ_o is the ambient density of the ISM. This dependence is found from analysis of magnetic field amplification in non–linear DSA theory (Bell, 2004), and evidence for this dependence has been found from measuring the widths of synchrotron X–ray filaments at the outer shocks of galactic SNR (Völk et al., 2005; Vink, 2006, 2008). We estimate the constant of proportionality by fitting a line to the compilation of magnetic field strengths, measured from the widths of X–ray filaments, and ambient particle densities presented in Vink (2006):

$$B_d \approx 4 \times 10^{-10} \left(\frac{n_o}{\mathrm{cm}^{-3}}\right)^{0.5} \left(\frac{V_s}{\mathrm{km\,s}^{-1}}\right)^{1.5} \mathrm{G}, \tag{4.4}$$

where n_o is the ambient particle density in the surrounding ISM. It is important to note that this magnetic field strength only corresponds to that found near the outer shock, and may not be representative of the magnetic field strengths found within the SNR where turbulence may enhance the magnetic field further (e.g., Ji et al., 2016). Typically the magnetic field strengths measured from radio observations are a factor of ~ 10 larger than those measured from the widths of X–ray filaments (Vink and Laming, 2003; Vink, 2006; Reynolds et al., 2012), which provides evidence for this interpretation. Therefore, to estimate the magnetic fields within the SNR interior that the radio emitting CRe are interacting with, we simply multiply Equation 4.4 by a factor of 10. We combine Equation 4.4 with the analytic solutions for how the shock velocity varies with time from Truelove and McKee (1999) to create a rough model for how the SNR magnetic field strength varies with time.

Next we need to estimate how the adiabatic loss timescale varies as the SNR expands. From Longair (2011), the energy loss rate due to adiabatic losses for a relativistic gas is given by:

$$\frac{dE}{dt} = -\frac{1}{3}\left(\nabla \cdot \mathbf{v}\right) E, \tag{4.5}$$

where $\mathbf{v}$ is the velocity distribution of the gas. If we assume that the SNR can be modeled as a uniformly expanding sphere, the velocity distribution is given through:

$$\mathbf{v} = v_o \frac{r}{R} \hat{\mathbf{r}}, \tag{4.6}$$

where v_o is the expansion velocity of the edge of the sphere, R is the radius of the sphere and $\hat{\mathbf{r}}$ is a unit vector pointing in the radial direction. The adiabatic loss timescale is then given by:

$$\tau_{ad}(t) = \frac{R(t)}{V_s(t)}, \tag{4.7}$$

where $R(t)$ describes how the SNR radius changes with time and $V_s(t)$ describes how the SNR shock velocity changes with time. Again, analytical solutions for $R(t)$ and $V_s(t)$ can readily be found in Truelove and McKee (1999).

As we are assuming that the break frequency forms over the adiabatic loss timescale, the instantaneous magnetic field strength predicted by Equation 4.4 may vary significantly over this time period, especially at early times in the SNR expansion. The break frequency should then be determined from the adiabatic loss timescale and the average magnetic field strength over this time period. The average magnetic field strength 'seen' by the radio emitting CRe as a function of SNR age is then given by:

$$\langle B \rangle (t) = 10 \times \frac{\int_{t_{min}}^{t} B_d(t')\,dt'}{\tau_{ad}(t_{min})}, \tag{4.8}$$

where τ_{ad} is the adiabatic loss timescale and t_{min} is the minimum limit for in integration, found by solving:

$$t = t_{min} + \tau_{ad}(t_{min}). \tag{4.9}$$

We plot Equation 4.8 for an example SNR in Figure 4.6.

Our simple model derived from the X–ray emission predicts that the break frequency should lie in the X–ray regime, which is promising as breaks in non–thermal X–ray spectra are typically observed in X–ray studies of galactic SNR (Reynolds, 2008). If we multiply the magnetic field strength by a factor of 10 to account for the radio emitting CRe, we find that the break frequency is predicted to be found in the $\sim \mu$m regime, i.e. we should observe a pure power–law SED at GHz frequencies. To produce a break at 10 GHz, we require the magnetic field strength to be a factor of 10 higher still (of order 10 mG, see Figure 4.6). Magnetic fields of this strength are not observed in evolved SNR (Reynolds, 2008), therefore the observed break cannot be attributed to radiative losses within NGC1569–38 itself.

The contribution of Inverse Compton scattering to radiative synchrotron losses can be estimated by computing the ratio of their energy densities. For a magnetic field strength equal to 200 μG and a radiation energy density equal to that of the CMB ($\approx 10^{-13}$ Jm^{-3}), we find a ratio equal to 7×10^{-4}. In the solar neighbourhood, the CMB is the dominant

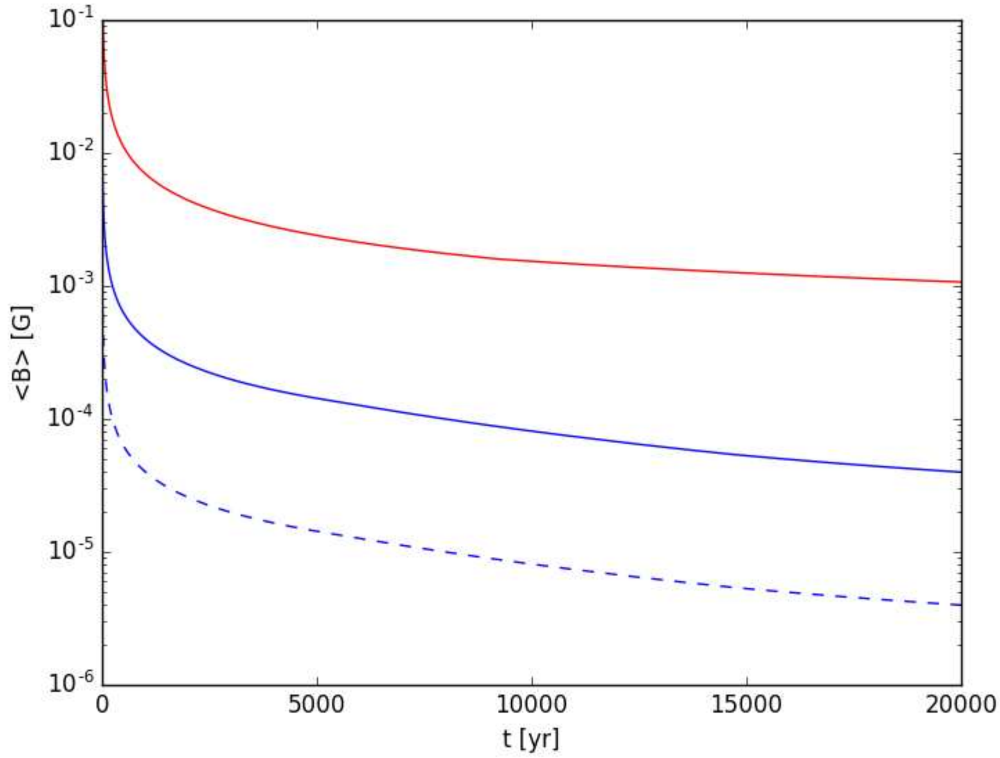

FIGURE 4.6: Plot showing the predicted average magnetic field strength as a function of time for an example SNR. The blue dashed line corresponds to a SNR with ejecta mass $M_{ej} = 30\,\mathrm{M}_{\odot}$, an explosion energy equal to 10^{44} J expanding into a ambient particle density $n_o = 1\,\mathrm{cm}^{-3}$ with a power–law ejecta density profile, $n = 7$, and was constructed using the X–ray data from Vink (2006). The blue line represents the observed magnetic field strength experienced by the radio emitting CRe (which is the X–ray model multiplied by a factor of 10; Vink and Laming 2003; Reynolds et al. 2012). The red line corresponds to the magnetic field strength required to produce a break at 10 GHz due to radiative losses only.

photon field (e.g., Vernetto and Lipari, 2016) and we would expect the energy denstiy to not vary by more than a factor of a few if the emission from dust and starlight is included. This indicates that Inverse Compton scattering is not playing a large role in producing the observed break. We would require the radiation field energy density to be $\sim 10^4$ times larger to be able to bring our simple model in line with a break at 10 GHz. It is therefore very unlikely that Inverse Compton scattering can be invoked to explain the magnetic field discrepancy between our predicted model and observed break.

Our current model does not take into account stages of SNR evolution past the Sedov–Taylor phase, which could affect whether a break is observed at ~GHz frequencies. For example, once the SNR has swept up a mass comparable to the ejecta mass, it enters the snowplow phase (Draine, 2011; Longair, 2011). Here the expansion velocity significantly slows down and we would expect from Equation 4.7 a much longer adiabatic loss timescale. The CRe that have been advected into the SNR interior would then have much longer to interact with magnetic fields and could produce an observable break at GHz frequencies. As NGC1569–38 is bright in the low–resolution VLA observations, it is likely to be young, hence we would not expect radiative losses to produce the observed break.

Is The Observed Break Due To Energy Dependent Particle Escape?

An alternative explanation for the observed break involves the preferential escape of higher energy CRe over lower energy CRe upstream of the shock during the DSA acceleration process. To see how this could produce a break, we relax the assumption that the accelerated particles will always return to the shock in the upstream medium.

The probability that the particle remains in the shock region after an entire cycle is given by:

$$P = P_{\mathrm{up}} P_{\mathrm{down}}, \tag{4.10}$$

where P_{up} is the probability that the particle remains after diffusing into the upstream medium and P_{down} is the probability that the particle is not advected into the SNR interior in the downstream medium. If we continue working through the test particle derivation of DSA (see Section 1.2.2), we arrive at the integral particle number density:

$$N(> E) = N_o \left(\frac{E}{E_o}\right)^{\frac{\ln P}{\ln \xi}}, \tag{4.11}$$

where N_o is the total number of particles at energy E_o and ξ is the fractional energy gain during a single cycle. After substituting Equation 4.10 into Equation 4.11 and noting that for strong shocks:

$$\frac{\ln P_{\mathrm{down}}}{\ln \xi} \approx -1, \tag{4.12}$$

we find that the exponent becomes:

$$\frac{\ln P}{\ln \xi} \approx -1 + \frac{\ln P_{\mathrm{up}}}{\ln \xi}. \tag{4.13}$$

As P_{up} is always between 0 and 1, the second term will be either 0 or negative and always result in a steepening of the accelerated particle energy spectrum.

We now turn our attention to how an accelerated particle could escape upstream of the shock front. Here we assume that if a particle is diffusing away from the shock front at a larger speed than the shock velocity, it has a chance to escape upstream of the shock. This condition is met if:

$$V_D \cos(\theta) \geq V_S, \tag{4.14}$$

where V_D is the average speed at which a particle diffuses, V_S is the shock speed and θ is the angle between the direction the particle is diffusing in and the direction that the shock is travelling in. We define the critial angle for escape as:

$$\theta_c = \cos^{-1}\left(\frac{V_S}{V_D}\right), \tag{4.15}$$

where $V_D \geq V_S$. θ_C corresponds to the largest angle between the particle direction and the shock direction a particle can diffuse and still escape the shock. If we assume that the particles are diffusing isotropically in the upstream medium, the probability that a particle escapes is found by calculating the solid angle subtended by angle θ_c divided by the solid angle of a sphere (4π):

$$P_{\text{esc}} = \frac{\int_0^{2\pi}\int_0^{\theta_c} \cos(\theta)\, d\theta\, d\phi}{4\pi} = \frac{1}{2}\sin(\theta_c). \tag{4.16}$$

If we substitute Equation 4.15 into 4.16, we find:

$$P_{\text{esc}} = \begin{cases} \frac{1}{2}\sqrt{1-\left(\frac{V_S}{V_D}\right)^2}, & V_D > V_S \\ 0, & V_D \leq V_S. \end{cases} \tag{4.17}$$

The probability that a particle remains within the shock front is simply $P_{\text{rem}} = 1 - P_{\text{esc}}$, which we plot in Figure 4.7. The probability that a particle remains in the shock is 1, until the diffusion speed is equal to the shock speed. After this point, the probability of remaining sharply drops towards 0.5.

Finally, we relate the diffusion velocity to the diffusing particle's energy. The particles that have been accelerated to a powerlaw energy distribution are ultra–relativistic, and so each travel at $\approx c$. Instead of streaming away from the source at this velocity, the

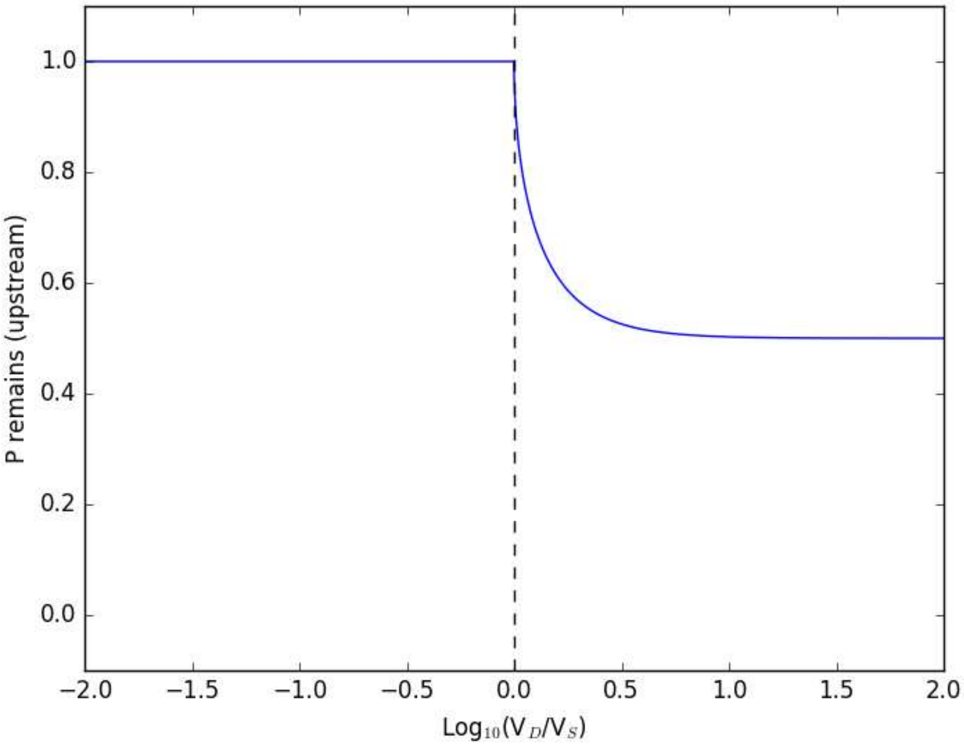

FIGURE 4.7: Plot showing how the probability a particle remains in the upstream region of the shock, P_{rem}, changes as a function of diffusion velocity. The vertical dashed line corresponds to the point at which the diffusion velocity is equal to the shock velocity.

accelerated particles undergo a random walk where they scatter off magnetic inhomogeneities that are on a comparable size scale to the accelerated particle's gyroradius. The complicated physics involved can be summarised by an isotropic diffusion coefficient in 3 spatial dimensions, given by:

$$D = \frac{\langle \Delta r^2 \rangle}{6t}, \tag{4.18}$$

where $\langle \Delta r^2 \rangle$ is the average squared particle displacement after time t. We can relate the average squared particle displacement to the diffusion velocity by considering the definition of $\langle \Delta r^2 \rangle$:

$$\langle \Delta r^2 \rangle = \frac{1}{N} \sum_{N=0}^{i} \left[R_i(t) - R_i(0) \right]^2 . \tag{4.19}$$

Here N is the total number of particles that are undergoing diffusion and $R_i(t)$ is the i'th particle position at time t. The particle's position at time t can be found through:

$$R_i(t) = R_i(0) + V_i t, \tag{4.20}$$

where V_i is the velocity required for the particle to travel in a straight line from position $R_i(0)$ to $R_i(t)$ in time t. If a particle is free streaming with no scattering events, this velocity is $\approx c$. Substituting Equation 4.20 into 4.19 we find:

$$\left\langle \Delta r^2 \right\rangle = \frac{1}{N} \sum_{N=0}^{i} V_i^2 t^2 = \left\langle V^2 \right\rangle t^2. \tag{4.21}$$

We now define the diffusion velocity as $V_D^2 = \left\langle V^2 \right\rangle$ and find that the diffusion coefficient is related to the diffusion velocity through:

$$D = \frac{V_D^2 t}{6}. \tag{4.22}$$

If the diffusion coefficient is independent of energy, then we would expect all accelerated particles to diffuse away from the shock at the same velocity. In this case, we would not observe a break as all particles will either always return to the shock, preserving the classical DSA energy spectrum, or all will escape the shock, reducing the observable radio emission equally at all frequencies.

For a break to form we require that the diffusion coefficient for the upstream medium depends upon the accelerated particle energy. In this case, some accelerated particles will be free to escape the shock front upstream whereas the others will be confined to the shock region or SNR interior. The energy dependence of the diffusion coefficient in the ISM is frequently parameterised as a power–law:

$$D(E) = \kappa E^{\mu}, \tag{4.23}$$

(Mulcahy et al., 2016; Heesen et al., 2018b). μ is poorly constrained by current observations, with literature estimates varying between 0 (i.e. no energy dependence) and 0.6 (Schlickeiser, 2002; Shalchi and Schlickeiser, 2005; Trotta et al., 2011; Mulcahy et al., 2016). As μ is generally observed to be positive, we expect that higher energy CRe will diffuse faster than lower energy CRe, and therefore that a break should form towards higher energies (frequencies). Assuming that the time the particles have been diffusing for at all energies is the same, we find:

$$V_D \propto E^{\frac{\mu}{2}}. \tag{4.24}$$

We relate 4.24 to the shock velocity by supposing that CRe with energy E_S are diffusing at the shock velocity. We can then express the diffusion velocity in terms of the shock velocity through:

$$V_D = V_S \left(\frac{E}{E_S}\right)^{\frac{\mu}{2}}. \tag{4.25}$$

From this assumed parameterisation, we can derive the differential energy spectrum. For energies $E \leq E_S$:

$$\frac{dN}{dE} = \frac{N_o}{E_o}\left(\frac{E}{E_o}\right)^{\frac{\ln(P_{\text{down}})}{\ln(\xi)}-1}, \tag{4.26}$$

and for energies $E > E_S$:

$$\frac{dN}{dE} = \left(\frac{\mu\psi}{4E_S\ln(\xi)P_{\text{up}}}\left(\frac{E}{E_S}\right)^{-(\mu+1)}\ln\left(\frac{E}{E_o}\right) - \frac{\ln(P_{\text{up}}P_{\text{down}})}{E\ln(\xi)}\right) N_o \left(\frac{E}{E_o}\right)^{\frac{\ln(P_{\text{up}}P_{\text{down}})}{\ln(\xi)}}, \tag{4.27}$$

In Equations 4.26 and 4.27:

$$\psi = \left(\sqrt{1-\left(\frac{E}{E_S}\right)^{-\mu}}\right)^{-1}, \tag{4.28}$$

$$P_{\text{down}} = 1 - \frac{V_S}{c}, \tag{4.29}$$

and:

$$\xi = 1 + \frac{V_S}{c}. \tag{4.30}$$

We plot the integrated and differential particles spectra in Figure 4.8. The spectra show the familiar test particle DSA result for strong shocks at energies $\leq E_S$, but dramatically steepens at energies $> E_S$. We investigate how much the differential energy spectrum steepens by taking the limit of Equation 4.27, assuming that $E >> E_S$. We find that the exponent tends towards:

$$\frac{dN}{dE} \propto E^{\frac{-\ln(2)c}{V_S}-2}. \tag{4.31}$$

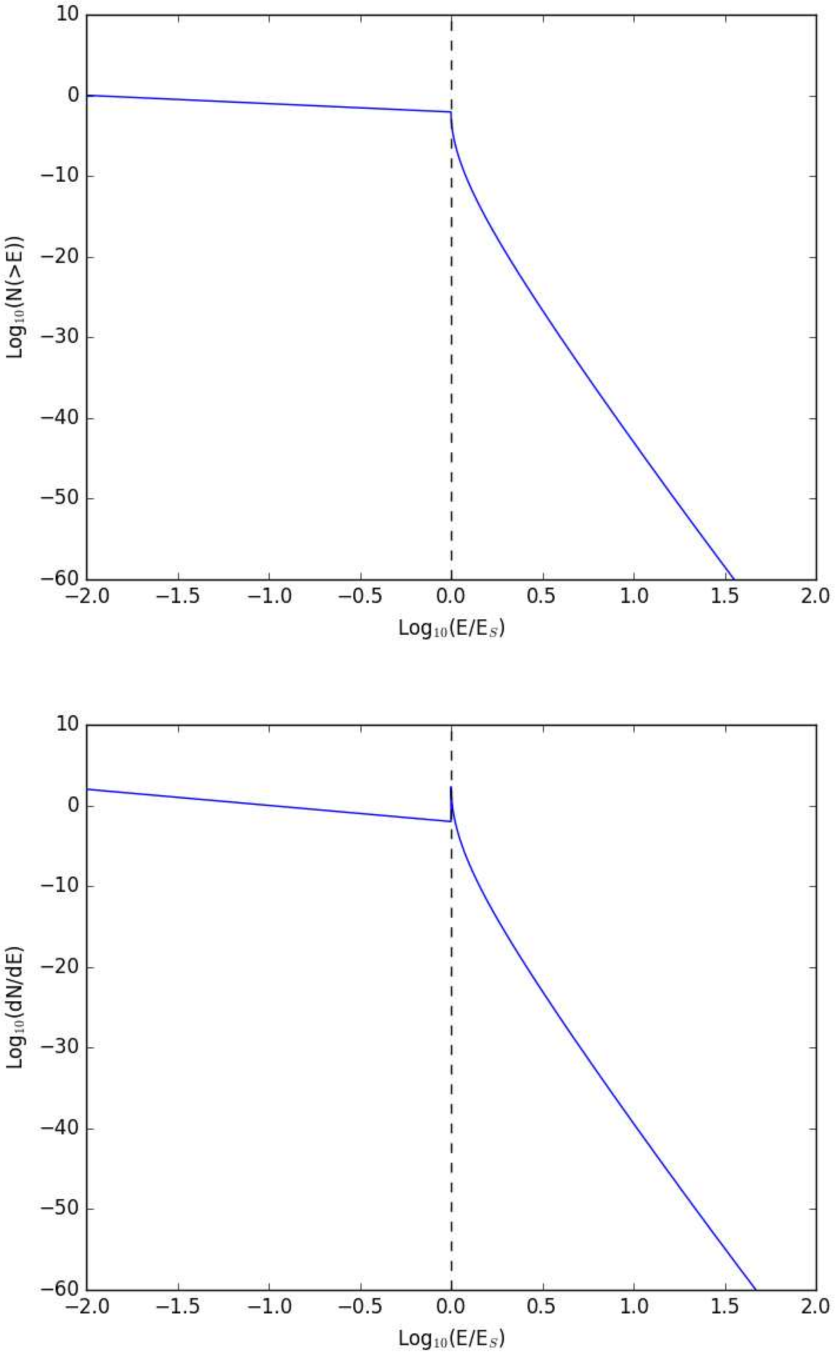

FIGURE 4.8: **Top:** Predicted integrated particle energy spectrum, assuming that particles can escape upstream of the shock at energies $E > E_S$. **Bottom:** Corresponding differential energy spectrum for the integrated energy spectrum. The normalisation on the y–axis is arbitrary as it depends upon the number of accelerated particles. The x–axis is expressed in terms of the energy normalised to that at the shock speed, E_S. The vertical line corresponds to E_S.

At high energies, the exponent is closely linked to the shock speed V_S, with slower shocks producing steeper breaks. For example, a shock with an expansion velocity equal to $1000\,\mathrm{kms^{-1}}$ will produce an exponent equal to ≈ -210 when $E >> E_S$. As this dropoff is steep and sudden, we would expect an exponential dropoff in the observed radio SED, not dissimilar to that seen in the Jaffe and Perola (1973) spectral ageing model.

As we have shown that particle escape with an energy dependent diffusion coefficient can produce a break in the observed radio SED, it is important to ask when during the SNR lifetime is this mechanism relevant? To determine this, it is useful to estimate the typical diffusion speed for accelerated particles that radiate at $\sim 10\,\mathrm{GHz}$. If we assume that the upstream diffusion coefficient is not affected by the shock (test particle approximation), we can use the measured diffusion coefficient measurements from large scale observations of nearby galaxies as an approximation for the upstream diffusion coefficient. From Mulcahy et al. (2016), for M 51 the diffusion coefficient is estimated to be $6.6 \times 10^{28}\,\mathrm{cm^2s^{-1}}$ at an observing frequency of 151 MHz. Assuming a magnetic field strength equal to $10\,\mu\mathrm{G}$, this emission originates from CRe with energy $\approx 1\,\mathrm{GeV}$. At 10 GHz, the emission originates from CRe with energy $\approx 8\,\mathrm{GeV}$, so we would expect the diffusion coefficient to scale to $1.2 \times 10^{29}\,\mathrm{cm^2s^{-1}}$, assuming $\mu = 0.3$ (Schlickeiser, 2002). Using Equation 4.22 and assuming t is equal to the synchrotron loss timescale at 10 GHz, we estimate that average diffusion speed at 8 GeV is $\approx 500\,\mathrm{kms^{-1}}$. This estimate indicates that a break due to particle escape will only be observable in evolved SNR which are approaching the fade out stage of their evolution (Draine, 2011; Longair, 2011). For a star–forming environment, the diffusion coefficient is expected to be much smaller due to turbulence from the star–forming event (Heesen et al., 2018b), and hence we would expect the diffusion velocity to be even smaller. Therefore it is unlikely that a break from this mechanism will be observable in any extra–galactic SNR, as SNR near their fade–out stage of evolution are typically too faint to be observed with current instruments. Although the observed break cannot be explained as being due to particle escape, these calculations yield useful insight as to when CRe are able to escape from their sites of acceleration into the surrounding ISM.

From this analysis, we find that NGC1569–38 likely does not contribute to the observed break. Instead we expect its radio SED to be accurately described by a power–law at radio frequencies, which is measured to have a flux density of $3.12 \pm 0.36\,\mathrm{mJy}$ at

1.5 GHz. We will assume this to be the case whilst carrying out detailed modeling the observed SED derived, from the VLA observations, in Section 4.4.4.

4.4.3 Can The Observed Break Be Attributed To The ISM Surrounding NGC1569–38?

As we have shown above, the observed break is unlikely to originate from NGC1569–38 itself. As the background emission accounts for up to $\sim 60\,\%$ of the emission observed in the low–resolution VLA maps, it is plausible that this emission is driving the observed break. If this is the case, the CRe responsible for the background non–thermal emission were accelerated in earlier SNe explosions, which have diffused into the ISM surrounding NGC1569–38 whilst undergoing various loss processes. These loss processes modify the CRe energy spectrum to depart from their initial injection spectrum ($N(E) \propto E^{-2}$). The observed break is then due to the accumulation of all of the CRe populations that are found within the vicinity of NGC1569–38, each of which is in various stages of loss.

The key process that can produce a break with the required characteristics is the synchrotron emission mechanism (Longair, 2011). It is also possible that a break can form if particles escape the galaxy through energy dependent diffusion, however a break that is formed this way is too gradual to explain the observed break due to the weak observed energy dependence and superposition of many CRe populations (Lisenfeld et al., 2004). We do not consider mechanisms that can flatten the CRe energy spectrum at lower energies (such as bremsstrahlung losses; Longair, 2011) as the low frequency spectral index is observed to be close to the expected injection index ($\alpha \approx -0.5$). If we assume that the SNe rate remains constant and that the time between SNe explosions (that accelerate the CRe) is much shorter than the loss timescale, the observed break can be interpreted according to two different scenarios, depending upon the duration of the burst of star–formation responsible for the accelerated CRe.

If the duration of the burst is shorter than or comparable to the loss timescale added to the average main sequence lifetime of the massive stars that accelerated the CRe, the break should be interpreted as having time dependent behaviour. The interpretation is then that the break corresponds to the first population of CRe, which were injected when the first massive stars ($\geq 8\,\mathrm{M}_{\odot}$) that formed during the last burst of star–formation, exploded as SNe. The oldest CRe population has experienced significant losses and is combined with many newer CRe populations (that were injected by more recent SNe) to form the break. We obtain a break with the same form to that found for the constant acceleration case (Equation 4.34; Heavens and Meisenheimer, 1987) if the star formation rate starts suddenly and remains constant for the duration of the burst. Assuming that the average magnetic field strength in NGC 1569 is $\approx 34\,\mu$G (Kepley et al., 2010; Westcott et al., 2018), we find that the break frequency corresponds to CRe that were accelerated ~ 2Myr ago. Further assuming that the main sequence lifetime for a massive star that will explode as a SNe is typically ≈ 30Myr, we find that the break would correspond with a recent starburst phase that started ≈ 32Myr ago. From the CMD analysis by McQuinn et al. (2010), we find that the most recent starburst phase started ≈ 100Myr ago, which is discrepant although not inconsistent if we take into account the large uncertainties associated their method for isolating the star formation history (≈ 0.25dex; Dolphin, 2002). Therefore it is plausible that the break could originate from CRe that were accelerated during the last burst of star–formation.

Alternatively, if the duration of the star–formation burst is much longer than the loss timescale, then the break may be due to the system reaching a steady state, where the CRe injection is balanced by the loss mechanisms. As we are looking at a small resolved section of NGC 1569. The CRe are likely to have originated from nearby SNe. If we apply the SPINNAKER steady state diffusion model from Heesen et al. (2016, 2018a), we find that with an energy independent diffusion coefficient equal to $10^{28}\,\mathrm{cm}^2\mathrm{s}^{-1}$ and an assumed magnetic field strength equal to $34\,\mu$G, we would expect to find a break at ≈ 10GHz if the region we are analysing is $\approx$1 kpc from the CRe injection site (see Figure 4.9). At the assumed distance of 3.36Mpc, NGC 1569's main star–forming region is ≈ 1kpc away from NGC1569–38. It is plausible that the break originates from CRe that have been accelerated in this region of NGC 1569 and have diffused towards NGC1569–38 if the star formation in this region has been constant for $>> 30$Myr.

From this analysis, it is certainly plausible that the break may originate from the ISM surrounding NGC1569–38, rather than NGC1569–38 itself. Additional galaxy–wide simulations should be employed to further understand how similar breaks could be formed from the combination of CRe transport and energy loss, and how these processes may vary within a given galaxy.

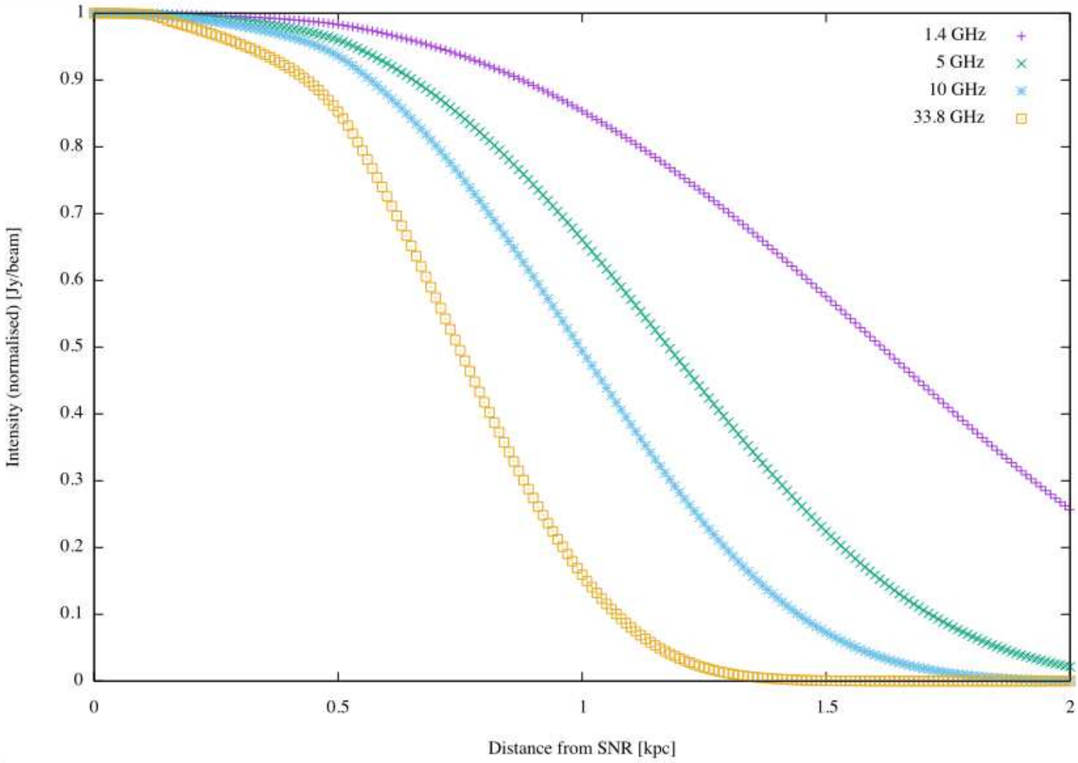

FIGURE 4.9: Results from the SPINNAKER steady state diffusion model presented in Heesen et al. (2016, 2018a) for an energy independent diffusion coefficient equal to $10^{28}\,\mathrm{cm^2 s^{-1}}$ and an ISM magnetic field strength equal to $34\,\mu$G. Each of the lines corresponds to the observable radio continuum emission at a particular frequency as a function of radius from the injection location. The profiles are narrower at higher frequencies as the corresponding CRe have a short lifetime due to radiative losses. This plot was supplied by Volker Heesen (private communication).

4.4.4 Model Fitting And Comparison

The observations of a break in the low–resolution VLA photometry (see Figure 4.4) combined with the fact that NGC1569–38 only accounts for ≈40 % of the total radio continuum emission at 1.5 GHz warrants more detailed modeling of the observed SED. Here we use the Markov–Chain Monte–Carlo (MCMC) fitting procedure detailed in Chapter 3 to fit 4 different models to the dataset presented in Table 4.2 in order to constrain the radio properties of NGC1569–38 and its surrounding ISM.

The first model we consider consists of an optically thin thermal component with a power–law non–thermal component:

$$S_\nu = A\left(\frac{\nu}{\nu_o}\right)^{-0.1} + B\left(\frac{\nu}{\nu_o}\right)^{\alpha}. \tag{4.32}$$

Here A is the thermal flux density normalisation at a reference frequency, ν_o (which is taken to be 1 GHz), B is the non–thermal normalisation at the reference frequency and α is the non–thermal spectral index. This model is the simplest that we consider, and assumes that the underlying CRe populations responsible for the observed radio emission have indistinguishable characteristics from one another (i.e. the CRe from NGC1569–38 and the background ISM have the same power–law index). This model represents the case that neither CRe population has experienced any losses and does not feature a break in the observed SED.

The second model we consider is effectively the same as the first, except we assume that the CRe population from NGC1569–38 can be distinguished from the surrounding ISM. Here we assume (as discussed earlier) that the radio SED for NGC1569–38 can be described by a power–law with spectral index $\alpha = -0.5$:

$$S_\nu = A\left(\frac{\nu}{\nu_o}\right)^{-0.1} + B\left(\frac{\nu}{\nu_o}\right)^{\alpha} + C\left(\frac{\nu}{\nu_{\mathrm{SNR}}}\right)^{-0.5}. \tag{4.33}$$

Here C corresponds to the integrated flux density measured from the e–MERLIN maps at the observed frequency, ν_{SNR} (1.5 GHz). We assume for simplicity that the SNR has a non–thermal spectral index equal to that predicted from test particle DSA with strong shocks. Similarly to the first model we considered, this model cannot produce a sharp downwards break in the observed SED.

The third model we consider consists of an optically thin thermal component with a broken power–law non–thermal component:

$$S_\nu = A\left(\frac{\nu}{\nu_o}\right)^{-0.1} + \begin{cases} B\left(\frac{\nu}{\nu_o}\right)^{\alpha} & \nu \leq \nu_b \\ B\left(\frac{\nu_b}{\nu_o}\right)^{0.5}\left(\frac{\nu}{\nu_o}\right)^{\alpha-0.5} & \nu > \nu_b \end{cases}. \tag{4.34}$$

A, B, ν_o and α are the same as in Equations 4.32 and 4.33, and ν_b represents the break frequency. In this model, we are assuming that either the SNR or the background ISM is dominating the observed radio continuum emission. In the dominating source, particle acceleration is ongoing and the CRe experience significant synchrotron and Inverse Compton losses as they diffuse away from the shock fronts where they were initially accelerated (Heavens and Meisenheimer, 1987; Urošević, 2014). Although this model is not physically likely given the high–resolution observations of NGC1569–38's integrated flux density (contributing $\sim 40\,\%$ to the observed total emission), we include it for completeness.

The fourth model we consider is the broken power–law model with an additional power–law component for NGC1569–38:

$$S_\nu = A\left(\frac{\nu}{\nu_o}\right)^{-0.1} + \begin{Bmatrix} B\left(\frac{\nu}{\nu_o}\right)^{\alpha} & \nu \leq \nu_b \\ B\left(\frac{\nu_b}{\nu_o}\right)^{0.5}\left(\frac{\nu}{\nu_o}\right)^{\alpha-0.5} & \nu > \nu_b \end{Bmatrix} + C\left(\frac{\nu}{\nu_{\rm SNR}}\right)^{-0.5}. \quad (4.35)$$

This model is the most physically motivated and captures the assumption that the SNR is young and does not have an associated break. In this model the break originates from the background ISM, where CRe that were accelerated elsewhere in NGC 1569 have diffused into the vicinity of NGC1569–38 whilst undergoing synchrotron and Inverse Compton losses.

We fit the 4 models using the MCMC fitting procedure described in Chapter 3, where we assume physically motivated priors for each of the fitted parameters: A, B, α, ν_b and C (see Chapter 3 for details). For the thermal normalisation A, we construct a prior from the Hα map presented in Hunter and Elmegreen (2004). Following Chapter 3, we treat the Hα map as a radio observation and 'image' the data using the same *uv*–distribution the radio observations sample. We then measure the Hα flux using the same method that was used for the radio data, and finally convert the observed Hα emission to a thermal radio continuum flux density using the equations from Deeg et al. (1997). For the uncertainties on this measurement, we add in quadrature a 20% systematic uncertainty in the flux scale (Hunter and Elmegreen, 2004), a 20% uncertainty associated with the Hα isolation method (Vilella-Rojo et al., 2015), a 1% uncertainty on the [NII] contribution and the photometric uncertainty from the map itself. This procedure results in a measurement of the thermal radio continuum normalisation equal to $A_{H\alpha} = 0.34 \pm 0.11$ at 1 GHz. As we do not correct the Hα maps a priori for galactic foreground extinction or internal attenuation, we interpret the thermal measurement as a lower limit for the true thermal normalisation at 1 GHz. In our modelling we therefore use a uniform prior that is tapered towards lower values for the thermal normalisation, as shown in Chapter 3 (Westcott et al., 2018). For the non–thermal normalisation B, we assume a uniform prior, which cannot take negative values and for the non–thermal spectral index α we assume the prior takes the form of a broad Gaussian distribution with a mean equal to -0.8 and a standard deviation equal to 0.4. So far, all of the above priors are the same as were defined in Chapter 3, we now describe the new assumed priors for the extra parameters.

For the break frequency, ν_b, we assume the prior takes the form of a log–normal distribution centred on 10 GHz ($\mu_\nu = 23.03$) with a standard deviation equal to 1 dex ($\sigma_\nu = 2.3$):

$$J(\nu_b, \mu_\nu, \sigma_\nu) = \frac{1}{\nu_b \sqrt{2\pi\sigma_\nu^2}} \exp\left[\frac{-(\ln(\nu_b) - \mu_\nu)^2}{2\sigma_\nu^2}\right]. \tag{4.36}$$

Finally, for the SNR normalisation, C, we assume the prior takes the form of a normal distribution with a mean $\mu_C = 3.12\,\mathrm{mJy}$ and a standard deviation equal to $\sigma_C = 0.36\,\mathrm{mJy}$, as motivated by the integrated flux density measured in the e–MERLIN observations:

$$K(C, \mu_C, \sigma_C) = \frac{1}{\sqrt{2\pi\sigma_C^2}} \exp\left[\frac{-(C - \mu_C)^2}{2\sigma_C^2}\right]. \tag{4.37}$$

We combine these new priors with the priors for A, B and α to compute the total prior distribution for use in the fitting procedure. We plot the best fitting models and corresponding posterior distributions from this procedure in Figures 4.10 and 4.12 and present the obtained parameter constraints for each model in Table 4.3.

From the model fits we find that parameter constraints are similar for both the models with the SNR included in the modelling and for those without the SNR. The thermal normalisation at 1 GHz is reliably found at $\sim 0.37\,\mathrm{mJy}$ and the non–thermal normalisation at 1 GHz is either $\sim 8\,\mathrm{mJy}$ for the models without the SNR and $\sim 4.4\,\mathrm{mJy}$ for the models with the SNR. The non–thermal spectral index is observed to be steeper in the single power–law models $\alpha \approx -0.6$ than in the broken power–law models $\alpha \approx -0.54$. These relatively shallow spectral indices correspond to those expected for a freshly accelerated CRe population (Longair, 2011) and is similar to that observed in Galactic SNR (Green, 2014). The SNR normalisation is recovered to be $\approx 3\,\mathrm{mJy}$ which is consistent with the e–MERLIN observations; the break frequency is consistently found in both broken power–law models at $\sim 7\,\mathrm{GHz}$.

From inspecting the model fits, it is apparent that the constraint on the thermal normalisation is very similar to the constraint recovered from the Hα map from Hunter and

Elmegreen (2004). The lower limit is similar to the Gaussian taper, indicating that the prior is driving the fit on the thermal normalisation. The recovered non–thermal normalisation is generally well constrained and appears roughly Gaussian in all fits, and does not appear to be affected much by the thermal prior (especially when a SNR component is included). This is due to the fact that the thermal emission plays a small role in the region's SED. In all cases the constraints on the non–thermal normalisation and non–thermal spectral index are narrower than the assumed prior, indicating that the fit is driven by the data. The SNR normalisation factor (where included) typically follows the assumed prior, indicating that we cannot gain any additional constraints on this parameter from the current observations. Finally, the break frequency appears well constrained by the observations, although there appears to be an extension towards higher break frequencies in both broken power–law models. This appears to be due to the assumed prior on the break frequency. We check this is the case by re–running the fits with only the priors. We find that the thermal and non–thermal normalisations are unconstrained in the absence of data, the non–thermal spectral index reflects the prior, the SNR normalisation reflects the Gaussian prior and the break frequency is constrained by the prior to $8.38^{+75.61}_{-7.79}$ GHz. This result shows that the observations are effectively constraining the lower–limit to the break frequency, but the upper–limit may be influenced by the assumed prior. In future fits, it will be nessesary to broaden the prior distribution on the break frequency and take extra care to ensure we are not biasing our interpretation of the data with our assumed priors.

Before we interpret these constraints, we first need to compare the models to find which one provides the best fit to the observed data.

Model Comparison

Following our model fitting, we would like to know which model best describes the observed data. We can answer this question within the Bayesian framework by adapting Equation 3.3 to ask 'What is the probability that the assumed model is correct, given the observed data?':

$$P(M|D) = \frac{P(D|M)P(M)}{P(D)}. \tag{4.38}$$

In Equation 4.38, $P(D|M)$ is the Bayesian evidence (as seen earlier in Equation 3.4), $P(M)$ is the a prior probability that the model is correct and $P(D)$ is the prior probability of observing the data. We can eliminate $P(D)$ by taking the ratio of Equation 4.38 with a

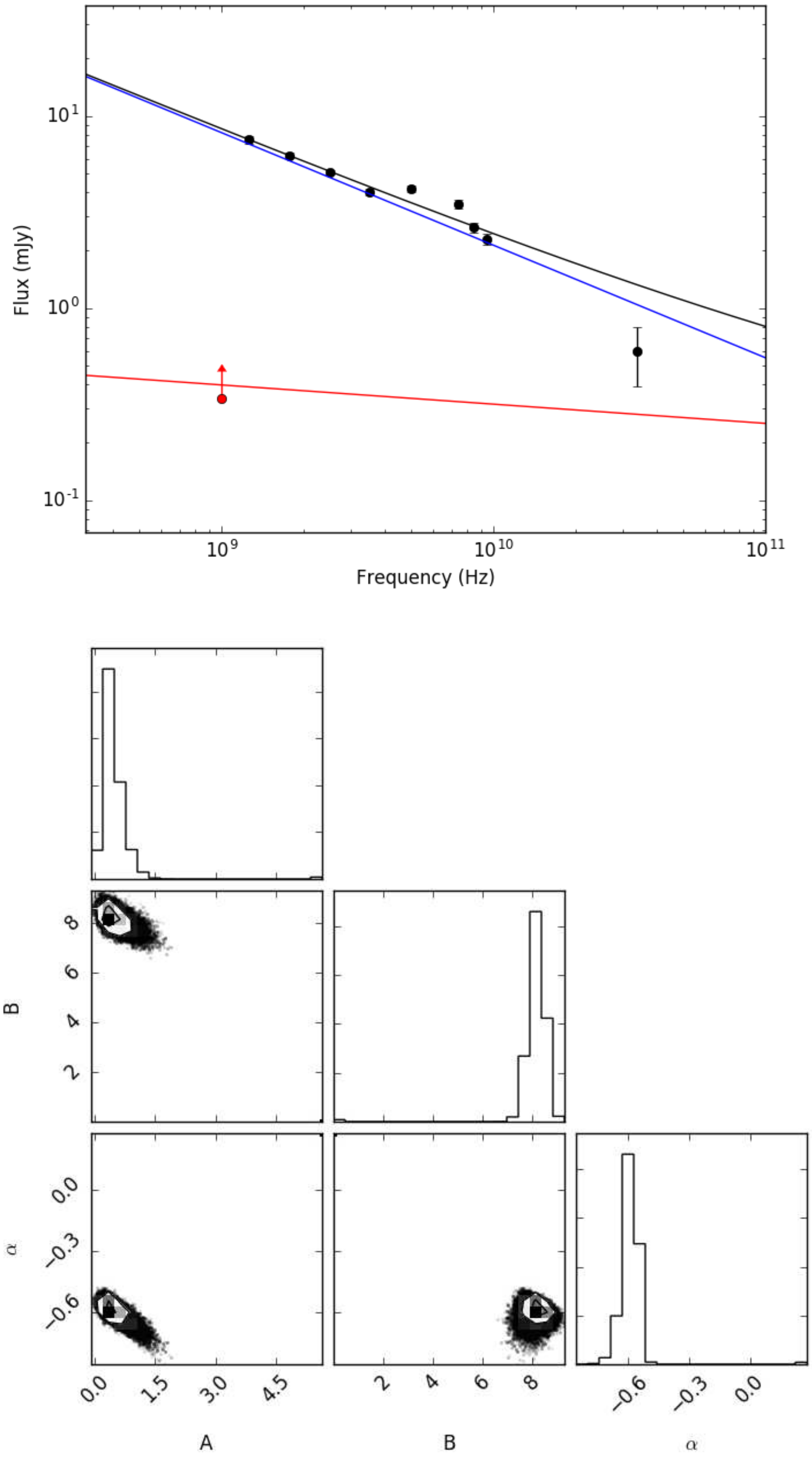

FIGURE 4.10: Best fit for the single power–law model fitted to NGC1569–38's radio SED. The top panel shows the best fitting single power–law non–thermal component model and the bottom panel shows the corresponding posterior distribution from the MCMC fitting procedure. In the top plot, the black points represent the low–resolution VLA observations presented in Table 4.2 and the red point shows the thermal prior, as determined from the Hα map. The red line corresponds to the best fitting thermal component, the solid blue line corresponds to the best fitting non–thermal component. The black line represents the total radio–continuum spectrum, i.e., the sum of all components.

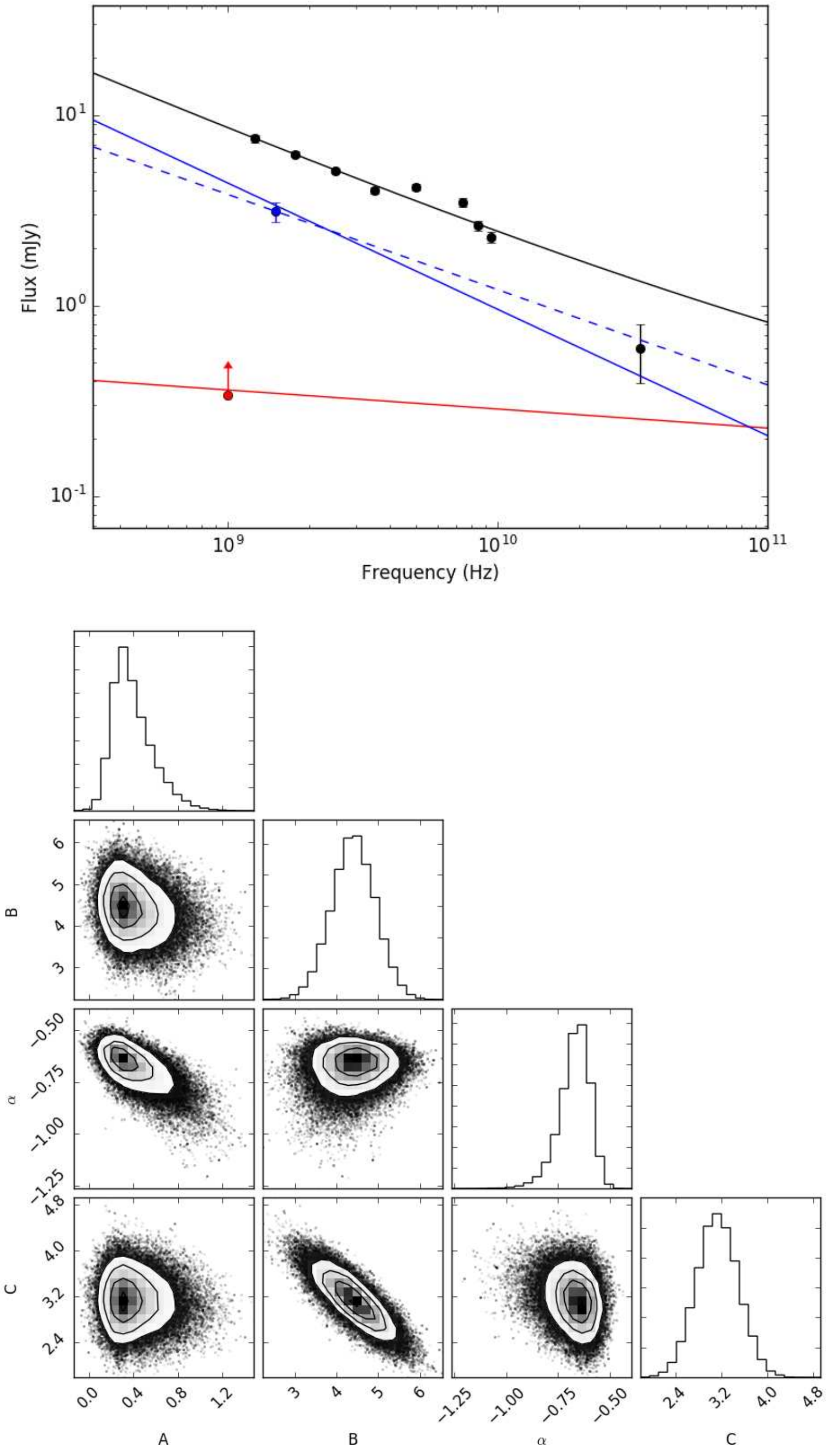

FIGURE 4.11: Best fit for the power–law model with SNR component fitted to NGC1569–38's radio SED. The top panel shows the best fitting double power–law non–thermal component model and the bottom panel shows the corresponding posterior distribution from the MCMC fitting procedure. The lines represent the same quantities as described in Figure 4.10, apart from the blue dashed line which represents the non–thermal contribution from from NGC1569–38.

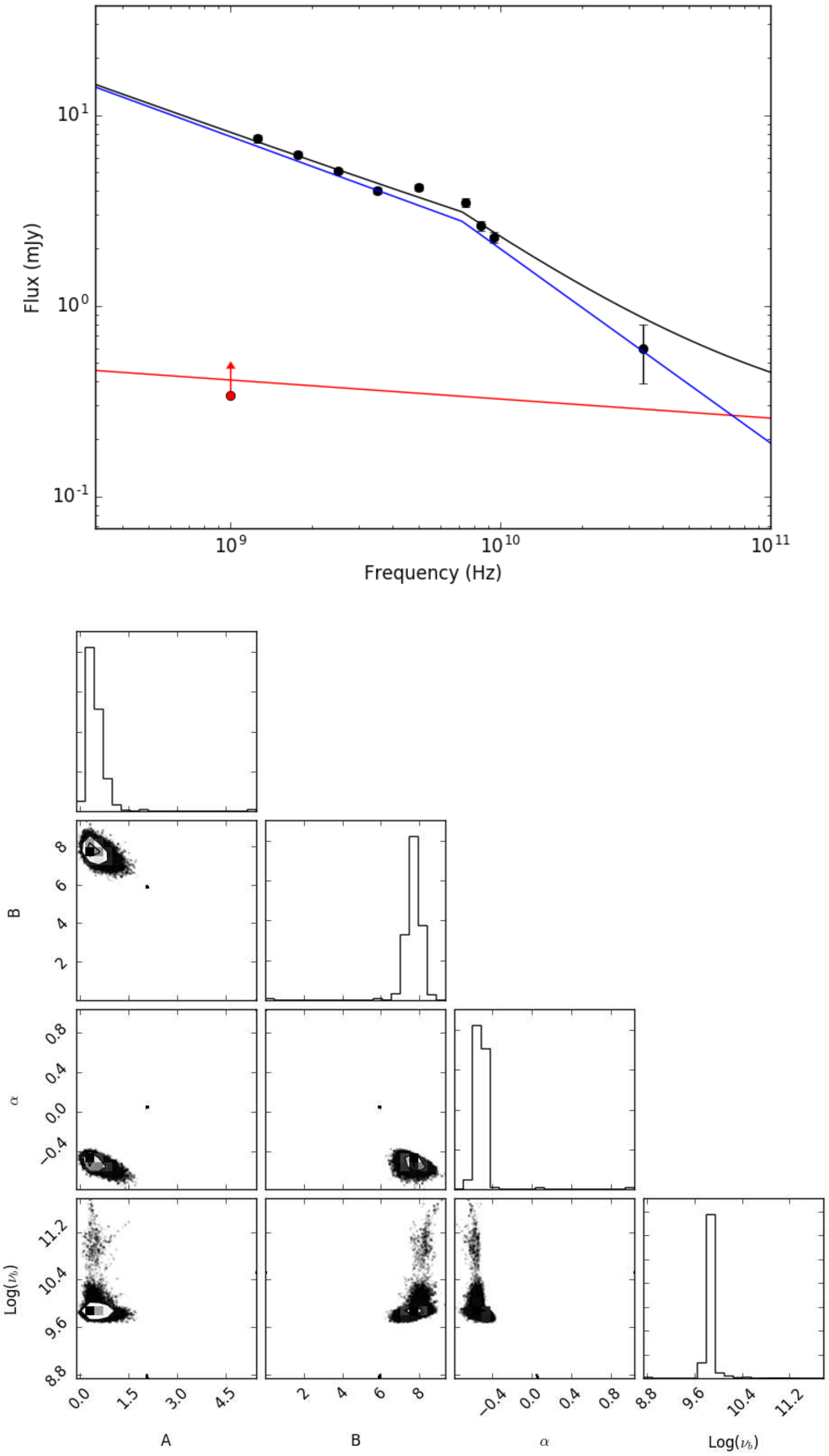

FIGURE 4.12: Best fit for the broken power–law model fitted to NGC1569–38's radio SED. The top panel shows the best fitting double power–law non–thermal component model and the bottom panel shows the corresponding posterior distribution from the MCMC fitting procedure. The lines represent the same quantities as described in Figure 4.10.

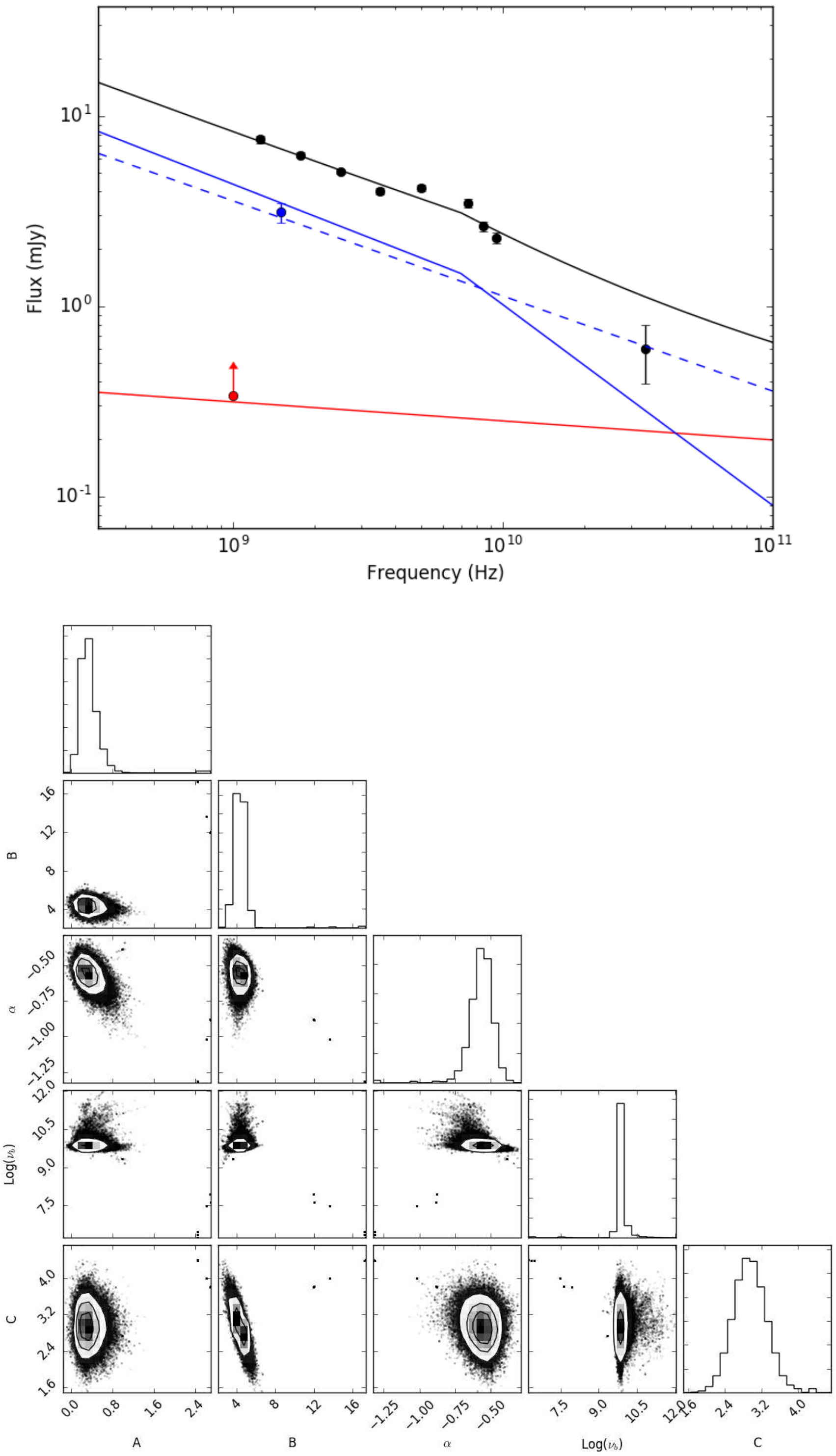

FIGURE 4.13: Best fit for the broken power–law model with SNR component fitted to NGC1569–38's radio SED. The top panel shows the best fitting double power–law non–thermal component model and the bottom panel shows the corresponding posterior distribution from the MCMC fitting procedure. The lines represent the same quantities as described in Figure 4.10, apart from the blue dashed line which represents the non–thermal contribution from from NGC1569–38.

TABLE 4.3: Parameter Constraints From MCMC Fitting Procedure

Model Designation -	Model -	A (mJy)	B (mJy)	α -	C (mJy)	ν_b (GHz)	Bayesian Evidence ($\ln[P(D\|M)]$)
M1	Single Power Law	$0.39^{+0.28}_{-0.15}$	$8.20^{+0.30}_{-0.32}$	$-0.59^{+0.03}_{-0.04}$	-	-	-23.98
M2	Single Power Law With SNR	$0.36^{+0.21}_{-0.13}$	$4.40^{+0.52}_{-0.52}$	$-0.66^{+0.06}_{-0.08}$	$3.13^{+0.36}_{-0.36}$	-	-24.43
M3	Broken Power Law	$0.41^{+0.27}_{-0.15}$	$7.73^{+0.32}_{-0.35}$	$-0.52^{+0.04}_{-0.04}$	-	$7.22^{+0.62}_{-0.67}$	-15.96
M4	Broken Power Law With SNR	$0.32^{+0.18}_{-0.12}$	$4.38^{+0.52}_{-0.52}$	$-0.56^{+0.07}_{-0.07}$	$2.94^{+0.37}_{-0.35}$	$7.03^{+1.41}_{-1.20}$	-20.33

Note: The presented best fits correspond to the median of the samples obtained through MCMC fitting procedure and the upper and lower bounds correspond to the 84th and 16th percentiles respectively.

second model:

$$\frac{P(M_1|D)}{P(M_2|D)} = \frac{P(D|M_1)}{P(D|M_2)}\frac{P(M_1)}{P(M_2)} = K\frac{P(M_1)}{P(M_2)}, \tag{4.39}$$

where K is known as the Bayes' factor. If we assume that the prior probabilities for each model are identical, the ratio of the conditional probabilities that either model 1 or model 2 is correct given the observed data is equal to the ratio of their Bayesian evidences (i.e. the Bayes' factor).

The Bayesian evidence is calculated by marginalising the product of the likelihood and prior distributions over all model parameters for a given model:

$$P(D|M) = \int P(D|\theta,M)P(\theta|M)\,d\theta. \tag{4.40}$$

Although this integration is difficult to carry out, we can approximate it through the use of the Parallel–Tempering Ensemble MCMC sampler (PTsampler) implemented in the Python package EMCEE (Foreman-Mackey et al., 2013). This sampler operates in the same way as the affine–invariant ensemble sampler presented by Goodman and Weare (2010), however the PTsampler runs multiple samplers in parallel, each at a different 'temperature'. A sampler at temperature T samples from the modified distribution:

$$\Pi_\beta = P(D|\theta,M)^\beta P(\theta|M), \tag{4.41}$$

where

$$\beta = \frac{1}{T}. \tag{4.42}$$

As the temperature gets higher, the likelihood becomes flatter and the walkers can explore a larger area of parameter space, until $T \to \infty$ where the sampler will only see the prior. During the simulation the walkers periodically swap temperatures so that 'cool' walkers can explore regions of parameter space that only 'hot' walkers can get to during the finite simulation time. Not only is this sampler well suited for sampling complex multi–modal posterior distributions, the Bayesian evidence can also be approximated through thermodynamic integration.

Following Goggans and Chi (2004), the evidence integration at temperature T can be written as:

$$Z(\beta) = \int P(D|\theta,M)^\beta P(\theta|M)\,d\theta. \tag{4.43}$$

TABLE 4.4: Bayes' Factor comparison across each model

-	M1	M2	M3	M4
M1	-	0.9	-16.0	-7.3
M2	-0.9	-	-16.9	-8.2
M3	16.0	16.9	-	8.7
M4	7.3	8.2	-8.7	-

The rows correspond to the numerator when calculating the Bayes' factor, and the columns correspond to the denominator.

For $\beta = 0$ ($T \to \infty$), the integral is equal to 1 (as we are simply integrating the normalised prior distribution). The quantity we are interested in is the case where $\beta = 1$, which corresponds to the Bayesian evidence, $P(D|M)$. Taking the natural logarithm of the left hand side of Equation 4.43 and differentiating with respect to β yields:

$$\frac{d\ln(Z(\beta))}{d\beta} = \frac{1}{Z(\beta)}\frac{dZ(\beta)}{d\beta} = \frac{\int \ln(P(D|\theta,M))P(D|\theta,M)^{\beta}P(\theta|M)\,d\theta}{\int P(D|\theta,M)^{\beta}P(\theta|M)\,d\theta}. \tag{4.44}$$

The right hand side of Equation 4.44 is the expectation value of the log likelihood, weighted by the modified distribution, Π_β, at a particular value of β:

$$\frac{d\ln(Z(\beta))}{d\beta} =< \ln(P(D|\theta,M)) >_{\beta} . \tag{4.45}$$

Finally, we integrate with respect to β to obtain the sought Bayesian evidence:

$$\ln(P(D|M)) = \ln(Z(1)) = \int_0^1 < \ln(P(D|\theta,M)) >_{\beta} \, d\beta. \tag{4.46}$$

By running the PTsampler at many temperatures and by estimating the average log likelihood at each temperature, the integral in Equation 4.46 can be approximated. For each of the 4 models we analyse, we run the PTsampler with the NTEMPS parameter set to 20 to approximate the Bayesian evidence for each model, which we present in Table 4.3.

We asses how each model compares to every other model by computing a table of the quantity $2\ln(K)$ (where K is the Bayes' factor) for each model pair, which we present in Table 4.4. We use the table presented in Kass and Raftery (1995) to asses the strength of the evidence. If this quantity is between 0 and 2, the evidence is not very strong for model 1 over model 2, if it is between 2 and 6 there is positive evidence, if it is between 6 and 10 there is strong evidence and if it is greater than 10 there is very strong evidence.

From this model comparison analysis, we find that there is strong evidence for the models including the broken power–law non–thermal component compared to the single power–law models, with the broken power–law model without the SNR being the most likely model. This result indicates that the break is likely a real feature of the data, and is likely due to the background ISM based upon the physical arguments made earlier. Although the broken power–law model with the SNR component is the more physically justified model, the broken power–law model fits the data better. Further high–resolution multi–frequency observations of NGC1569–38 are required to improve the estimate of the spectral index of the SNR and improve our understanding of the origin of the observed break.

4.4.5 Minimum Energy Magnetic Field Strength Estimation

Magnetic fields play a key role in accelerating cosmic rays to ultra–relativistic velocities in SNR shock fronts through the DSA mechanism (Bell, 1978a,b). As the observed non–thermal radio continuum emission is related to the local magnetic field strength, with some assumptions we can infer the magnetic field strength required to produce the observed emission. Through analysing the magnetic field strengths found within a SNR, we can gain insight into both the DSA mechanism and where the observed large scale radio continuum emission and magnetic fields originate.

The observed non–thermal radio continuum emission depends on the energy spectrum of the underlying ultra–relativistic CRe population and the magnetic field that they are interacting with. One set of assumptions that can be employed to extract the magnetic field strength involves assuming that the cosmic rays and magnetic fields are arranged in such a way as to minimize the total energy density. The magnetic field strength that minimises the total energy is known as the minimum energy magnetic field strength. It is important to note however that the minimum energy magnetic field strength does not necessarily correspond to the actual magnetic field strength that the particles are interacting with, instead it is the corresponding lower limit for the energy density that has true physical value. The minimum energy magnetic field strength should be used to estimate the true magnetic field strength to an order of magnitude accuracy only (Longair, 2011). Having said that, different sources can still be compared if they are subject to the same initial assumptions.

To calculate the minimum energy magnetic field strength, we start by first calculating the total energy density contained within the CRe, cosmic ray protons and the magnetic field:

$$\varepsilon_{tot} = \int EN(E)_e \, dE + \int EN(E)_p \, dE + \frac{B^2}{2\mu_o}. \tag{4.47}$$

Here $N(E)_e$ is the electron number density as a function of energy, $N(E)_p$ is the proton number density as a function of energy and B is the magnetic field strength. We now make the assumption that the electron energy spectrum takes the form $N(E)_e = \kappa_e E^{-p}$ (i.e. the electrons have not yet undergone any losses, which, as shown earlier, is a valid assumption for SNR), that the proton energy spectrum has the same form but is multiplied by the ratio of the number densities K at energy E, i.e. $K(E) = \frac{N(E)_p}{N(E)_e}$, and that we are only considering particles with energies between two limits, E_{min} and E_{max}. The equation for the total energy density then changes to:

$$\varepsilon_{tot} = \int_{E_{min}}^{E_{max}} \kappa_e E^{(1-p)} \, dE + \int_{E_{min}}^{E_{max}} K(E) \, \kappa_e E^{(1-p)} \, dE + \frac{B^2}{2\mu_o}, \tag{4.48}$$

Before we go any further, we will briefly investigate the form of $K(E)$ and the values we should assume for E_{min} and E_{max}.

From Bell (1978b), the energy spectrum for a charged particle species that has been accelerated through the classical DSA mechanism is given by:

$$N(E) = N_o(p-1)\left(E_o^2 + 2E_R E_o\right)^{\frac{(p-1)}{2}} (E + E_R)(E^2 + 2EE_R)^{\frac{-(p+1)}{2}}, \tag{4.49}$$

where N_o is the total number of injected particles, E_o is the particle injection energy and E_R is the particle rest–mass energy. In the non–relativistic regime ($E << E_R$), the energy spectra is proportional to $N(E) \propto E^{\frac{-(p+1)}{2}}$. At energies comparable to the particle rest–mass energy, the energy spectrum gradually steepens till the ultra–relativistic regime ($E >> E_R$), where $N(E) \propto E^{-p}$ (which gives rise to the assumed $N(E) = \kappa E^{-p}$ dependence). If we assume that the same number of protons and electrons are injected into the shock, from Equation 4.49 we would expect the corresponding proton and electron energy spectra to turn over at different points due to their different rest–mass energies. We present an example proton and electron energy spectrum in the left panel of Figure 4.14 and $K(E)$ for several assumed injection indices in the right panel.

We see from Figure 4.14 that $K(E)$ tends towards a constant value in the ultra–relativistic

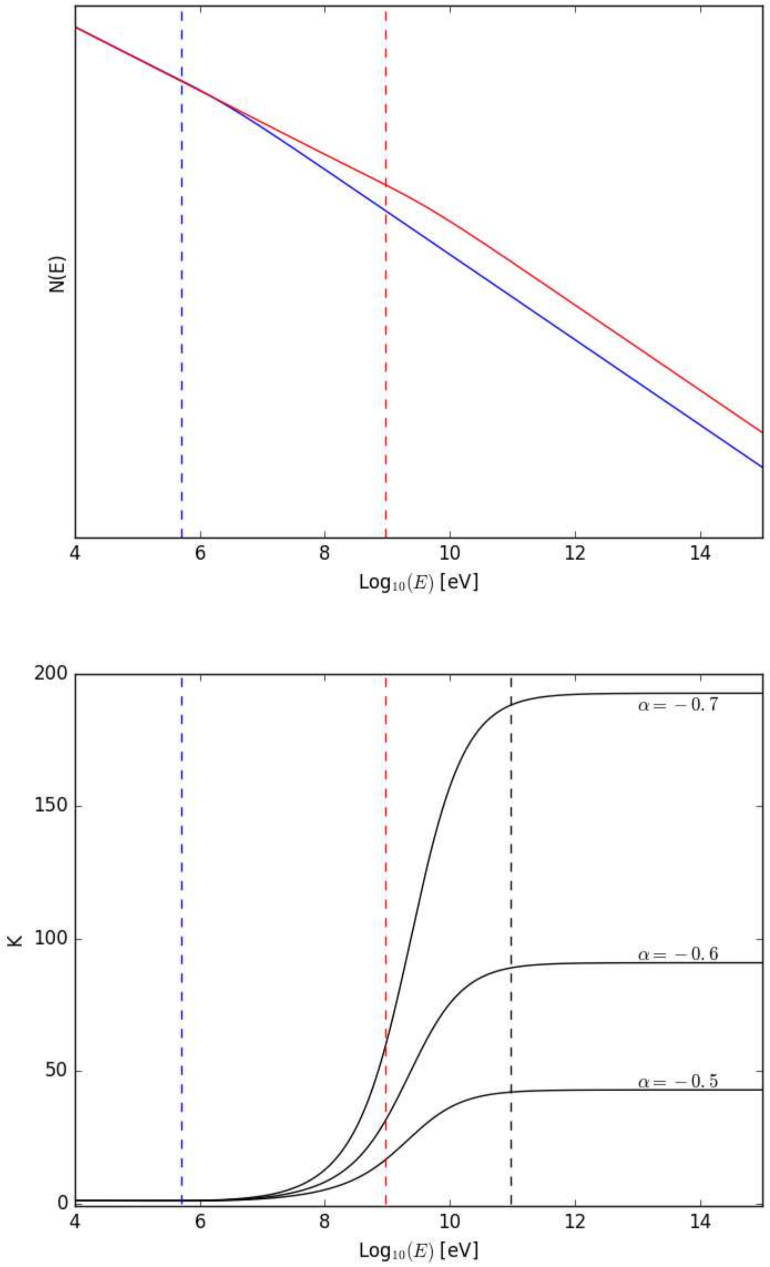

FIGURE 4.14: **Top Panel:** Energy spectra from Bell (1978b) for cosmic ray protons and CRe assuming the total number of particles is the same. The red line corresponds to the protons and the blue line corresponds to the electrons. We have plotted the proton and electron rest mass energies as the vertical dashed lines (with the same colour scheme). **Bottom Panel:** Plot showing how the ratio of the number densities of protons to electrons changes with energy for various observed spectral indices. The coloured vertical lines are the same as in the left panel, with the vertical black dashed line corresponding to the lower limit assumed in the integration ($E_{min} = 100 m_p c^2$).

regime. From Equation 4.49, we can calculate this constant value by assuming we are considering ultra–relativistic energies ($E >> E_R$) and that the particle rest–mass energy is much larger than the injection energy ($E_R >> E_o$). If these conditions are met, then $K(E)$ takes the form:

$$K(E) \approx k(p) = \left(\frac{m_p}{m_e}\right)^{\frac{(p-1)}{2}}, \tag{4.50}$$

where m_p and m_e are the masses of the proton and electron respectively. We can assume that $K(E)$ is a constant as long as we restrict our analysis to the ultra–relativistic part of the electron and proton energy spectra. We will therefore let $E_{min} = 100 m_p c^2$ to ensure we are considering the constant $K(E)$ phase only (see the right panel of Figure 4.14). For E_{max} we will assume that the maximum energy that is attained by the charged particles is equal to the 'knee' energy that is observed in the cosmic ray proton energy spectra on Earth (e.g. Bell, 2004; Eriksen et al., 2011; Thoudam et al., 2016), i.e. $E_{max} \approx$ 1 PeV. We again emphasise that we are only considering a particular energy range of the proton and electron energy spectra, hence the retrieved magnetic field strengths should not be interpreted as the true magnetic field strength. Rather they should be used for comparison purposes only with other sources under the same assumptions.

We now return to the expression for the total energy density, which takes the form:

$$\varepsilon_{tot} = \frac{(1+k(p))\kappa_e}{(2-p)} \left[E_{max}^{(2-p)} - E_{min}^{(2-p)}\right] + \frac{B^2}{2\mu_o}, \tag{4.51}$$

where we have substituted in for $K(E)$ and carried out the integration. For the special case $p = 2$, we arrive at a slightly different form:

$$\varepsilon_{tot} = (1+k(p))\kappa_e \ln\left(\frac{E_{max}}{E_{min}}\right) + \frac{B^2}{2\mu_o}. \tag{4.52}$$

We now relate the observed radio continuum properties to the energy spectrum normalisation constant κ_e. For the assumed power–law electron energy spectrum where the electrons are interacting with a randomly orientated magnetic field, the synchrotron emissivity is given in Longair (2011) as:

$$J_\nu(B) = c_1\, c_2(p)\, c_3(p)\, \kappa_e B^{\frac{(1+p)}{2}} \nu^{\frac{(1-p)}{2}}, \tag{4.53}$$

where

$$c_1 = \frac{\sqrt{3}e^3}{4\pi\varepsilon_o m_e c}, \tag{4.54}$$

$$c_2(p) = \left(\frac{3e}{2\pi m_e^3 c^4}\right)^{\frac{(p-1)}{2}}, \tag{4.55}$$

and

$$c_3(p) = \frac{\sqrt{\pi}}{2}\frac{\Gamma\left(\frac{p}{4}+\frac{19}{12}\right)\Gamma\left(\frac{p}{4}-\frac{1}{12}\right)\Gamma\left(\frac{p}{4}+\frac{5}{4}\right)}{(p+1)\Gamma\left(\frac{p}{4}+\frac{7}{4}\right)}. \tag{4.56}$$

The synchrotron emissivity can be related to the observed source flux density (assuming no absorption) through:

$$S_\nu = \int_{source}\int_l J_\nu(B, r, \alpha, \delta)\, dl\, d\Omega, \tag{4.57}$$

where l is the pathlength through the emitting material for a particular line of sight, determined through right–ascension, α, and declination, δ. For a cylindrical geometry which is uniformly filled, the flux density is:

$$S_\nu \approx l\,\Omega\, c_1\, c_2(p)\, c_3(p)\, \kappa_e B^{\frac{(1+p)}{2}} \nu^{\frac{(1-p)}{2}}, \tag{4.58}$$

where Ω is the observed source solid angle. From Equation 4.58, we identify that the observed spectral index α is related to the injection index p through $\alpha = \frac{(1-p)}{2}$. Re–arranging Equations 4.58 for κ_e and substituting into Equations 4.51 and 4.52 yields:

$$\varepsilon_{tot} = \frac{(1+k(1-2\alpha))S_\nu B^{(\alpha-1)}\nu^{-\alpha}}{(1+2\alpha)\, l\,\Omega\, c_1\, c_2(1-2\alpha)\, c_3(1-2\alpha)}\left[E_{max}^{(1+2\alpha)} - E_{min}^{(1+2\alpha)}\right] + \frac{B^2}{2\mu_o}, \tag{4.59}$$

and for the case where $\alpha = -0.5$ ($p = 2$):

$$\varepsilon_{tot} = \frac{(1+k(1-2\alpha))\, S_\nu B^{(\alpha-1)}\nu^{-\alpha}}{l\,\Omega\, c_1\, c_2(1-2\alpha)\, c_3(1-2\alpha)} \ln\left(\frac{E_{max}}{E_{min}}\right) + \frac{B^2}{2\mu_o}. \tag{4.60}$$

From Equations 4.59 and 4.60, we can understand how the derived minimum energy magnetic field strength is affected by our initial assumptions. To aid our intuition, we plot Equation 4.59 as a function of B in Figure 4.15. We see that the energy density in the Cosmic rays term (1st term; red line in Figure 4.15) is proportional to $B^{(\alpha-1)}$ and the energy density in the magnetic fields (2nd term; blue line) is proportional to B^2. If we raise the energy density in the cosmic rays (by for example, changing the limits of integration), the red line will be translated vertically and the minimum energy

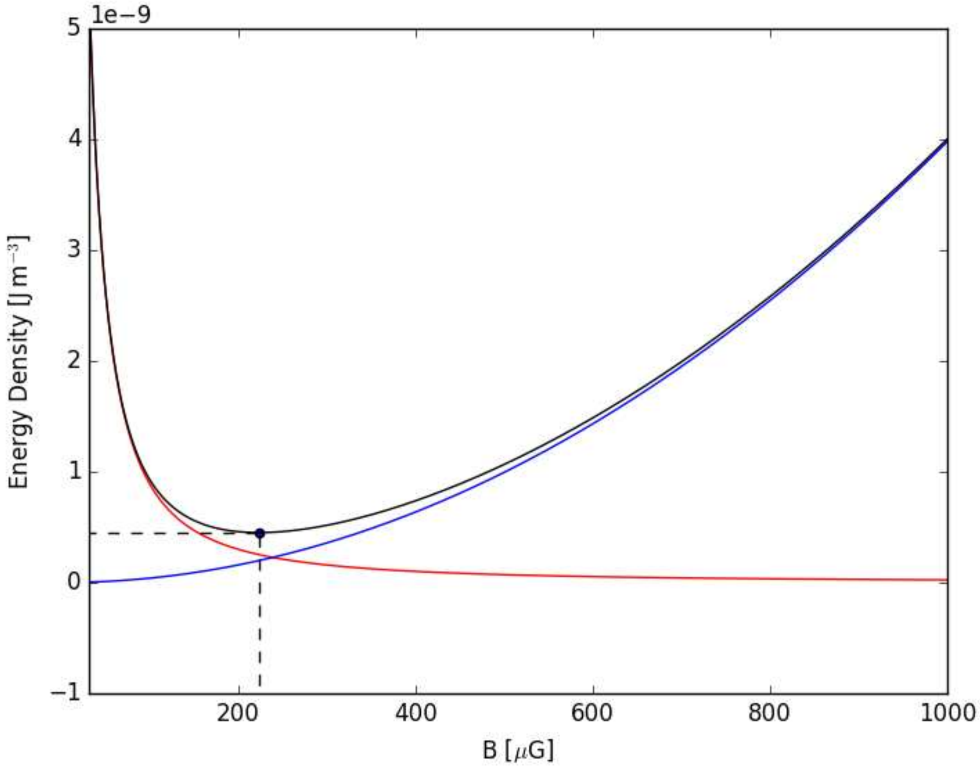

FIGURE 4.15: Plot showing energy density as a function of magnetic field strength for NGC1569–38. The red line corresponds to the energy density within the Cosmic ray protons and electrons, the blue line corresponds to the energy density within the magnetic field and the black line corresponds to the sum of the two. The black point shows the location of the minimum energy magnetic field strength found using Equation 4.61.

magnetic field strength will move to a different value. Furthermore, as the cosmic ray term depends upon the observed spectral index, steeper spectral indices result in lower overall energy densities and a lower recovered minimum energy magnetic field strength. The fact that the total energy density in the Cosmic rays is highly dependent upon our initial assumptions illustrates the limitation in this approach to measure the true magnetic field strength, and emphasises caution when interpreting magnetic fields that have been estimated in this way (or through the equipartition assumption).

Finally, we calculate the minimum energy magnetic field strength by differentiating Equations 4.59 and 4.60 with respect to B and finding the function's turning point. The minimum energy magnetic field strength is given by:

$$B_{min} = \left(\frac{\mu_o(1+k(1-2\alpha))(1-\alpha)S_\nu \nu^{-\alpha}}{(1+2\alpha)l\Omega c_1 c_2(1-2\alpha)c_3(1-2\alpha)} \left[E_{max}^{(1+2\alpha)} - E_{min}^{(1+2\alpha)} \right] \right)^{\frac{1}{(3-\alpha)}}, \tag{4.61}$$

or for the case $\alpha = -0.5$ ($p = 2$):

$$B_{min} = \left(\frac{\mu_o(1+k(1-2\alpha))(1-\alpha)S_\nu \nu^{-\alpha}}{l\Omega c_1\, c_2(1-2\alpha)\, c_3(1-2\alpha)} \ln\left(\frac{E_{max}}{E_{min}}\right)\right)^{\frac{1}{(3-\alpha)}}. \tag{4.62}$$

Equation 4.61 is functionally very similar to the minimum energy magnetic field strength derived in Beck and Krause (2005), however it is in SI units and the inclusion of the integration limits prevents the Cosmic ray energy diverging for spectral indices $\alpha \geq -0.5$ (as they assume the upper limit for the integration is $E_{max} = \infty$).

We apply Equation 4.61 to NGC1569–38, where we assume that the SNR has a flux density, S_ν, and solid angle, Ω, equal to that measured in the presented e–MERLIN observation. We also assume that the spectral index α is equal to that measured for the single power law fit to the low–resolution SED (i.e. assuming no electron losses have taken place). Finally, we calculate the pathlength through the SNR by assuming that the SNR has an approximately spherical geometry. As Equation 4.61 has been calculated for a cylindrical geometry, we calculate the effective pathlength by equating the volume of the sphere with radius R to that of a cylinder with base area πR^2 and length l:

$$\pi R^2 l = \frac{4}{3}\pi R^3, \tag{4.63}$$

therefore:

$$l = \frac{4}{3}R. \tag{4.64}$$

From this analysis we calculate that NGC1569–38 has a minimum energy magnetic field strength equal to $B_{min} = 220 \pm 20\,\mu$G and a corresponding lower–limit to the SNR remnant energy equal to $E_{SNR} \geq 3 \times 10^{42}$ J. This number is $\sim 1\,\%$ of the canonical kinetic energy associated with SNR expansion (10^{44} J; Reynolds 2008) and is a similar order of magnitude to that that estimated for Cas A by Longair (2011).

As discussed earlier, the estimated magnetic field strength does not mean much by itself as it cannot be interpreted as the true magnetic field strength. As the magnetic field strength estimate strongly depends upon the initial assumptions, we calculate the minimum magnetic field strengths for the SNR within the Green (2014) galactic and Urošević et al. (2005) extra–galactic SNR catalogues using the same assumptions as for NGC1569–38. From these catalogues, we only consider SNR with reliable spectral

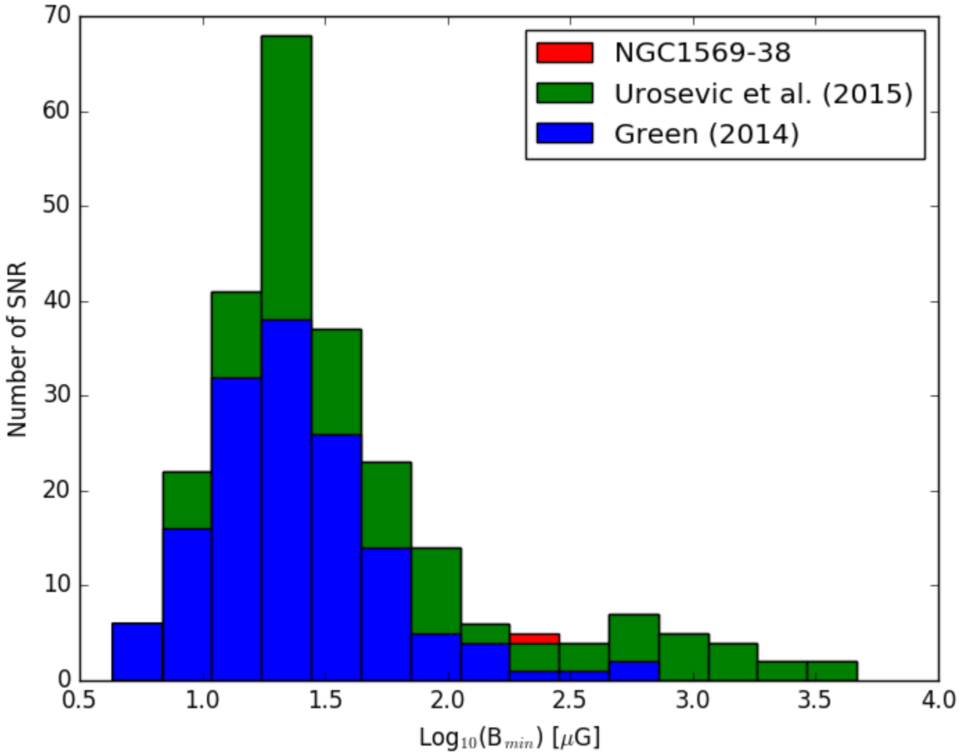

FIGURE 4.16: Histogram of B_{min} determined for the galactic SNR sample from Green (2014) and the extra–galactic SNR sample from Urošević et al. (2005). The galactic sample is presented in blue, the extra–galactic sample is presented in green and NGC1569–38 is presented in red.

index measurements, yielding a sample of 145 galactic and 100 extra–galactic SNR to compare with NGC1569–38. For each of the SNR, we estimate the minimum energy magnetic field strength using Equations 4.61 and 4.62. For the pathlength through the emitting medium, we apply Equation 4.64 to the extra–galactic SNR, as the distances to these objects are well known. For the galactic SNR we we use the empirical Σ–D relationship presented in Pavlović et al. (2013) to estimate the radius of the SNR, and then use Equation 4.64 to estimate the path length through the emitting material. In this work, we only consider their orthogonal fit, given by $\Sigma = 10^{-13.4877} D^{-4.8161}$. We present a histogram summarising the results from this analysis in Figure 4.16.

From Figure 4.16, we see that the distribution of the SNR minimum energy magnetic field strengths has a peak at $\approx 30\,\mu$G and a tail that extends towards higher magnetic field strengths as large as $\sim 1\,$mG. This trend is also seen in both the distributions for the galactic and extra–galactic SNR if they are considered separately. It is apparent the

NGC1569–38 has minimum magnetic magnetic field strength that is an order of magnitude larger than that typically found for SNR. If the minimum energy magnetic field strength can be interpreted as a proxy for the true magnetic field strength, then the distribution in Figure 4.16 could be interpreted as an evolutionary sequence, where young SNR have high magnetic field strengths which quickly decrease as the SNR expands. SNR spend the majority of their time in the Sedov–Taylor phase of expansion, which would correspond to the peak in Figure 4.16. This interpretation would also explain why we see more extra–galactic SNR at high minimum energy magnetic field strengths as observationally we are probing a much larger volume so we increase our chances of observing very young SN explosions. Furthermore, we are also observationally biased to detect brighter SNR in an extra–galactic setting, whereas in our own galaxy lower brightness SNR are more easily observed. From this interpretation, NGC1569–38 may be a young SNR which is just about to enter the Sedov–Taylor phase of expansion.

4.5 Conclusions

We present high–resolution e–MERLIN observations of the SNR NGC1569–38 at 1.5 GHz and present an analysis of the the radio SED of NGC1569–38 and its surrounding ISM found from the lower–resolution VLA observations presented in Chapter 3. Our main conclusions are as follows:

1. NGC1569–38 is resolved in the presented e–MERLIN observation with diameter 13 ± 1 pc and an integrated flux density equal to 3.12 ± 0.36 mJy at 1.5 GHz. These values are consistent with earlier MERLIN observations, however the observed flux density is $\sim 50\%$ smaller than that previously found in A–array VLA observations. The discrepancy is found to be due to diffuse contaminating emission from the ISM surrounding NGC1569–38, which is resolved out by e–MERLIN.
2. We estimate NGC1569–38's age and expansion velocity through comparison of the SNR radius with analytic models presented in the literature. We find that for physically justified explosion initial conditions, the SNR is constrained to be between 1000 and 13000 years old and is constrained to be expanding at a velocity

between 300 and 3000 $\mathrm{km s^{-1}}$. These constraints can be improved upon with additional VLBI observations of NGC1569–38 with a large enough time baseline or with deep X–ray spectroscopy of the SNR.

3. We observe a break in the spectrum derived from the low–resolution VLA observations of NGC1569–38 and its surrounding ISM. We find that NGC1569–38 only contributes 40% of the total emission recovered in the analysed aperture at 1.5 GHz, indicating that there is significant contamination from the background ISM. We analyse the cases that the break is either due to radiative losses within NGC1569–38 or due to particle escape with an energy dependent diffusion coefficient. Neither of these possibilities can produce a break within the SNR itself so we conclude that the break must be due to the background ISM.

4. We fit 4 models to the low–resolution VLA SED and find that the models with a broken power–law non–thermal component best represent the data. In these models, the non–thermal spectral index is constrained to values $\alpha \approx -0.54$ which is similar to the predicted injection spectrum for CRe. The break frequency is constrained to $\nu_b \approx 7\,\mathrm{GHz}$, which is interpreted as being due to radiative losses from CRe that are diffusing through the background ISM.

5. We estimate NGC1569–38's minimum energy magnetic field strength, and determine it to be $B_{min} = 220 \pm 20\,\mu\mathrm{G}$. This value is larger than that typically found for galactic and extra–galactic SNR, which we interpret as NGC1569–38 being a young SNR that is just entering the Sedov–Taylor phase of expansion. We find that at least 1% of the canonical kinetic energy associated with SNe explosions must go into accelerating cosmic rays and amplifying magnetic fields, which is consistent with estimates for Cassiopeia A.

Further observations at frequencies higher than 10 GHz are required to further improve constraints on the shape of the break. In addition, high–frequency observations with similar angular resolution and sensitivity to the presented e–MERLIN observation are required to analyse the spectral behaviour of NGC1569–38 in more detail.

Chapter 5

Conclusions

Over the course of this thesis, we have studied the radio continuum emission originating from the two dIrr galaxies, IC 10 and NGC 1569 over a range of spatial resolutions. Our main results are as follows:

1. High–resolution radio continuum studies of nearby galaxies at linear resolutions of ~ 1 pc are a valuable tool that can be used to identify the individual star–formation products resulting from a recent star–formation event, which we demonstrate through e–MERLIN observations of IC 10. We observe 11 compact sources coincident with IC 10's star–forming disk at 1.5 GHz, 5 of which are also detected at 5 GHz. Through a multi–wavelength classification procedure, where we take into account emission at X–ray, Hα and 70 μm as well as radio continuum emission at other frequencies, we classify 4 of the sources as HII regions belonging to IC 10, 6 of the sources as contaminating background galaxies and 1 source that is yet to be conclusively classified. We do not detect any SNR with our high resolution obervations, which may either be due to their rarity, interferometric effects or that we are observing IC 10 at a special time, where the SN explosions have not yet followed the recent star–formation burst.
2. Most of the observed sources that are associated with IC 10 are classified as HII regions, which indicates that the observed radio continuum emission from these compact sources is predominantly thermal in origin. We convert this observed thermal emission to a Lyman Continuum photon production rate, which we compare to Starburst99 stellar synthesis models to estimate lower–limits for IC 10's

current star–formation rate. We find that the star–formation rate inferred from the observed HII regions is $\mathrm{SFR}_{\mathrm{HII}} \geq 0.01\,\mathrm{M}_{\odot}\mathrm{yr}^{-1}$, which is approximately an order of magnitude smaller than that found from Hα observations, $\mathrm{SFR}_{\mathrm{H}_{\alpha}} \approx 0.08\,\mathrm{M}_{\odot}\mathrm{yr}^{-1}$. This result demonstrates that high–resolution radio–continuum studies of compact HII regions in nearby galaxies can be used to place valuable constraints on the current star–formation rate.

3. The high–resolution radio continuum observations can be used to remove the contribution of contaminating background galaxies from the integrated spectrum of the galaxy in question. For IC 10, we find this correction is small, resulting in a 4 % reduction at 1.5 GHz and a 2 % reduction at 4.85 GHz. Although this correction is small for IC 10, it could be considerably larger for fainter dwarf galaxies.

4. On larger linear scales of $\sim$ 10 pc, the thermal and non–thermal emission components can be effectively separated through the use of a Bayesian fitting procedure, where the observed Hα emission is used as a proxy for the thermal emission component. We demonstrate this procedures effectiveness by appplying it to radio continuum observations of NGC 1569 that sample a broad frequency interval (1–34 GHz).

5. On a spatially resolved basis, we find that the thermal fraction in the major star–forming regions of NGC 1569 can approach values as large as $\approx$ 50 % at 1 GHz, and on an integrated basis considering the main disk, this value drops to 25 % . Both of these thermal fractions are significantly larger than those typically found in integrated studies of larger spiral galaxies, but reflects those found to characterise other dwarf galaxies. We also find that the spatially resolved spectral indices vary between $\alpha \approx -0.4$ to -0.7 with a median value of $\alpha = -0.53$. This median value reflects the injection spectrum expected if SNR are the primary source of CRe. Together, these results indicate that NGC 1569 has recently ended its star–formation phase, which is in close agreement with the literature.

6. Once the radio–continuum emission components have been separated from the total spectrum, the resulting maps can be used to further infer useful galaxy properties. From the recovered thermal radio continuum maps, we estimate the optical line of sight reddening to NGC 1569 on a resolved basis. The average

reddening is $E(B-V) \approx 0.50\,\mathrm{mag}$, which is in excellent agreement with galactic foreground estimates in the literature. There is however significant variation in the reddening on a resolved basis, which indicates that extinction internal to NGC 1569 is significantly contributing to the observed average value.

7. We use the recovered non–thermal emission properties to infer equipartition magnetic field strengths on a resolved basis. We derive equipartition magnetic field strengths ranging from $25\,\mu\mathrm{G}$ in more quiescent regions to $38\,\mu\mathrm{G}$ in the main star–forming regions found within NGC 1569, with an average value of $32\,\mu\mathrm{G}$. These magnetic field strengths are considerably larger than those found in other dwarf galaxies, and are more similar to the magnetic field strengths found in the star–forming spiral arms of larger spiral galaxies.

8. From high–resolution e–MERLIN observations of the SNR NGC1569–38, we find that previous literature measurements concerning its integrated flux density are contaminated by emission originating from the surrounding ISM. Even compared to VLA A–Array observations, this contamination can be as large as $\approx 50\%$. We use these high–resolution observations to further constrain NGC1569–38's age to between 1000 and 13000 years old and constrain NGC1569–38's expansion velocity to be between 300 and $3000\,\mathrm{kms}^{-1}$. These constraints can be significantly improved upon with additional VLBI observations of NGC1569–38 with a large enough time baseline to observe the expansion of the SNR or with deep X–ray spectroscopy.

9. From lower–resolution VLA observations of NGC 1569, we observe a break in the integrated non–thermal radio–continuum spectrum of NGC1569–38 at $\approx 7\,\mathrm{GHz}$. By considering the cases that the break is due to radiative losses within NGC1569–38 or particle escape with an energy dependent diffusion coefficent, we determine that the observed break is not due to NGC1569–38, but instead originates from the ISM surrounding the SNR. These results have implications for the interpretation of breaks associated with synchrotron losses in radio SEDs of young, extra–galactic SNR in the literature.

10. We estimate NGC1569–38's minimum energy magnetic field strength, and determine it to be $\approx 220\,\mu\mathrm{G}$. This value is large compared to known galactic and

extra–galactic SNR, which we interpret as NGC1569–38 being a young SNR, that is just entering the Sedov–Taylor phase of expansion.

These results lead us to the following picture for the relationship between radio–continuum emission and star–formation. The observed thermal radio continuum emission provides a direct tracer of the current number of massive stars, which can be translated to a star–formation rate. The thermal radio continuum emission is predominantly confined to the individual HII regions surrounding these massive stars, which is where the majority of free–free absorption occurs. When these massive stars end their lives in SN explosions, they inject CRe with a power–law energy distribution, $N(E) = \kappa E^{-p}$ (at least at radio continuum emitting energies), where $p \approx 2$. These CRe then undergo various loss processes (principally synchrotron and Inverse Compton losses) as they diffuse away from their sites of acceleration. The observed high frequency radio continuum spectral index should be similar to the injection index if a star–forming burst has recently occurred (e.g. in IC 10 or NGC 1569), or steeper if there has been a significant time period since the last burst of star formation (in a dwarf galaxy case) or in constant star–formation scenarios (such as those found in larger spiral galaxies).

So far, current radio continuum–star formation studies have focused on the ∼GHz properties, which may be different to those found at lower frequencies, where an increasing fraction of CRe may escape before losing all of their energy, and absorption processes may become more important. These properties can be investigated with new low–frequency instruments such as LOFAR or the MWA.

Chapter 6

Future Work

Following this thesis, there is huge scope for further research. Here we outline some of the projects that we aim to complete in the near future.

6.1 Probing the Spatial and Spectral Variation of the Radio Continuum Star Formation Relation in Nearby Dwarf Galaxies

As we have shown in this thesis, the radio continuum properties of normal star–forming galaxies are very complex and still require a lot of work to fully understand. To further improve our current understanding, we should start by analysing the radio–continuum properties of nearby dwarf galaxies. Dwarf galaxies are the simplest extra–galactic star–forming objects in the Universe, and therefore serve as a natural starting point for further analysis. Additionally, dwarf galaxies are close analogues to individual $\sim$ kpc^2 regions of larger spiral galaxies (e.g., Bigiel et al., 2010; Elmegreen and Hunter, 2015) and can significantly aid in interpreting the radio–continuum emission originating from these larger systems.

The monochromatic radio continuum properties at 5 GHz have already been analysed for the LITTLE THINGS sample of dwarf galaxies (Hunter et al., 2012) by Hindson et al. (2018), yet the spectral properties at radio frequencies remain largely unknown. As we have demonstrated in Chapter 3, there is a great deal of additional information that can be retrieved by analysing the resolved radio spectral properties, such as the resolved

TABLE 6.1: available Observations of the LITTLE THINGS dwarf galaxies from VLA project code 14B–359.

Galaxy	B–Array	C–Array	D–Array
NGC 2366	L S	L S C X	S C X K
NGC 3738	L S	L S C X	S C X K
NGC 4214	L S	L S C X	C X K
DDO 50	L S	L S C X	S C X K
Mrk 178	L S	L S C X	S C X K
Haro 29	L S	L S C X	S C X K
VIIZw 403	L S	L S C X	S C X K

Note: The columns correspond to the various VLA array configurations and the letters correspond to the observed wavebands. L corresponds to 1.5 GHz, S corresponds to 3.0 GHz, C corresponds to 5.0 GHz, X corresponds to 10.0 GHz and K corresponds to 22.25 GHz.

thermal fraction, non–thermal spectral index, equipartition magnetic field strengths and estimates of the optical reddening along the line of sight. By finding similarities between these properties for the LITTLE THINGS sample, we can gain a more general view of the radio–continuum properties of dwarf galaxies and its relationship to star–formation.

A project analysing the spectral properties of dwarf galaxies using the same Bayesian methodology as discussed in Chapter 3 requires a large number of radio continuum observations at many different frequencies to be achievable. Fortunately, a lot of this data has already been taken (VLA project code: 14B–359) and is in the process of being reduced. We present an overview of the current observations available for use in this analysis in Table 6.1. Although this project already consists of a huge amount of work, it has scope to combine additional radio–continuum observations as they become available to determine additional properties, such as low–frequency LOFAR and VLA P–band (330 MHz) maps to constrain the importance of free–free absorption and CRe escape, or higher frequency observations in the 10–50 GHz range to search for AME in these low–mass systems.

6.2 Simulating the Radio–Continuum properties Originating from an Individual Star–Formation Event

In order to fully interpret the results from the project described above, it is necessary to also be able to model the radio continuum properties as a function of time for a single star–formation event in a given environment. The thermal radio continuum properties are currently well understood (see Chapter 1) and can easily be predicted from the number of massive stars that are in existence at any time. The non–thermal properties on the other hand are much more complex and can only be completely predicted by solving the diffusion loss equation for a given set of loss processes and diffusion mechanisms. The observed thermal and non–thermal radio continuum emission are produced at different times during the star–formation event, and persist for significantly different timescales. If these properties can be effectively modelled, then the integrated radio–continuum properties for entire star–forming galaxies could be estimated for a given star–formation history, by linearly combining the effects of these star–formation events at a particular time.

In the context of dwarf galaxies, the observed radio continuum emission effectively originates from a single burst of recent star–formation (e.g., McQuinn et al., 2010) which could be modelled in the discussed fashion. If this can be achieved, the observed properties such as the shape of the non–thermal component and the thermal fraction could then be used to constrain both the current star–formation rate and the recent star–formation history in these simple systems. The results from this project could then be applied to more complex star–forming galaxies to aid in interpreting their observed radio continuum properties.

6.3 Probing the Spatial and Spectral Variation of the Radio Continuum Star Formation relation in Nearby Spiral Galaxies

Although the dwarf galaxies are close analogues to the outer disk regions of larger spiral galaxies, the latter are far more complex due to the individual CRe populations from each star–formation event mixing together. Furthermore, the ordered large scale magnetic field component that is typically found in spiral galaxies (e.g. Beck, 2015) could further complicate the diffusion of CRe in these systems. On a sufficiently resolved basis however, we can limit our analysis to individual star–forming regions, allowing the reliable separation of the thermal and non–thermal radio continuum emission components. These recovered components could then used to improve current (or produce new) radio–continuum star–formation rate calibrations.

As there are many individual star–forming regions in larger spiral galaxies, we can get a much more general view of how star–formation occurs through resolved studies of these larger systems. It would also be of interest to compare the results from the larger spiral galaxies to the dwarf galaxies in order to see if there are significant differences between the observed radio continuum properties. Similar to the dwarf galaxy project, we would require a large number of radio continuum observations spanning a large range of radio frequencies to reliably separate the thermal and non–thermal emission components. Again a large number of these observations have already been taken, which we summarise in Table 6.2. In addition to the VLA observations, we also have access to low–frequency LOFAR data for a couple of the larger spirals, enabling the study of free–free absorption and CRe escape on a resolved basis in these systems.

TABLE 6.2: available Observations of the Larger Spirals from VLA projects 16B–224 and 17B–121.

Galaxy	A–Array	B–Array	C–Array	D–Array	LOFAR?
NGC 925		PLS	LSC	LSC	✗
NGC 2403		PLS	LSC	LSC	✓
NGC 6946		PLS	LSC	LSC	✓
NGC 7793	LS	LSC	LSC	LSC	✗

Note: The columns correspond to the various VLA array configurations and the final column corresponds to whether LOFAR observations are available for the galaxy. The letters correspond to the observed wavebands. P corresponds to 330 MHz, L corresponds to 1.5 GHz, S corresponds to 3.0 GHz and C corresponds to 5.0 GHz. The LOFAR observations are taken at 150 MHz.

6.4 Analysing the Low–Frequency Behaviour for a Large Sample of Nearby Star–Forming Galaxies

Recently, Chyży et al. (2018) demonstrated that free–free absorption does appear to significantly alter the observed low–frequency radio continuum properties of a sample of nearby star–forming galaxies, and showed statistically that the low frequency (50 MHz – 1.5 GHz) radio spectral indices of star–forming galaxies are flatter than those measured at higher frequencies (1.3 GHz – 5.0 GHz). The observed low–frequency spectral indices ($\alpha_{low} = -0.57 \pm 0.01$) are reasonably close to the injection index from SNR (Green, 2014), yet the range over which this spectral index is calculated is too broad to directly confirm this to be the case.

To more directly confirm that the low–frequency radio continuum spectra from star–forming galaxies tends towards the injection index (or that other loss processes are important at these low–frequencies, such as ionisation losses), one would need to compare the low–frequency spectral indices over smaller frequency intervals. These spectral indices could be recovered from ongoing or already existing large area sky surveys such as the LOFAR Two–metre Sky Survey (LoTSS; Shimwell et al., 2017) at 150 MHz, the Westerbork Northern Sky Survey (WENSS; Rengelink et al., 1997) at 330 MHz and the NRAO VLA Sky Survey (NVSS; Condon et al., 1998) at 1.4 GHz. With the larger sample sizes from these surveys we can constrain the importance of free–free absorption across galaxy type and inclination and confirm whether or not the low–frequency radio continuum spectrum reflects the CRe injection index from SN explosions.

Appendix A

The Lorentz Transformations And Their Applications

A.1 The Lorentz Transformations

The following largely follows the discussion of the Lorentz transformations from Rybicki and Lightman (1979). The Lorentz transformations between a stationary reference frame (with space–time coordinates: t, x, y, z) and a reference frame moving with constant velocity, v (with corresponding space–time coordinates: t', x', y', z') are defined as:

$$\begin{aligned} t' &= \gamma\left(t - \frac{vx}{c^2}\right) \\ x' &= \gamma(x - vt) \\ y' &= y \\ z' &= z, \end{aligned} \tag{A.1}$$

where γ is the Lorentz factor, defined as:

$$\gamma = \frac{1}{\sqrt{1 - \left(\frac{v}{c}\right)^2}} = \frac{1}{\sqrt{1 - \beta^2}}. \tag{A.2}$$

The corresponding inverse transformations are given by:

$$\begin{aligned} t &= \gamma\left(t' + \frac{vx'}{c^2}\right) \\ x &= \gamma(x' + vt) \\ y &= y' \\ z &= z'. \end{aligned} \tag{A.3}$$

The Lorentz transformations apply to any set of physical quantities that make up a four vector. Another four vector consists of Energy, E, and momentum, p. Thus the Lorentz transformations in this case can be written as:

$$\begin{aligned} E' &= \gamma(E - \beta p_x c) \\ p'_x c &= \gamma(p_x c - \beta E) \\ p'_y c &= p_y c \\ p'_z c &= p_z c, \end{aligned} \tag{A.4}$$

with corresponding inverse transformations given by:

$$\begin{aligned} E &= \gamma(E' + \beta p'_x c) \\ p_x c &= \gamma(p'_x c + \beta E') \\ p_y c &= p'_y c \\ p_z c &= p'_z c. \end{aligned} \tag{A.5}$$

All of the results derived using the Lorentz transformations can equivalently be used for another four vector (by simply substituting in the desired quantities).

A.2 Time Dilation

From the Lorentz transformations, we can derive how the period of time measured in a moving (primed) reference frame differs from a stationary (non primed) reference frame. To do this, we assume that a time difference is measured in the moving reference frame, $\Delta t' = t_2' - t_1'$, at a constant position, $x_2' = x_1'$. From the Lorentz transformations:

$$\Delta t' = \gamma\left(t_2 - \frac{v}{c^2}x_2\right) - \gamma\left(t_1 - \frac{v}{c^2}x_1\right) = \gamma\left(\Delta t - \frac{v}{c^2}(x_2 - x_1)\right). \tag{A.6}$$

as $x_2 \neq x_1$, we need to again apply the Lorentz transformations to x_2 and x_1:

$$x_2 - x_1 = \gamma(x_2' + vt_2') - \gamma(x_1' + vt_1') = \gamma v \Delta t'. \tag{A.7}$$

Substituting Equation A.7 into A.6, we find:

$$\Delta t' = \gamma\left(\Delta t - \gamma\frac{v^2}{c^2}\Delta t'\right), \tag{A.8}$$

which can be re–arranged to find:

$$\left(1 + \gamma^2\frac{v^2}{c^2}\right)\Delta t' = \gamma\Delta t. \tag{A.9}$$

As $\left(1 + \gamma^2\frac{v^2}{c^2}\right) = \gamma^2$:

$$\Delta t = \gamma\Delta t', \tag{A.10}$$

i.e., observers in the moving (primed) reference frame will always measure shorter times than those in the stationary (non primed) reference frame. This effect is symmetrical as both observers would argue the other is experiencing time differently.

A.3 Velocity Transformations

If an object has a velocity u' in the moving (primed) frame, the velocity components in the stationary frame can be found through:

$$u_x = \frac{dx}{dt} = \frac{dx}{dt'}\frac{dt'}{dt} = \frac{u_x' + v}{(1 + \frac{\beta}{c}u_x')}$$

$$u_y = \frac{dy}{dt} = \frac{dy}{dt'}\frac{dt'}{dt} = \frac{u'_y}{\gamma(1+\frac{\beta}{c}u'_x)}$$

$$u_z = \frac{dy}{dt} = \frac{dz}{dt'}\frac{dt'}{dt} = \frac{u'_z}{\gamma(1+\frac{\beta}{c}u'_x)}. \tag{A.11}$$

It is useful to write the velocity transformation equations in terms of the components parallel and perpendicular to the direction of the frames velocity, $u_\parallel$ and $u_\perp$:

$$u_\parallel = u\cos(\theta) = \frac{u'\cos(\theta') + v}{(1+\frac{\beta}{c}u'\cos(\theta'))}$$

$$u_\perp = u\cos(\theta) = \frac{u'\sin(\theta')}{\gamma(1+\frac{\beta}{c}u'\cos(\theta'))} \tag{A.12}$$

where θ' is the angle between the direction of the object's movement and the reference frames movement in the moving frame, and θ is the angle in the stationary frame. It should be noted that as these results are symmetric about $\theta = 0$, the azimuthal component ϕ does not change. In the special case that $c = u' = u$, then the velocity addition equations change to:

$$\cos(\theta) = \frac{\cos(\theta') + \beta}{1 + \beta\cos(\theta')}$$

$$\sin(\theta) = \frac{\sin(\theta')}{\gamma(1+\beta\cos(\theta'))}. \tag{A.13}$$

A.4 Acceleration Transformations

If the object is instead accelerating in the moving (primed) reference frame, the acceleration components in the stationary frame can be found through:

$$a_x = \frac{du_x}{dt} = \frac{du_x}{dt'}\frac{dt'}{dt} = \frac{a'_x}{\gamma^3(1+\frac{\beta}{c}u'_x)^3}$$

$$a_y = \frac{du_y}{dt} = \frac{du_y}{dt'}\frac{dt'}{dt} = \frac{a'_y\left(1+\frac{\beta}{c}u'_x\right) - \frac{\beta}{c}u'_y a'_x}{\gamma^2\left(1+\frac{\beta}{c}u'_x\right)^3}$$

$$a_z = \frac{du_z}{dt} = \frac{du_z}{dt'}\frac{dt'}{dt} = \frac{a'_z\left(1+\frac{\beta}{c}u'_x\right) - \frac{\beta}{c}u'_z a'_x}{\gamma^2\left(1+\frac{\beta}{c}u'_x\right)^3}. \tag{A.14}$$

Similarly to the velocity transformations, we can express the acceleration components in terms of the parallel and perpendicular components, $a_{\|}$ and $a_{\perp}$:

$$a_{\|} = \frac{a'_{\|}}{\gamma^3\left(1+\frac{\beta}{c}u'_{\|}\right)^3}$$

$$a_{\perp} = \frac{a'_{\perp}\left(1+\frac{\beta}{c}u'_{\|}\right) - \frac{\beta}{c}\,u'_{\perp}\,a'_{\|}}{\gamma^2\left(1+\frac{\beta}{c}u'_{\|}\right)^3}. \tag{A.15}$$

For the special case that the object is instantaneously at rest in the moving (primed) frame of reference ($u'_{\|} = u'_{\perp} = 0$), we find:

$$a_{\|} = \frac{a'_{\|}}{\gamma^3}$$

$$a_{\perp} = \frac{a'_{\perp}}{\gamma^2}. \tag{A.16}$$

A.5 The Angular Distribution Of Power From A Relativistic Charge

Using the above results, we can derive how the power emitted from a charged particle moving at relativistic speeds is seen by a stationary observer. We first note that in the moving frame, the charged particle emits its power in a dipole pattern:

$$\frac{dE'}{dt'd\Omega'} = \frac{Z^2e^2}{16\pi^2\varepsilon_0 c^3}\,|a'|^2\sin^2(\psi'), \tag{A.17}$$

where ψ is taken from the direction of acceleration. To obtain the desired result, we need to transform the emitted power pattern to that observed in the stationary frame. This task is simple if we consider each of the primed quantities individually.

The first quantity we consider is the dE' in the numerator of the differential. We can obtain the transformation to the observed frame by considering the Lorentz transformations in Equations A.4:

$$E' = \gamma(E+\beta p_x c). \tag{A.18}$$

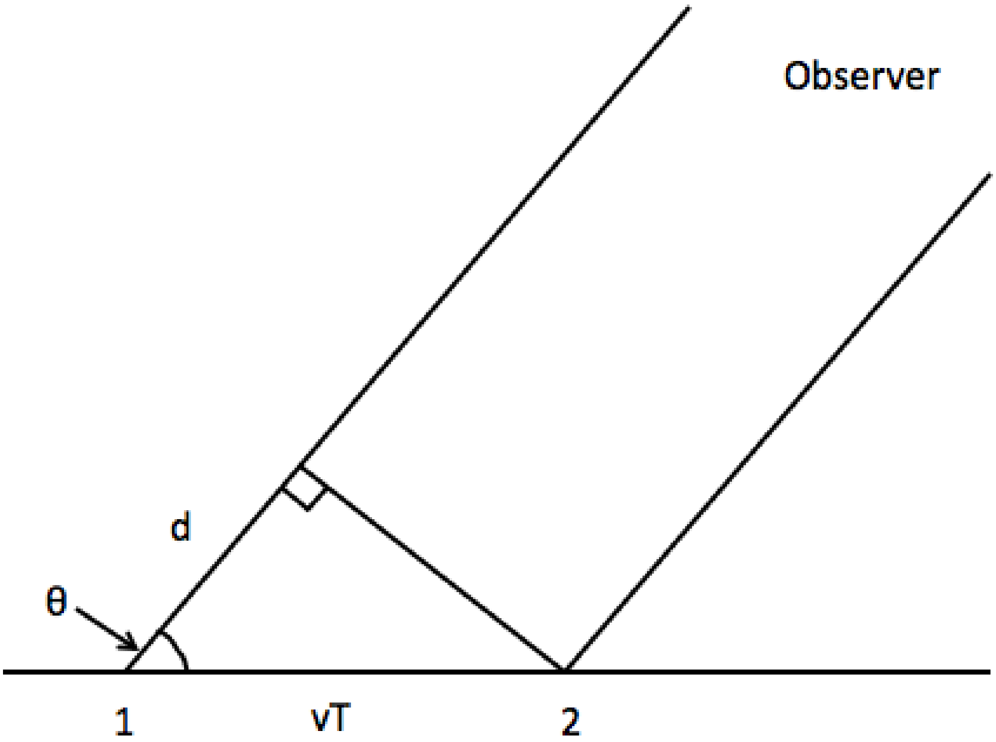

FIGURE A.1: Diagram illustrating the geometry for the Doppler effect.

The momentum in the x–direction can be written in terms of the total momentum through $p_x = p\cos(\theta)$:

$$E' = \gamma(E + \beta p \cos(\theta)\, c). \tag{A.19}$$

After noting that $E = pc$, we differentiate A.19 with respect to E, we find:

$$\frac{dE'}{dE} = \gamma(1 + \beta \cos(\theta)). \tag{A.20}$$

Therefore, the energy increment in the moving frame is related to the energy increment in the stationary frame through:

$$dE' = \gamma(1 + \beta \cos(\theta))\, dE. \tag{A.21}$$

The next quantity we consider is the dt' in the denominator of the differential. The transformation for this quantity can be found by considering the relativistic Doppler effect. Consider an object that is traveling along a path at a constant velocity, v (see

Figure A.1). At positions 1 and 2, the particle emits a pulse of light which is detected by an observer. According to an observer perpendicular to the object's motion, the time between pulses is T. At an angle θ, the Doppler effect modifies the observed time between pulses to:

$$T_{obs} = T - \frac{d}{c} = T - T\frac{v}{c}\cos(\theta) = T(1-\beta\cos(\theta)). \tag{A.22}$$

The time between pulses according to the particle is T', which is related to the time between pulses by the stationary observer (with no Doppler effect) through the time dilation equation:

$$T = \gamma T'. \tag{A.23}$$

Therefore:

$$T_{obs} = \gamma(1-\beta\cos(\theta))\,T'. \tag{A.24}$$

We obtain the desired transformation by differentiating Equation A.24 with respect to T' and re–arranging the result:

$$dt' = \frac{1}{\gamma(1-\beta\cos(\theta))}\,dt. \tag{A.25}$$

Next we consider the transformation of $d\Omega'$ in the denominator of the differential. If we let $\mu = \cos(\theta)$ and $\mu' = \cos(\theta')$:

$$d\Omega = \sin(\theta)\,d\theta\,d\phi = d\mu\,d\phi,$$

$$d\Omega' = \sin(\theta')\,d\theta'\,d\phi' = d\mu'\,d\phi'. \tag{A.26}$$

From Equation A.13, we find:

$$\mu' = \frac{\mu-\beta}{1-\beta\mu}, \tag{A.27}$$

which, differentiated with respect to μ yields:

$$\frac{d\mu'}{d\mu} = \frac{1}{\gamma^2(1-\beta\mu)^2}. \tag{A.28}$$

As $d\phi = d\phi'$:

$$d\Omega' = \frac{d\Omega}{\gamma^2(1-\beta\mu)^2} = \frac{d\Omega}{\gamma^2(1-\beta\cos(\theta))^2}. \tag{A.29}$$

Bringing Equations A.21, A.25 and A.29 together, we find:

$$\frac{dE}{dt\,d\Omega} = \frac{1}{\gamma^4(1-\beta\,\cos(\theta))^4}\,\frac{dE'}{dt'\,d\Omega'}. \tag{A.30}$$

We now explore two scenarios for the direction of the acceleration, the case where it is parallel to the direction of motion of the moving frame, and the case where it is perpendicular to the direction of motion of the moving frame. In the case where it is parallel, we find that $\psi' = \theta'$, and $|a'|^2 = \gamma^6\,|a_{\parallel}|^2$. After applying the angle transformations given in Equation A.13 we find:

$$\frac{dE}{dt\,d\Omega} = \frac{Z^2 e^2 |a_{\parallel}|^2}{16\pi^2 \varepsilon_0 c^3}\,\frac{\sin^2(\theta)}{(1-\beta\,\cos(\theta))^6}. \tag{A.31}$$

For the perpendicular case, we can relate ψ' to θ' and ϕ' by taking the dot product of the direction of acceleration (assumed to be in $[\theta' = \frac{\pi}{2}, \phi' = 0]$) with the direction of radiation. We find $\cos(\psi') = \sin(\theta')\cos(\phi')$, which gives rise to $\sin^2(\psi') = 1 - \sin^2(\theta')\cos^2(\phi')$. As $|a'|^2 = \gamma^4\,|a_{\parallel}|^2$, we find:

$$\frac{dE}{dt\,d\Omega} = \frac{Z^2 e^2 |a_{\perp}|^2}{16\pi^2 \varepsilon_0 c^3}\,\frac{1}{(1-\beta\,\cos(\theta))^4}\left[1 - \frac{\sin^2(\theta)\,\cos^2(\phi)}{\gamma^2(1-\beta\,\cos(\theta))^2}\right]. \tag{A.32}$$

We plot Equations A.31 and A.32 in Figure A.2.

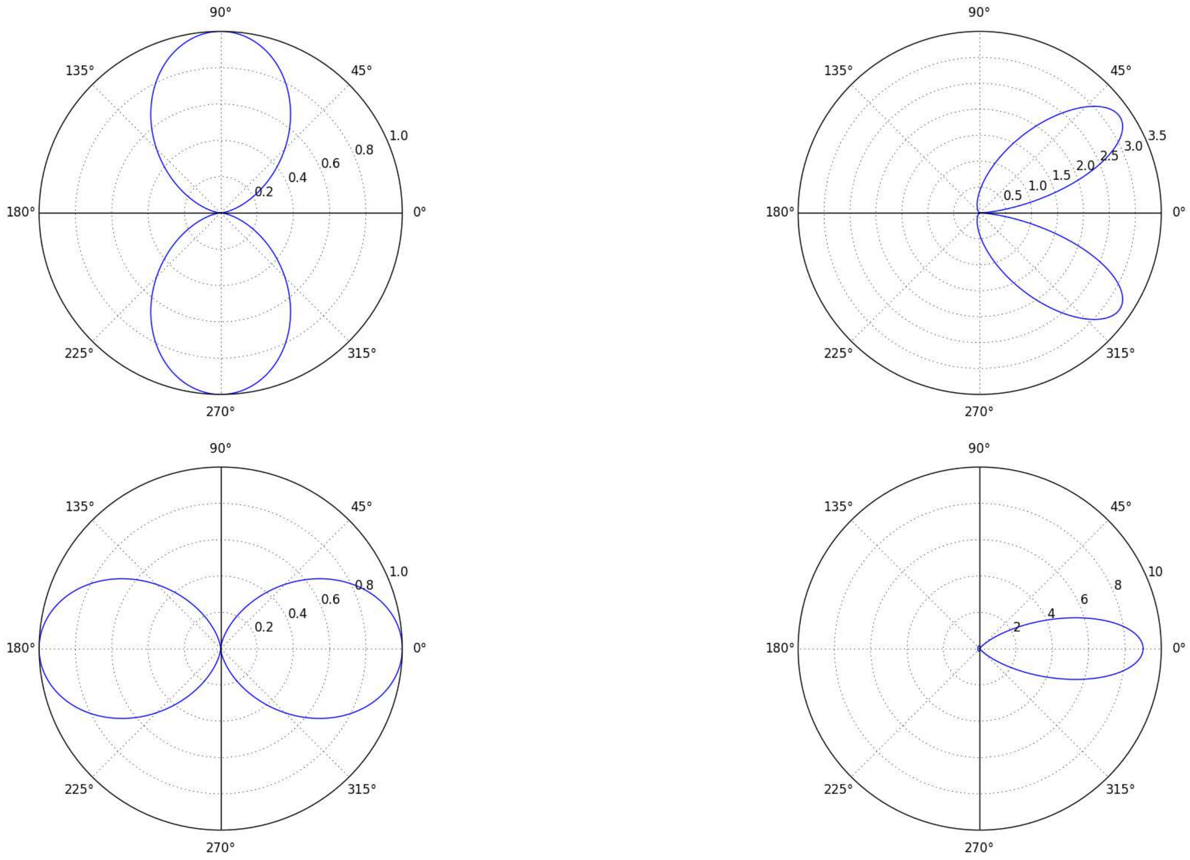

FIGURE A.2: Diagrams showing the power patterns from a relativistically moving charge. The diagrams on the left are in the charge reference frame, and the diagrams on the right are for a stationary observer. The solid black line corresponds to the direction of acceleration that is producing the observed radiation. In the right panels, the charged particle is traveling at velocity, $v = 0.5c$ towards $\theta = 0^\circ$. The top panels correspond to case where the acceleration is parallel to the direction of motion (Equation A.31) and the bottom panels correspond to case where the acceleration is perpendicular to the direction of motion (Equation A.32).

Appendix B

Publication List

The following is a list of publication I either authored or co–authored to date:

1. Beswick et al. (2014); LeMMINGs e–MERLIN survey of nearby galaxies, Proceedings of the 12th European VLBI Network Symposium and Users Meeting (EVN 2014). 7–10 October 2014. Cagliari, Italy.
2. Argo et al. (2016); The nearby universe, Astronomy and Geophysics, 57, p3.36–3.39.
3. Westcott et al. (2017); A High-Resolution Radio Continuum Study Of The Dwarf Irregular Galaxy IC 10, MNRAS, 467, 2113–2126.
4. Basu et al. (2017); New insights into the interstellar medium of the dwarf galaxy IC 10: connection between magnetic fields, the radio-infrared correlation and star formation, MNRAS, 471, 337–354.
5. Williams et al. (2017); Radio jets in NGC 4151: where e–MERLIN meets HST, MNRAS, 472, 3842–3853.
6. Hindson et al. (2018); A Radio Continuum Study of Dwarf Galaxies: 6 cm Imaging of LITTLE THINGS, ApJS, 234, 29–69.
7. Dullo et al. (2018); The nuclear activity and central structure of the elliptical galaxy NGC 5322, MNRAS, 475, 4670–4682.
8. Westcott et al. (2018); A spatially resolved radio spectral index study of the dwarf irregular galaxy NGC 1569, MNRAS, 475, 5116–5132.

9. Heesen et al. (2018b); Exploring the making of a galactic wind in the starbursting dwarf irregular galaxy IC 10 with LOFAR, MNRAS, 476, 1756–1764.
10. Baldi et al. (2018); LeMMINGs - I. The e–MERLIN legacy survey of nearby galaxies. 1.5-GHz parsec-scale radio structures and cores, MNRAS, 476, 3478–3522.
11. Westcott et al. in prep; A break in NGC1569–38's spectral energy distribution?

Bibliography

Allen, G.E., Chow, K., DeLaney, T., et al., 2015. On the Expansion Rate, Age, and Distance of the Supernova Remnant G266.2-1.2 (Vela Jr.). *ApJ*, 798:82.

Alves, M.I.R., Davies, R.D., Dickinson, C., et al., 2010. Diffuse radio recombination line emission on the Galactic plane between l = 36 and 44. *MNRAS*, 405:1654.

Andersen, M., Zinnecker, H., Moneti, A., et al., 2009. The Low-Mass Initial Mass Function in the 30 Doradus Starburst Cluster. *ApJ*, 707:1347.

Angeretti, L., Tosi, M., Greggio, L., et al., 2005. The Complex Star Formation History of NGC 1569. *AJ*, 129:2203.

Argo, M., 2015. The e-MERLIN Data Reduction Pipeline. *ArXiv e-prints 1502.04936*.

Argo, M., Beswick, R., Perez-Torres, M., et al., 2016. The nearby universe. *Astronomy and Geophysics*, 57(3):3.36.

Ashley, T., Elmegreen, B.G., Johnson, M., et al., 2014. The H I Chronicles of LITTLE THINGS BCDs II: The Origin of IC 10's H I Structure. *AJ*, 148:130.

Axford, W.I., Leer, E., and Skadron, G., 1977. The acceleration of cosmic rays by shock waves. *International Cosmic Ray Conference*, 11:132.

Baade, W. and Minkowski, R., 1954. Identification of the Radio Sources in Cassiopeia, Cygnus A, and Puppis A. *ApJ*, 119:206.

Bagchi, M., 2013. Luminosities of Radio Pulsars. *International Journal of Modern Physics D*, 22:1330021.

Baldi, R.D., Williams, D.R.A., McHardy, I.M., et al., 2018. LeMMINGs - I. The eMERLIN legacy survey of nearby galaxies. 1.5-GHz parsec-scale radio structures and cores. *MNRAS*, 476:3478.

Banerjee, A., Jog, C.J., Brinks, E., et al., 2011. Theoretical determination of H I vertical scale heights in the dwarf galaxies DDO 154, Ho II, IC 2574 and NGC 2366. *MNRAS*, 415:687.

Basu, A. and Roy, S., 2013. Magnetic fields in nearby normal galaxies: energy equipartition. *MNRAS*, 433:1675.

Basu, A., Roychowdhury, S., Heesen, V., et al., 2017. New insights into the interstellar medium of the dwarf galaxy IC 10: connection between magnetic fields, the radio-infrared correlation and star formation. *MNRAS*, 471:337.

Bauer, F.E. and Brandt, W.N., 2004. Chandra and Hubble Space Telescope Confirmation of the Luminous and Variable X-Ray Source IC 10 X-1 as a Possible Wolf-Rayet, Black Hole Binary. *ApJ*, 601:L67.

Beck, R., 2015. Magnetic fields in spiral galaxies. *Astronomy & Astrophysics Review*, 24:4.

Beck, R., Brandenburg, A., Moss, D., et al., 1996. Galactic Magnetism: Recent Developments and Perspectives. *Annual Review of Astronomy and Astrophysics*, 34:155.

Beck, R. and Krause, M., 2005. Revised equipartition and minimum energy formula for magnetic field strength estimates from radio synchrotron observations. *Astronomische Nachrichten*, 326:414.

Bell, A.R., 1978a. The acceleration of cosmic rays in shock fronts. I. *MNRAS*, 182:147.

Bell, A.R., 1978b. The acceleration of cosmic rays in shock fronts. II. *MNRAS*, 182:443.

Bell, A.R., 2004. Turbulent amplification of magnetic field and diffusive shock acceleration of cosmic rays. *MNRAS*, 353:550.

Bell, E.F., 2003. Estimating Star Formation Rates from Infrared and Radio Luminosities: The Origin of the Radio-Infrared Correlation. *ApJ*, 586:794.

Bendo, G.J., Galliano, F., and Madden, S.C., 2012. MIPS 24-160 μm photometry for the Herschel-SPIRE Local Galaxies Guaranteed Time Programs. *MNRAS*, 423:197.

Bennett, C.L., Hill, R.S., Hinshaw, G., et al., 2003. First-Year Wilkinson Microwave Anisotropy Probe (WMAP) Observations: Foreground Emission. *ApJ*, 148:97.

Berkhuijsen, E.M., 1984. Supernova rate and the number of supernova remnants in M31, M33 and the Galaxy. *A&A*, 140:431.

Berkhuijsen, E.M., 1986. Properties of supernova remnants at known distances. I - Surface brightness and radio spectral index. *A&A*, 166:257.

Berta, S., Magnelli, B., Nordon, R., et al., 2011. Building the cosmic infrared background brick by brick with Herschel/PEP. *A&A*, 532:A49.

Beswick, R., Argo, M.K., Evans, R., et al., 2014. LeMMINGs e-MERLIN survey of nearby galaxies. In *Proceedings of the 12th European VLBI Network Symposium and Users Meeting (EVN 2014). 7-10 October 2014. Cagliari, Italy.*, page 10.

Beswick, R.J., Riley, J.D., Marti-Vidal, I., et al., 2006. 15 years of very long baseline interferometry observations of two compact radio sources in Messier 82. *MNRAS*, 369:1221.

Béthermin, M., Dole, H., Beelen, A., et al., 2010. Spitzer deep and wide legacy mid- and far-infrared number counts and lower limits of cosmic infrared background. *A&A*, 512:A78.

Biermann, P., 1976. On the radio continuum flux from the disks of spiral galaxies. *A&A*, 53:295.

Bigiel, F., Leroy, A., Walter, F., et al., 2008. The Star Formation Law in Nearby Galaxies on Sub-Kpc Scales. *AJ*, 136:2846.

Bigiel, F., Leroy, A., Walter, F., et al., 2010. Extremely Inefficient Star Formation in the Outer Disks of Nearby Galaxies. *AJ*, 140:1194.

Blandford, R.D. and Ostriker, J.P., 1978. Particle acceleration by astrophysical shocks. *ApJ*, 221:L29.

Bolton, J.G. and Stanley, G.J., 1949. The Position and Probable Identification of the Source of the Galactic Radio-Frequency Radiation Taurus-A. *Australian Journal of Scientific Research A Physical Sciences*, 2:139.

Bonato, M., Negrello, M., Mancuso, C., et al., 2017. Does the evolution of the radio luminosity function of star-forming galaxies match that of the star formation rate function? *MNRAS*, 469:1912.

Bot, C., Ysard, N., Paradis, D., et al., 2010. Submillimeter to centimeter excess emission from the Magellanic Clouds. II. On the nature of the excess. *A&A*, 523:A20.

Bozzetto, L.M., Filipovic, M.D., Crawford, E.J., et al., 2010. Multifrequency Radio Observations of a SNR in the LMC. The Case of SNR J0527-6549 (DEM L204). *Serbian Astronomical Journal*, 181:43.

Brandt, W.N., Ward, M.J., Fabian, A.C., et al., 1997. ROSAT HRI observations of the Local Group galaxies IC 10, NGC 147 and NGC 185. *MNRAS*, 291:709.

Burstein, D. and Heiles, C., 1982. Reddenings derived from H I and galaxy counts - Accuracy and maps. *AJ*, 87:1165.

Callingham, J.R., Gaensler, B.M., Ekers, R.D., et al., 2015. Broadband Spectral Modeling of the Extreme Gigahertz-peaked Spectrum Radio Source PKS B0008-421. *ApJ*, 809:168.

Calzetti, D., 1997. Reddening and Star Formation in Starburst Galaxies. *AJ*, 113:162.

Calzetti, D., Kennicutt, R.C., Engelbracht, C.W., et al., 2007. The Calibration of Mid-Infrared Star Formation Rate Indicators. *ApJ*, 666:870.

Calzetti, D., Wu, S.Y., Hong, S., et al., 2010. The Calibration of Monochromatic Far-Infrared Star Formation Rate Indicators. *ApJ*, 714:1256.

Caplan, J. and Deharveng, L., 1986. Extinction and reddening of H II regions in the Large Magellanic Cloud. *A&A*, 155:297.

Cardelli, J.A., Clayton, G.C., and Mathis, J.S., 1989. The relationship between infrared, optical, and ultraviolet extinction. *ApJ*, 345:245.

Case, G.L. and Bhattacharya, D., 1998. A New Σ-D Relation and Its Application to the Galactic Supernova Remnant Distribution. *ApJ*, 504:761.

Charbonnel, C., Meynet, G., Maeder, A., et al., 1993. Grids of Stellar Models - Part Three - from 0.8 to 120-SOLAR-MASSES at Z=0.004. *A&A Supp.*, 101:415.

Chevalier, R.A., 1982. Self-similar solutions for the interaction of stellar ejecta with an external medium. *ApJ*, 258:790.

Chomiuk, L. and Wilcots, E.M., 2009. A Search for Radio Supernova Remnants in Four Irregular Galaxies. *AJ*, 137:3869.

Chyży, K.T., Drzazga, R.T., Beck, R., et al., 2016. The Magnetized Galactic Wind and Synchrotron Halo of the Starburst Dwarf Galaxy IC 10. *ApJ*, 819:39.

Chyży, K.T., Jurusik, W., Piotrowska, J., et al., 2018. LOFAR MSSS: Flattening low-frequency radio continuum spectra of nearby galaxies. *A&A*, 619:A36.

Chyży, K.T., Weżgowiec, M., Beck, R., et al., 2011. Magnetic fields in Local Group dwarf irregulars. *A&A*, 529:A94.

Ciliegi, P., McMahon, R.G., Miley, G., et al., 1999. A deep VLA survey at 20 CM of the ISO ELAIS survey regions. *MNRAS*, 302:222.

Clark, B.G., 1980. An efficient implementation of the algorithm 'CLEAN'. *A&A*, 89:377.

Clark, D.H. and Caswell, J.L., 1976. A study of galactic supernova remnants, based on Molonglo-Parkes observational data. *MNRAS*, 174:267.

Clements, D.L., Bendo, G., Pearson, C., et al., 2011. The AKARI Deep Field-South: Spitzer 24- and 70-μm observations, catalogues and counts. *MNRAS*, 411:373.

Condon, J.J., 1983. Strong radio sources in bright spiral galaxies. III - Disk emission. *ApJ*, 53:459.

Condon, J.J., 1992. Radio emission from normal galaxies. *Annual Review of Astronomy and Astrophysics*, 30:575.

Condon, J.J., Condon, M.A., Gisler, G., et al., 1982a. Strong radio sources in bright spiral galaxies. II - Rapid star formation and galaxy-galaxy interactions. *ApJ*, 252:102.

Condon, J.J., Condon, M.A., and Hazard, C., 1982b. Complete samples of active extragalactic objects. I - A 1411-MHz VLA survey centered on alpha = 12h04m, delta = +11 deg 30 arcmin. *AJ*, 87:739.

Condon, J.J., Cotton, W.D., and Broderick, J.J., 2002. Radio Sources and Star Formation in the Local Universe. *AJ*, 124:675.

Condon, J.J., Cotton, W.D., Greisen, E.W., et al., 1998. The NRAO VLA Sky Survey. *AJ*, 115:1693.

Condon, J.J. and Mitchell, K.J., 1982. Complete samples of active extragalactic objects. II - A deep 1.452-GHz VLA survey centered on alpha = 08h 52m 15s, delta = +17deg 16 arcmin. *AJ*, 87:1429.

Condon, J.J. and Yin, Q.F., 1990. A new starburst model applied to the clumpy irregular galaxy Markarian 325. *ApJ*, 357:97.

Cornwell, T.J., 2008. Multiscale CLEAN Deconvolution of Radio Synthesis Images. *IEEE Journal of Selected Topics in Signal Processing*, 2:793.

Crawford, E.J., Filipovic, M.D., de Horta, A.Y., et al., 2008. Radio-Continuum Study of the Supernova Remnants in the Large Magellanic Cloud - An SNR with a Highly Polarised Breakout Region - SNR J0455-6838. *Serbian Astronomical Journal*, 177:61.

Crowther, P.A., 2007. Physical Properties of Wolf-Rayet Stars. *Annual Review of Astronomy and Astrophysics*, 45:177.

Crowther, P.A., Drissen, L., Abbott, J.B., et al., 2003. Gemini observations of Wolf-Rayet stars in the Local Group starburst galaxy IC 10. *A&A*, 404:483.

de Horta, A.Y., Filipović, M.D., Bozzetto, L.M., et al., 2012. Multi-frequency study of supernova remnants in the Large Magellanic Cloud. The case of LMC SNR J0530-7007. *A&A*, 540:A25.

de Vaucouleurs, G., de Vaucouleurs, A., Corwin, Jr., H.G., et al., 1991. *Third Reference Catalogue of Bright Galaxies. Volume I: Explanations and references. Volume II: Data for galaxies between* 0^h *and* 12^h*. Volume III: Data for galaxies between* 12^h *and* 24^h*.*

Deeg, H.J., Duric, N., and Brinks, E., 1997. Star formation histories in H II galaxies. I. Optical and radio observations. *A&A*, 323:323.

Demers, S., Battinelli, P., and Letarte, B., 2004. A Carbon star approach to IC 10: Distance and correct size. *A&A*, 424:125.

Devost, D., Roy, J.R., and Drissen, L., 1997. The Ionized Gas in the Aftermath of a Starburst: The Case of NGC 1569. *ApJ*, 482:765.

Dickinson, C., Ali-Haïmoud, Y., Barr, A., et al., 2018. The State-of-Play of Anomalous Microwave Emission (AME) research. *New Astronomy Reviews*, 80:1.

Dolphin, A.E., 2002. Numerical methods of star formation history measurement and applications to seven dwarf spheroidals. *MNRAS*, 332:91.

Draine, B.T., 2011. *Physics of the Interstellar and Intergalactic Medium, Princeton University Press, New Jersey. ISBN: 978-0-691-12214-4.*

Drury, L.O., 1983. An introduction to the theory of diffusive shock acceleration of energetic particles in tenuous plasmas. *Reports on Progress in Physics*, 46:973.

Dullo, B.T., Knapen, J.H., Williams, D.R.A., et al., 2018. The nuclear activity and central structure of the elliptical galaxy NGC 5322. *MNRAS*, 475:4670.

Duric, N. and Seaquist, E.R., 1986. A theoretical interetation of the Sigma-D relation for supernova remnants. *ApJ*, 301:308.

Eilek, J.A. and Arendt, P.N., 1996. The Synchrotron Spectrum of Diffuse Radio Sources: Effects of Particle and Field Distributions. *ApJ*, 457:150.

Elmegreen, B.G. and Hunter, D.A., 2015. A Star Formation Law for Dwarf Irregular Galaxies. *ApJ*, 805:145.

Eriksen, K.A., Hughes, J.P., Badenes, C., et al., 2011. Evidence for Particle Acceleration to the Knee of the Cosmic Ray Spectrum in Tycho's Supernova Remnant. *ApJ*, 728:L28.

Fabbiano, G., 2006. Populations of X-Ray Sources in Galaxies. *Annual Review of Astronomy and Astrophysics*, 44:323.

Fender, R.P. and Hendry, M.A., 2000. The radio luminosity of persistent X-ray binaries. *MNRAS*, 317:1.

Fenech, D.M., Muxlow, T.W.B., Beswick, R.J., et al., 2008. Deep MERLIN 5GHz radio imaging of supernova remnants in the M82 starburst. *MNRAS*, 391:1384.

Fermi, E., 1949. On the Origin of the Cosmic Radiation. *Physical Review*, 75:1169.

Filipovic, M.D. and Bozzetto, L.M., 2017. Supernova remnants in the Magellanic Clouds. *Publications de l'Observatoire Astronomique de Beograd*, 96:185.

Fomalont, E.B., Bridle, A.H., and Davis, M.M., 1974. Improved count of radio sources at 1400 MHz. *A&A*, 36:273.

Foreman-Mackey, D., Hogg, D.W., Lang, D., et al., 2013. emcee: The MCMC Hammer. *PASP*, 125:306.

Frayer, D.T., Fadda, D., Yan, L., et al., 2006a. Spitzer 70 and 160 μm Observations of the Extragalactic First Look Survey. *AJ*, 131:250.

Frayer, D.T., Huynh, M.T., Chary, R., et al., 2006b. Spitzer 70 Micron Source Counts in GOODS-North. *ApJ*, 647:L9.

Garnett, D.R., 1990. Nitrogen in irregular galaxies. *ApJ*, 363:142.

Geha, M., Brown, T.M., Tumlinson, J., et al., 2013. The Stellar Initial Mass Function of Ultra-faint Dwarf Galaxies: Evidence for IMF Variations with Galactic Environment. *ApJ*, 771:29.

Gelman, A., 2008. Objections to Bayesian statistics. *Bayesian Anal*, 3:445.

Georgakakis, A., Aird, J., Buchner, J., et al., 2015. The X-ray luminosity function of active galactic nuclei in the redshift interval z=3-5. *MNRAS*, 453:1946.

Gerardy, C.L. and Fesen, R.A., 2007. Discovery of extensive optical emission associated with the X-ray bright, radio faint Galactic SNR G156.2+5.7. *MNRAS*, 376:929.

Gil de Paz, A., Boissier, S., Madore, B.F., et al., 2007. The GALEX Ultraviolet Atlas of Nearby Galaxies. *ApJ*, 173:185.

Ginzburg, V.L. and Syrovatskii, S.I., 1964. *The Origin of Cosmic Rays, Macmillan, New York*.

Goggans, P.M. and Chi, Y., 2004. Using Thermodynamic Integration to Calculate the Posterior Probability in Bayesian Model Selection Problems. In G.J. Erickson and Y. Zhai, editors, *Bayesian Inference and Maximum Entropy Methods in Science and Engineering*, volume 707 of *American Institute of Physics Conference Series*, pages 59–66.

Goodman, J. and Weare, J., 2010. Ensemble samplers with affine invariance. *Communications in Applied Mathematics and Computational Science, Vol. 5, No. 1, p. 65-80, 2010*, 5:65.

Green, D.A., 2014. A catalogue of 294 Galactic supernova remnants. *Bulletin of the Astronomical Society of India*, 42:47.

Grenier, I.A., Black, J.H., and Strong, A.W., 2015. The Nine Lives of Cosmic Rays in Galaxies. *Annual Review of Astronomy and Astrophysics*, 53:199.

Greve, A., Tarchi, A., Hüttemeister, S., et al., 2002. A search for radio supernovae and supernova remnants in the region of NGC 1569's super star clusters. *A&A*, 381:825.

Grocholski, A.J., Aloisi, A., van der Marel, R.P., et al., 2008. A New Hubble Space Telescope Distance to NGC 1569: Starburst Properties and IC 342 Group Membership. *ApJ*, 686:L79.

Gruppioni, C., Ciliegi, P., Rowan-Robinson, M., et al., 1999. A 1.4-GHz survey of the southern European Large-Area ISO Survey region. *MNRAS*, 305:297.

Gruppioni, C., Zamorani, G., de Ruiter, H.R., et al., 1997. Radio observations of the Marano Field and the faint radio galaxy population. *MNRAS*, 286:470.

Guo, F., Li, S., Li, H., et al., 2012. On the Amplification of Magnetic Field by a Supernova Blast Shock Wave in a Turbulent Medium. *ApJ*, 747:98.

Gürkan, G., Hardcastle, M.J., Smith, D.J.B., et al., 2018. LOFAR/H-ATLAS: the low-frequency radio luminosity-star formation rate relation. *MNRAS*, 475:3010.

Hanbury Brown, R. and Hazard, C., 1952. Radio-Frequency Radiation from Tycho Brahe's Supernova (A.D. 1572). *Nature*, 170:364.

Hanbury Brown, R. and Hazard, C., 1959. The radio emission from normal galaxies, I. Observations of M31 and M33 at 158 Mc/s and 237 Mc/s. *MNRAS*, 119:297.

Hanbury Brown, R. and Hazard, C., 1960. The non-thermal emission from the disk of the Galaxy. *The Observatory*, 80:137.

Hancock, P.J., Murphy, T., Gaensler, B.M., et al., 2012. Aegean: Compact source finding in radio images. Astrophysics Source Code Library.

Hardcastle, M.J., 2013. Synchrotron and inverse-Compton emission from radio galaxies with non-uniform magnetic field and electron distributions. *MNRAS*, 433:3364.

Harris, D.E., 1962. The Radio Spectrum of Supernova Remnants. *ApJ*, 135:661.

Harwood, J.J., Hardcastle, M.J., Croston, J.H., et al., 2013. Spectral ageing in the lobes of FR-II radio galaxies: new methods of analysis for broad-band radio data. *MNRAS*, 435:3353.

Hastings, W.K., 1970. Monte Carlo Sampling Methods using Markov Chains and their Applications. *Biometrika, Vol. 57, No. 1, p. 97-109, 1970*, 57:97.

Heavens, A.F. and Meisenheimer, K., 1987. Particle acceleration in extragalactic sources - The role of synchrotron losses in determining the spectrum. *MNRAS*, 225:335.

Heesen, V., Brinks, E., Krause, M.G.H., et al., 2015. The non-thermal superbubble in IC 10: the generation of cosmic ray electrons caught in the act. *MNRAS*, 447:L1.

Heesen, V., Brinks, E., Leroy, A.K., et al., 2014. The Radio Continuum-Star Formation Rate Relation in WSRT SINGS Galaxies. *AJ*, 147:103.

Heesen, V., Dettmar, R.J., Krause, M., et al., 2016. Advective and diffusive cosmic ray transport in galactic haloes. *MNRAS*, 458:332.

Heesen, V., Krause, M., Beck, R., et al., 2018a. Radio haloes in nearby galaxies modelled with 1D cosmic ray transport using SPINNAKER. *MNRAS*, 476:158.

Heesen, V., Rafferty, D.A., Horneffer, A., et al., 2018b. Exploring the making of a galactic wind in the starbursting dwarf irregular galaxy IC 10 with LOFAR. *MNRAS*, 476:1756.

Heesen, V., Rau, U., Rupen, M.P., et al., 2011. Deep Radio Continuum Imaging of the Dwarf Irregular Galaxy IC 10: Tracing Star Formation and Magnetic Fields. *ApJ*, 739:L23.

Helou, G., Soifer, B.T., and Rowan-Robinson, M., 1985. Thermal infrared and nonthermal radio - Remarkable correlation in disks of galaxies. *ApJ*, 298:L7.

Hess, V.F., 1912. Über Beobachtungen der durchdringenden Strahlung bei sieben Freiballonfahrten. *Physikalische Zeitschrift*, 13:1084.

H.E.S.S. Collaboration, Abdalla, H., Abramowski, A., et al., 2018. The H.E.S.S. Galactic plane survey. *A&A*, 612:A1.

Hewish, A., Bell, S.J., Pilkington, J.D.H., et al., 1968. Observation of a Rapidly Pulsating Radio Source. *Nature*, 217:709.

Hindson, L., Johnston-Hollitt, M., Hurley-Walker, N., et al., 2016. A Large-Scale, Low-Frequency Murchison Widefield Array Survey of Galactic H ii Regions between 260 $< l <$ 340. *Publications of the Astronomical Society of Australia*, 33:e020.

Hindson, L., Kitchener, G., Brinks, E., et al., 2018. A Radio Continuum Study of Dwarf Galaxies: 6 cm Imaging of LITTLE THINGS. *ApJ*, 234:29.

Hodge, P. and Lee, M.G., 1990. The H II regions of IC 10. *PASP*, 102:26.

Hogg, D.W., Bovy, J., and Lang, D., 2010. Data analysis recipes: Fitting a model to data. *ArXiv e-prints 1008.4686*.

Hopkins, A.M., Afonso, J., Chan, B., et al., 2003. The Phoenix Deep Survey: The 1.4 GHz Microjansky Catalog. *AJ*, 125:465.

Hu, H., 2009. Status of the EAS studies of cosmic rays with energy below 10**16 eV. *arXiv e-prints 0911.3034*.

Hubeny, I. and Mihalas, D., 2014. *Theory of Stellar Atmospheres, Princeton University Press, New Jersey*.

Hummer, D.G. and Storey, P.J., 1987. Recombination-line intensities for hydrogenic ions. I - Case B calculations for H I and He II. *MNRAS*, 224:801.

Hunter, D.A., 2001. The Stellar Population and Star Clusters in the Unusual Local Group Galaxy IC 10. *ApJ*, 559:225.

Hunter, D.A. and Elmegreen, B.G., 2004. Star Formation Properties of a Large Sample of Irregular Galaxies. *AJ*, 128:2170.

Hunter, D.A., Elmegreen, B.G., Dupuy, T.J., et al., 2003. Cluster Mass Functions in the Large and Small Magellanic Clouds: Fading and Size-of-Sample Effects. *AJ*, 126:1836.

Hunter, D.A., Ficut-Vicas, D., Ashley, T., et al., 2012. Little Things. *AJ*, 144:134.

Hunter, D.A., O'Connell, R.W., Gallagher, J.S., et al., 2000. The Star Clusters in the Starburst Irregular Galaxy NGC 1569. *AJ*, 120:2383.

Hunter, D.A., Shaya, E.J., Holtzman, J.A., et al., 1995. The Intermediate Stellar Mass Population in R136 Determined from Hubble Space Telescope Planetary Camera 2 Images. *ApJ*, 448:179.

Ilovaisky, S.A. and Lequeux, J., 1972. A Study of Galactic Supernova Remnants. II. Supernova Rate, Galactic Radio Emission and Pulsars. *A&A*, 20:347.

Israel, F.P., 1980. Radio observations of H II regions in external galaxies. III - Thermal emission, H II regions and star formation in 14 late-type galaxies. *A&A*, 90:246.

Israel, F.P., 1988. A detailed study of the post-starburst galaxy NGC 1569. I - Global parameters and starburst properties. *A&A*, 194:24.

Israel, F.P. and de Bruyn, A.G., 1988. Synchrotron radiation losses in the post-starburst galaxy NGC 1569. *A&A*, 198:109.

Jaffe, W., Meisenheimer, K., Röttgering, H.J.A., et al., 2004. The central dusty torus in the active nucleus of NGC 1068. *Nature*, 429:47.

Jaffe, W.J. and Perola, G.C., 1973. Dynamical Models of Tailed Radio Sources in Clusters of Galaxies. *A&A*, 26:423.

James, P.A., Shane, N.S., Knapen, J.H., et al., 2005. The Hα Galaxy Survey. II. Extinction and [NII] corrections to Hα fluxes. *A&A*, 429:851.

Janka, H.T., 2012. Explosion Mechanisms of Core-Collapse Supernovae. *Annual Review of Nuclear and Particle Science*, 62:407.

Jarrett, T.H., Chester, T., Cutri, R., et al., 2003. The 2MASS Large Galaxy Atlas. *AJ*, 125:525.

Jenkins, C.R., 1984. ARP 91 - Interaction and star formation in a galaxy pair. *ApJ*, 277:501.

Ji, S., Oh, S.P., Ruszkowski, M., et al., 2016. The efficiency of magnetic field amplification at shocks by turbulence. *MNRAS*, 463:3989.

Johnson, M., 2013. Determining the Nature of the Extended H I Structure around LITTLE THINGS Dwarf Galaxy NGC 1569. *AJ*, 145:146.

Johnson, M., Hunter, D.A., Oh, S.H., et al., 2012. The Stellar and Gas Kinematics of the LITTLE THINGS Dwarf Irregular Galaxy NGC 1569. *AJ*, 144:152.

Jurusik, W., Drzazga, R.T., Jableka, M., et al., 2014. Magnetic fields and star formation in low-mass Magellanic-type and peculiar galaxies. *A&A*, 567:A134.

Kapińska, A.D., Staveley-Smith, L., Crocker, R., et al., 2017. Spectral Energy Distribution and Radio Halo of NGC 253 at Low Radio Frequencies. *ApJ*, 838:68.

Kass, R.E. and Raftery, A.E., 1995. Bayes factors. *Journal of the American Statistical Association*, 90(430):773.

Kellermann, K.I. and Verschuur, G.L., 1988. *Galactic and extragalactic radio astronomy (2nd edition), Springer, New York*.

Kennicutt, R.C., Calzetti, D., Aniano, G., et al., 2011. KINGFISH – Key Insights on Nearby Galaxies: A Far-Infrared Survey with Herschel: Survey Description and Image Atlas. *PASP*, 123:1347.

Kennicutt, R.C. and Evans, N.J., 2012. Star Formation in the Milky Way and Nearby Galaxies. *Annual Review of Astronomy and Astrophysics*, 50:531.

Kennicutt, Jr., R.C., 1983. The rate of star formation in normal disk galaxies. *ApJ*, 272:54.

Kennicutt, Jr., R.C., 1998. Star Formation in Galaxies Along the Hubble Sequence. *Annual Review of Astronomy and Astrophysics*, 36:189.

Kennicutt, Jr., R.C., Hao, C.N., Calzetti, D., et al., 2009. Dust-corrected Star Formation Rates of Galaxies. I. Combinations of Hα and Infrared Tracers. *ApJ*, 703:1672.

Kepley, A.A., Mühle, S., Everett, J., et al., 2010. The Role of the Magnetic Field in the Interstellar Medium of the Post-Starburst Dwarf Irregular Galaxy NGC 1569. *ApJ*, 712:536.

Kettenis, M., van Langevelde, H.J., Reynolds, C., et al., 2006. ParselTongue: AIPS Talking Python. In C. Gabriel, C. Arviset, D. Ponz, and S. Enrique, editors, *Astronomical Data Analysis Software and Systems XV*, volume 351 of *Astronomical Society of the Pacific Conference Series*, page 497.

Kim, M., Kim, E., Hwang, N., et al., 2009. Reddening and Distance of the Local Group Starburst Galaxy IC 10. *ApJ*, 703:816.

Klein, U., Lisenfeld, U., and Verley, S., 2018. Radio synchrotron spectra of star-forming galaxies. *A&A*, 611:A55.

Klein, U., Wielebinski, R., Haynes, R.F., et al., 1989. A new radio continuum survey of the Magellanic Clouds at 1.4 GHz. II - The radio morphology, and thermal and nonthermal emission of the LMC. *A&A*, 211:280.

Ko, H.C. and Kraus, J.D., 1955. Radio-Frequency Radiation from the Rosette Nebula. *Nature*, 176:221.

Kovalev, Y.Y., Kellermann, K.I., Lister, M.L., et al., 2005. Sub-Milliarcsecond Imaging of Quasars and Active Galactic Nuclei. IV. Fine-Scale Structure. *AJ*, 130:2473.

Krause, M., Fierlinger, K., Diehl, R., et al., 2013. Feedback by massive stars and the emergence of superbubbles. I. Energy efficiency and Vishniac instabilities. *A&A*, 550:A49.

Krymskii, G.F., 1977. A regular mechanism for the acceleration of charged particles on the front of a shock wave. *Akademiia Nauk SSSR Doklady*, 234:1306.

Labrie, K. and Pritchet, C.J., 2006. Near-Infrared [Fe II] Emission in Starburst Galaxies. I. Measured Properties. *ApJ*, 166:188.

Lacki, B.C., Thompson, T.A., and Quataert, E., 2010. The Physics of the Far-infrared-Radio Correlation. I. Calorimetry, Conspiracy, and Implications. *ApJ*, 717:1.

Large, M.I., Mathewson, D.S., and Haslam, C.G.T., 1959. A High-resolution Survey of the Andromeda Nebula at 408 Mc./S. *Nature*, 183:1250.

Larson, R.B., 1981. Turbulence and star formation in molecular clouds. *MNRAS*, 194:809.

Lee, J.H. and Lee, M.G., 2014. Properties of Optically Selected Supernova Remnant Candidates in M33. *ApJ*, 793:134.

Leitherer, C., Schaerer, D., Goldader, J.D., et al., 1999. Starburst99: Synthesis Models for Galaxies with Active Star Formation. *ApJ*, 123:3.

Lelli, F., Verheijen, M., and Fraternali, F., 2014. Dynamics of starbursting dwarf galaxies. III. A H I study of 18 nearby objects. *A&A*, 566:A71.

Lequeux, J., 1971. The Radio Continuum of Galaxies. II. The Origin of the Continuum Emission in Spiral Galaxies. *A&A*, 15:42.

Lequeux, J., 1980. Empirical Information on Star Formation in Galaxies. In A. Maeder and L. Martinet, editors, *Saas-Fee Advanced Course 10: Star Formation*, page 9999.

Lerche, I., 1980. On the spectral index distribution of supernova remnants. *A&A*, 85:141.

Leroy, A., Bolatto, A., Walter, F., et al., 2006. Molecular Gas in the Low-Metallicity, Star-forming Dwarf IC 10. *ApJ*, 643:825.

Leverenz, H., Filipović, M.D., Bojičić, I.S., et al., 2016. Radio planetary nebulae in the Small Magellanic Cloud. *Astrophysics & Space Science*, 361:108.

Lisenfeld, U., Wilding, T.W., Pooley, G.G., et al., 2004. Multifrequency radio-continuum observations of NGC 1569: evidence for a convective wind. *MNRAS*, 349:1335.

Long, K.S., Blair, W.P., Winkler, P.F., et al., 2010. The Chandra ACIS Survey of M33: X-ray, Optical, and Radio Properties of the Supernova Remnants. *ApJ*, 187:495.

Longair, M.S., 2011. *High Energy Astrophysics (3rd Edition), Cambridge University Press, Cambridge*.

Loredo, T.J., 2013. Bayesian Astrostatistics: A Backward Look to the Future. In J.M. Hilbe, editor, *Astrostatistical Challenges for the New Astronomy, Edited by Joseph M. Hilbe. Springer, 2013, p. 1013, p. 14-50*, page 1013.

Loru, S., Pellizzoni, A., Egron, E., et al., 2018. Investigating the high-frequency spectral features of SNRs Tycho, W44 and IC443 with the Sardinia Radio Telescope. *MNRAS*.

Lozinskaya, T.A. and Moiseev, A.V., 2007. A synchrotron superbubble in the IC10 galaxy: a hypernova remnant? *MNRAS*, 381:L26.

Machalski, J., 1978. The differential radio source count at 1400 MHz from the GB2 sky survey. *A&A*, 65:157.

Madden, S.C., Rémy-Ruyer, A., Galametz, M., et al., 2013. An Overview of the Dwarf Galaxy Survey. *PASP*, 125:600.

Martin, C.L., Kobulnicky, H.A., and Heckman, T.M., 2002. The Metal Content of Dwarf Starburst Winds: Results from Chandra Observations of NGC 1569. *ApJ*, 574:663.

Massardi, M., Bonaldi, A., Negrello, M., et al., 2010. A model for the cosmological evolution of low-frequency radio sources. *MNRAS*, 404:532.

Massey, P., Armandroff, T.E., and Conti, P.S., 1992. IC 10 - A ’poor cousin’ rich in Wolf-Rayet stars. *AJ*, 103:1159.

Matthews, J.H., Bell, A.R., Blundell, K.M., et al., 2017. Amplification of perpendicular and parallel magnetic fields by cosmic ray currents. *MNRAS*, 469:1849.

McMullin, J.P., Waters, B., Schiebel, D., et al., 2007. CASA Architecture and Applications. In R.A. Shaw, F. Hill, and D.J. Bell, editors, *Astronomical Data Analysis Software and Systems XVI*, volume 376 of *Astronomical Society of the Pacific Conference Series*, page 127.

McQuinn, K.B.W., Skillman, E.D., Cannon, J.M., et al., 2010. The Nature of Starbursts. II. The Duration of Starbursts in Dwarf Galaxies. *ApJ*, 724:49.

McQuinn, K.B.W., Skillman, E.D., Dalcanton, J.J., et al., 2012. The Nature of Starbursts. III. The Spatial Distribution of Star Formation. *ApJ*, 759:77.

Miller, G.E. and Scalo, J.M., 1979. The initial mass function and stellar birthrate in the solar neighborhood. *ApJ*, 41:513.

Mills, B.Y., 1959. The Radio Continuum Radiation from the Galaxy. *PASP*, 71:267.

Morrison, G.E., Owen, F.N., Dickinson, M., et al., 2010. Very Large Array 1.4 GHz Observations of the GOODS-North Field: Data Reduction and Analysis. *ApJ*, 188:178.

Mulcahy, D.D., Fletcher, A., Beck, R., et al., 2016. Modelling the cosmic ray electron propagation in M 51. *A&A*, 592:A123.

Murphy, E.J., Bremseth, J., Mason, B.S., et al., 2012. The Star Formation in Radio Survey: GBT 33 GHz Observations of Nearby Galaxy Nuclei and Extranuclear Star-forming Regions. *ApJ*, 761:97.

Murphy, E.J., Condon, J.J., Schinnerer, E., et al., 2011. Calibrating Extinction-free Star Formation Rate Diagnostics with 33 GHz Free-free Emission in NGC 6946. *ApJ*, 737:67.

Neugebauer, G., Habing, H.J., van Duinen, R., et al., 1984. The Infrared Astronomical Satellite (IRAS) mission. *ApJ*, 278:L1.

Nicholls, D.C., Jerjen, H., Dopita, M.A., et al., 2014. Nebular Metallicities in Two Isolated Local Void Dwarf Galaxies. *ApJ*, 780:88.

Nidever, D.L., Ashley, T., Slater, C.T., et al., 2013. Evidence for an Interaction in the Nearest Starbursting Dwarf Irregular Galaxy IC 10. *ApJ*, 779:L15.

Niklas, S. and Beck, R., 1997. A new approach to the radio-far infrared correlation for non-calorimeter galaxies. *A&A*, 320:54.

Nilson, P., 1973. *Uppsala general catalogue of galaxies, Uppsala Astronomiska Observatoriums Annaler, Uppsala*.

Onić, D., Urošević, D., and Leahy, D., 2017. A New Look at the Integrated Radio/Microwave Continuum Spectrum of Galactic Supernova Remnant IC 443. *AJ*, 153:32.

Pacholczyk, A.G., 1970. *Radio astrophysics. Nonthermal processes in galactic and extragalactic sources, Freeman, San Francisco*.

Padovani, P., Alexander, D.M., Assef, R.J., et al., 2017. Active galactic nuclei: what's in a name? *Astronomy & Astrophysics Review*, 25:2.

Pavlović, M.Z., Urošević, D., Vukotić, B., et al., 2013. The Radio Surface-brightness-to-Diameter Relation for Galactic Supernova Remnants: Sample Selection and Robust Analysis with Various Fitting Offsets. *ApJ*, 204:4.

Peck, L.W. and Fenech, D.M., 2013. SERPent: Automated reduction and RFI-mitigation software for e-MERLIN. *Astronomy and Computing*, 2:54.

Peel, M.W., Dickinson, C., Davies, R.D., et al., 2011. Radio to infrared spectra of late-type galaxies with Planck and Wilkinson Microwave Anisotropy Probe data. *MNRAS*, 416:L99.

Perley, R.A. and Butler, B.J., 2017. An Accurate Flux Density Scale from 50 MHz to 50 GHz. *ApJ*, 230:7.

Pivato, G., Hewitt, J.W., Tibaldo, L., et al., 2013. Fermi LAT and WMAP Observations of the Supernova Remnant HB 21. *ApJ*, 779:179.

Pooley, G.G., 1969a. 5C 3: a radio continuum survey of M 31 and its neighbourhood. *MNRAS*, 144:101.

Pooley, G.G., 1969b. Radio-frequency observations of the edge-on spiral galaxy NGC 4631. *MNRAS*, 144:143.

Prandoni, I., Gregorini, L., Parma, P., et al., 2001. The ATESP radio survey. III. Source counts. *A&A*, 365:392.

Prialnik, D., 2009. *An Introduction to the Theory of Stellar Structure and Evolution, Cambridge University Press, Cambridge, ISBN: 9780521866040*.

Randall, K.E., Hopkins, A.M., Norris, R.P., et al., 2011. An unbiased sample of bright southern compact steep spectrum and gigahertz peaked spectrum sources. *MNRAS*, 416:1135.

Rau, U. and Cornwell, T.J., 2011. A multi-scale multi-frequency deconvolution algorithm for synthesis imaging in radio interferometry. *A&A*, 532:A71.

Read, S.C., Smith, D.J.B., Gürkan, G., et al., 2018. The Far-Infrared Radio Correlation at low radio frequency with LOFAR/H-ATLAS. *MNRAS*, 480:5625.

Relaño, M., Lisenfeld, U., Vilchez, J.M., et al., 2006. Distribution of extinction and star formation in NGC 1569. *A&A*, 452:413.

Rengelink, R.B., Tang, Y., de Bruyn, A.G., et al., 1997. The Westerbork Northern Sky Survey (WENSS), I. A 570 square degree Mini-Survey around the North Ecliptic Pole. *A&A Supp.*, 124:259.

Reynolds, S.P., 2008. Supernova Remnants at High Energy. *Annual Review of Astronomy and Astrophysics*, 46:89.

Reynolds, S.P., Gaensler, B.M., and Bocchino, F., 2012. Magnetic Fields in Supernova Remnants and Pulsar-Wind Nebulae. *Space Science Reviews*, 166:231.

Richards, E.A., 2000. The Nature of Radio Emission from Distant Galaxies: The 1.4 GHZ Observations. *ApJ*, 533:611.

Rieke, G.H., Lebofsky, M.J., Thompson, R.I., et al., 1980. The nature of the nuclear sources in M82 and NGC 253. *ApJ*, 238:24.

Roychowdhury, S. and Chengalur, J.N., 2012. The radio-far-infrared correlation in the faintest star-forming dwarf galaxies. *MNRAS*, 423:L127.

Rybicki, G.B. and Lightman, A.P., 1979. *Radiative processes in astrophysics, Wiley, New York*.

Ryle, M. and Hewish, A., 1960. The synthesis of large radio telescopes. *MNRAS*, 120:220.

Sakai, S., Madore, B.F., and Freedman, W.L., 1999. Cepheid and Tip of the Red Giant Branch Distances to the Dwarf Irregular Galaxy IC 10. *ApJ*, 511:671.

Salpeter, E.E., 1955. The Luminosity Function and Stellar Evolution. *ApJ*, 121:161.

Sanna, N., Bono, G., Stetson, P.B., et al., 2009. On the Stellar Content of the Starburst Galaxy IC10. *ApJ*, 699:L84.

Scaife, A.M.M., Nikolic, B., Green, D.A., et al., 2010. Microwave observations of spinning dust emission in NGC6946. *MNRAS*, 406:L45.

Schlafly, E.F. and Finkbeiner, D.P., 2011. Measuring Reddening with Sloan Digital Sky Survey Stellar Spectra and Recalibrating SFD. *ApJ*, 737:103.

Schlegel, D.J., Finkbeiner, D.P., and Davis, M., 1998. Maps of Dust Infrared Emission for Use in Estimation of Reddening and Cosmic Microwave Background Radiation Foregrounds. *ApJ*, 500:525.

Schlickeiser, R., 2002. *Cosmic Ray Astrophysics, Springer, Berlin, ISBN 3-540-66465-3*.

Schober, J., Schleicher, D.R.G., and Klessen, R.S., 2017. Tracing star formation with non-thermal radio emission. *MNRAS*, 468:946.

Sedov, L.I., 1959. *Similarity and Dimensional Methods in Mechanics, Academic Press, New York*.

Seymour, N., McHardy, I.M., and Gunn, K.F., 2004. Radio observations of the 13^hXMM-Newton/ROSAT Deep X-ray Survey Area. *MNRAS*, 352:131.

Shalchi, A. and Schlickeiser, R., 2005. Evidence for the Nonlinear Transport of Galactic Cosmic Rays. *ApJ*, 626:L97.

Sharma, S., 2017. Markov Chain Monte Carlo Methods for Bayesian Data Analysis in Astronomy. *Annual Review of Astronomy and Astrophysics*, 55:213.

Shimwell, T.W., Röttgering, H.J.A., Best, P.N., et al., 2017. The LOFAR Two-metre Sky Survey. I. Survey description and preliminary data release. *A&A*, 598:A104.

Shklovskii, I., 1953. On the Nature of the Crab Nebula's Optical Emission. *Doklady Akademii Nauk SSR*, 91:475.

Shopbell, P.L., Buckalew, B.A., Dufour, R.J., et al., 2000. HST Observations of the Starburst-ISM Interaction in NGC 1569. In *American Astronomical Society Meeting Abstracts*, volume 32 of *Bulletin of the American Astronomical Society*, page 1531.

Shostak, G.S. and Skillman, E.D., 1989. Neutral hydrogen observations of the irregular galaxy IC 10. *A&A*, 214:33.

Simpson, C., Martínez-Sansigre, A., Rawlings, S., et al., 2006. Radio imaging of the Subaru/XMM-Newton Deep Field - I. The 100-μJy catalogue, optical identifications, and the nature of the faint radio source population. *MNRAS*, 372:741.

Strauss, M.A., Davis, M., Yahil, A., et al., 1990. A redshift survey of IRAS galaxies. I - Sample selection. *ApJ*, 361:49.

Strömgren, B., 1939. The Physical State of Interstellar Hydrogen. *ApJ*, 89:526.

Strong, A.W., Moskalenko, I.V., and Ptuskin, V.S., 2007. Cosmic-Ray Propagation and Interactions in the Galaxy. *Annual Review of Nuclear and Particle Science*, 57:285.

Subrahmanyan, R., Goss, W.M., and Malin, D.F., 2001. Radio Continuum Structure of the Orion Nebula. *AJ*, 121:399.

Tabatabaei, F.S., Schinnerer, E., Krause, M., et al., 2017. The Radio Spectral Energy Distribution and Star-formation Rate Calibration in Galaxies. *ApJ*, 836:185.

Tammann, G.A., 1982. Supernova statistics and related problems. In M.J. Rees and R.J. Stoneham, editors, *NATO Advanced Science Institutes (ASI) Series C*, volume 90 of *NATO Advanced Science Institutes (ASI) Series C*, pages 371–403.

Tang, X., 2018. Gamma-ray emission from middle-aged supernova remnants interacting with molecular clouds: the challenge for current models. *MNRAS*.

Taylor, G., 1950. The Formation of a Blast Wave by a Very Intense Explosion. I. Theoretical Discussion. *Proceedings of the Royal Society of London Series A*, 201:159.

Terzian, Y., 1968. Observations of Planetary Nebulae at Radio Wavelengths. In D.E. Osterbrock and C.R. O'dell, editors, *Planetary Nebulae*, volume 34 of *IAU Symposium*, page 87.

Thompson, T.A., Quataert, E., Waxman, E., et al., 2006. Magnetic Fields in Starburst Galaxies and the Origin of the FIR-Radio Correlation. *ApJ*, 645:186.

Thoudam, S., Rachen, J.P., van Vliet, A., et al., 2016. Cosmic-ray energy spectrum and composition up to the ankle: the case for a second Galactic component. *A&A*, 595:A33.

Tingay, S.J. and de Kool, M., 2003. An Investigation of Synchrotron Self-absorption and Free-Free Absorption Models in Explanation of the Gigahertz-peaked Spectrum of PKS 1718-649. *AJ*, 126:723.

Tinsley, B.M., 1972. Galactic Evolution. *A&A*, 20:383.

Trotta, R., Jóhannesson, G., Moskalenko, I.V., et al., 2011. Constraints on Cosmic-ray Propagation Models from A Global Bayesian Analysis. *ApJ*, 729:106.

Truelove, J.K. and McKee, C.F., 1999. Evolution of Nonradiative Supernova Remnants. *ApJ*, 120:299.

Tsujimoto, M., Hosokawa, T., Feigelson, E.D., et al., 2006. Hard X-Rays from Ultracompact H II Regions in W49A. *ApJ*, 653:409.

Tsujimoto, T., Nomoto, K., Yoshii, Y., et al., 1995. Relative frequencies of Type Ia and Type II supernovae in the chemical evolution of the Galaxy, LMC and SMC. *MNRAS*, 277:945.

Urošević, D., 2014. On the radio spectra of supernova remnants. *Astrophysics & Space Science*, 354:541.

Urošević, D., Pannuti, T.G., Duric, N., et al., 2005. The Σ D relation for supernova remnants in nearby galaxies. *A&A*, 435:437.

Vacca, W.D., Sheehy, C.D., and Graham, J.R., 2007. Imaging of the Stellar Population of IC 10 with Laser Guide Star Adaptive Optics and the Hubble Space Telescope. *ApJ*, 662:272.

Vallée, J.P., 1995. Magnetic Field versus Gas Density, in Different Physical Conditions. *Astrophysics & Space Science*, 234:1.

van der Kruit, P.C., Allen, R.J., and Rots, A.H., 1977. Radio continuum emission from the H II complexes and the nonthermal disc of NGC 6946. *A&A*, 55:421.

Vernetto, S. and Lipari, P., 2016. Absorption of very high energy gamma rays in the Milky Way. *Physical Review D*, 94(6):063009.

Vilella-Rojo, G., Viironen, K., López-Sanjuan, C., et al., 2015. Extracting Hα flux from photometric data in the J-PLUS survey. *A&A*, 580:A47.

Vink, J., 2006. X-ray High Resolution and Imaging Spectroscopy of Supernova Remnants. In A. Wilson, editor, *The X-ray Universe 2005*, volume 604 of *ESA Special Publication*, page 319.

Vink, J., 2008. Multiwavelength Signatures of Cosmic Ray Acceleration by Young Supernova Remnants. In F.A. Aharonian, W. Hofmann, and F. Rieger, editors, *American Institute of Physics Conference Series*, volume 1085 of *American Institute of Physics Conference Series*, pages 169–180.

Vink, J., 2012. Supernova remnants: the X-ray perspective. *Astronomy & Astrophysics Review*, 20:49.

Vink, J. and Laming, J.M., 2003. On the Magnetic Fields and Particle Acceleration in Cassiopeia A. *ApJ*, 584:758.

Völk, H.J., 1989. The correlation between radio and far-infrared emission for disk galaxies - A calorimeter theory. *A&A*, 218:67.

Völk, H.J., Berezhko, E.G., and Ksenofontov, L.T., 2005. Magnetic field amplification in Tycho and other shell-type supernova remnants. *A&A*, 433:229.

Völk, H.J., Klein, U., and Wielebinski, R., 1989. M82, the Galaxy, and the dependence of cosmic ray energy production on the supernova rate. *A&A*, 213:L12.

Waller, W.H., 1991. Relics of an eruptive starburst in NGC 1569. *ApJ*, 370:144.

Wang, B. and Heckman, T.M., 1996. Internal Absorption and the Luminosity of Disk Galaxies. *ApJ*, 457:645.

Wang, Q.D., Whitaker, K.E., and Williams, R., 2005. An XMM-Newton and Chandra study of the starburst galaxy IC 10. *MNRAS*, 362:1065.

Weiler, K.W., Panagia, N., Montes, M.J., et al., 2002. Radio Emission from Supernovae and Gamma-Ray Bursters. *Annual Review of Astronomy and Astrophysics*, 40:387.

Westcott, J., Brinks, E., Beswick, R.J., et al., 2017. A High-Resolution Radio Continuum Study Of The Dwarf Irregular Galaxy IC 10. *MNRAS*, 467:2113.

Westcott, J., Brinks, E., Hindson, L., et al., 2018. A spatially resolved radio spectral index study of the dwarf irregular galaxy NGC 1569. *MNRAS*, 475:5116.

White, R.L., Becker, R.H., Helfand, D.J., et al., 1997. A Catalog of 1.4 GHz Radio Sources from the FIRST Survey. *ApJ*, 475:479.

Wilcots, E.M. and Miller, B.W., 1998. The Kinematics and Distribution of H I in IC 10. *AJ*, 116:2363.

Williams, D.R.A., McHardy, I.M., Baldi, R.D., et al., 2017. Radio jets in NGC 4151: where eMERLIN meets HST. *MNRAS*, 472:3842.

Windhorst, R.A., Miley, G.K., Owen, F.N., et al., 1985. Sub-millijansky 1.4 GHz source counts and multicolor studies of weak radio galaxy populations. *ApJ*, 289:494.

Windhorst, R.A., van Heerde, G.M., and Katgert, P., 1984. A deep Westerbork survey of areas with multicolor Mayall 4 M plates. I - The 1412 MHz catalogue, source counts and angular size statistics. *A&A Supp.*, 58:1.

Woltjer, L., 1972. Supernova Remnants. *Annual Review of Astronomy and Astrophysics*, 10:129.

Xiao, L., Fürst, E., Reich, W., et al., 2008. Radio spectral properties and the magnetic field of the SNR S147. *A&A*, 482:783.

Yang, H. and Skillman, E.D., 1993. A nonthermal superbubble in the irregular galaxy IC 10. *AJ*, 106:1448.

Yun, M.S., Reddy, N.A., and Condon, J.J., 2001. Radio Properties of Infrared-selected Galaxies in the IRAS 2 Jy Sample. *ApJ*, 554:803.

Zavrtanik, D., 2000. The Pierre Auger Observatory. *Nuclear Physics B Proceedings Supplements*, 85:324.